CONSTRAINING SOURCE PROPERTIES OF THE 1509, 1766 and 1894 ISTANBUL EARTHQUAKES

by

Nesrin Yenihayat

B.S., Physics, Balıkesir University, 2008

M.S., Physics, Gazi University, 2012

Submitted to Kandilli Observatory and Earthquake Research Institute
in partial fulfillment of the requirements for the degree of
Doctor of Philosophy

Graduate Program in Earthquake Engineering

Boğaziçi University

2022

ACKNOWLEDGEMENTS

The successful end of this journey could not be possible with help of specific people. I would like to express my deepest appreciation and sincere gratitude to my supervisor, Prof. Dr. Eser Çaktı, for her unlimited support, extreme effort, high motivation and deep knowledge to finalize this work. Many thanks to my co-advisor Assist. Prof. Dr. Karin Şeşetyan, who generously provided knowledge and expertise. I had the pleasure of working with them throughout this experience.

An immense thanks to my committee members for their insightful comments and constructive criticism. I am extremely grateful to Prof. Dr. Deniz Mazlum, for her review and support to understand the city texture. I am deeply grateful to Prof. Dr. Ayşegül Askan Gündoğan, for her encouragement whenever I felt lost, and her precious suggestions in the study.

I would like to offer my special thanks to Prof. Dr. Erdal Şafak for his precious contributions to the methodology and content from the first day to the last. I would also like to thank Prof. Dr. Friedemann Wenzel for his continuous support since my early days at the KIT.

I wish to extend my special thanks to Dr. Shaghayegh Karimzadeh for her help with EXSIM12. I also want to express my appreciation to Mehmet Mazak, an author, for his help with the pictures taken after the 1894 earthquake. I'd like to acknowledge my colleagues in KOERI, especially to my dearest friend İpek Dolağan for her extreme help to print this work.

Finally, my deepest appreciation goes out to my family for their endless support and love. Words cannot express my gratitude to my little brother Özer Yenihayat, without whom this world would be deadly boring.

ABSTRACT

CONSTRAINING SOURCE PROPERTIES OF THE 1509, 1766 and 1894 ISTANBUL EARTHQUAKES

In this thesis, stochastic simulations were performed for the 10 September 1509, 22 May 1766, and 10 July 1894 Istanbul earthquakes to constrain their source parameters with a detailed characterisation and classification of associated damages and their distributions. Damage information was obtained as spatial distributions of observed data assembled from various sources and interpreted on the MMI scale.

Using a finite fault simulation approach, numerous scenarios were modeled with calibrated and validated source, path and site parameters. In calibration, simulations were performed for 59 recordings of the 26 September 2019 Silivri (Mw=5.8) earthquake. In order to test our model on a larger Marmara earthquake recordings obtained at 19 stations of the 17 August 1999 Kocaeli (Mw=7.4) earthquake were also simulated.

Through an iterative selection of source parameters and comparison of simulation-based synthetic intensity distributions with intensities assessed from actual damage, evaluations of source parameters of three earthquakes were made. Findings indicated that most likely the magnitude of the 1894 Istanbul earthquake was Mw=[6.8 to 6.9], and its epicenter was either at the midpoint of the Prince Islands segment with a 42 km rupture or at the intersection of the Prince Islands segment with the Izmit segment as a 60 km total rupture. The 1766 earthquake likely had a rupture length of about 80 km along the Central Marmara Fault with a magnitude of Mw=[7.0 to 7.1]. Our findings suggested that the 1509 earthquake most probably occurred as a combined rupture of the Prince Islands segment and the Central Marmara Fault, and created a 120 km rupture with a magnitude of Mw=7.6.

ÖZET

1509, 1766 ve 1894 ISTANBUL DEPREMLERİNİN KAYNAK PARAMETRE ÖZELLİKLERİNİN BELİRLENMESİ

Bu tezde, stokastik simulasyon yöntemi ile 10 Eylül 1509, 22 Mayıs 1766 ve 10 Temmuz 1894 İstanbul depremlerinin hasar dağılımları kullanılarak, söz konusu depremlerin kaynak parametreleri belirlenmiştir. Çeşitli kaynaklardan derlenen ve geniş bir alana yayılan hasar gözlem ve bilgileri MMI skalasında yorumlanmış ve bölgesel olarak değerlendirilmiştir.

Kalibre edilip doğrulanmış bölgesel kaynak, dalga yayınım ve zemin parametreleri ile stokastik sonlu fay yöntemi kullanılarak birçok deprem senaryosu modellenmiştir. Kalibrasyonda 26 Eylül 2019 Silivri (Mw=5.8) depreminin 59 istasyondaki kayıtları kullanılmıştır. Modelin büyük ölçekli bir depremdeki performansı 17 Ağustos 1999 Kocaeli (Mw=7.4) depreminin modellenmesiyle test edilmiştir.

Oluşturduğumuz model tarihi depremlerin simulasyonunda kullanılmıştır. Çok sayıda simulasyondan elde edilen sentetik şiddet dağılımları, hasar bilgisinden bulunmuş şiddet dağılımları ile karşılaştırılmış ve optimum kaynak parametreleri saptanmıştır. Buna göre, 1894 depreminin büyüklüğü Mw=[6.8 ila 6.9] arasında, merkez üstü ya 42 km fay kırılımı ile Adalar segmentinin orta noktasında, ya da toplam 60 km fay kırığı ile Adalar segmenti ile İzmit segmentinin kesişim noktasında olmalıdır. 1766 depremi, Orta Marmara fayında, toplam 80 km uzunluğundaki fay kırılımı ile gerçekleşmiş, büyüklüğü Mw=[7.0 ila 7.1] arasında olan bir depremdir. 1509 depremi ise büyük olasılıkla, Adalar segmenti ile Orta Marmara fayı üzerinde 120 km uzunluğunda bir fay kırılımı ile gerçekleşen, Mw=7.6 büyüklüğünde bir depremdir.

TABLE OF CONTENTS

ACKNOWLEDGEMENTS iii
ABSTRACT iv
ÖZET v
LIST OF FIGURES ix
LIST OF TABLES xxiv
LIST OF SYMBOLS xxviii
LIST OF ACRONYMS/ABBREVIATIONS xxx
1. INTRODUCTION 1
1.1. Purpose and Outline 1
1.2. Active Faulting 4
1.3. Background Information on Historical Earthquakes 5
1.3.1. 10 September 1509 Earthquake 6
1.3.2. 25 May 1719 Earthquake 11
1.3.3. 2 September 1754 Earthquake 13
1.3.4. 22 May 1766 Earthquake 14
1.3.5. 5 August 1766 Earthquake 19
1.3.6. 10 July 1894 Earthquake 21
1.3.7. Tsunami Effects 36
1.4. Literature Survey on Discrepancies in Source Parameter 37
2. THE GROWTH OF ISTANBUL OVER CENTURIES and ASSOCIATED BUILDING INVENTORIES 41
2.1. Brief Overview of the Population Growth and Structural Typology in Istanbul 41
2.1.1. The Fifteenth and Sixteenth Centuries 41
2.1.2. The Seventeenth and Eighteenth Centuries 45
2.1.3. The Nineteenth Century 47
2.2. Generating Building Inventories 51
2.2.1. City Maps 51
2.2.2. The Map of Istanbul in the 19th Century (Ayverdi Maps) . . . 51

2.2.3. Insurance Plan of Constantinople (Goad Maps) 52
2.2.4. German Blues 52
2.2.5. Pervititch Maps 53
2.2.6. Internet Sources 55
3. MACROSEISMIC EVALUATION OF THE HISTORICAL EVENTS 56
3.1. Basic Definitions 56
3.1.1. Vulnerability Class 56
3.1.2. Damage Grades 56
3.1.3. Intensity 57
3.1.4. Intensity Assignment Method 58
3.1.5. Instrumental Seismic Intensity Estimation Method 59
3.1.6. Conversion of Intensity Scales 61
3.2. Damage Inventories 61
3.2.1. 10 July 1894 Earthquake 64
3.2.2. 22 May 1766 Earthquake 65
3.2.3. 10 September 1509 Earthquake 65
3.3. Intensity Maps 66
3.3.1. 10 July 1894 Earthquake 66
3.3.2. 22 May 1766 Earthquake 67
3.3.3. 10 September 1509 Earthquake 68
3.4. Determination of magnitude and epicenter 69
3.4.1. The Boxer Method 70
3.4.2. Examining The Boxer method in Istanbul 71
3.4.3. Findings for the Historical Earthquakes with Boxer 72
4. STOCHASTIC APPROACH TO FINITE FAULT GROUND MOTION MODELING AND CREATING OUR MODEL; Mw 5.8 SILIVRI (ISTANBUL) CASE AND Mw 7.4 KOCAELİ CASE 75
4.1. Stochastic Approach to Finite Fault Ground Motion Modeling 75
4.1.1. Source Parameters 77
4.1.2. Regional Crustal Properties (Path Properties) 77
4.1.3. Site Effects 78

4.2. Stochastic Ground Motion Simulation of the 26 September 2019 Mw 5.8 Silivri (Istanbul) Earthquake 79
4.2.1. Background 80
4.2.2. The Earthquake 82
4.2.3. Recorded Ground Motion Data 83
4.2.4. Model Parameters and Sensitivity of Results to Parameter Values 87
4.2.5. Comparison and Validation of Simulation Results with Recorded Data 96
4.2.6. Regional Simulation and Comparison with Damage 103
4.3. Stochastic Simulation of the 17 August 1999 Mw 7.4 Kocaeli Earthquake 111
4.4. Chapter Discussions 118
5. GROUND MOTION SIMULATION FOR THE 1894, 1766 and 1509 EARTHQUAKES 121
5.1. 10 July 1894 Earthquake 123
5.2. 22 May 1766 Earthquake 143
5.3. 10 September 1509 Earthquake 158
5.4. Chapter Results 169
5.5. Discussion on Uncertainties 174
6. SUMMARY and CONCLUSIONS 175
REFERENCES 178
APPENDIX A: ILLUSTRATING CLASSIFICATION OF DAMAGE FOR THE 10 JULY 1894 ISTANBUL EARTHQUAKE 195
APPENDIX B: COMPARISON OF OBSERVED AND SIMULATED GROUND MOTIONS IN TIME AND FREQUENCY DOMAIN 218
B.1. 26 September 2019 Silivri Earthquake (59 Stations) 218
B.2. 17 August 1999 Kocaeli Earthquake (19 Stations) 223

LIST OF FIGURES

Figure 1.1. Seismicity of the Marmara Sea Region. 6

Figure 1.2. Damaged structures in Suriçi district after the 1509 earthquake, using the damage information given by Ambraseys and Finkel, (1995). Map adapted from Cplakidas (2011). 11

Figure 1.3. Assessed intensities of the 1509 earthquake by Ambraseys (2001) in MSK. 12

Figure 1.4. Damaged structures in Suriçi district after the 1766 earthquake, using the damage information given by Ambraseys and Finkel, (1995). Map adapted from Cplakidas (2011). 15

Figure 1.5. Isoseismal map prepared by Eginitis in 1894 (Eginitis, 1895). . . . 22

Figure 1.6. Pulsations of the 10 July 1894 Istanbul Earthquake Recorded by the Vicentini Micro-Seismograph at Siena (Davison, 1896). The original seismograph record has been corrected using GNU Image Manipulation Program (GIMP 2.10.30). 24

Figure 1.7. Damaged structures in Suriçi district after the 1894 earthquake, using the inventory given by Oztin, (1994). Map adapted from Cplakidas (2011). 27

Figure 1.8. Assessed intensities of the 1894 earthquake by Ambraseys (2001) in the MSK scale. A = Albania, B = Bulgaria, G = Greece, M = Macedonia, R = Rumania and T = Turkey. 28

Figure 1.9. Estimated epicenters of the 1509 event by different researchers. . . 39

Figure 1.10. Estimated epicenters of the 1766 event by different researchers. . . 40

Figure 1.11. Estimated epicenters of the 1894 event by different researchers. . . 40

Figure 2.1. Istanbul in 1532 by Matrakçı Nasuh. 1. Topkapı Palace, 2. Hagia Irene, 3:Hagia Sophia, 4. Hippodrome, 5. Ahırkapı, 6. Grand Bazaar, 7. Ibrahim Pasha Palace, 8. Beyazid Mosque, 9. Fatih Mosque, 10. The Valens Aqueduct, 11. Yedikule Fortress, 12. Kadirga Harbour, 13. City Walls, 14. Yavuz Selim Mosque, 15. Leander's Tower, 16. Galata Tower, 17. Tophane, 18. Uskudar . . 44

Figure 2.2. Expansion of the city boundaries between the 15th and 20th centuries (Kuban, 1998). 48

Figure 2.3. The Istanbul Plan in 1882 by C. Stolpe. 50

Figure 2.4. A section taken from the New Mosque (Yeni Cami) in Eminonu represented in (a) Ayverdi Maps (b) German Blues (c) Goad Maps (d) Pervititch Maps 54

Figure 2.5. Laleli Mosque and the Tayyare Apartmanları Blocks those cited as "Laleli Apartemani" on the left side and the meaning of colors used in the Pervititch maps (in Turkish and French) on the right side. . 54

Figure 3.1. Classifications used in the European Macroseismic Scale (EMS). . 57

Figure 3.2. Classification of damage to masonry buildings according to EMS-98. Drawings at the left-hand side show what is meant by the different damage grades. 58

Figure 3.3. EMS-98 Intensity assignment. Few: Sum of damaged structure in the given damage level is up to 20% of total, Many means number of damaged structure corresponds to 10% to 60% of total, and Most is when damaged buildings are between 50% to 100% of total . . . 59

Figure 3.4. Intensity estimation of the 2019 Silivri Earthquake with Sokolov's method on the estimated Fourier Spectra of the grid based simulations. 61

Figure 3.5. Damage distribution map of the 1894 earthquake. 64

Figure 3.6. Damage distribution map of the 1894 earthquake. 65

Figure 3.7. Damage distribution map of the 1766 earthquake. 66

Figure 3.8. Damage distribution map of the 1766 earthquake. 66

Figure 3.9. Damage distribution map of the 1509 earthquake. 67

Figure 3.10. Damage distribution map of the 1509 earthquake. 67

Figure 3.11. Intensity distribution of the 1894 earthquake. 68

Figure 3.12. Comparison of the obtained intensity distribution of the 1894 earthquake to isoseismals of Eginitis. 68

Figure 3.13. Intensity distribution map of the 1766 earthquake. 69

Figure 3.14. Intensity distribution map of the 1509 earthquake. 69

Figure 3.15. Rupture estimation with Boxer for the 26 September 2019 Silivri Earthquake and fault projection calculated by Karabulut et al. (2020) on the simulation based intensity map. Epicenter is represented with the red star. 72

Figure 3.16. The 1894 Earthquake Intensity Map and rupture estimation with Boxer 73

Figure 3.17. The 1766 Earthquake Intensity Map and rupture estimation with Boxer 74

Figure 3.18. The 1509 Earthquake Intensity Map and rupture estimation with Boxer 74

Figure 4.1. 26.9.2019 Silivri earthquake. The red star corresponds to the epicenter of the mainshock. Stations of the Istanbul Earthquake Rapid Response and Early Warning System that recorded the earthquake are indicated with green triangles. Red lines represent the fault segmentation in the Marmara Sea. Fault projection on ground surface and beach ball representation are also included. The fault map is compiled from Active Fault Maps of Turkey, MTA (Mineral Research and Exploration General Directorate (Emre et al., 2013). 82

Figure 4.2. Slip Distribution proposed by Karabulut et al., (2020). The red star represents the hypocenter of the 26 September 2019 Silivri earthquake. 84

Figure 4.3. Station specific PGA distribution. PGAs (white circles) estimated from the geometric mean of two horizontal components are shown. The red star represents the epicenter. 84

Figure 4.4. Effect of generic site amplification models on B site at representative station KARSO by using (a) Boore and Joyner, (1997) (Vs30=2900 m/s) (b) Atkinson and Boore, (2006) (Vs30=760 m/s) (c) Pischiutta et al., (2021) (Vs30=1163m/s). 89

Figure 4.5. Effect of generic site amplification models on PGA distribution at all of the rock stations (green color) by using (a) Boore and Joyner, 1997 (Vs30=2900 m/s) (b) Atkinson and Boore, 2006 (Vs30=760 m/s) (c) Pischiutta et al., 2021 (Vs30=1163m/s). 91

Figure 4.6. Evaluation of duration models at two randomly selected representative stations AMALI, and BUYA for path duration models (a) by Herrmann, (1985) for stations AMALI, and (b) BUYA, (c) by Boore and Thompson, (2014) for stations AMALI, and (d) BUYA. (Blue color is for simulated motion, red color is for recordings in the N and E directions) 91

Figure 4.7. Comparing observed and predicted (a) Arias intensity (b) D75 effective duration, (c) D95 effective duration versus epicentral distance and (d) Arias intensity, (e) D75 effective duration, (f) D95 effective duration versus epicentral distance. 92

Figure 4.8. Effect of different Q models. Synthetic FAS simulated using four Q models are compared with recorded FAS for station BBAIO. (a) Akinci et al., (2006) (b) Süleyman, (2018) (c) Boore, (1984) (d) Horasan et al., (1998). The models are indicated in the sub-figure captions. Qmin is taken as 60 in all models, other variables are kept the same. 94

Figure 4.9. Effect of the high frequency decay parameter, kappa, at stations GOPPL, KAPIO, and MODAI for station specific kappa (upper part), and constant kappa (below). 95

Figure 4.10. Comparing observed and predicted PGAs (a) versus epicentral distance using station specific kappa values, (b) versus Vs30 using station specific kappa values, (c) versus epicentral distance using constant kappa values, (d) versus Vs30 using constant kappa values, (colors represent NEHRP site classes). Following constant kappa values are used: B= 0.048, GR= 0.048, C=0.054, GS=0.054, and D=0.072. Observed PGAs are estimated as the geometric mean of two horizontal components. 97

Figure 4.11. Comparison of observed and simulated acceleration-time histories and FAS for selected stations at different site conditions (BUYA and HHBLI are C site class, CENLI and DATIO are B site class, USCUL is GR class, and ZYTAL is GS class) 98

Figure 4.12. Comparison of acceleration-time histories and FAS of the simulated and recorded data for the worst estimated stations. 99

Figure 4.13. Station based misfits. Stations are illustrated with triangles. Colors indicate model bias ranges: green stations are less than ± 0.4; orange stations are ± 0.5, purple stations are beyond ± 0.5. The base map is the Vs30 Map for Istanbul (IBB-OYO-KOERI, 2009). The faults are compiled from the Active Fault Map of Turkey, MTA (Mineral Research and Exploration General Directorate (Emre et al., 2013). 101

Figure 4.14. Station misfits (ratios of observed to simulated spectra) at three frequencies, 2 Hz, 6 Hz, and 13 Hz versus (a) epicentral distance and (b) Vs30. 102

Figure 4.15. Averaged model misfit obtained from the error functions of 59 stations in frequency domain. Grey lines represent 59 stations independently while the bold black line corresponds to the overall misfit. 102

Figure 4.16. Comparison of the simulated and recorded fround motions with sets of model parameters used by study of Zengin and Çaktı (2012) (upper part) and created in this study (below part) for stations AVCLI (NEHRP D site class), LAFA (NEHRP C site class), and EHAIO (NEHRP B site class). 104

Figure 4.17. Comparison of observed and predicted PGAs in the model set used by Zengin and Çaktı (2012) (a) versus epicentral distance and (b) versus Vs30, (colors represent NEHRP site classes). Observed PGAs are estimated as the geometric mean of two horizontal components. 105

Figure 4.18. Simulation based regional distribution in terms of (a) PGAs (g%), (b) PGVs (cm/s), (c) SA at T=0.2 s (g%) (d) and SA at T=1.0 s (g%) using calibrated model parameters and Vs30 Soil Classification Map of Istanbul. 106

Figure 4.19. Simulation based regional distribution in terms of (a) PGAs (g%), (b) PGVs (cm/s), (c) SA at T=0.2 s (g%) (d) and SA at T=1.0 s (g%) using calibrated model parameters and regional geology maps, QTM. 106

Figure 4.20. Comparison of the synthetics and recordings with Akkar et al., (2014) and Chiou and Youngs (2014). GMMs in terms of PGAs (g), PGVs (cm/s), and SAs at periods 0.2 and 1.0 seconds versus Boore and Joyner closest distances for generic rock and generic soil. Recordings are in terms of the geometric mean of the horizontal components. 108

Figure 4.21. Neighborhoods where damages were reported. Squares represent locations of heavily damaged buildings while circles show slight damage. Regional simulated PGAs (g%) given in colors. 110

Figure 4.22. Estimated damages for the 26 September 2019 Silivri earthquake by ELER, (ELER, 2010). On the left: distribution of slightly damaged buildings (about 5,000 in total); on the right: distribution of moderately damaged buildings (about 800 in total). Number of heavily damaged buildings are estimated about 60. 110

Figure 4.23. Locations of 19 stations and their site classes, shown as colored triangles. The red star represents the epicenter. Dashed line corresponds to used fault model in this study. 113

Figure 4.24. Comparison of acceleration-time histories and FAS of the simulated and recorded data for the best estimated stations. 115

Figure 4.25. Comparison of acceleration-time histories and FAS of the simulated and recorded data for the worst estimated stations. 116

Figure 4.26. Comparison of the synthetic and recorded PGAs with Akkar et al., (2014), and Chiou and Youngs (2014). 117

Figure 4.27. Averaged model misfit obtained from the error functions of 19 stations. Grey lines represent 19 stations while the bold black line corresponds to average misfit. 117

Figure 4.28. Comparison of intensities estimated from real (horizontal axis) and synthetic recordings (vertical axis) for the 1999 Kocaeli earthquake. 118

Figure 4.29. Model misfit comparison with Yalçınkaya in terms of six stations and their average model bias. 119

Figure 5.1. RMSE Regions of the 1894 Earthquake 124

Figure 5.2. Representation of estimated epicenter locations for the 1894 Earthquake (a) the PIS (b) Izmit Segment (c) Çınarcık Fault (d) Combined Rupture Scenario 124

Figure 5.3. The 1894 Earthquake PIS S2 Scenario First Assessment 126

Figure 5.4. The 1894 Earthquake PIS S2 Scenario Magnitude and Stress Assessment 128

Figure 5.5. Slip distribution generated by RUPGEN along the PIS 129

Figure 5.6. The 1894 Earthquake PIS S2 Scenario Slip Assessment 130

Figure 5.7. The 1894 Earthquake PIS S3 Scenario Magnitude and Stress Assessment 131

Figure 5.8. The 1894 Earthquake PIS S3 Different Rupture Dimensions 132

Figure 5.9. The 1894 Earthquake PIS S3 Slip Assessment 132

Figure 5.10. The 1894 Earthquake Izmit Segment Magnitude and Stress Assessment 135

Figure 5.11. The 1894 Earthquake Izmit Segment Rupture Dimension Assessment 136

Figure 5.12. The 1894 Earthquake Çınarcık Fault Assessment 137

Figure 5.13. The 1894 Earthquake Combined Rupture Assessment 138

Figure 5.14. The 1894 Earthquake Final Assessment 139

Figure 5.15. The 1894 Earthquake Stochastic Based Intensity Distribution for (a) the Prince Islands Scenario, (b) Combined Rupture Scenario . 140

Figure 5.16. The 1894 Earthquake Stochastic Based Intensity Distribution for (a) the Prince Islands Scenario, (b) the Combined Rupture Scenario 141

Figure 5.17. Comparison of the best estimated simulation scenarios with GMMs for the 1894 Earthquake (a) the PIS, S2 Scenario with Mw 6.8 (b) the PIS, S3 Scenario with Mw 6.7 (c) Çınarcık Fault Scenario, with Mw 6.9 (d) Izmit Segment, S1 Scenario with Mw 7.0 (e) Izmit Segment, S1 Scenario with Mw 7.1 (f) Izmit Segment, S3 Scenario with Mw 6.8 144

Figure 5.18. RMSE Regions of the 1766 Earthquake 145

Figure 5.19. Representation of estimated epicenter locations for the 1766 Earthquake (a) the CMF Scenarios (b) Combined Rupture Scenario . . 145

Figure 5.20. The 1766 Earthquake CMF S1 Scenario Magnitude and Stress Drop Assessment 147

Figure 5.21. The 1766 Earthquake CMF S2 Scenario Magnitude and Stress Drop Assessment 148

Figure 5.22. The 1766 Earthquake CMF S1 Scenario Rupture Length Assessment 149

Figure 5.23. The 1766 Earthquake CMF S2 Scenario Rupture Length Assessment 150

Figure 5.24. The 1766 Earthquake CMF S1 Scenario Slip Assessment 151

Figure 5.25. The 1766 Earthquake CMF S2 Scenario Slip Assessment 152

Figure 5.26. The 1766 Earthquake Combined Scenario Case 1 Assessment . . . 153

Figure 5.27. The 1766 Earthquake Combined Scenario Case 2 Assessment . . . 154

Figure 5.28. The 1766 Earthquake Final Assessment 154

Figure 5.29. Comparison of the best estimated simulation scenarios with GMMs for the 1766 Earthquake for the CMF (a) S1 Scenario with Mw 6.9 (b) S1 Scenario with Mw 7.0 (c) S1 Scenario, with Mw 7.1 (d) S2 Scenario with Mw 7.1 (e) S2 Scenario with Mw 7.2 (66 km Rupture) (f) S2 Scenario with Mw 7.4 RupGEN 155

Figure 5.30. The 1766 Earthquake Stochastic Based Intensity Distribution for the CMF (a) S1 Scenario, (b) S2 Scenario 156

Figure 5.31. The 1766 Earthquake Stochastic Based Intensity Distribution for the CMF (a) S1 Scenario, (b) S2 Scenario 157

Figure 5.32. RMSE Regions of the 1509 Earthquake 158

Figure 5.33. Representation of Estimated Epicenter locations for the 1509 Earthquake (a) the CMF Scenarios (b) Combined Scenario 158

Figure 5.34. The 1509 Earthquake, Scenario S1 on the CMF, Magnitude and Stress Drop Assessment 160

Figure 5.35. The 1509 Earthquake, Scenario S2 on the CMF, Magnitude and Stress Drop Assessment 161

Figure 5.36. The 1509 Earthquake Rupture Dimension Assessment 162

Figure 5.37. The 1509 Earthquake Slip Assessment for Scenario S1 on CMF . . 163

Figure 5.38. The 1509 Earthquake Slip Assessment for Different Rupture Lengths on CMF 164

Figure 5.39. The 1509 Earthquake Magnitude and Stress Drop Assessment for the Combined Rupture Scenario 166

Figure 5.40. The 1509 Earthquake Final Assessment 167

Figure 5.41. Comparison of the best estimating scenarios with GMMs for the 1509 Earthquake for the CMF (a) S1 Scenario with Mw 7.3 (b) S1 Scenario with Mw 7.4 Specialized Slip (c) S2 Scenario, with Mw 7.4 (d) S1 Scenario with Mw 7.6 168

Figure 5.42. The 1509 Earthquake Synthetic Intensity Distribution for The Combined Rupture Scenario of Mw 7.6 for (a) Istanbul Region, (b) Marmara Region. 169

Figure 5.43. The 1894 Earthquake Synthetic Intensity Distribution for (a) the Prince Islands Scenario, (b) Combined Rupture Scenario (Circles Represent Intensities Estimated Using the Damage Information). . 171

Figure 5.44. The 1766 Earthquake Stochastic Based Intensity Distribution for (a) the CMF S1 Scenario, (b) the Central Marmara S2 Scenario (Circles Represent Estimated Intensities Using the Damage Distribution Maps). 172

Figure 5.45. The 1509 Earthquake Synthetic Intensity Distribution for The Combined Rupture Scenario with Mw 7.6 for (a) Istanbul Region, (b) Marmara Region (Circles Represent Estimated Intensities Using Damage Information). 173

Figure A.1. Eminönü, Unkapanı Mosque Damage Definition: Spire of the minaret collapsed. Damage Level: D1 196

Figure A.2. Fatih, Kariye Mosque Damage Definition: The minaret demolished from the balcony level (half part). The madrasa was partially ruined. Damage Level: D2, D4 197

Figure A.3. Kınalıada, Panagia Greek Church Damage Definition: The walls were largely cracked. Damage Level: D3 198

Figure A.4. Fatih, Topkapı City Walls Damage Definition: Demolition of the bastions and city walls in Topkapı. Damage Level: D4 199

Figure A.5. Heybeliada, Ecole de Theologie Damage Definition: Its several buildings have been dislocated and became inhabitable. Damage Level: D4 200

Figure A.6. Damage Level of Edirnekapı, with different views from inside and outside of the city walls. Damage Definition: The Edirnekapi Gate collapsed and five shops located under the gates were destroyed. Damage Level: D5 201

Figure A.7. Murat Paşa Mosque Damage Definition: Damaged. Damage Level: D3 202

Figure A.8. Grand Bazaar Yağlıkçılar Street Damage Definition: Completely collapsed. Damage Level: D4/D5 203

Figure A.9. A kebap house and three other shops next to the Nuruosmaniye Gate. Damage Definition: Completely collapsed. Damage Level: D5 204

Figure A.10. Grand Bazaar Çadırcılar Street. Damage Definition: Çadırcılar Gate collapsed and one shop has been rebuilted. Damage Level: D5 205

Figure A.11. Fatih Mosque Damage Definition: One of the minaret in the direction of the Black Sea fell and the top of the other minaret was curved. Some of the courtyard wall collapsed. Damage Level: D1, D4 206

Figure A.12. Amcazade Hüseyin Paşa Madrasah Damage Definition: Its several domes were destroyed and some parts of the madrasa were damaged. Damage Level: D4 207

Figure A.13. Süleyman Paşa Inn Damage Definition: Collapsed. Some parts were completely destroyed. Some part and the soda factory located in the middle of the inn were demolished. Damage Level: D4 . . . 208

Figure A.14. Kantarcılar / Sarı Demir /Sarı Timur Mosque Damage Definition: The wall was destroyed. Half of its minaret was destroyed. Damage Level: D4, D4 209

Figure A.15. Kaptan İbrahim Paşa Mosque, School and Lodge Damage Definition: The front of the school and its roof were damaged. Damage Level: According to picture, damage level is D4, but the definition expresses a slight damage, D2.) 210

Figure A.16. Vezir Inn. Damage Definition: Mostly demolished/ Partly collapsed /Ruined. Damage Level: D4 211

Figure A.17. Matbaa-i Osmaniye. Damage Definition: Its benches were disturbed. Damage Level: The picture shows D3, but the definition expresses more slight damage, D1. 212

Figure A.18. Atik Ali Paşa Madrasah. Damage Definition: Damaged, completely collapsed. Damage Level: The picture shows D4 while the definition describes D5 213

Figure A.19. Sofcular Inn Damage Definition: Its walls were damaged and became dilapidated, several rooms collapsed. Damage Level: D4 . . 214

Figure A.20. Maliye Nezareti Damage Definition: Damaged, its eaves fell and the walls partly collapsed. Damage Level: D4 215

Figure A.21. Coppersmiths close to the tramway in Beyazıt. Damage Definition: Completely collapsed. Damage Level: D5 216

Figure A.22. Kemankeş Kara Mustafa Paşa Madrasah. Damage Definition: Partly ruined. Damage Level: D4 217

LIST OF TABLES

Table 1.1 Number of the damaged dwellings different damage levels in the corresponding regions. The numbers were obtained from the official allowance list (Iane-i Musabin Commission) for the victims of the 10 July 1894 earthquake (Özkılıç, 2015, page: 321). (*: Total number is given here as written on the list.) 34

Table 1.2. Epicenter, Intensity, and Magnitude Evaluation by different researchers for the 1509 Istanbul Earthquake. 38

Table 1.3. Epicenter, Intensity, and Magnitude Evaluation by different researchers for the 1766 Istanbul Earthquake. 38

Table 1.4. Epicenter, Intensity, and Magnitude Evaluation by different researchers for the 1894 Istanbul Earthquake. 39

Table 3.1. Calibrated coefficients of Boxer Code for Turkey (N_{EQ} is number of earthquakes used in the corresponding intensity, σ is standard deviation of the model; R^2 is percentage of the coefficient of variation). 71

Table 3.2. Comparison of the source parameters estimated by Boxer to the findings by Karabulut et al., (2020) for the 26 September 2019 Silivri Earthquake. 72

Table 4.1. Source Parameters of the 26 September 2019 Silivri Event 83

Table 4.2 Station information (Repi is epicentral distance; B, C, and D are NEHRP soil classes, GS is generic soil, and GR is generic rock). . . 85

Table 4.3. Input Model Parameters and Parameter Values Used in the Simulation of the 26 September 2019 Silivri Earthquake by EXSIM12 . 90

Table 4.4. Differences in Parameter Values between this study and Zengin and Çaktı, (2012) 103

Table 4.5. Reported damages for the 26 September 2019 Silivri earthquake . . 109

Table 4.6 Station information of the 1999 Kocaeli earthquake (Repi is epicentral distance; B, C, and D are NEHRP soil classes, GS is generic soil, and GR is generic rock). 111

Table 4.7 Input Model Parameters and Parameter Values Used in the Simulations of the 17 August 1999 Kocaeli Earthquake by EXSIM12. . 113

Table 5.1. Input model parameters Used in the Simulation of the 10 July 1894 Earthquake 125

Table 5.2. The 1894 Earthquake Epicenter Assessment Along the PIS 126

Table 5.3. The 1894 Earthquake Magnitude Assessment for S2 Scenario on the PIS 126

Table 5.4. The 1894 Earthquake Stress Drop Assessment for S2 Scenario on the PIS 127

Table 5.5. The 1894 Earthquake Magnitude Stress Assessment for S2 Scenario on the PIS 127

Table 5.6. The 1894 Earthquake Hypocentral Depth Assessment for the S2 Scenario on the PIS 128

Table 5.7. The 1894 Earthquake Slip Assessment for the S2 Scenario on the PIS129

Table 5.8. The 1894 Earthquake Magnitude and Stress Drop Assessment for S3 Scenario on the PIS 130

Table 5.9. The 1894 Earthquake Different Rupture Dimensions for S3 Scenario on the PIS 131

Table 5.10. The 1894 Earthquake Slip Assessment for S3 Scenario on the PIS . 133

Table 5.11. The 1894 Earthquake Magnitude, Stress Drop and Epicenter Assessment Along the Izmit Fault 134

Table 5.12. The 1894 Earthquake Izmit Segment Rupture Dimension Assessment 135

Table 5.13. The 1894 Earthquake Çınarcık Scenario 136

Table 5.14. The 1894 Earthquake Combined Scenario 60 km Rupture Length . 137

Table 5.15. The 1894 Earthquake Combined 40 km Rupture Length 138

Table 5.16. The 1766 Earthquake Magnitude and Stress Drop Assessment for the CMF S1 Scenario 146

Table 5.17. The 1766 Earthquake Magnitude and Stress Drop Assessment for the CMF S2 Scenario 147

Table 5.18. The 1766 Earthquake Rupture Length Assessment for the CMF S1 Scenario 148

Table 5.19. The 1766 Earthquake Rupture Length Assessment for the CMF S2 Scenario 149

Table 5.20. The 1766 Earthquake Slip Assessment for the CMF S1 Scenario . . 150

Table 5.21. The 1766 Earthquake Slip Assessment for the CMF S2 Scenario . . 151

Table 5.22. The 1766 Earthquake Combined Scenario Assessment for Case 1 . 152

Table 5.23. The 1766 Earthquake Combined Scenario Assessment for Case 2 . 153

Table 5.24. The 1509 Earthquake Magnitude and Stress Drop Assessment for Scenario S1 on the CMF 159

Table 5.25. The 1509 Earthquake Magnitude and Stress Drop Assessment for Scenario S2 on the CMF 160

Table 5.26. The 1509 Earthquake, Different Rupture Dimensions for Scenario S1 on the CMF 162

Table 5.27. The 1509 Earthquake Slip Assessment for Scenario S1 on CMF . . 163

Table 5.28. The 1509 Earthquake Slip Assessment for Different Rupture Lengths for Scenario S1 on CMF 164

Table 5.29. The 1509 Earthquake Combined Rupture Scenario 165

Table 5.30. Obtained Source Parameters 173

LIST OF SYMBOLS

D_{75}	Effective Duration between 5% to 75% Time Interval
D_{95}	Effective Duration between 5% to 95% Time Interval
D1 - D5	Damage Level 1 to 5
E	EW Component
f	Frequency
H1	Horizontal Component
H2	Horizontal Component
I_0	Epicentral Intensity
I	Intensity
L	Fault Length
M_b	Body Wave magnitude
M_L	Local Magnitude
M_s	Surface Wave Magnitude
M_w	Moment Magnitude
N_{EQ}	Number of Earthquakes
N	NS Component
P	Probability
Q_f	Frequency Dependent Quality Factor
R	Source to Site Distance
R1 - R8	Region 1 to 8
Repi	Epicentral Distance
Rjb	Joyner–Boore Distance
Rrup	Rupture Distance
S1 - S3	Scenario 1 to 3
SA or S_a	Spectral Acceleration
T_0	Source Duration
T	Period
Vs30	Time-Averaged Shear-Wave Velocity to 30m Depth

W	Fault Width
Z(R)	Geometric Spreading
$\Delta\sigma$	Stress Drop

LIST OF ACRONYMS/ABBREVIATIONS

AFAD	Disaster and Emergency Management Authority
AHEAD	European Archive of Historical Earthquake Data
CMF	Central Marmara Fault
DASK	Natural Disaster Insurance Institution
EMEC	European-Mediterranean Earthquake Catalogue
EMS	European Macroseismic Scale
EW	East West
FAS	Fourier Amplitude Spectra
GMM	Ground Motion Model
GR	Generic Rock
GS	Generic Soil
Harvard CMT	Harvard Centroid Moment Tensor Catalog
KOERI	Kandilli Observatory And Earthquake Research Institute
Lat	Fault Length
Lon	Fault Length
Mag	Magnitude
MMI	Modified Mercalli Intensity
MSK	Medvedev–Sponheuer–Karnik Intensity Scale
MTA	Mineral Research and Exploration General Directorate
NAF	North Anatolian Fault
NAFZ	North Anatolian Fault Zone
NEHRP	National Earthquake Hazards Reduction Program
NS	North South
PGA	Peak Ground Acceleration
PGV	Peak Ground Velocity
PIS	Prince Islands Segment
TCIP	Turkish Catastrophe Insurance Pool
QTM	Quaternary, Tertiary, Mesozoic

$RMSE_R$	Regional Root Mean Square Error
RMSE	Root Mean Square Error
Sim	Simulated
USGS	United States Geological Survey

1. INTRODUCTION

1.1. Purpose and Outline

The Marmara region is one of the most active tectonic regions with its high population and rapid but irregularly growing cities in Turkey. Located in this active zone, Istanbul has always been under the danger of being hit by destructive earthquakes, which have caused serious damage in the city more than once in the past. There were many large earthquakes in Istanbul during the Byzantine period, between 342- 1453, especially the 437, 447, 554, 557, 740, 860, 869, 989, 1343 earthquakes caused great damage. There is still no consensus about their magnitudes, and epicentral location because little is known about damage interpretation of these earthquakes. During the Ottoman period, major earthquakes which affected Istanbul took place in 1509, 1719, 1754, 1766 (22 May and 5 August), and 1894. Since 1509, written damage descriptions from various sources allow us to understand destructiveness of these earthquakes and their intensity distribution. As the latest one, we have relatively rich knowledge about the 10 July 1894 earthquake. On the other hand, we have limited records about the earthquake of 10 September 1509, which happened almost half-century later from the conquest of Istanbul. By looking their damage distribution, the 10 September 1509, 22 May 1766 and 10 July 1894 events are considered as the Istanbul earthquakes.

According to official records, the 10 July 1894 earthquake resulted in 474 losses of life and 482 injuries, at least 21,000 dwellings were damaged, which corresponds to 1/7 of the total dwellings of the city at that time. Without any doubt, the exact losses were higher. Because of the censorship, the exact loss remained unknown. It is estimated that 4,000 people lost their lives in the 22 May 1766 earthquake. Many masonry and wooden buildings, shops, palaces, public buildings, commercial centers completely collapsed. Another independent earthquake happened on 5 August of the same year and increased the damage level and fatalities. Our information is limited on the 10 September 1509 earthquake, which is known as the Little Apocalypse due to its extensive area of devastation. After these massive earthquakes, Istanbul, which

was the capital at the time, had high level of damage and losses. Researchers have been split in opinion about the intensity, epicenter, magnitude, and rupture length of these events. Local and foreign sources can be explicating the consequences with either exaggeration of the loss and damage or applying censorship.

There are few attempts that present different approach to understand the associated faults, possible epicenters and magnitudes of the historical İstanbul earthquakes. Hubert-Ferrari et al., (2000) studied the stress distribution change after the 1999 İzmit earthquake by considering the six largest events that happened from 1700 to 1900 around the Marmara Sea. They associated segments of the events using the reported damages, and determined their magnitudes by using scaling relations. The slips are distributed between the dislocations representing the segments. Ambraseys (2002) evaluated long-term seismic activity over the last 2000 years and estimated epicentral locations of the historical earthquakes by using damage distributions. The surface magnitudes were calculated using the regional equations that was derived from Greece and Western Turkey earthquakes. Parsons (2004) studied probability calculations for the Marmara Sea by evaluating locations and magnitudes of the historical earthquakes that happened in the region since A.D. 1500. Parsons (2004) interpreted intensities by using the damage information data compiled by Ambraseys and Finkel (1990, 1991 and 1995) and estimated magnitudes and epicenters from MMI by using the methods of Bakun and Wentworth (1997) in combination with the attenuation relation of Ambraseys (2002). Due to the lack of diverse data sources and missing different interpretations, he assigned different and mostly higher MMI values than the values estimated in this study and also the evaluation of Ambrasey's. This situation resulted in different magnitude estimations and different fault considerations. Recently, Bulut et al., (2019) analyzed GPS slip rate measurements with long-term slip rate along the Marmara Sea and revised locations and magnitudes of the 1509, 1719, 1766s, and 1912 earthquakes, which are considered to occur on a dextral slip. Even though there are some books and articles especially on the 1894 earthquake, most of them have written with the point of view of the historians and not comprehensive enough for scientific studies.

The main objective of this study to reconstruct the intensities, locations, magnitudes, and the source mechanisms of the 10 September 1509, 22 May 1766, and 10 July 1894 Istanbul earthquakes using damage and intensity distribution and ground motion modeling by using stochastic simulation method. Damage distribution maps were obtained from the wide spatial distributions of the observed data. Ottoman Empire archive records, scientific reports, and papers, newspapers, government correspondence, letters, notes of voyagers, and diaries, court records are the major sources to make an evaluation on the earthquake damage inventories. Damages were interpreted on the MMI scale and intensity maps associated with the earthquakes were prepared based on macro-seismic intensity classification. The location and the vulnerability of the structures have been based on the old city maps. For generating ground motions with a stochastic finite fault simulation approach with a dynamic corner frequency, the EXSIM12 (Motazedian and Atkinson, 2005; Assatourians and Atkinson, 2012; Boore, 2009) software was used. Using EXSIM12, several scenarios were modeled with calibrated and validated source, path, and site parameters in the region. For validation, stochastic simulations were performed for the recordings of the 26 September 2019 Silivri, Istanbul earthquake. In calibration, we have used the recordings at 59 widely distributed stations around Istanbul located on different site conditions with epicentral distances ranging from 23 to 101 km. With the comparison of the generated ground motions to the observed ones, optimum source parameters and crustal characteristics of the region have been estimated. The calibrated model parameters have been obtained from the set of best-fit data with observed ground motion in frequency domain. We also tested the performance of our stochastic simulation model for larger earthquakes by simulating the recordings at 19 stations of the 17 August 1999 Mw 7.4 Kocaeli, Marmara earthquake using the same parameters. Obtained input parameters have been used for generating synthetics of the historical earthquakes. With the comparison of the simulated ground motion parameter distributions with the actual damage and intensity maps, a first-order assessment has been made. By analyzing how overlappings of the scenario earthquakes with the historical damage distribution, we deduced possible epicenter, magnitude, depth, source mechanism and all other possible properties of these historical events. This thesis presents the first seismic investigation

of the source parameters of the 10 September 1509, 22 May 1766, and 10 July 1894 Istanbul earthquakes with a better classification of the damage distribution of existing structures at those times. Identifying the source parameters of historical earthquakes are not the concern of only earthquake scientists, but also the historians, city planners, and architects. The outputs of this study will result in more reliable hazard and risk estimations in the Marmara region.

The outline of this thesis is as follows: Background information about the M $\geq$7 Marmara Sea historical earthquakes which caused important damage in and around Istanbul between 1500-1900. The literature survey, discrepancies between findings in fault length, epicenter, magnitude, and related fault from various researchers can be found in Section 1.3. Brief information about the population, typical structure types are given in Section 2. A comprehensive discussion of damage observation, basic definitions for the parameter used for damage distribution, and intensity maps for the 1509, 1766 (May) and 1894 earthquakes are given in Section 3. Section 4 describes the basis of the stochastic finite fault simulation and the required parameters for EXSIM12 software. This section is followed by an example of the simulation and validation of the 26 September 2019 (Mw=5.8) Silivri Earthquake, which will provide the details on how the input source parameters were constituted in the simulation. As a complementary example, we present stochastic simulation of the 17 August 1999 (Mw=7.4) Kocaeli earthquake in the following section. Simulation and findings for the historical events are given in Section 5 along with their discussion and comparison with the obtained intensity maps. Because we have relatively more knowledge of the 1894 event, the earthquakes were sorted from the latest to the oldest. The conclusions are given in the last chapter.

1.2. Active Faulting

The NAFZ (The North Anatolian Fault Zone) under the Marmara Sea consists of five fault branches, namely from west to east: Tekirdağ Segment (46 km), Central Marmara Segment (Avcılar and Kumburgaz, 105 km), Prince Islands Segment (42 km), Çınarcık Segment, and İzmit Segments (Darıca, Karamürsel, and Gölcük, 56 km).

These segments are right-lateral strike-slip oriented in the East-West direction and right lateral oblique normal faults with high slip velocities (over 20mm/year). Here, the Prince Islands and Çınarcık Faults need to be clarify more: The Prince Islands Segment (PIS) of the NAFZ is approximately 43 km long and it has component of both dip slip and right lateral strike slip (Normal oblique fault). Its strike, dip and rake angles are obtained from Active Fault Maps of Turkey, MTA (Mineral Research and Exploration General Directorate) as dip angle is 70° , strike is 130° , and rake is 165° -195°. Çınarcık Fault is approximately 35 km long, and an active normal fault. According to MTA, its dip angle is between 55°-85° , strike is between 264°- 295° and rake is 255°-285°.

All given five segments have a high potential of generating large magnitude earthquakes and heavy damage independently. In addition to these, there are also small and discontinuous, active, and mainly normal slip segmentations. Because of their low slip rates and small lengths, their capacity to produce large earthquakes is physically not possible.

1.3. Background Information on Historical Earthquakes

Figure 1.1 provides the estimated locations of large historical earthquakes (Ms $\geq$6.8) that occurred in and around the Sea of Marmara region over the last 2000 years (Ambraseys, 2002). In this figure, locations and sizes of earthquakes in instrumental period between 1900 to 2022 (taken from KOERI catalog) and estimated locations of the large historical earthquakes (Ms $\geq$6.8) in and around the Marmara Sea Region over the last 2000 years (Ambraseys, 2002). Estimated magnitudes are in terms of surface magnitude, Ms, and the instrumental magnitudes are expressed in terms of the largest value of Ms, Mw and Mb). The fault mapping (black solid lines) is obtained from MTA.

Little is known about the damage distribution of the events that happened before 1509. Instrumental calculations are available for the 1912 earthquake and the later ones. The six prior big events (M $\geq$7), which are the 1509, 1719, 1754, 1766 May, 1766

August, and the 1894 earthquakes, are explained in the following part. According to compiled damage, the 1719 and the 1754 earthquakes were correlated with the Izmit segment due to their high destruction in the eastern side. Similarly, the 5 August 1766 earthquake was linked with the Tekirdağ Segment due to its high intensity distribution in the western side of the Sea of Marmara.

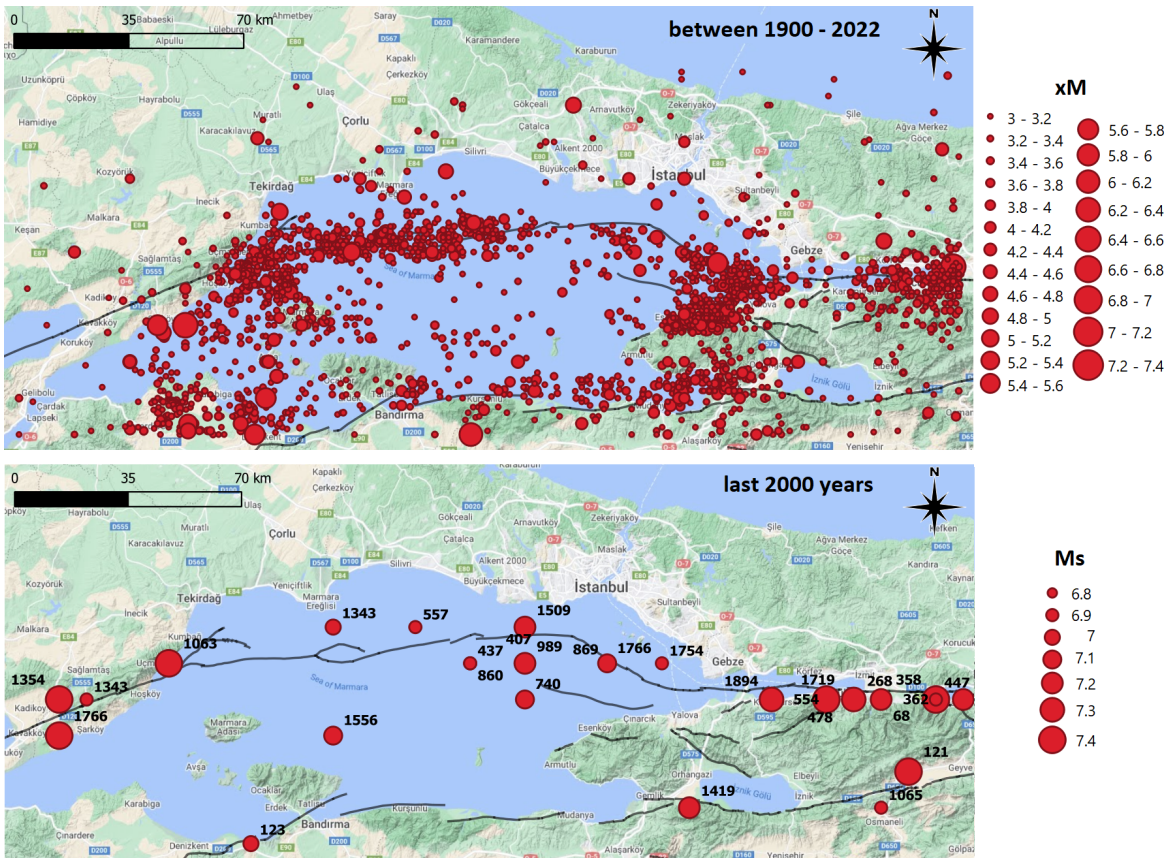

Figure 1.1. Seismicity of the Marmara Sea Region.

1.3.1. 10 September 1509 Earthquake

The great Istanbul earthquake of 10 September 1509 took place only a half-century later from the conquest. Unfortunately, there is not enough information about this catastrophic event in official records, because at that time Ottoman archives were not well-established. Our knowledge is limited to the expressions of the contemporary chroniclers, a few archive records, statements in the personal notes and letters.

There are contradictory statements up to a month regarding the date of the earthquake in the primary references. As stated by the contemporary Ottoman chronicler Rûhî, the earthquake happened on 12 August 1509, at night (Ménage, 1976). According to another contemporary historian Kemalpaşazede, and Venetian Sanuto who was in Pera at that time, the occurrence time was the night of September 10, 1509 (Uğur, 1985; Sanuto, 1879-1903), which contributed to the number of casualties. The earthquake was strongly felt in Bursa, Bolu, Gallipoli, and Edirne (Sanuto, 1879-1903). The shock was noticeable even in Greece, the Danube area, Transylvania, and Cairo and Nile Delta (Ambraseys and Finkel, 1995).

In this earthquake, numerous well-built structures received damage (Uğur, 1985). 109 mosques and 1,070 dwellings collapsed (Uğur, 1985; Ménage, 1976). 5,000 people lost their lives (Uğur, 1985; Solakzâde, 2016), and 10,000 were injured (Uğur, 1985; Sanuto, 1879-1903). These numbers indicate the damages and losses only in Istanbul and do not include the numbers in the neighboring towns and cities. The number of ruined houses, mosques, and churches were more than 3,000 (Uğur, 1985). Countless buildings were damaged at their roofs and windows (Uğur, 1985). All minarets in Istanbul collapsed, all domes and roof tiles of the structures fell down (Uğur, 1985; Ménage, 1976). The land walls from Eğrikapı to Yedikule collapsed completely (Ménage, 1976). The sea walls between Narlıkapı Gate and Ishakpaşa Gate (Ahırkapı) and from Dilsizkapı Gate (Değirmenkapı Gate) to Bahçekapı Gate were partly destroyed (Ménage, 1976).

There was no undamaged minaret left in Istanbul (Solakzâde, 2016). Domes of all the madrasas collapsed (Solakzâde, 2016). Dome of the Beyazıt Mosque, which was a newly built mosque at that time collapsed. Its semi-domes and arches, and one minaret were demolished. Its kitchen and food storage room fell apart (Ménage, 1976). Pillars of the four main columns of the Fatih Mosque (built between 1462-1469) cracked; the great dome of the Fatih Mosque was cleft; the dome plasters were ruined and repaired later; the iron beam on the right-hand side of the mosque was displaced, and another beam on the left-hand side buckled. (Ménage, 1976; Solakzâde, 2016). Many domes of the madrasah, the hospital, and the imaret of the Fatih Mosque Complex were ruined

(Ménage, 1976). The classroom of the Zamiri Madrasah and its three domes collapsed, two other domes also fell (Ménage, 1976). Hagia Sophia obtained slight damage at its plasters, which were added when it was converted into a mosque, were detached (Hammer, 1835), also its minaret collapsed (Sanuto, 1879-1903). All the shops in the Karaman Bazaar were completely damaged (Ménage, 1976). Six columns in the Hippodrome fell down (Ménage, 1976). Joint openings were observed on the gate of the Atik Ali Paşa Mosque (Ménage, 1976). Because the top of the minaret of Davud Paşa Mosque fell over, a dome and two arches were ruined (Ménage, 1976). The Isa Kapısı Gate that existed over 1900 years cracked and fell (Ménage, 1976). Edirnekapı Gate and Sivrikapı Gate received damage (Ambraseys and Finkel, 1995). The Galata Tower was ruined (Sanuto, 1879-1903). According to Ambraseys (2001) however, only the cantilevering parts of the Galata Tower fell (Ambraseys, 2001).

This earthquake created large waves in the sea, and since the waves crossed the city walls in Galata and Istanbul, streets were flooded (Hammer, 1835). In Istanbul (today's historical peninsula) and Pera, ground slits were observed (Sanuto, 1879-1903). Because water bends had collapsed during the earthquake, many places were flooded (Hammer, 1835).

The Topkapı Palace received slight damage at its hammam (Ménage, 1976). A temporary tent-room was built for the Sultan Beyazid II for ten days for precaution (Ménage, 1976; Solakzâde, 2016). Due to fear and panic, the Sultan chose to go to Edirne (Solakzâde, 2016). On 23 October 1509, another strong earthquake occured in Edirne. (Ménage, 1976). On 16 November 1509, a triggered strong earthquake hit Edirne (Ménage, 1976). Aftershocks were felt for 45 days (Âlî, 2009). There is not more information about these two events and their affected area. People were in panic. They couldn't enter their homes, and they slept in open areas for 2 months (Ménage, 1976). The churches were damaged severely and people could not dare to enter the houses and churches (Sanuto, 1879-1903). Kemalpaşazade stated that some people could be pulled alive from the rubble after some time from the earthquake (Uğur, 1985). On 26 May 1511, another aftershock (or, may be an independent event) happened in Edirne (Sanuto, 1879-1903).

The numbers of the damaged houses and casualties in Galata and Pera are not clear. In a letter sent on 15 September 1509, Sanuto mentions about a collapsed house which belonging to a Florentine family with ten members in Pera, and tells that three family members died while remaining seven were miraculously rescued as injured (Sanuto, 1879-1903). In the mansion of the Grand Vizier Mustafa Pasha (its location is unknown), 360 cavalry and their horses died (Sanuto, 1879-1903).

This earthquake did not only affect Istanbul, but caused devastation in the neighboring settlements as well. Many houses received damage in Edirne and the number of fatalities was high (Uğur, 1985; Solakzâde, 2016). In Edirne, two shops and upper parts of four minarets fell in Uzumculer (or Ezmeciler) district. The porticos of two mosques collapsed in Kazancılar and Sarraçlar districts (Ménage, 1976). In Çorlu, minarets, masjids, and two entire districts were destroyed during the earthquake (Here, Solakzâde gives the city as Çorum located in Anatolia which is around 500 km away from Istanbul, and it is probably a typing or transliteration error) (Solakzâde, 2016). The town of Dimetoka, where Sultan Beyazıt was born, was razed by the earthquake (Hammer, 1835). Trenches in Gallipoli were destroyed (Hammer, 1835). In Bolu (expressed as Bolomon), city walls and towers were demolished; aftershocks of the earthquake were felt in Bolu for eighteen days (Sanuto, 1879-1903). Here, it should be noted that neither any other evidence about damage in Bolu, nor any expression in the contemporary sources is found. Bursa and Iznik needed to be repaired. All domes of the mosques and the castles were ruined in the towns of the Izmit Gulf (Ambraseys and Finkel, 1995). Besides, In Izmit, Süleyman Pasha Madrassa, five mosques, and more than 300 houses collapsed (Ekin, 2005). In addition, Tuzla, Eskihisar and Hereke castles in the Gulf of Izmit were damaged (Ekin, 2005). Domes of the mosques in Gebze collapsed and some neighborhoods and the shipyard became submerged (Öztüre, 1981).In the Princes Islands of Burgaz and Heybeliada two churches were damaged at their domes (Ambraseys and Finkel, 1995). Dimetoka Palace had to be repaired (Ambraseys and Finkel, 1995). Given expressions should be evaluated in contemplation of biases and rehashing between the late sources which may cause false information. It should be spurious information that two-thirds of the population swallowed up in the ground as a result of the splitting of the Earth in Çorlu, as stated by historian Hammer. Am-

braseys (2001) provides an extensive evaluation of contradictory information between the sources on the 1509 earthquake.

After the massive devastation of the 1509 event, studies to repair damaged structures in Istanbul began on 29 March 1510. To do this, 22 akçe per house, and one worker from every 20 houses were taken. Besides, 37,000 workers from Anatolia and 29,000 more from Rumelia, totalling of 66,000 workers were transported to the city. 3,000 master builders were assigned to these workers and 11,000 workers were tasked with the lime process (Details on the reconstruction works can be found in Orgun, 1941). Reconstruction lasted 3 months and all the city walls, the Galata Tower, the Maiden's Tower, the Yoros Castle, the Anatolian Fortress, the Rumeli Fortress, the Çekmece Bridges and their towers, the walls in Fener, and the Castle of Silivri were repaired within 64 days (Ménage, 1976).

There are a few official documents at the Prime Ministry Ottoman Archives related to the 1509 earthquake (Sawai, 2015). Orgun (1940) used one of these official registers which provides detailed information on financial issues, the number of workers and also describes the tools and construction materials utilized. The expenses of reconstruction after the earthquake were provided with the additional taxes. Numerous workers including professionals and labor force that were sent to Istanbul from all over the Empire (Orgun, 1940). Even though Ruhi claims that reconstruction works were completed in 64 days, another official document related with rebuilding of a small mosque in Istanbul shows that it lasted until November of 1511 even though it was aimed to finish the construction immediately (Sawai, 2005).

Information given by Solakzâde, who was an Ottoman historian in 1590-1658, on the damage, effectiveness, and repair work after the 1509 event is a duplication of Kemalpaşazade and Rûhî. As an important constituent, Solakzâde states that this catastrophe affected the construction tradition in Istanbul. Building all the palaces, mansions, and houses using timber started after the 1509 earthquake (Solakzâde, 2016) because, during the ground motion, the weakness of masonry buildings compared to the wooden ones scared the local people. As it is expressed in further sections, this

tendency caused a new calamity besides earthquakes: the fire hazard.

Figure 1.2. Damaged structures in Suriçi district after the 1509 earthquake, using the damage information given by Ambraseys and Finkel, (1995). Map adapted from Cplakidas (2011).

1.3.2. 25 May 1719 Earthquake

25 May 1719 earthquake was one of the largest earthquakes occured in the Marmara Region. Contemporary historian Silahdar Fındıklılı Mehmed Ağa reported damage after the earthquake in his literary work, Nusretname (Topal, 2001). According to Silahdar, there was no structure left unruined in Istanbul. Domes of the Fatih Mosque, Beyazit Mosque, and Mihrimah Mosque (in Edirnekapı) cracked, lots of minarets fell down (Topal, 2001). 40 mosques and 27 towers were ruined in Istanbul and damage extended as far as Thrace (Ambraseys, 2009). The city walls were intensely damaged. Most parts of the land walls from Yedikule to Ahırkapı were destroyed (Cezar, 1963). Numerous domes of the mosques and Turkish baths either collapsed or cracked (Cezar,

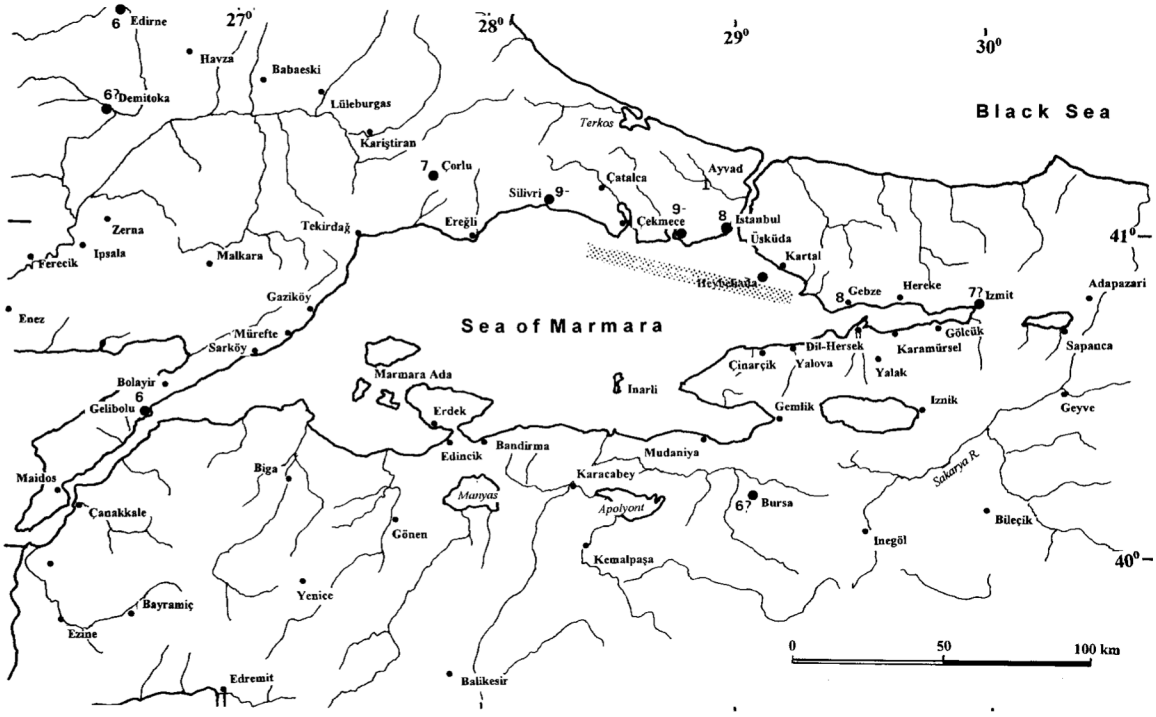

Figure 1.3. Assessed intensities of the 1509 earthquake by Ambraseys (2001) in MSK.

1963).

Substantial damages were reported in the Gulf of Izmit. Half of the structures in Yalova and four fifth of structures in İzmit were ruined (Topal, 2001). Karamürsel and Kazıklı villages (in Bursa) were totally destroyed (Topal, 2001). The damage was intense and the number of fatalities was high in Düzce and Sapanca (Topal, 2001). Five aqueducts were destroyed in Izmit (Topal, 2001).

Silahdar gives casualties in Izmit as 4,000 lives and also mentions that 600 people died due to collapse of six mosques (Topal, 2001). In Sapanca, casualties were 1,000 people due to destruction of 4-5 villages (Ambraseys, 2009). In Istanbul, the Yağlıkçılar Arch collapsed and 10 people were killed under its debris (Topal, 2001). Four people were buried in the wreckage of a restaurant due to downfall of the wall of the Galata Prison, and three of them lost their lives (Topal, 2001).

Official letters about the repairs in some specific structures located in Kocaeli, Izmit, Karamürsel and Orhangazi following the earthquake are given in Erdoğan (1968). Sultan Orhan Mosque in Orhangazi was damaged during the shake, but the ceiling woods of the mosque were already in a bad condition before the earthquake (Erdoğan, 1968). Similarly, also Silahdar mentions that highly damaged villages were especially the ones that were already dilapidated (Topal, 2001). Little is known about the structural properties of the villages in these cities. Low structural strength and poor conditions of the buildings in villages to the eastern part of the Marmara Sea might be responsible in the damage.

1.3.3. 2 September 1754 Earthquake

The 2 September 1754 earthquake created big panic and caused damage in Istanbul. According to the letter of Mackenzie, who claims to be an eye-witness but clearly exaggerates the effects, four towers of the Yedikule Fortress were seriously damaged, and two of them collapsed causing casualties of several guarding Janissaries (Mackenzie, 1754). From Yedikule to Edirnekapi, all the bastions of the land walls were also damaged during the shake, but none of them collapsed (Mackenzie, 1754). The domes of the Fatih and the Beyazit Mosques were damaged but repaired quickly (Cezar, 1963). All the small domes of the Fatih Mosque collapsed (Mackenzie, 1754). Seven minarets of some small mosques fell down, the Little Hagia Sophia was badly damaged, the Galata Prison collapsed and all its convicts stayed under its debris (Mackenzie, 1754). Hagia Sophia also experienced some level of damage (Ambraseys, 2009). The Sirkeci Inn was badly destroyed, the wall of the Kara (written as Cara Han) Inn partly fell down, the Katırcı Inn (written as Cautirligee Han) and the Vezir Inn were also damaged (Mackenzie, 1754).

Balat suburbs were widely damaged (Mackenzie, 1754). Probably, there was some level of damage also in Uskudar and Bosphorus (Mackenzie, 1754). It is important to state that the majority of the damaged structures were either old stone or brick buildings in Istanbul, and there were only a few old timber frame houses among them (Ambraseys, 2009).

Destruction statements from the Gulf of Izmit were more serious than Istanbul (Ambraseys, 2009). Gevye was completely ruined, large parts of Izmit were destroyed and resulted in high casualties (Ambraseys, 2009). Even though slight damage was reported in Iznik and Bursa, there were not any loss of life or injuries (Ambraseys, 2009).

Mackenzie states that the 1754 earthquake was much stronger than the 1730 Izmir earthquake and it was felt in Ankara and Izmir (Mackenzie, 1754). The casualties are varying between 50 to 2000 lives lost (Mackenzie, 1754; Ambraseys, 2009). Its aftershocks lasted until October and these shakes increased the total loss of the main shock. (Ambraseys, 2009).

1.3.4. 22 May 1766 Earthquake

The Istanbul earthquake of 22 May 1766 was one of the most destructive earthquakes that occurred in the Marmara region. This catastrophic event resulted in severe damage to many buildings with high casualties in and around Istanbul. The massive shake happened on the third day of the feast of sacrifice, half an hour after sunrise. The first movement was slight which was followed immediately by strong shaking that lasted around 2 minutes (Hâkim, 1166-1172). In the following hours and days, many aftershocks were reported. The 22 May 1766 earthquake caused a wide area of damage from Izmit on the east to the southern coasts of the Sea of Marmara and Edirne in the north. Structures in Istanbul, Edirne, Bursa, Izmit were ruined. The earthquake was felt from Bozcaada, İzmir, Thessaloniki, and Southern Balkans (Ambraseys and Finkel, 1995).

The effect of the 22 May 1766 event was very destructive and the heaviest damage was in Istanbul. The historians named Hâkim, Çeşmizade, Şemdanizade and Vasıf report the casualties of the 1766 earthquake as 4,000 lives lost. Due to the strong movement, many wooden and masonry houses, shops, and other types of buildings were damaged, some of them completely collapsed (Sağlam, 2014). Some parts of the city walls were destroyed, Edirne Gate, Bahçekapı, and Odun Kapısı collapsed. The

earthquake was also destructive in the western part of the region. Many houses and walls fell in Çatalca, a dome of the Gazi Ali Paşa Mosque cracked. Edirne received slight damage. (Ambraseys and Finkel, 1995). The damage on the eastern side of Istanbul was more serious than in the west; some villages in the Gulf of Izmit were destroyed, the dome of the Mehmet Bey Mosque collapsed, and the walls of the Çalık Ahmet mosque were destroyed in Izmit. Besides, seismic sea waves that accompanied the earthquake were more effective around Bosphorus, and Gulf of Mudanya (Ambraseys and Finkel, 1995). The damaged structures in the Suriçi district were illustrated in Figure 1.4 based on the damaged information given by Ambraseys and Finkel (1995).

Figure 1.4. Damaged structures in Suriçi district after the 1766 earthquake, using the damage information given by Ambraseys and Finkel, (1995). Map adapted from Cplakidas (2011).

Many contemporary historians reported on the 22 May 1766 earthquake and its devastation. According to Şemdanizade The Fatih Mosque was damaged seriously and

ruined, the Sultan Beyazit Mosque and the Mihrimah Sultan Mosque (in Edirnekapı) were almost destroyed (Şemdanizade, 1976). The Grand Bazaar and its surrounding area were also damaged. Şekerciler Inn, Kalpakçılar Street, Dua Meydani Vezir Inn were damaged. Yedikule, Esir Bazaar, Saray-i Atik were also damaged. Masonry masjids and some wooden buildings were demolished. There were destructions in Galata, Usküdar, and Küçükçekmece. Chimneys collapsed and walls cracked in the suburbs of Galata and Pera (Ambraseys and Finkel, 1995). Baruthane, Saraçhane, Arasta, Enderûn-ı Hümâyûn, Janissary barracks (Yeniçeri Kışlaları) and Tophane, needed repair. Villages along the Bosphorus such as Istinye in further north were also damaged by the earthquake (Ambraseys and Finkel, 1995). Besides, underground waterways were also wrecked (Şemdanizade, 1976).

According to Çeşmizade, another contemporary historian, the earthquake devastated Istanbul and its surroundings. The dome of the Fatih Mosque was completely destroyed. Many small domes and walls of the mosque were so ruined that it became irreparable. As stated by Sarkis Hovannesyan, the dome of the Atik Ali Pasha Mosque in Çemberlitaş was partially damaged, the dome of the Kariye Mosque collapsed, Eyüp Sultan Mosque was destroyed, Davut Pasha Mosque and Rüstem Pasha Mosque received intense damage, Şah Sultan Mosque in Eyüp collapsed, the minaret of the Behruz Aga Mosque in Şehremini fell, the minaret of the Kemankeş Kara Mustafa Pasha Mosque in Galata was ruined and dome of the Koca Mustafa Pasha Mosque was damaged, the minaret of the Kurşunlu Mosque (Kurşunlu Mağazası) collapsed, and Cebehane-i Amire fell (Pamukciyan, 1987). One minaret of the Sultanahmet Mosque collapsed (Ambraseys and Finkel, 1995).

Palaces also suffered from the intense shake. According to Şemdanizade, Topkapı Palace was among the damaged structures. Its walls were damaged and partly destroyed. As reported by Inciciyan, the Beşiktaş Palace was partially damaged (Pamukciyan, 1987).

As reported by historians Ahmet Vasıf Efendi and Hâkim, many masonry and wooden houses and shops were damaged due to the severity of the ground shaking.

Sultan Selim Mosque, Şehzade Mosque, Süleymaniye Mosque, Nuruosmaniye Mosque, Laleli Mosque, Yeni Valide Mosque, and Hagia Sophia needed to be repaired. The shake was felt and caused intense damage in Küçükçekmece and Büyükçekmece, Lüleburgaz, Çorlu, and Karışdıran (Sağlam, 2014; Hâkim, 1166-1172). Domes and minarets of many mosques and masjids were destroyed and there was not an unaffected house left (Hâkim, 1166-1172). Most of the buildings, which appeared undamaged at first glance, were later found to be largely damaged (Şemdanizade, 1976).

As stated by Hâkim, (Hâkim, 1166-1172), shakes continued for 80 hours following the mainshock. Aftershocks of the earthquake lasted around 8 months to one year. People were in a panic and stayed in open areas (Hâkim, 1166-1172; Şemdanizade and Pamukciyan, 1987). Aftershocks inflicted more damage to the buildings. Some structures that were already damaged due to the first shake couldn't resist more and collapsed. As reported by Sarkis Tıbir, on the 6 July aftershock, Aynalıkavak Palace was destroyed, and on 25 July Edirnekapı Gate completely collapsed (Pamukciyan, 1987). Moreover, during the aftershock of 25 July, 3 towers of Yedikule collapsed, damage to the city walls increased and some of the previously damaged buildings collapsed (Pamukciyan, 2002).

The official Istanbul Court Records contain important information regarding the 1766 earthquakes. According to these records, The Balkapani Inn was damaged by the earthquake. Some of its rooms were destroyed (25/76-313). The rooms and the surrounding walls of the Süleyman Pasha Inn were ruined, and domes of its 12 rooms were completely destroyed. Furthermore more damage was inflicted on the 5 August event (25/76-401). Debbağzade Hacı Hüseyin Efendi Mosque in Altımermer was damaged (25/76-476). In Balat, a synagogue, which was not in good condition before the earthquake, was destructed and became uninhabitable (25/76-309). In Kumkapı, because domes of the dressing rooms in the Nişancı Pasha Hammam were damaged, destroyed parts of a wooden roof were reconstructed (25/76-330). Next to the city walls in Ayvansaray, a mosque and an imam house became uninhabitable and needed demolition (25/76-400). Istanbul Court Records also give an idea about the identification of severely damaged structures and studies after the investigation. As stated on

the records, heavily damaged structures were to be demolished by their owners as soon as possible (25/76-109, 110). Otherwise, it endangered the adjacent buildings even 13 days after (25/76-181, 182, 184).

After the 1766 earthquakes, the most important issue was choosing the structural material of newly built structures. The government desired to use masonry against fire danger. For instance, reconstruction of destroyed bread bakeries was given priority (25/76-111) and wanted to be built fire-resistant; in case of a neighbor on a wooden building, construction of a masonry firewall on that side was an obligatory (25/76-120). Moreover, raising the price of the construction materials and wages of workers were banned (25/76-114). On the other hand; the public preferred timber due to various reasons. These conflicts are more remarkable especially in and around Grand Bazaar. It is understood that all the expenses of repairing and rebuilding of the demolished arches were covered by the state in Grand Bazaar streets and roofs; expenses of damaged shops, and private rooms were covered by their owners (25/76-116). As stated by the court records; destroyed inns within the Bazaar are required to be reconstructed in masonry. If the owner does not have enough economic power, and with the permission of the neighbors, there was an allowance for building masonry walls with wooden roof for fire protection (25/76-213). For example; in the rebuilding of collapsed masonry shops and street arches of Haffaflar Çarşısı around Sarachane, in fire-resistant manner rescripts, the material type should have been in masonry. Because owners of shops notified that they do not feel safe under the masonry arches, and they do not want to be waited for a long time until rebuilding such large masonry arches, the arches were made of wood (25/76-127). Similarly, near Rüstempaşa, during the reconstruction of destroyed arches of masonry shops, the shopkeepers wanted to rebuild using wood. Even though their desire was not allowed for fire prevention, the roof of adjoined sides of each shop was built from the stone wall and their street sides became wooden (25/76-137). Likewise, in Mercan, the reconstruction of damaged street arches and roofs of Örücüler Street was partly made of wood upon demand by shop owners (25/76-270). The same situation can be seen during the reconstruction of the shops in the Sırıkçılar, Çadırcılar, and Maytapçılar Streets, despite the state mandate to build in masonry, with the desire of shopkeepers the streets were partly rebuilt in timber (25/76-153).

These court records are clear examples of how people were afraid of masonry structures and feel unsafe after seeing their low resistance under seismic forces. It also shows that despite the danger of fire, how they chose again wooden structures. Istanbul court records are good examples of the lack of clarity and precision in the structural material type during the reconstruction and also they are well indicators of the tendency to bend the rules at that time.

Here, making a comparison of the events of the 22 May 1766 Istanbul earthquake with the 1 November 1755 Lisbon is necessary to understand general trends at that time after any catastrophe. The 1 November 1755 Lisbon earthquake affected a big part of Europe and gave birth to seismology science and disaster management. Both mentioned earthquakes took place on religious festivals and happened in historical cities in 11 years apart. Their occurrence times affected fatalities; while being at home after praying in mosques reduced the casualties in the former, being in crowded churches during the earthquake increased the number of life losses in the latter. After the great devastation, strict technical constraints and latest developments had been applied while repairing and reconstruction of Lisbon for the protection of the city against seismic forces (Mendes-Victor and Oliveira et al., 2008). After such a big devastation, unrestrained construction would create more catastrophic results with time. Lack of extensive repairs and comprehensive enhancing after the Izmit earthquake occurred on 2 September 1754, which also affected Istanbul, may give rise to the high level of damage after the 1766 earthquakes (Mazlum, 2011). Similarly, after the 1766 massive earthquakes, instead of enhancing the structures to ground motions and making a suitable city planning, almost all the studies were only for repairing the damaged zones (Mazlum, 2011). We can understand this situation by looking at the severe damages on the same buildings after the 1894 catastrophic earthquake.

1.3.5. 5 August 1766 Earthquake

75 days later from the massive shake of the 22 May 1766, on 5 August 1766, another ruinous earthquake hit the region and increased the devastation. This event can be triggered event or can be totally independent.

Damage in Istanbul was slight after this earthquake and damaged buildings were previously harmed structures on 22 May. After this ruinous shock, damage levels of the Sultanahmet Mosque (the Blue Mosque) and Saray-i Atik increased (Mazlum, 2011).

Heavy damage reported in the East Thrace, especially around Tekirdağ (Ambraseys, 2009). One tenth of the houses were remained standing in the villages of Tekirdağ including Uçmakdere, Erinochori, Gaziköy, Gölcük, Hoşköy, İnceköy, Eriklice, Aşağıkalamış, Kastanbol, Loupida, Güzelköy, Mürefte, Yeniköy. Palamut, Şarköy, Çınarlı, Senduk and Sternaköy. Following the earthquake destruction, Gaziköy was destroyed by a fire. All the houses were ruined in Hoşköy, which corresponds to nearly 800 houses and majority of its population stayed under debris (Ambraseys, 2009). Gallipoli has affected this shock seriously; Kilitbahir Fortress and a mosque inside it, Seddülbahir Castle, Gazi Süleyman Pasha and Sarı Pasha Mosques in Gelibolu, Bozcaaada Castle, Sultan Mehmet Mosque in Çimenlik, Ali Çelebi mosque and school in Şarköy, gunpowder factory, Inöz Castle were damaged and needed repair (Sakin, 2002). In addition to the records of historians, the 22 May and 5 August 1766 earthquakes have been the subject of epics and poems. For example; Ceranyan, who was a contemporary Armenian minstrel, states that many masonry structures were flattened, besides, mosques, minarets, commercial buildings, and houses ruined (Pamukciyan, 2002).

Şemdanizade mentions damage of the 5 August earthquake in the eastern side as the wooden Court in Karamürsel collapsed in the earthquake and that 4 people died inside it (Şemdanizade, 1976).

Considering its highly influence area, 5 August 1766 earthquake is centered in the Western part of the Sea of Marmara (Ambraseys and Finkel, 1995) and linked with the Tekirdağ Segment.

1.3.6. 10 July 1894 Earthquake

On 10 July 1894 at 12.24 p.m., a massive earthquake hit Istanbul. This earthquake was the largest event that caused wide destruction after the 1766 earthquakes and has been the latest big earthquake so far in Istanbul. Many houses, public structures, city walls were destroyed during the extremely destructive shake. At least 21,000 houses were damaged which corresponds to 1/7 of the total dwellings of the city at that time. According to the official reports, the 1894 earthquake resulted in 474 losses of life and 482 injuries. These numbers reflect information only in Istanbul and its villages. On the other hand, we have limited information about surrounding districts which increases the possibility of having higher fatalities and economic loss. After the 1894 earthquake, Sultan Abdulhamid II applied a publication ban on the newspapers to prevent panic among people. Because of the censorship and limited information about the neighboring cities, the exact number remained unknown.

Demetrius Eginitis, the director of the Greek National Observatory, came to Istanbul to investigate the earthquake by accepting an invitation of Sultan Abdulhamid II. Eginitis visited the damaged areas by his assigned ferry and prepared the first scientific report on this earthquake to present to the Sultan on 20 August 1894. Mr. Coumbary, the Director of the Istanbul Observatory, and his assistant director Emil Lacoine Efendi accompanied him in this investigation. This report was prepared based on the field studies and the information received by telegraph from the neighboring provinces. In what follows the main points of the report are presented: The earthquake lasted about 17-18 seconds in the form of three consecutive severe shakes. The first one was horizontal and took 4-5 seconds and was the lightest one, even the items did not move. The second shake was vertical and rotational, very severe, and lasted for 8-9 seconds. It was followed by the slighter third horizontal, undulatory wave, which lasted 5 seconds. Arrivals of these three waves were on North-East and South-West direction with a small diversion. Based on the site examinations and the information received from the governorates, Eginitis determined the isoseismal map of the earthquake (Figure 1.5). Isoseismals indicate the level of experienced seismic damage and contours represent equal earthquake intensities within the bound areas. Eginitis di-

vided the shaken zone into five areas. The first elliptical zone includes the epicenter and covers the most damaged areas. Well-built structures in this region have been destroyed. The major axis of the ellipse is from Çatalca to Adapazarı, which continues along the Gulf of Izmit with a length of 175 km. The small axis covers the land between the villages of Katırlı (Esenköy) near the Gulf of Izmit and Maltepe as 39 km long. The direction of the shakes is approximately parallel to the small axis and vertical to the large axis. The second region contains the badly built houses; few of them collapsed and most of them received slight damage. This elliptical region includes Çorlu, Rodosto (Tekirdağ), Mudanya, Akhisar, Üsküdar, Ortaköy, Terkos as 248 km long axis and 74 km small axis. In the third region, the earthquake did not cause any structural damage but only small items displaced or overturned. The fourth region, which is not shown on the map, involves Yanya (Ioannina), Crete, Bucharest, Greece, Konya, and Anatolia which are undamaged but where the shaking is felt by people. The last region corresponds to an immense area including Europe, Asia, and part of Africa where the shake is very slight and only recognizable with seismic devices (Eginitis, 1894).

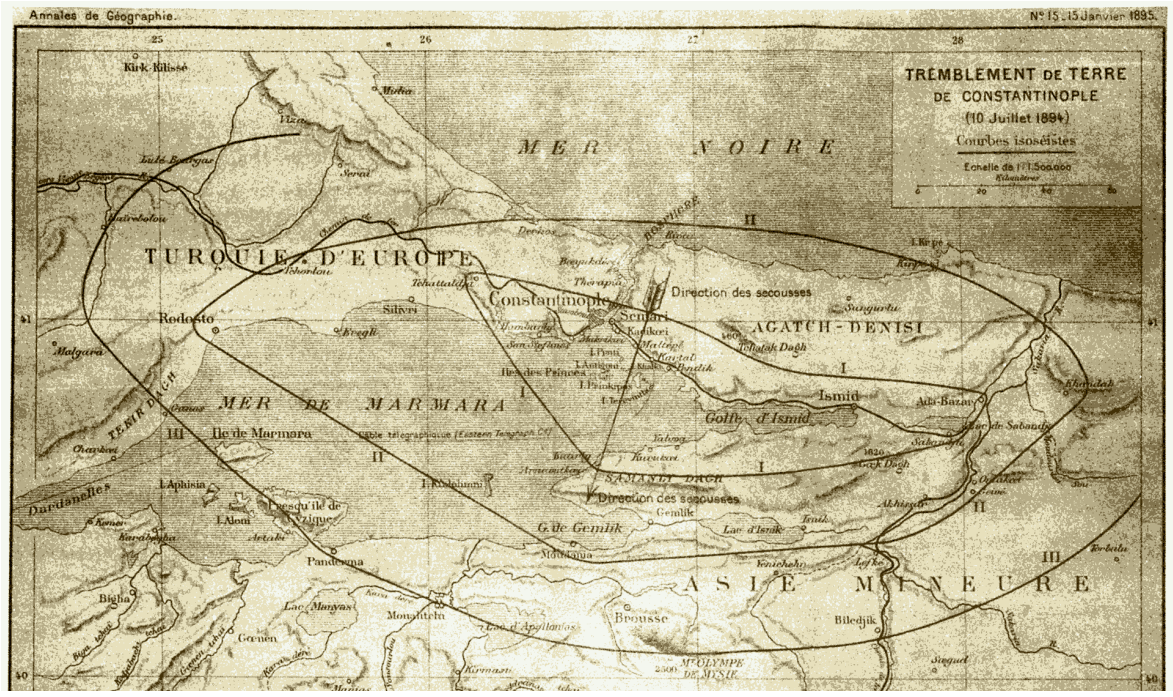

Figure 1.5. Isoseismal map prepared by Eginitis in 1894 (Eginitis, 1895).

According to Eginitis, in the first region on the isoseismal map, economic loss was enormous and many people were injured and died by the earthquake. Many buildings were almost completely demolished, while others became uninhabitable. There was no home remained undamaged. The damage was severe in the historical peninsula. Particularly, the Grand Bazaar had been ruined and many people lost their lives inside it. Eginitis saw the maximum damage on Prince Islands; especially in Heybeliada (Halki), and Kınalıada. Heybeliada Greek Seminary (Ecole de Théologie) had been ruined and many walls of it collapsed. In Yeşilköy, Ambarlı, Kınalıada, Büyükada, and Katırlı (Esenköy), many houses had been totally demolished, numerous mosques and churches either collapsed or seriously cracked, and most of the minarets fell down.

Eginitis observed that soft sediment soils enhanced the observed damage. In Katırlı (Esenköy) the houses, which are built on alluvial sites, had been collapsed, while the others built on hard soils remained. In Yalova, the village itself was not damaged but the farms which were on the sandy base, collapsed (Eginitis, 1894). For example; in Yalova, while the Millet Farm was not affected by the earthquake, the Baltacı Farm was completely destroyed. There was no damage in the hot springs or nearby villages. The most damaged villages were those between Mere Lake and Sapanca (Batur, 1994).

During the earthquake, ground cracks were observed in and around Istanbul. In Ambarli, a 3 km-long and 8cm-wide slit formed parallel to the beach, and another 100 m-long and 6 cm-wide slit was observed parallel to the former. At Heybeliada, a very narrow and 200 m long slit was seen in North-East and South- West direction to the beach. In Burgazada, there were some small slits around the sea in the direction of Northeast to Southwest, and land subsidence was observed around them. In Kinaliada, slits had been noticed as the largest of which is 200 m long and 6 cm wide on North-South direction parallel to the beach. Besides, two small slits around the sea in Ortaköy and some slits parallel to the beach in Katirli had been observed (Eginitis, 1894; Oztin, 1994, pages: 226-229).

The evaluation of damage distribution after a destructive earthquake is mostly

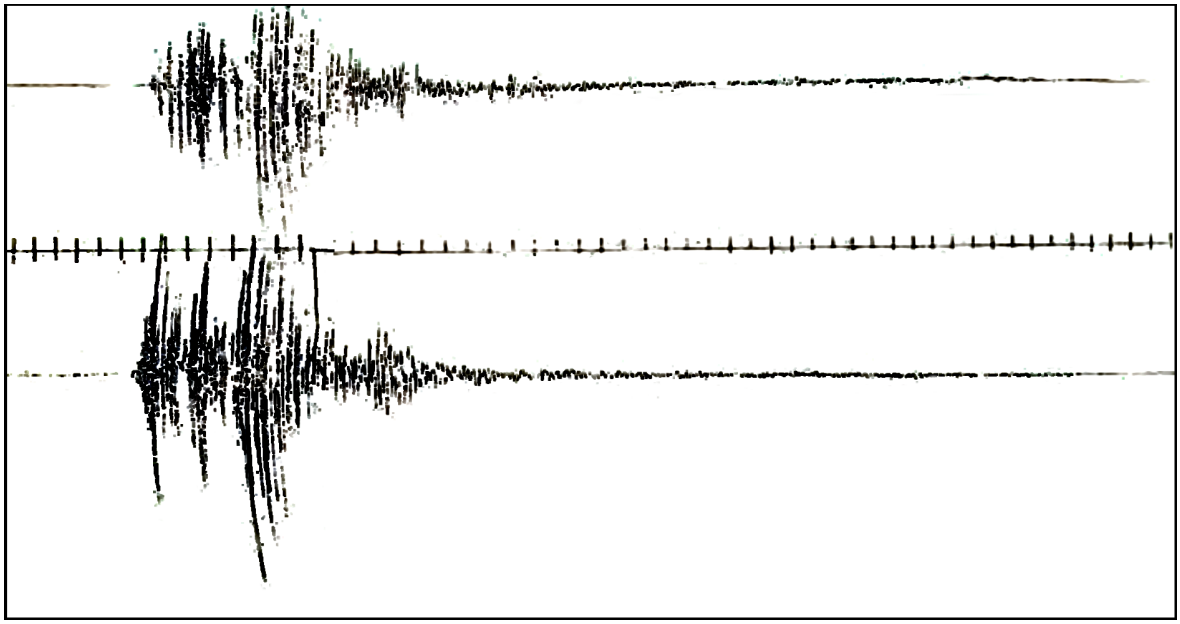

Figure 1.6. Pulsations of the 10 July 1894 Istanbul Earthquake Recorded by the Vicentini Micro-Seismograph at Siena (Davison, 1896). The original seismograph record has been corrected using GNU Image Manipulation Program (GIMP 2.10.30).

done by focusing on the historical regions because these areas were the urban centers at that time and also rich with the number of well-known buildings. The damaged structures in Suriçi district using the inventory shared by Oztin, 1994 is illustrated in Figure 1.7. Many monumental structures were damaged. Fatih, Edirnekapı, Balat, Eminönü, Gedikpaşa, Samatya, Kumkapı, Kadırga had the worst damage. Many houses, mosques, churches either collapsed or cracked. Chimneys, water gauges, minarets fell. Since minarets of many mosques fell over mosques, especially their last prayer halls were destroyed (Eyice, 2016).

Hagia Sophia was slightly damaged; only the decorations on the dome were demolished (Eginitis, 1894). Blue Mosque and its madrasa were partially destroyed. The entrance section of the Nuruosmaniye Mosque had been ruined. The minaret spire of the New Mosque (Turkish: Yeni Cami) twisted and dislodged. Both minarets of the Sultan Selim Mosque were completely destroyed, the mosque itself was also damaged and its dome cracked. The complex of the Fatih Mosque had also damage. The

balcony level of one of the minarets collapsed, and the spire (minaret külahının ucu) of another minaret collapsed. Some parts of the courtyard walls had been destroyed. Also, the wall of the primary school was destroyed, domes of the madrasa, classroom, and laundry rooms were destroyed. Pieces of stone and brick fell from the dome of the Beyazid Mosque. The Topkapı Palace was also affected. Damage in the Bab-ı Ali was slight; plaster dropped and the rooms had small cracks. The Little Hagia Sophia was damaged and its madrasa was completely devastated. The minaret of the Kariye Mosque was destroyed from its half, and its madrasah was partially ruined. The dome of the Fatih Aya Nikola Church (St. Nicholas Church) was destroyed. The Column of Marcian was ruined. Amcazade Hüseyin Pasha Madrasa has been damaged; the masjid was ruined, the school was partially destroyed and the madrasa was completely demolished (Öztin, 1994; Ürekli, 2000; Ambraseys, 2001; Çalık, 2003; Özkılıç, 2015).

Commercial buildings and famous historical bazaars also suffered damage in the earthquake. The damage level in the Spice Bazaar was slight; only the entrance door on the side of Balıkpazarı was slightly damaged. On the other hand, the Grand Bazaar has been affected terribly, the shock caused the worst fatalities and damages here. Most of the streets in the Grand Bazaar were demolished. The roofs were completely collapsed. The arches of the Hakkaklar Gate were destroyed. The arch on the side of the Nuruosmaniye Gate was destroyed, and big pieces of stones dropped from the arches and caused completely collapsing of the shops. The arch around the Flea Market Gate (Bit Bazaar) was destroyed. Yağlıkçılar Gate side was destroyed. Many shops and stores were ruined. One room of the Cebeci Inn was destroyed. The side of the Çadırcılar Gate was destroyed. Some parts of the Bodrum Inn has been collapsed. The corner of the Fesciler side was destroyed. The Baltacı Inn was terribly damaged. The Sorguçcu Inn collapsed. Kazzazlar Street was almost completely destroyed. Two shops were destroyed in Gaytancılar. Kuyumcular Street was completely ruined. The bedesten was partially devastated. The Yarımtaş Inn, Yuncu Inn, and some parts of the Kellekesen Inn were destroyed. Until 11 July 1894, the number of deaths removed from the rubbles was 135 and the number of injured was 144, and removal of the debris was continuing (Öztin, 1994; Ürekli, 2000; Ambraseys, 2001; Çalık, 2003; Özkılıç, 2015).

The day after the earthquake, newspapers reported that 1,000 houses had been destroyed in Gedikpaşa, Kadırga, Kumkapı, Yenikapı, and Langa (Sakin, 2002). In Kariye Salmatomruk districts, 17 houses completely, 233 houses partially collapsed (Öztin, 1994). In Kumkapı Şehsuvar, 200 houses were highly damaged (Öztin, 1994). In Samatya, many houses collapsed and numerous houses obtained damage (Öztin, 1994; Özkılıç, 2015).

It should be noted that the earthquake was less severe in Pera and caused slight damage. Some houses cracked a bit and only a few chimneys fell (Eginitis, 1894). The walls of the Beyoğlu Hristaki Inn (Çiçek Pasaj) has been cracked, stones fell from its eaves. The Arab Mosque had damage and ruined. In Besiktaş, the Abbas Ağa Mosque was damaged. The Mecidiye mosque, which is also known as the Ortaköy Mosque was badly damaged; because the top of the minarets fell on it, the walls of the dome cracked, some columns were broken and dislodged, the gathering places in both sides needed to be demolished and rebuilt. In Dolmabahçe; the Bezm-i Alem Valide Sultan Mosque (the Dolmabahçe Mosque) was slightly affected by its wall and minaret. The Dolmabahçe Palace suffered slight to moderate damage as slight damage in the rooms, and small cracks on the dome. In the Harem-i Humayun part, the damage was serious; dangerous crack on the wall of the kitchen, and its chimney collapsed (Öztin, 1994; Ambraseys, 2001; Özkılıç, 2015).

Some stones fell from the walls of the Kadıköy Armenian Church, and its main gate slit dangerously. Some parts of the Kadıköy Greek Church were dangerously separated and its dome has cracked. The Cafer Ağa Mosque was damaged seriously. In Usküdar, the Serbostani Abdullah Ağa Mosque was ruined. Some of the mansions in Beylerbeyi became uninhabitable and the household items were completely ruined. The Kuleli military high school was extremely cracked and it was quite damaged. Leander's Tower has been cracked (Öztin, 1994; Ürekli, 2000; Ambraseys, 2001; Özkılıç, 2015).

In the Prince Islands, many houses, schools, and churches were damaged. In Büyükada (Prinkipo), there was no house remained without damage. Büyükada Hristos Church was damaged and the roof of the church collapsed completely, the bell tower

Figure 1.7. Damaged structures in Suriçi district after the 1894 earthquake, using the inventory given by Oztin, (1994). Map adapted from Cplakidas (2011).

fell. Many parts of the Heybeliada Ayios Spiridonos Arsenios-Terki Dünya Monastery and Church had been destroyed and became uninhabitable. Various buildings of the Heybeliada Greek Seminary and The Patriarchate badly dislocated. In Kınalıada, most of the houses were collapsed. Kınalıada Greek Church (Panagia Church) severely cracked and it was partly demolished. In Burgazada, while one official source says 20 houses were collapsed, the other claims except for 8 houses, all of them fell (Öztin, 1994; Ürekli, 2000; Ambraseys, 2001; Özkılıç, 2015). The shock was more destructive in Heybeliada and Burgaz as stated by an anonymous diary, many buildings partly collapsed; especially their chimneys fell (Çalık, 2003). In Yassıada, the castle collapsed and its guard was seriously injured (Batur, 1994).

The city walls, fortress, and gates were also damaged by the earthquake. The Charisius Gate was demolished; its wall collapsed by leaving four houses under it.

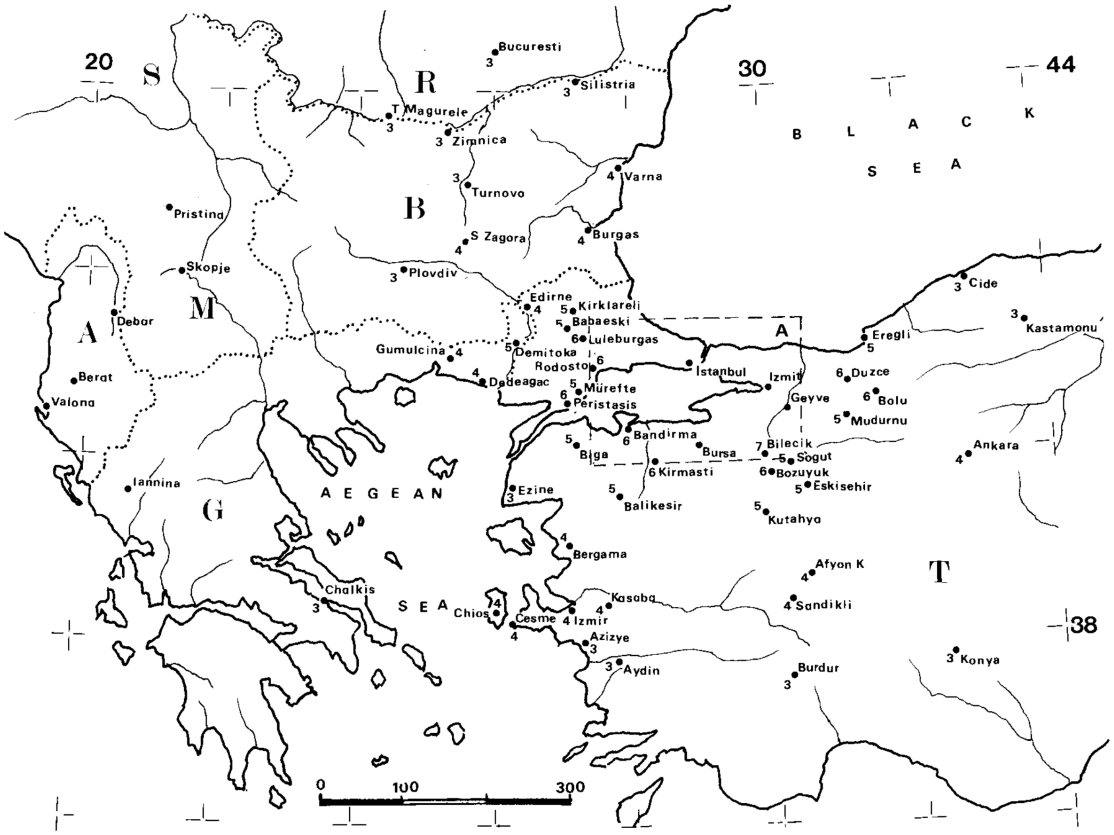

Figure 1.8. Assessed intensities of the 1894 earthquake by Ambraseys (2001) in the MSK scale. A = Albania, B = Bulgaria, G = Greece, M = Macedonia, R = Rumania and T = Turkey.

Some stones fell from the Rumeli Fortress and some parts of the dock have cracked. The wall of the Anatolian Fortress fell down the day after the earthquake. Some parts of the Castle of Silivri has been collapsed, many parts of the walls and bastions had to be demolished. Walls of the Çatalca Castle were partly demolished (Öztin, 1994; Ambraseys, 2001; Özkılıç, 2015).

In along Bosphorus, the effect of the shakes was relatively less serious than the other sides. The churches and the schools in Tarabya, Yeniköy were also disturbed. In Rumelikavağı; the Valide Yusuf Ağa Mosque was collapsed, the minaret of the Rumelikavağı Hisarı Mosque partly fell. After the earthquake, the tendency of people to rent houses in Tarabya and Büyükdere and the exorbitant increase in house rents

in this region (Batur, 1994) is indicative of the fact that this region was less affected by the earthquake. While soft soils and sandstones increase damage level especially in Suriçi and the Prince Islands, rock and hard soil type reduced the consequences of the event in Beyoğlu, Pera, and along Bosphorus as Bebek, Tarabya and Buyukdere (Öztin, 1994; Ürekli, 2000; Ambraseys, 2001; Özkılıç, 2015).

The railway stations in Pendik and Tuzla were partly demolished. In Pendik, many houses near the train station were collapsed, the rest had severe damage, and numerous people were buried in the wreckage. In Tuzla, lots of houses were collapsed and in there, loss of life was around 5-10. In Kartal, Armenian Church suffered damage, a roof of government office fell, a school and two houses completely collapsed. In Maltepe; the train station was completely devastated, three houses were collapsed, the Feyzullah Efendi Mosque was ruined, and the Greek Church (Aya Nikola) was partly demolished (Öztin, 1994; Ürekli, 2000; Ambraseys, 2001; Özkılıç, 2015).

In Yeşilköy, 250 houses became uninhabitable and there was no stone house remained undamaged (Eginitis 1894). The dome of the Latin Catholic Church was demolished. Bakırköy Greek School has been collapsed. A stone arch bridge which is built by chief architect Mimar Sinan, The Kanuni Sultan Suleiman bridge (also known as Büyükçekmece Bridge) has cracked, and the bridge shafts on both sides have been destroyed. Çatalca Ali Paşa Mosque has been cracked from its dome and walls (Öztin, 1994; Ürekli, 2000; Ambraseys, 2001; Özkılıç, 2015).

Waterways and aqueducts were also among the devastated structures during the earthquake. The Bahçeköy aqueduct, the arches belonging to Topuzlu, Valide, and Sultan Mahmut dams have been cracked and water leakage started. Halkalı waterways, which feeds Beyazıt, Sultanahmet, and Hagia Sophia regions, were collapsed (Öztin, 1994; Ürekli, 2000; Ambraseys, 2001; Özkılıç, 2015).

The destructiveness of the event was effective in the neighborhood cities besides Istanbul. In Izmit, buildings and shops were collapsed, many buildings and minarets were damaged. In Gebze, there were few collapsed buildings and most of them were

ruined. In Karamürsel, all the buildings had damage as; few of the houses were collapsed, most of them were moderately damaged and the remains had slight damage. In Adapazarı, the earthquake caused high economic loss; more than 236 houses were completely collapsed, one of each five houses became unable to use, there was no house remained as undamaged. In Sapanca, Rüstempaşa Mosque partly destroyed. Yalova was ruined completely; more than half of the houses were collapsed. In Bursa, there were massive ruins in the buildings. The minaret of the Ulu Cami Mosque was cracked (Finkel and Ambraseys, 1997). Molla Fenari Mosque was devastated, Bursa Central Government Office has been damaged. In Gemlik, a church cracked on the walls and its marble pillars were ruined, besides, walls of a mosque were demolished, people were in a panic. A minaret of a mosque in Mudanya fell down from its half, there were cracks on the walls. Iznik had massive damage. There was slight damage in Karacabey. In Mustafakemalpaşa, there were cracks on minarets, chimneys were collapsed and roof tiles fell down. Damage has been reported in Orhangazi. In Trilya and İnegöl, the shock wave felt strongly. In Bilecik the shake was felt strongly. In Yakacık, 18 houses were collapsed. The earthquake was felt in Söğüt and Osmaneli. In Tekirdağ, a post office (Telgrafhane) was ruined, stones dropped from the walls and the minarets. In Babaeski, there were cracks on the walls. The front wall of the Babaeski telegraph office cracked. In Kıyıköy, stones fell from the walls. In Vize, Çorlu, Lüleburgaz, and Pınarhisar damage levels were slight as cracks on the walls and some chimney damages. In Çanakkale and Lapseki, the shake was felt strongly. In Gallipoli, a flour factory was partly devastated and the chimney of the factory was destroyed, besides, the Hoca Masjid Mosque had damage from its front side, the walls of two houses were collapsed. The earthquake was felt in the wide region as Afyon, Sandıklı, Emirdağ, Bolvadin, Balıkesir, Bandırma, Edirne, Greece, Crete, Yanya (Ioannina), Dimetoka, Bucharest, besides Konya and in most regions of Anatolia. Ankara was quite slightly damaged (Öztin, 1994; Ürekli, 2000; Ambraseys, 2001; Özkılıç, 2015). Estimated intensity map by Ambraseys is given on Figure 1.8.

As the first scientific report which is prepared by an expert and using the observations right after the earthquake, given information in the report of Eginitis is quite important. On the other hand, his assessment may fail to describe the damage level in

the fields where he did not visit, like Adapazarı (Finkel and Ambraseys, 1997). At that time from Adapazarı, Dybowski gives important details on La Natura magazine. As stated by Dybowski, about 236 houses were ruined, 600 houses became uninhabitable, and one-fifth of the buildings were damaged (Dybowski, 1894). On the other hand, this information does not overlap with the official records. On 12 July, the daily press reported 200 collapsed buildings (Oztin 1994, page: 42). According to the records; there was 23 loss of life in Adapazari, while Dybowski claims 60. As stated in the "iane kayıtları" allowance had been given to 600 households whose houses were moderately damaged after the earthquake in Izmit Province. It should be noted that at that time the Province of Izmit covers many cities as Izmit, Adapazarı, Karamürsel, Kandıra, and Gevye. For that reason, 600 damaged house in Adapazarı must be exaggerated and cannot represent the truth (Özkılıç, 2015, pages: 64-65). In addition, a telegram sent from the Izmit command the day after the earthquake provides more information about the damage caused in Izmit and surrounding neighborhoods. According to the telegram, there was no loss of life after the earthquake in the city, but the Fevziye mosque and its minaret were destroyed above the balcony, the minaret of the Orhan Mosque was toppled in Adapazarı, and cracks formed on the walls of buildings allocated to soldiers. On the other hand, in Adapazarı, numerous houses were destroyed, and many people lost their lives, but the exact number is unknown. In Sapanca, a Lieutenant of Cavalry jumped out a window during the earthquake and broke his foot. The telegram also states that there are some damages in other places but not exactly known at that time and requests for damage investigation by the municipal architects (Ekin, 2005).

In the report, Eginitis stated that having wooden denser dwellings decreased the casualties in Istanbul, otherwise the shake could result in higher loss. Even the old wooden buildings with poor quality have survived, while the well-built, new masonry buildings even which are connected using iron ties, have been demolished. After wooden ones, the buildings most resistant to the earthquake were made with brick. In Büyükada, while the middle part of a house made of stone fell down, the brick part of it was still standing (Eginitis, 1894). We can also learn structural conditions of that time in Adapazarı from Dybowski. According to Dybowski, the houses in Adapazarı

were wooden chalets which were made with beams held with nails. The beams were surrounded with slats “like a basket” (Dybowski, 1894). The houses were either covered with mudbrick, or with mud and straw mixture. These houses were without a foundation, and were built on beams lying on stones. The floor of a house could be visible from the gaps of rafters. For this reason, ground floor of these houses frequently be flooded in heavy rain. The trees used in the construction may rot over time with the change of atmospheric conditions and begin to creak when someone walk on. The roofs were made of half cylindrical, very heavy bricks. As Dybowski’s own statement, the conditions of these houses were exactly terrible, and despite this, local people call these houses as ”konak” (which means a mansion in Turkish) (Dybowski, 1894).

Damaged structures will not be explained here longer to prevent repetitiveness with the inventory sources. More detailed information can be found in the references.

The 10 July 1894 earthquake was recorded from the outlying cities which are two pendulums in Bucharest, the horizontal pendulum in Nicolaiew, magnetic instruments at Pola, Potsdam, Wilhelmshaven, Utrecht, Parc Saint-Maur and Kew (Davison, 1894). The recorded pulsations by the Vicentini micro-seismograph at Siena given in Figure 1.6 (Davison, 1896).

After the July 10 earthquake, aftershocks continued for days until August 8, and there was a long period of panic among the public (Eginitis, 1894; Dybowski, 1894; Ozkılıç, 2015, page: 303-304; Oztin, 1994, pages: 39, 41-42, 45-48, 56-67). In particular, the strongest aftershock on July 12 caused the destruction of structures that were heavily damaged but not destroyed by the mainshock. For example; Yeşilköy Catholic Church had severe damage on July 10 but it was collapsed completely on July 12 (Oztin, 1994, page: 67; Ozkılıç, 2015, page: 27).

A day after the earthquake, the newspaper Sabah reported that the casualties are 70 dead, 700 injured and it is expected to increase in these losses (Sakin, 2002). To reduce panic, the newspaper Sabah was closed, foreign newspapers such as Zanta, Petit Journal, and others that said the earthquake would continue were banned (Genç and

Mazak, 2001; Batur and Tanyeli, 1993). The Sultan ordered newspapers to write with softened wording (Ürekli et al., 2018; Genç and Mazak, 2001). 2-3 days later from the earthquake, national and external press changed their previous expressions and reduced fatalities, as well as mentioned that the earthquake was effective in only some neighborhoods (Batur and Tanyeli, 1993). Since Dybowski reports the censorship in Adapazarı, it seems like this situation was not only valid in Istanbul, but all the regions (Dybowski, 1889). For that reason, the fatalities remained unknown and the lack of consistency in the sources indicate different numbers. In what follows, the number of casualties in İstanbul recorded in the archives is given as Oztin, (1994, pages: 9-13-20-23-47): In Prince Islands; 46 dead, 31 injured. In Bakırköy (including Zeytinburnu); 18 dead, 52 injured. In Beşiktaş; 8 dead. In Beyoğlu; 19 dead, 28 injured. In Eminönü; 72 dead, 53 injured. In the Grand Bazaar; 135 dead, 147 injured. In Eyüp; 4 dead, 13 injured. In Fatih; 136 dead, 111 injured. In Kadıköy; 2 dead, 5 injured. In Sarıyer; 1 injured. In Şişli; 1 injured. In Üsküdar; 12 dead, 37 injured. In Çatalca; 2 dead, 1 injured. In Kartal; 20 dead and 2 injured. In Istanbul, total fatalities were 474 dead and 482 injured. On the other hand, casualties are given by Ozkılıc as 161 dead and 378 injured (Ozkılıc, 2015, pages: 49-50).

The most affected structures by the earthquake were dwellings and they were not included in the damage inventories. According to the list showing the number of the given financial allowance to the earthquake victims, the number of households destroyed/damaged in the 1894 earthquake was 20,959 in only Istanbul. As stated by Cervati, in 1893-1894, the number of dwellings in Istanbul was 162,950. Of these, 158,000 were in Istanbul (including Pera, Eyüp, and the suburbs in the European and the Asian coasts of the Bosphorus), 4,950 of them are the dwellings in the Prince Islands; as 1,810 were precious villas and 3,140 were ordinary dwellings (Cervati, 1894). If the numbers of households who repaired with their own means are neglected, damaged dwellings will be approximately 1/7 of the number of households in Istanbul at that time (Ozkılıç, 2015, page:68). In Table 1, damage distribution of the dwellings of the districts In Istanbul and neighborhoods are given (Özkılıç, 2015, page:321). The highest damage seems in Suriçi, with 12,762 total number of the damaged structure.

Table 1.1: Number of the damaged dwellings different damage levels in the corresponding regions. The numbers were obtained from the official allowance list (Iane-i Musabin Commission) for the victims of the 10 July 1894 earthquake (Özkılıç, 2015, page: 321). (*: Total number is given here as written on the list.)

Districts	D4-D5 Very Heavy Damage and Destruction	D3 Substantial to Heavy Damage	D2 Moderate	Financial aid with special permission	Fire-wall collapsing	Total Damaged Dwellings
Eminonu, Beyazit, Aksaray, Sehzadebasi	1,210	2,097	60	1	-	3,368
Fatih, Edirnekapi	1,438	1,325	20	3	3	2,789
Cerrahpasa, Kocamustafapaşa, Yedikule, Silivrikapı, Mevlanakapı, Topkapı	4,926	1,644	27	-	8	6,605
Besiktas, Ortakoy	122	154	2	-	-	278
Yenikoy	28	185	-	-	-	213
Beyoglu, Galata, Pera	273	1,642	1	-	-	1,916
Buyukdere, Sariyer	16	210	2	-	-	228
Kanlica	182	160	-	-	-	342

Uskudar	171	910	-	-	-	1,081
Kadikoy, Maltepe	126	205	1	-	-	332
Kucukcekmece	601	602	12	-	-	1,215
Kartal, Gebze	686	184	3	-	-	873
The Prince Islands	392	51	3	-	-	446
Catalca, Buyukcekmece	-	509	-	-	-	509
Sile	-	117	-	-	-	117
Izmit, Adapazarı	-	600	-	-	-	600
Bursa	-	49	-	-	-	49
Total*	10,471	10,648	129	4	11	20,959

Especially in Istanbul and its villages, the catastrophic consequences of the earthquake increased significantly due to the narrowness of the streets, weak construction, and the devastation of buildings. Having the old, maintenance-free structures and soft soil settlements increased the level of devastation of the earthquake in Suriçi.

Some researchers have claimed that the buildings that were destroyed during the 1894 earthquake in the historical peninsula and Galata were maintenance-free structures and not built with engineering knowledge. Foundations of new built buildings were weak (Batur, 1994; Ürekli, 2000). Even though almost all masonry houses in Adapazarı collapsed (Batur, 1994), according to Ürekli (2000), the majority of houses in Adapazarı were poorly built structures. In Istanbul, the Grand Bazaar is another example of this argument (Ürekli, 2000). Moreover, its filled soil increased the damage

level (Öztin, 1994). On the other hand, the buildings and towers made in accordance with the rules of construction have not been demolished (Ürekli, 2000).

The first instrumental recording of earthquake waves started in the last two decades of the nineteenth century. When the 10 July 1894 earthquake happened, there was no one with expertise on seismology and earthquakes in the Ottoman Empire. After the catastrophe, the authorities decided to follow contemporary developments in this field. At that time, there was an observatory under the direction of Mr. Coumbary but without seismic equipment in Istanbul. For that reason, after the earthquake, there were attempts to obtain seismological measurements. Two seismographs were ordered from Italy; one was installed at the observatory, namely Rasathane-i Amire, and the other was at the Yıldız Palace, which was the residence of the Sultan. With the recommendation of M. Tacini, who was the Director of the Rome Observatory, Italian seismologist Prof. Agamemnone was invited to Istanbul. Within two years, he installed a number of seismographs, organized the Seismological Service, issued annual bulletins, and taught seismology to young students until his departure in January 1897 from Istanbul (Finkel and Ambraseys, 1997; Davison, 1896). Rasathane-i Amire has changed over time, had suspension and re-activated, and has become today's Boğaziçi University Kandilli Observatory and Earthquake Research Institute.

1.3.7. Tsunami Effects

Even though there is not any official record in the Ottoman Empire archives about tsunami, secondary sources give a few information on the observed sea wave rising during the 1509, 1766 and 1894 earthquakes. During the 10 September 1509 earthquake, in the historical peninsula and Galata streets flooded due to large sea waves around the city walls (Hammer, 1835; Sanuto, 1879-1903). The 22 May 1766 earthquake caused flooding around Bosphorus, Galata, and the opposite coast, and in Mudanya (Ambraseys and Finkel, 1995). In the 10 July 1894 earthquake, newspapers and official reports have some expressions on tsunami. According to the report of Eginitis, the rise of the sea level increased along the coastal area, and then the sea was pulled up without permanent change (Eginitis 1894). From Yeşilköy to Kartal, on

many parts of the Marmara such as Kadıköy, Uskudar, Tophane, Samatya, Sarayburnu the sea first pulled up to 200 meters, then hit ashore with strong waves (Sakin, 2002; Ürekli, 1999; Çalık, 2003). Along the coast of Yeşiköy to Çekmece, the wave amplitude could be approximately 1.5 m (Oztin, 1994). In Yesilköy, the sea rose 1.5 m above and caused flooding in the shore (Ambraseys, 2001). It was observed by locals that the temperature of the seawater was higher than it used to be (Eginitis, 1894). As stated by a newspaper Moniteur Oriental, the waves caused flooding in some bridges such as Karaköy and Azapkapı (Batur, 1994).

Since tsunami is beyond the scope of this work, this section is not described with details. Interested readers may find more information in recent studies written by various researchers.

1.4. Literature Survey on Discrepancies in Source Parameter

There are discrepancies between researchers about the intensity, epicenter, magnitude, rupture length, and associated fault segment of the event of the historical events. Tables 1.2, 1.3 and 1.4 provides available epicentral location, magnitude and intensity of the 1509, 1766 and 1894 earthquakes by different sources. Even though we have respectively more knowledge about the 1894 event, we have huge discrepancy in epicentral location and magnitute (Table 1.4).

Another discrepancy is the rupture length. Ambraseys and Finkel, 1991 indicated the rupture length of the 1509 event as more than 200 km. By contrast, it is stated as no more than 70 km of faulting by Ambraseys and Jackson, 2000. Similarly, Hubert Ferrari (2000) and KOERI (2003) located different epicenters and estimated different rupture lengths for the same events.

Figures 1.9, 1.10 and 1.11 illustrate the epicenters assigned by different researchers to the 1509, 1766 and 1894 Istanbul earthquakes.

Table 1.2. Epicenter, Intensity, and Magnitude Evaluation by different researchers for the 1509 Istanbul Earthquake.

Lat	**Lon**	**Intensity, Io**	**Magnitude**	**Source**
40.900	28.700	-	7.2	EMEC
41.022	28.786	10	7.15 +/- 0.33	AHEAD (SHEEC)
40.900	28.500	10	7.40	AHEAD Papazachos, P., (2003)
40.900	28.700	9	7.2	Ambraseys and Jackson, (2000)
40.750	29.000	9	-	KOERI
40.700	28.800	-	7.5	Bulut et al., (2019)

Table 1.3. Epicenter, Intensity, and Magnitude Evaluation by different researchers for the 1766 Istanbul Earthquake.

Lat	**Lon**	**Intensity, Io**	**Magnitude**	**Source**
40.800	29.000	-	7.1	EMEC
40.837	29.463	8	6.76 +/- 0.38	AHEAD (SHEEC)
40.800	29.100	9	7.10	AHEAD Papazachos, P., (2003)
41.000	29.000	-	6.80	AHEAD Soysal et al., (1981)
41.000	29.000	9	-	AHEAD Shebalin et al., (1974)
40.800	29.000	-	7.1	Ambraseys and Jackson, (2000)
41.000	29.000	9	-	KOERI

Table 1.4. Epicenter, Intensity, and Magnitude Evaluation by different researchers for the 1894 Istanbul Earthquake.

Lat	Lon	Io	Magnitude	Source
40.750	29.550	-	7.4	EMEC
40.943	29.039	8	6.71 +/- 0.44	AHEAD (SHEEC) Stucchi et al. (2013)
40.750	29.550	-	7.4	EMEC
40.750	29.200	9	7.20	AHEAD Papazachos, P., (2003)
40.600	28.700	10	-	AHEAD Soysal et al., (1981)
40.600	28.700	9	-	AHEAD Shebalin et al., (1974)
40.750	29.550	-	7.3	Ambraseys and Jackson, (2000)
40.600	28.700	9	6.94	Ergin and Guclu, (1967); Tezcan (1991)
40.750	29.550	-	7.3	Ambraseys, (2001)
40.900	27.700	-	-	Sezer, (1997)

Figure 1.9. Estimated epicenters of the 1509 event by different researchers.

Figure 1.10. Estimated epicenters of the 1766 event by different researchers.

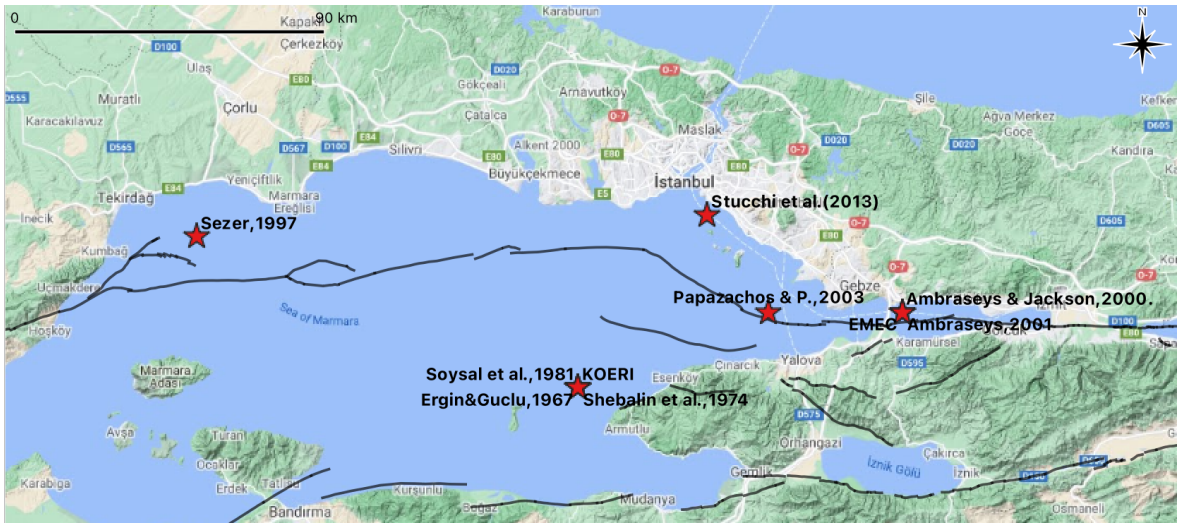

Figure 1.11. Estimated epicenters of the 1894 event by different researchers.

2. THE GROWTH OF ISTANBUL OVER CENTURIES and ASSOCIATED BUILDING INVENTORIES

2.1. Brief Overview of the Population Growth and Structural Typology in Istanbul

In Istanbul, it is known that except Topkapı Palace, mosques, madrasahs, imarets, libraries, inns, and tombs, many other buildings were all wooden (Ergin, 1995). Although Istanbul has experienced many earthquakes throughout its history, the impact of these earthquakes on dwellings were comparatively less since they were generally wooden (Cezar, 1963). Earlier in Istanbul, there were large masonry mansions, gardens, orchards, and large squares. With time, small wooden buildings were preferred because of the increase in population (Ergin, 1995). Locals preferred wooden construction because of its advantages including earthquake resistance. Earthquakes damaged mostly masonry buildings such as masjids and madrasahs and the most damaged parts of these were their minarets and domes (Ergin, 1995).

In this section information on city growth, population increase, construction area density, and the preferences in structural materials will be given for the related centuries.

2.1.1. The Fifteenth and Sixteenth Centuries

It is estimated that the total population of the city was around 70,000 during the conquest of Istanbul in 1453 (Ayverdi, 1958; Müller-Wiener, 2001). Only predictions can be made about the housing styles of this period. The majority of the population lived in modest wooden houses and in ruins where they could meet their basic needs (Müller-Wiener, 2001). During the first years after the conquest, people settled in the dwellings of the former residents, which are estimated to be around 10,000 houses. Due to the deterioration over time, many new houses were built and the city began to rise

from the coast to the hills (Ayverdi, 1958). Hagia Sophia, and some other churches were turned into mosques. The city walls, which had not lost their strategic importance yet, were immediately repaired (Kuban, 1998). The construction works during the Fatih period were intense and it gave a new face to Istanbul in a short time. According to the list given by Ayverdi, the number of well-built new constructions reached 300, mainly mosques, madrasas, tombs, baths, and bazaars (Ayverdi, 1953).

The first problem after ensuring the security of the city was to provide a sufficient population for a capital. During the reign of Fatih, Turks, Greeks, Armenians, and Jews brought from Anatolia and Rumelia were relocated in the city. The Turks were placed between Aksaray and Bayezid and on the slopes of the Golden Horn between the Fatih Mosque and the Old Palace (Eski Saray). The Greeks were settled mostly on the shores of Marmara, and some to Galata and the Armenians were settled in Samatya (Kuban, 1998). There is not enough documentation to determine the population of the city in this hectic age of development and settlement. In a document written towards 1477, it is stated that there were 8,951 Turkish, 3,151 Greek, and 2,695 other houses in the city with 3,667 shops, while in Galata there were 535 Turkish, 592 Greek, and 394 other dwellings with 260 shops. Thus, there were 16,318 houses and 3,927 shops in total in Istanbul and Galata (Ayverdi, 1958). Different interpretations exist on how much population this building count corresponds to, which does not include the population outside of the city walls like Eyüp, Üsküdar, and small settlements along the Bosphorus. The population per dwelling is considered to be at least 7 or 8 by Ayverdi (Ayverdi, 1958), and 4 or 5 by Schneider (Schneider, 1952). The number of people per household may differ in Turks and Christians. If this population is multiplied by a factor such as 5 or 6, the population may be more consistent within the economic and political conditions of that period. If the Palace, soldiers, and madrasahs are also included, the total population of Istanbul and Galata should be around 100,000 at the end of the Fatih period, and with the small villages around the city it should be between 110,000 and 120,000. At the end of the century, the population of the city must have approached 200,000 (Ayverdi, 1958).

According to Kuban (1998) the houses were generally one-storey houses called

beyt-i sufli. During the Bayezid II period (1481-1512) two-story houses began to be built. Until the period of Süleyman I (1520-1566), it is understood that Istanbul dwellings were mostly single storey and made of adobe, rubble, and brick (Kuban, 1998).

The first document showing the situation of Istanbul is the miniature of Matrakçı Nasuh (Figure 2.1). The miniature gives an idea about the large building complexes of the city and its ports. Single story wooden shops located along the streets between Divanyolu and Golden Horn can be seen in the miniature. It is also seen that large structures are located around the old Hippodrome, which should have been the palaces used during the Byzantine period. In this representation, it seems that the hippodrome and the city walls, which are thought to be around the Old Eleutheriun Harbor, were not completely demolished. The shipyards in Kasımpaşa and neighborhoods which started to develop in Tophane were also illustrated (Kuban, 1998). Matraki's map contains illuminating information on the residential architecture of the period. These houses are rubble or mudbrick, plastered, wooden roofed and with a bay window, and they are very different from the known Turkish houses. It confirms that the house type, known as the Turkish House, originated after the sixteenth century (Kuban, 2010). The Turkish House which started to be seen in the 16th century is a structure of half-timbered (Turkish: hımış) technique, where the rib of the building was constructed from wooden rafters and the spaces were filled with rubble. Examples of such construction can be seen in many places in Anatolia (Eyice, 2006).

At the beginning of the 16th century, Sultan Süleyman continued the construction of the city by building numerous structures with artistic characteristics. Monumental mosques were built in a short time as; the Sultan Selim Mosque (1519-1522), Şehzade Mosque (1543-1548), and Süleymaniye Mosque (1550-1557). In addition to the Sultan, his wife and his daughters also built mosques and charities: In 1539, Haseki Hürrem Sultan built the Haseki Mosque and its surrounding structures. In 1547, Mihrimah Sultan built two more complexes. These mosques were built in important places in terms of urban planning. Besides their sanctity, these complexes had educational and social functions for the public. Most of the mosques were associated with imarets to

Figure 2.1. Istanbul in 1532 by Matrakçı Nasuh. 1. Topkapı Palace, 2. Hagia Irene, 3:Hagia Sophia, 4. Hippodrome, 5. Ahırkapı, 6. Grand Bazaar, 7. Ibrahim Pasha Palace, 8. Beyazid Mosque, 9. Fatih Mosque, 10. The Valens Aqueduct, 11. Yedikule Fortress, 12. Kadirga Harbour, 13. City Walls, 14. Yavuz Selim Mosque, 15. Leander's Tower, 16. Galata Tower, 17. Tophane, 18. Uskudar

provide food and beverage to the needy in a large part of the society.

A large number of new domes and minarets completely changed the city's appearance. However, as can be seen from notes of travelogues and engravings of the 16th century, narrow cobblestone streets and up to two-storey wooden houses on both sides were the main elements that dominated the appearance of the city (Müller-Wiener, 2001). Only the avenue from Topkapi Palace and Hagia Sophia Mosque, which followed the old street, and lead to Edirnekapi was rebuilt since it was used for the ceremonial entrances and exits of the Sultan. It was the same even in the 18th Century (De Carbognano, 1993). Travelers who came to Istanbul in the 16th century wrote

that most of the houses were single storey. These houses were mostly timber framed with rubble stone and adobe infill (Kuban, 1998).

During the 16th century, the city of Istanbul consisted of four districts: Istanbul proper, Galata, Eyüp (outside of city walls) and Üsküdar. The quarters did not spread beyond the walls, and the population within the walls was dense. The increase in the density of settlement on the shores of the Bosphorus had started during the Sultan Süleyman period. Beginning from the 16th century, Üsküdar became increasingly crowded and an important district. By comparing the number of mosques built during this period, it can be assumed that one-tenth of the population of the city lived here. Between 1520-1535, the population may have reached 400,000 - 500,000 according to some historians (Kuban, 1998; Yazan, 1989; Mantran, 1990). In 1535, the number of dwellings in the city increased to 80,000 (Çelik, 1896; Mantran, 1990). It should be remembered that there were 16,324 dwellings with an expectation of approximately 200,000 population in 1478 (Ayverdi, 1958).

The rapid increase in the population caused densely placed structures. However, after the massive destruction and numerous life losses in the 1509 earthquake, the structural material of the construction turned into wood (Eyice, 2006). After the 1509 event, residential houses, mansions and even the palaces were built in timber because of its high earthquake resistance (Urekli, 1999). Wood construction may also be preferred for its fast, cheap, and temporary construction advantages (Kuban, 1998). As a result of this change, large fires started to occur frequently in the city beginning with mid-16th century.

2.1.2. The Seventeenth and Eighteenth Centuries

In the 17th century, the city was continuously expanding. Istanbul had gained two more monumental structures in the first half of the century; the Sultanahmet Mosque (Blue Mosque) (1609-1616) and the Yeni Cami (New Mosque) (1597-1665).

The appearance of the Galata region was quite different than that of Istanbul.

Although the surrounding walls were partially demolished, on either side of its narrow and steep streets, high stone Genoese structures were located. Outside of the Galata walls, Pera was full of fruit gardens, orchards, and large houses with gardens (Müller-Wiener, 2001; Çelik, 1986).

In the second half of the 17th century, despite the ordinance for the stone construction, the building style dominating the city was still wooden. From 17th to 18th century, the palaces were built in wood, even the palace of the Sultan was wooden until the great fire of 1665 (Müller-Wiener, 2001).

Until the 18th century, the Grand Bazaar, which was the commercial center of Istanbul, consisted of streets with wooden single-story shops on both sides, and each street was divided into a certain branch of commerce such as tailors, drapers, jewelers and so on. The shops were lined up the streets around the two bedestens. The Spice Bazaar, which is part of the Yeni Mosque complex, is one of the most important and monumental examples of the stone arastas of the 17th century. The inns were up to two-story, generally rectangular structures with a central courtyard and single entrance. Generally, their ground floors were made of rubble stone, and the first floors were made of wood with all their horizontal elements. An edict dated 1717 decreed that all the inns and shops should be made of masonry because of the fire hazard (Ergin, 1995). On the other hand, the inns and shops were still built of wood in the suburbs of Istanbul such as Edirnekapı, Fatih, Şehzadebaşı, and Üsküdar, the reason being the cheapness and quickness of wood construction (Kuban, 2010). The construction material of these shops gradually turned to masonry. This process lasted until the 19th century (Kuban, 1998).

In the 18th century, even though the settlements remained the same, the borders expanded. From Ayvansaray to Eyüp, only a row of mansions was located on the coast, and the residential area extended to the slopes of Eyüp. At that time, Bosphorus was only accessible by boat from the sea, its mansions had gardens until the hills with a small pier at the seaside. Since the fires forced people to settle outside of the city walls, the population of the Golden Horn, Bosphorus and Üsküdar increased more

than that of the historical peninsula. Beyoğlu started to develop but did not extend to Taksim. From Galatasaray to the walls of Galata, the settlement was concentrated on the slopes facing the Golden Horn. Boğazkesen widening to Tophane, and Cihangir slopes began to fill towards Fındıklı. Considering that a masjid was built in Teşvikiye at the end of the 18th century, it can be said that it also extended towards Beşiktaş. Besiktas also expanded until Vişnezade. In the slopes of Cihangir, Sıraselviler, and Fındıklı, sparse settlements were formed (Kuban, 1998). According to the Istanbul court records, the number of wooden houses, in which almost all of the population of the city lived, was 88,185 (İnciciyan, 1976). The architectural features of these wooden houses were unregulated. The houses usually were up to two floors. Their interior timber framed walls plastered with lime mortar and exterior walls clad with timber or plastered. These houses included bay windows to allow for a more comfortable life for the residents (De Carbognano, 1993).

At the end of the 18th Century, the total population of Suriçi, Galata, Üsküdar, Eyüp, and Bosphorus estimated as at least 400,000 (Mazlum, 2011; Kuban 1998). Starting from the reign of Ahmet III (1703-1730), edicts were issued to stop the migration to the city (Aktepe, 1958). This indicates the continuation of migration and the authorities desired to control the growth of population.

2.1.3. The Nineteenth Century

As stated earlier in Istanbul the houses might be one-story, rubble stone buildings with wooden roofs. Construction of masonry houses became widespread in the nineteenth century. It is possible to follow the development of Istanbul from the maps of the 19th century.

In order to build and repair a building in Istanbul, it was essential to obtain permits from the head of architects and many other authorities. Especially outside of the city walls, building a house outside predetermined regions was not possible to prevent unrestrained expanding (Ergin, 1995).

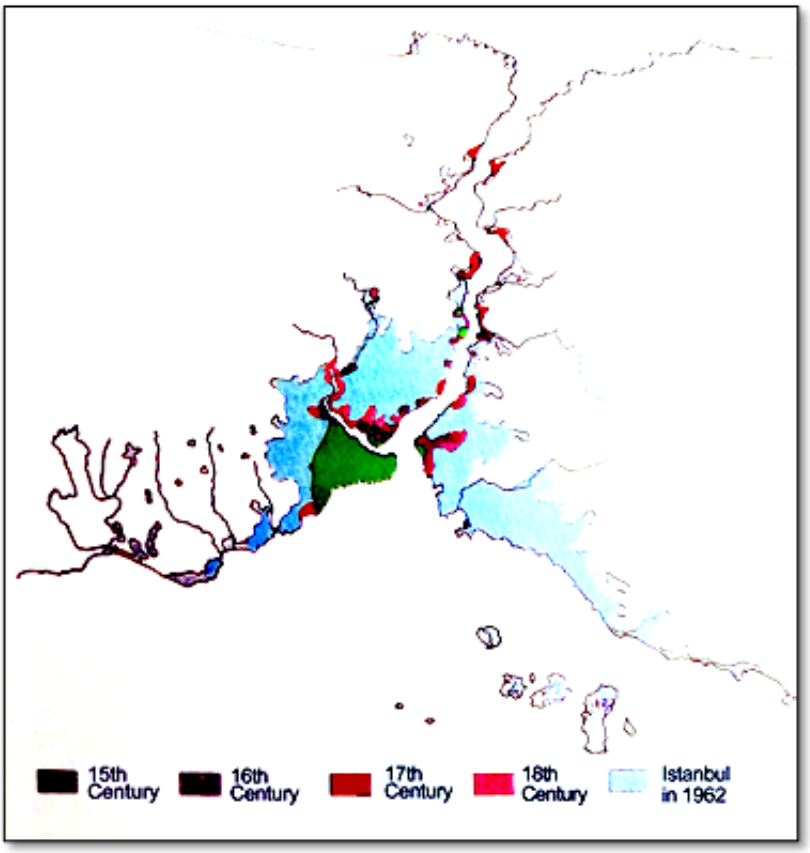

Figure 2.2. Expansion of the city boundaries between the 15th and 20th centuries (Kuban, 1998).

Until the nineteenth century, stone-masonry construction was used mostly in the monumental and public buildings. In the second half of the 19th century, the European and Art Nouveau style dominated the stone architecture, especially in the districts where minorities are concentrated. These houses were usually two or three stories, up to five meters of facade, and with one family resident. Apartments up to seven stories were first built in Pera. The most glossy examples were in Galata and Beyoğlu where the city's commercial and modern life were concentrated. Fener, Balat, Kumkapı, Gedikpaşa, Kadıköy, Talimhane, Kuzguncuk were the typical districts with masonry residences. In 1875, the most spectacular apartment row sets were built in Akaretler (Kuban, 1998). On the other hand, it was not a general trend, wooden construction was still highly preferred in most settlements. In these years, numerous wooden row houses were built in the villages of Bosphorus as Arnavutköy, Ortaköy.

Today, it is possible to see the wooden examples of the late Ottoman Era especially in the Prince Islands (Kuban, 1998; Kuban, 2010; Eyice, 2006).

Until mid-19th century, the streets were quite narrow in Istanbul. Usually, the alleyways were up to 1.5m, and the streets up to 4m wide, which can be seen on the old city maps. Overbuilding on these narrow streets lead to high damage after hazards. Despite numerous calamities, the first arrangements to make wider streets, and environmental planning started in 1839 (Ergin, 1995).

Besides earthquakes, the big fires changed the fabric of urban Istanbul. Especially the 1856 Aksaray Fire, and the 1865 Hocapasa Fire played major roles in city planning. After the Aksaray Fire, not only the damaged structures but also the entire Aksaray district was renewed. After the Hocapaşa Fire, financial support was provided to the locals to build masonry properties. In 1864, there was governmental encouragement to transform all the structures into masonry except the poor residents. In 1875, the capital was divided into two zones as the main city and subareas. Wooden construction was strictly banned in the main parts. The main parts included the axis from Unkapanı to Aksaray, Şişli, Cadde-i Kebir (Istiklal Street) in Pera, and the shoreline from Azapkapı to Ortaköy (Çelik, 1998). Despite the law in 1882, transforming wooden structures to masonry could never be fully implemented (Çelik, 1998). Accordingly, the official construction rules (Turkish: Ebniye Nizamnamesi) dated 1894, almost all the dwellings were still wooden in the historical peninsula (Ergin, 1995). The reason was not only economic; wood was providing easy and quick construction. These wooden structures were not long lasting, but it produced more design flexibility to the residents compared to the masonry. There were also cultural backgrounds in this preference. In the Islamic Society, a house had a secondary position because people believe that everything is temporary. In addition, the Turks had a nomadic culture as well (Kuban, 2010).

According to the first census records, the number of inhabitants in Istanbul was 873,575 in 1885, and 864,576 in 1906 (Shaw, 1976). The population was concentrated especially in Galata and Suriçi districts.

The Stolpe's city map of 1882 describes changes inside the city walls and the settlement expanding outside (Figure 2.3). According to this map, a large neighborhood was formed outside Yedikule. Bakırköy and Yeşilköy were the largest residential areas in the west. New settlements were formed in Golden Horn. In Galata, Hasköy and Piripaşa neighborhoods had not reached to the hills yet. The area parallel to the city walls between Bayrampasa, Langa, Yedikule, Topkapı, and Davutpasa were still full with orchards. There were also large orchards in Ayazpaşa, Pangaltı, Osmanbey, Bomonti, Şişli, and Maçka. Inhabitation around Pangaltı and Nişantaşı had not started yet. The boundaries of Uskudar were extending to Karacaahmet Cemetery; Kadıköy was a residential area with large gardens and orchards extending to Altiyol (Kuban, 1998).

Figure 2.3. The Istanbul Plan in 1882 by C. Stolpe.

In the palaces, masonry was not a preferable construction material until the construction of the Dolmabahçe Palace, which was built between 1843-1856. In the period of Sultan Abdulhamid II (1876-1909), the reconstruction works of Istanbul were

inspired by Paris. Even though palaces were built in similar styles with European examples, the mansions and pavilions continued to be built in wood. Towards the end of the 19th century, hybrid houses were created as a mutual interaction between the wood construction and the masonry (Kuban, 1998).

2.2. Generating Building Inventories

2.2.1. City Maps

Locations and structural types of the damaged buildings after the 1894 earthquake were based on old city maps. Since the positions of the monumental buildings remained the same, the same methodology was followed for the older earthquakes, if there is not available information about the location or structural material. In case of uncertainties and lack of reliable information, the most likely position was selected, and vulnerabilities were classed either by looking at the general tendency of the region or structural type of the buildings cited as unknown. While the churches mostly were of masonry and the wooden ones were rare, the mosques could be both wooden and masonry. If the neighborhood of the damaged structure is unknown, it was excluded from further evaluation. Brief information about the maps utilized can be found below.

2.2.2. The Map of Istanbul in the 19th Century (Ayverdi Maps)

Locations of the damaged buildings were mainly found by using the Map of Istanbul in the 19th Century of Ekrem Hakkı Ayverdi. The map does not contain exact date information, no explanation of signs, and no abbreviation list. It is known as Ayverdi Maps since the map was examined and published by Ekrem Hakkı Ayverdi. The Ayverdi map consists of colorless 20 sheets at 1/2000 scale with 45x60 cm from the historical peninsula, excluding Eyüp, Galata, and Asian side. Possible date range of the map is estimated between 1875 to 1882. It makes these sheets more important because they represent the settlements before the catastrophic fire series like Çırçır (1908), Aksaray, Mercan and Balat (1910), Ishak Paşa (1912), Cibali-Cerrahpaşa- Şehremini and Vefa (1918), Karagümrük (1919) which changed the city texture dramatically

(Ayverdi, 1958).

2.2.3. Insurance Plan of Constantinople (Goad Maps)

In the nineteenth century, the rapid growth of the city triggered fire hazard, and fire insurance companies were set up. After the 1870 Beyoglu Fire, which affected the commercial center of the city, fire insurance companies started to do business in Istanbul, and required detailed city plans. The first one of these maps issued by Charles Edward Goad, a civil engineer from London, as Insurance Plan of Constantinople (Plan d'Assurance de Constantinople) between 1904 to 1906. The first part of these maps was published in 1904 as 20 sheets with 1/600 scale which represents some part of the historical peninsula, from the seasides of Eminönü and Golden Horn to Divanyolu. The plans of Galata and Pera were published in 1905 as 18 sheets with 1/600 scale again. Kadikoy part from Haydarpasa to Moda of these maps were published in 1906 as 14 sheets with 1/1,200 scale. Each part included a key plan. The maps were written in French and using the French spelling of Turkish names. The Goad maps clearly show location, footprint, height, usage, roof material and construction material type of each building. Construction materials were represented using different colors, red indicates brick or stone buildings while yellow is wooden.

2.2.4. German Blues

German Blue Istanbul maps are published before World War I, between 1913 to 1914. German Blues were prepared for the purpose of city planning, and all the districts of the city were mapped by a German company, Deutsch Syindikat für Staebaliche Arbeiten. German Blues consist of three volumes; the first volume has plans of Uskudar and Kadikoy from the Asian side and partly includes Besiktas from the European side. The second volume involves Beyoğlu, Eminonu, and partly Fatih. The last volume is for Fatih and Eyup districts. The sheets were drawn with varying scales (1/500, 1/1000 and 1/2000), colored and include the Turkish names of the buildings with their French spellings. German Blues mostly focused on the public and monumental structures in Istanbul, and dwellings were excluded.

2.2.5. Pervititch Maps

A topographer Jacques Pervititch drew another set of precious fire insurance maps in an extended-time period between 1922 to 1945. Information provided in Pervititch maps are superior to the Goad maps which were completed in a short period to meet the first needs. The Pervititch maps consisted of over 230 sheets including key sheets as:

- Beşiktaş (Between 1922-1923, 14 Sheets and a key sheet)
- Ortaköy (Between 1927, 5 Sheets)
- Beyazıt-Nişanca-Küçük Ayasofya (Between 1922-1923, 17 Sheets, and a key sheet)
- Beyoğlu- Taksim (Between 1925-1945, 37 Sheets with 5 key sheets)
- Eminönü (Between 1940-1943, 20 Sheets and 2 key sheets)
- Fatih (Between 1928-1946, 55 Sheets with 3 key sheets)
- Kadıköy (Between 1936-1939, 15 Sheets with 3 key sheets)
- Erenköy (1923, 2 Sheets)
- Şişli (Between 1923-1925, 11 Sheets with a key sheet)
- Üsküdar (Between 1930-1935, 27 Sheets, with 3 key sheets)

Pervititch Maps include name, street number, material type of the construction including its roof, height, number of floors, and some other detailed information. The maps were drawn with different scales as 1:250, 1:375, 1:500, 1:600, 1:750, and 1:1.000 including their key sheets at 1:2.000, 1:2400, 1:4000, and 1:5000. Even though the first plotted regions were written in French with the French spelling of Turkish names, in time new plotted regions were prepared in Turkish. Construction material types of buildings were represented using different colors like rose for masonry and yellow for wooden. By looking at the sheets, it is clearly seen that pink colors are concentrated in the city center, and yellow marked buildings are getting denser in exurban areas. It should be noted that some buildings (such as Laleli Mosque that was built in the 1760s) were colored in purple, which indicates concrete material. However, the first applications of concrete buildings in Istanbul started with the “Tayyare Apartman-

ları"buildings by Architect Kemaleddin in 1919 (Figure 2.5). For that reason, we do not distinguish the purple colored structures from the rose-colored ones.

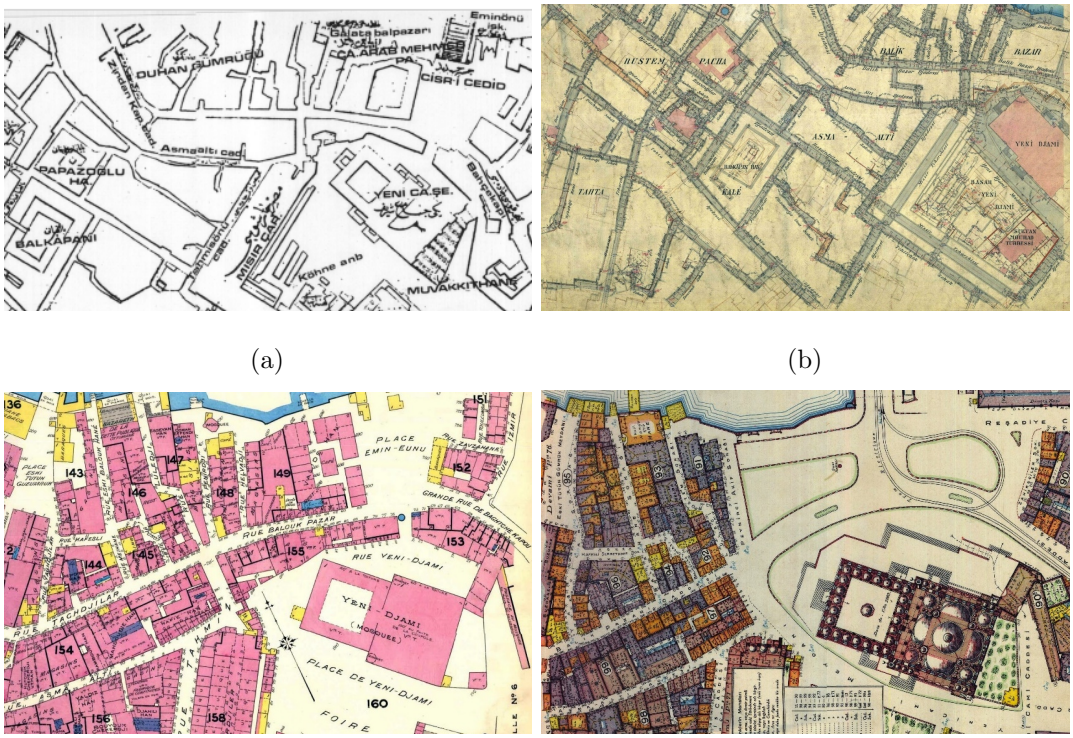

(a) (b)

(c) (d)

Figure 2.4. A section taken from the New Mosque (Yeni Cami) in Eminonu represented in (a) Ayverdi Maps (b) German Blues (c) Goad Maps (d) Pervititch Maps

(a) (b)

Figure 2.5. Laleli Mosque and the Tayyare Apartmanları Blocks those cited as "Laleli Apartemani" on the left side and the meaning of colors used in the Pervititch maps (in Turkish and French) on the right side.

For researchers with varying interests and from diverse disciplines, these maps are

essential to understand changing neighborhoods over time, and determining position and structural properties of the old buildings including demolished or modified ones. In Fatih and Eminonu, positions of the demolished or modified structures were determined by using Ayverdi Maps, which has the earliest completion date. On the other hand, it represents a limited number of districts, which were highly populated. Since the Goad and Pervititch maps were prepared for the purpose of fire insurance, the maps do not comprise all the regions. Because the German Blues involve a broader scope, it became a primary resource to locate the damaged buildings. In order to find positions and material types of the demolished or modified structures in the exclusive districts such as Eyüp, Tuzla, Pendik, Kartal, Maltepe, Bakırköy, Yeşilköy, Büyükçekmece, Küçükçekmece etc., either appropriate assumptions were accepted by looking at the history and general structural tendencies of the districts or they remained unknown.

2.2.6. Internet Sources

Besides maps, some internet sources were utilized while collecting information for the building inventories. One of them was `www.istanbulium.net`, which created by Cangül (2011). This personal web site includes old city maps, notes, pictures, and much other information from the old city. Locating the water gauges, for example, could be possible using this web site. Another web source used was Istanbul Urban Database (IUDB), which is a historical map overlapping application, developed by Tuzcu (2017). UIUDB database is an interactive web mapping digital platform that presents a set of tools for users to overlay historical Istanbul maps. Istanbul Culture and Tourism Directorate (2010) also provides information on modifications of historical buildings in Istanbul urban area as well as the location of demolished buildings.

3. MACROSEISMIC EVALUATION OF THE HISTORICAL EVENTS

3.1. Basic Definitions

3.1.1. Vulnerability Class

After determining locations and construction material type of the damaged buildings, the next step is classifying these structures in terms of their strength. Construction material type and condition of a building affect its vulnerability. The European Macroseismic Scale (EMS) categorized the strength of buildings by considering structure type and other factors to estimate how they respond to seismic forces (Figure 3.1).

3.1.2. Damage Grades

EMS-98 defines damage grades from 1 to 5 evaluating the seismic response of masonry buildings. An important point is distinguishing between structural damage (damage on the load-bearing system of a building) and non-structural damage. From Grade 1 to 5, the damage level of the building increases as follows: Grade 1 corresponds to slight damage on nonstructural elements with no structural damages. Grade 2 means moderate damage on nonstructural elements and/or slight structural damage. Grade 3 is heavy damage on nonstructural and/or moderate damage on structural members. Grade 4 indicates heavy damage on structural members and/or serious damage on nonstructural parts. Grade 5 corresponds to heavy structural damage or collapse. Their illustrations are given in Figure 3.2.

In this work, damage grades were defined by looking for the best-matching damage level definitions.

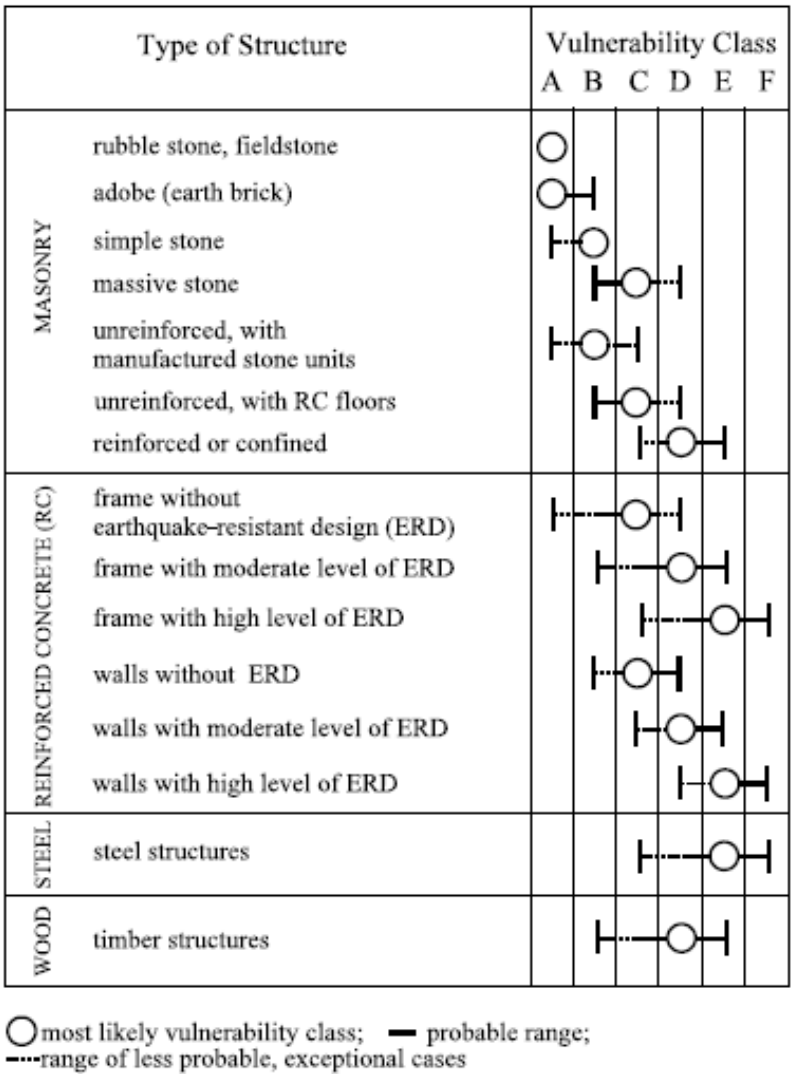

Figure 3.1. Classifications used in the European Macroseismic Scale (EMS).

3.1.3. Intensity

Intensity represents the effects of ground shaking on buildings with different vulnerabilities, reactions of living things, and effects on the natural environment. Intensity can be estimated by observational or instrumental methods. In this study, observational intensity estimation method was utilized to create intensity maps from the compiled damage inventories. The instrumental intensity estimation method was used to estimate intensities from the generic ground motions.

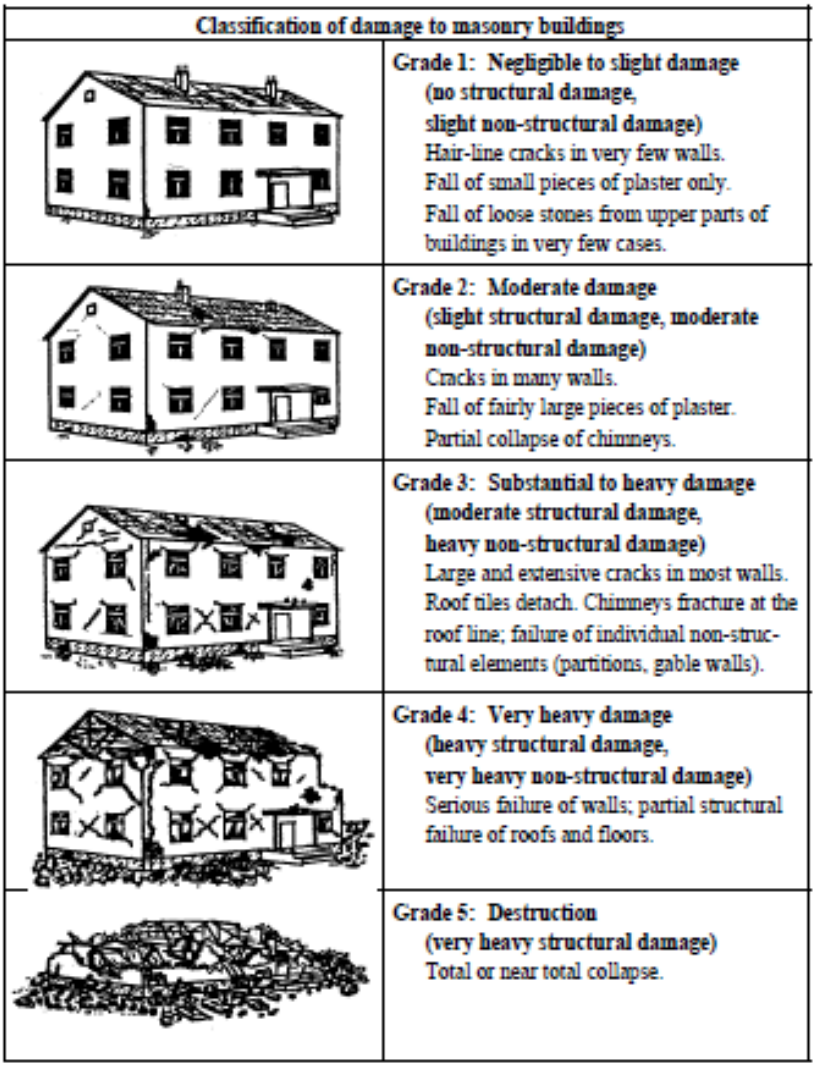

Figure 3.2. Classification of damage to masonry buildings according to EMS-98. Drawings at the left-hand side show what is meant by the different damage grades.

3.1.4. Intensity Assignment Method

In order to assign intensity using the obtained damage, we followed the description given in the EMS-98 intensity scale (Figure 3.3). Regarding the amount of damage levels in each vulnerability class, estimated intensity has been assigned. Felt reports (≈III) were not used in these calculations.

Intensity	Vulnerability	D1	D2	D3	D4	D5
XI	A					
	B					Most
	C				Most	Many
	D				Many	Few
	E			Many	Few	
	F		Many	Few		

Intensity	Vulnerability	D1	D2	D3	D4	D5
X	A					Most
	B					Many
	C				Many	Few
	D			Many	Few	
	E		Many	Few		
	F		Few			

Intensity	Vulnerability	D1	D2	D3	D4	D5
IX	A					Many
	B				Many	Few
	C			Many	Few	
	D		Many	Few		
	E		Few			
	F					

Intensity	Vulnerability	D1	D2	D3	D4	D5
VIII	A				Many	Few
	B			Many	Few	
	C		Many	Few		
	D		Few			
	E					
	F					

Intensity	Vulnerability	D1	D2	D3	D4	D5
VII	A			Many	Few	
	B		Many	Few		
	C		Few			
	D	Few				
	E					
	F					

Intensity	Vulnerability	D1	D2	D3	D4	D5
VI	A	Many	Few			
	B	Many	Few			
	C	Few				
	D					
	E					
	F					

Figure 3.3. EMS-98 Intensity assignment. Few: Sum of damaged structure in the given damage level is up to 20% of total, Many means number of damaged structure corresponds to 10% to 60% of total, and Most is when damaged buildings are between 50% to 100% of total

3.1.5. Instrumental Seismic Intensity Estimation Method

There are varying approaches to estimate seismic intensity by instrumental methods. In this study, using the synthetic acceleration time histories, the empirical intensity estimation method proposed by Sokolov and Chernov (1998); Chernov and Sokolov (1999), and revised version in Sokolov (2002) have been applied. Briefly in this method, seismic intensity (in terms of MMI or MSK) is assigned using the probability functions obtained from the distribution of the Fourier Amplitude Spectra (FAS) of ground accelerations at the considered frequencies.

By evaluating the horizontal components of about 1,150 data throughout the world, Sokolov, (2002) has found observed characteristics of the empirical model as mean $a_{i,j}$ and standard deviation $\sigma_{i,j}$ of base 10 logarithms of the observed acceleration spectrum at the representative frequency f_j within the range of 0.4-13 Hz and the intensity level i between III-IX. For the assigned intensity level I, the probability that the base 10 logarithms of the amplitude of the acceleration spectrum x_j at frequency

f_j will not exceed the given mean value a_{ij} is calculated as:

$$P\left[x_j \leq a_{i,j}\right] = 1 - \frac{1}{\sqrt{2\pi\sigma_{i,j}^2}} \int_{x_{min}}^{x_j} exp\left(\frac{-\left(a_{i,j}-x\right)^2}{2\sigma_{i,j}^2}\right) dx \tag{3.1}$$

where x_{min} =$a_{i,j}$ - $5\sigma_{i,j}$. The weighted probability that takes account of the influences of all the considered frequencies is obtained as:

$$P\left[x \leq a_i\right] = \frac{\left(\sum_{j=1}^{j=n_f} \left[x_j \leqslant a_{i,j}\right] w_{i,j}\right)}{\sum_{j=1}^{j=n_f} w_{i,j}} \tag{3.2}$$

where n_f is the number of considered frequencies, and $w_{i,j}$=$\sigma^2{}_{i,m\,in}/\sigma^2{}_{i,j}$. The probability that the intensity level I of the interested earthquake will not exceed the given value i is estimated as follows:

$$P\left[I \leqslant i\right] = \prod_{i}^{i=12} P\left[x \leqslant a_i\right] \tag{3.3}$$

The instrumental intensity value is estimated by the maximum of the first derivative of the probability function, P. Higher intensities between X-XII was obtained by extrapolation. In this thesis, the intensity level is assigned by using the mean of the maximum of the first derivative of the probability function, and the intensity value at P=0.5 (Böse, 2006).

Figure 3.4 illustrates estimated intensity distribution of the 26 September 2019 Silivri earthquake, Mw 5.8. Fourier Spectra is obtained from grid based simulations (Details are given in Chapter 3). The resulting intensity distribution shows high consistency with the other estimations using ELER, a quick hazard and loss tool (`https://eqe.boun.edu.tr/en/26-september-2019-1359-istanbul-silivri-earthquake`) and instrumental intensity distribution (`https://deprem.afad.gov.tr/downloadDocument?id=1822`).

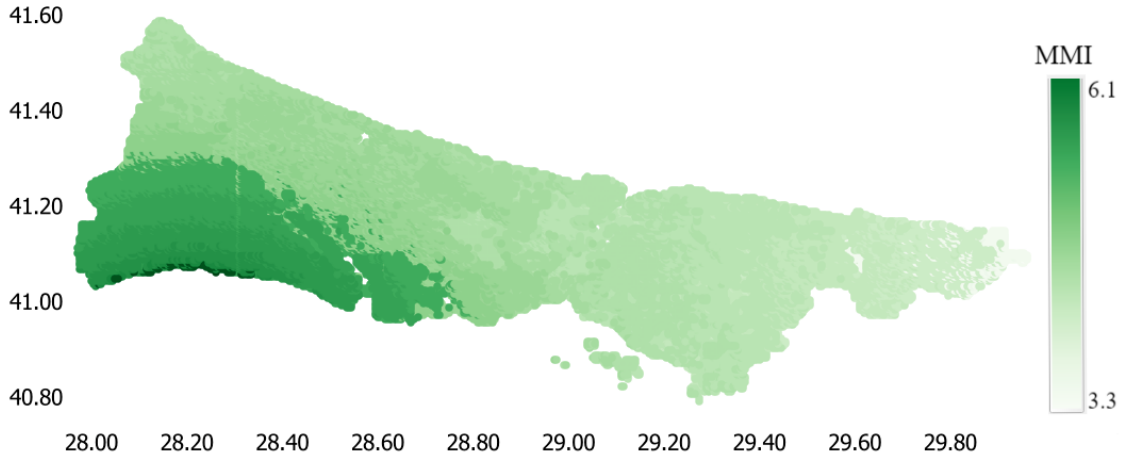

Figure 3.4. Intensity estimation of the 2019 Silivri Earthquake with Sokolov's method on the estimated Fourier Spectra of the grid based simulations.

3.1.6. Conversion of Intensity Scales

In this study, historical damage inventories were converted to seismic intensities by considering the definitions given in EMS98. On the other hand, instrumental intensities obtained from Fourier Amplitude Spectra were presented in MMI and MSK scale by assuming that they are identical (Sokolov, 2002). While converting seismic intensities between MSK and EMS, we followed recommendations given in EMS98 (Grünthal, 1998, Page:55) and for simplification, they all are accepted equal (MMI=MSK=EMS).

3.2. Damage Inventories

Constraining source properties of the historical earthquake requires firstly accumulating damage information from the affected regions with their damage level. To do this, the Ottoman Empire archive records, scientific reports (if available), newspapers, government correspondence, letters, notes of voyagers, and diaries are the major sources to make an evaluation. Ottoman Empire had vast archive records, which are mostly available in the Ottoman Archives of the Prime Minister's Office (Başbakanlık Osmanlı Arşivi). Unfortunately, at that time the Ottoman Empire mostly focused on the old city part named Suriçi, which contains Eminönü, Fatih, and Aksaray districts,

we have limited records about the rest. For example, despite its close distance to Istanbul, there is no information about the total loss of life in Yalova after the 1894 event (Sezer, 1997). There are uncertainties, discrepancies, and sometimes false information in the main sources. For instance, in the 1509 earthquake, the variations in the dates are as much as four weeks in the contemporary sources. Another difficulty in studying historical earthquakes is the censorship and exaggeration in both local and external press. Even though different researchers published a number of books, their contents are almost the same and they are just the repetition of each other.

Damages of dwellings after natural calamities were rarely recorded in the Ottoman Empire archives except if they were damaged due to collapse of a structure that was under the responsibility of the government (Mazlum, 2011). On the compiled damage inventories in this study, we have information about various structures such as the religious buildings (mosques, masjids, monasteries and churches, synagogues), tombs, dervish lodges, hospitals, police stations, other public buildings, inns, commercial centers, factories, Turkish baths (hammams), schools, madrasahs, some mansions and pavilions, palaces, city walls, castles and bastions, bridges, hotels, some cylindrical structures like minarets, bell towers, historical water gages, towers and so on. In the archive records, since the main goal is to identify the governmental allowance, the damage is often defined roughly and damage levels are mostly phrased using stereotyped forms. The most frequently used words are: harmed/damaged (Turkish: hasar gördüğü, rahnedar olduğu), collapsed (Turkish: yıkıldığı, yerle yeksan olduğu/), needs to be repaired (tamirinin gerektiği), ruined/devastated (Turkish: harap olduğu), became uninhabitable (Turkish: içinde oturulamayacak duruma geldiği). Sometimes, the expressions partly and totally (in Turkish: kısmen, tamamen) accompany these words to define the level of damage. These unclear statements impair the accurate definition of the damage level. Besides, these expressions may overestimate or underestimate the level of damage and be erroneous. To reduce the error caused by these formulaic expressions, it is important to collect information from various sources especially from the contemporary ones and differentiating structural and nonstructural damages. Besides, by looking at pictures that were taken after the 1894 event, it is possible to understand what is meant to be expressed. These pictures are accessible as three albums in

Atatürk Library, under Muallim Cevdet Catalog photography collection. In addition, Genç and Mazak (2000) published some of these photographs with additional archival records. In addition, Istanbul University, Rare Works Library shares 19 frames of the 1894 event.

Damage grades were examined by categorizing all the damage expressions given in different sources under the five damage classes, and by comparing them with the pictures of the well-known structures taken after the 10 July 1894 event. Some examples of the evaluated photographs (not all of them) are given in Appendix A in order to clarify the definition of the damage classification.

Based on Figure 3.3, the buildings in the damage inventory were differentiated into three main vulnerability classes as A, B, and D:

- A: Garden and lot-line walls, slummed masonry buildings.
- B: Stone and brick masonry buildings such as tombs, schools, monasteries, churches, mosques, dervish lodges (tekke), inn, hammam, firewalls, fountains, aqueducts. Besides, by looking at their structural resistance, B class buildings were categorized under 4 subclasses in terms of quality of masonry as:
  - B4: City walls, castles, bastions due to their high strength
  - B3: Minarets, bell towers, water gauges, and similar structures due to their slenderness ratio which represents the propensity of buckling.
  - B2: Domed structures that provide high strength, stiffness, and stability, resist out-of-plane bending (For example Hagia Sophia, Blue Mosque, Fatih Mosque.)
  - B1: The rest of the B class, stone, or brick masonry buildings.
- D: Wooden buildings like residential houses, mosques, dervish lodges (tekke), shops, schools, cafes, madrasahs, and similar.

The main sources that were used to compile the damage inventories in this work and to produce damage distribution maps for the 1894, 1766, and 1509 events are given in the following part. As explained before, while public buildings were mostly masonry,

the main structural material of the residential buildings was predominantly wood.

3.2.1. 10 July 1894 Earthquake

This study is based on the detailed inventories compiled by Eginitis (1894, 1895), Oztin (1994), Finkel and Ambsareys (1997), and Ozkılıç (2015) using preliminary sources like official archival records, daily press, and other documentations. A comprehensive inventory has been created by collecting information shared in these sources. The damage inventory includes approximately 2,150 damage entries with their coordinates and structure types. Besides, there are 600 more structures of which the spatial neighborhood information is known, but the exact coordinates remain unknown. We excluded around 75 records the locations of which could not be identified. Figures 3.5 and 3.6 show damage distribution of the 1894 event classified with respect to damage level and structural material type.

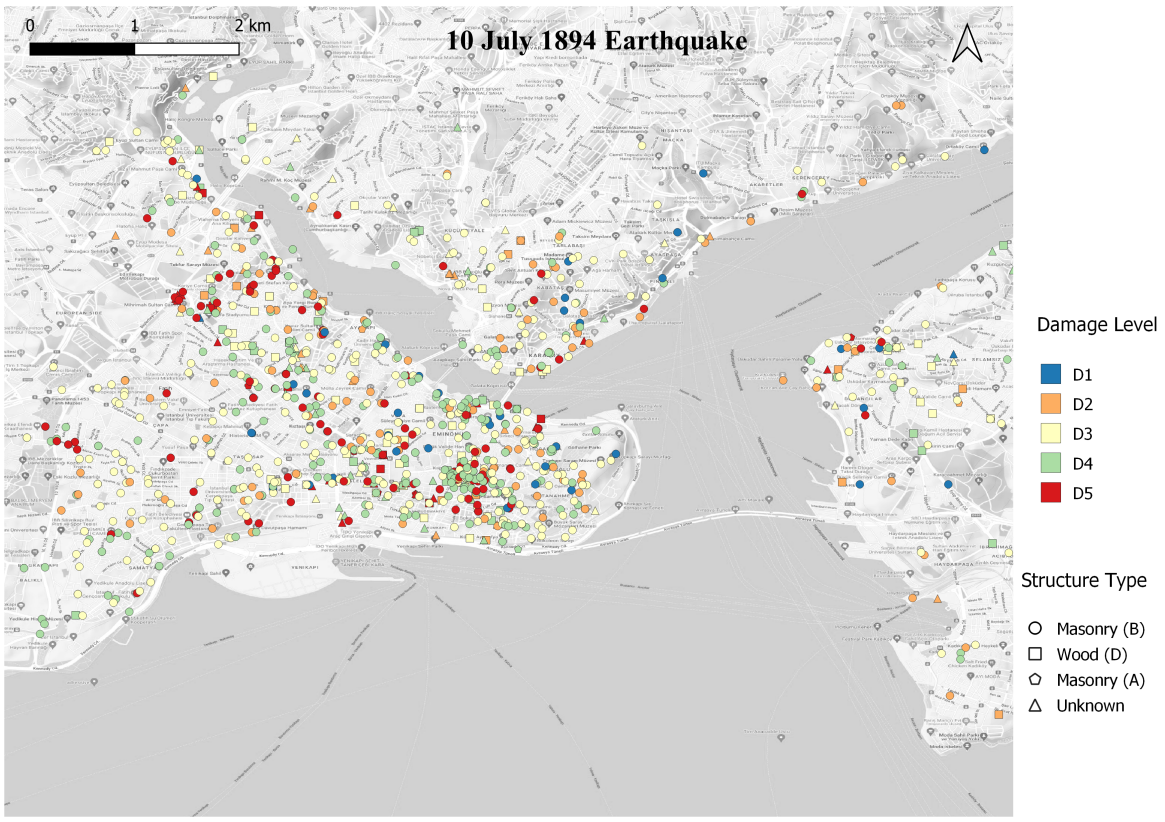

Figure 3.5. Damage distribution map of the 1894 earthquake.

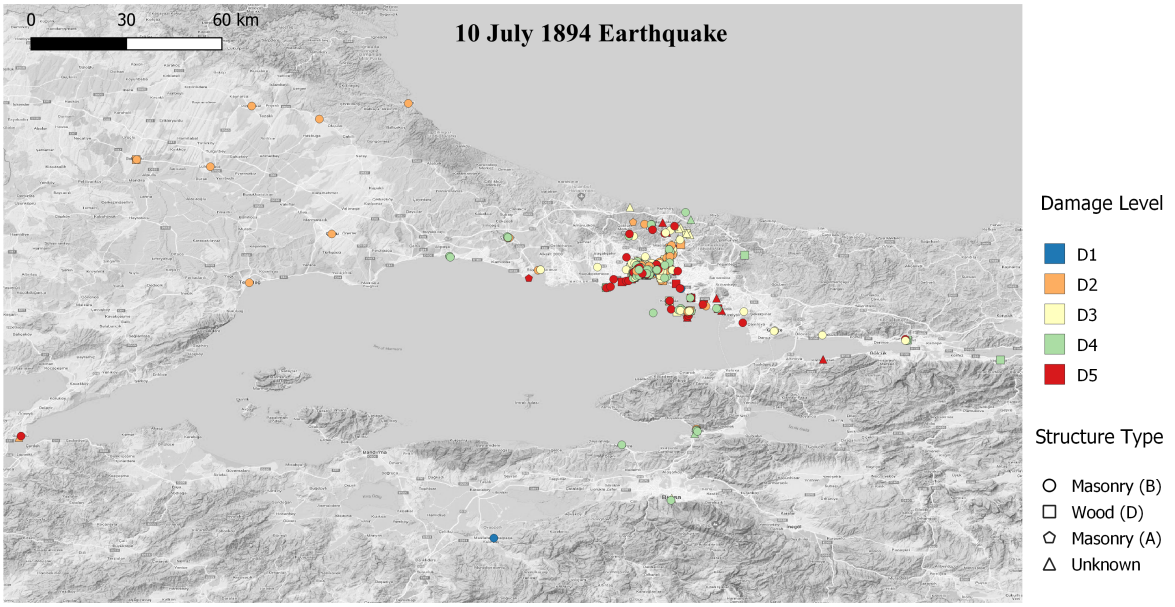

Figure 3.6. Damage distribution map of the 1894 earthquake.

3.2.2. 22 May 1766 Earthquake

The main sources that we used to compile damage inventory of the 22 May 1766 event are Mazlum (2011) who used only primary sources to collect the list of damaged structures, Ambraseys and Finkel (1995), Şemdanizade, Ahmet Vasıf, Hâkim, Çeşmizade, Hammer, Pamukciyan, İnciciyan, Sarkıs Tıbir, Hovannesyan, Evliya Çelebi and the official court records (Kadı Sicilleri). We have compiled 152 damage points with known location and 8 more structures with unknown position which were not included for further discussion. Figures 3.7 and 3.8 show damage distribution of the 1766 event classified with respect to damage level and structural material type.

3.2.3. 10 September 1509 Earthquake

Utilized sources to compile a damage inventory of the 10 September 1509 earthquake were Ambraseys (2011), Ambraseys and Finkel (1995), Sanuto (1879-1903), Kemalpaşazade (Uğur, 1985), Ruhi (Ménage, 1976), Hammer (1835), and Solakzade (2016). We could compile only 55 damage points with their location and one more with unknown location. Figures 3.9 and 3.10 show damage distribution in the 1509 event with respect to damage level and structural material type.

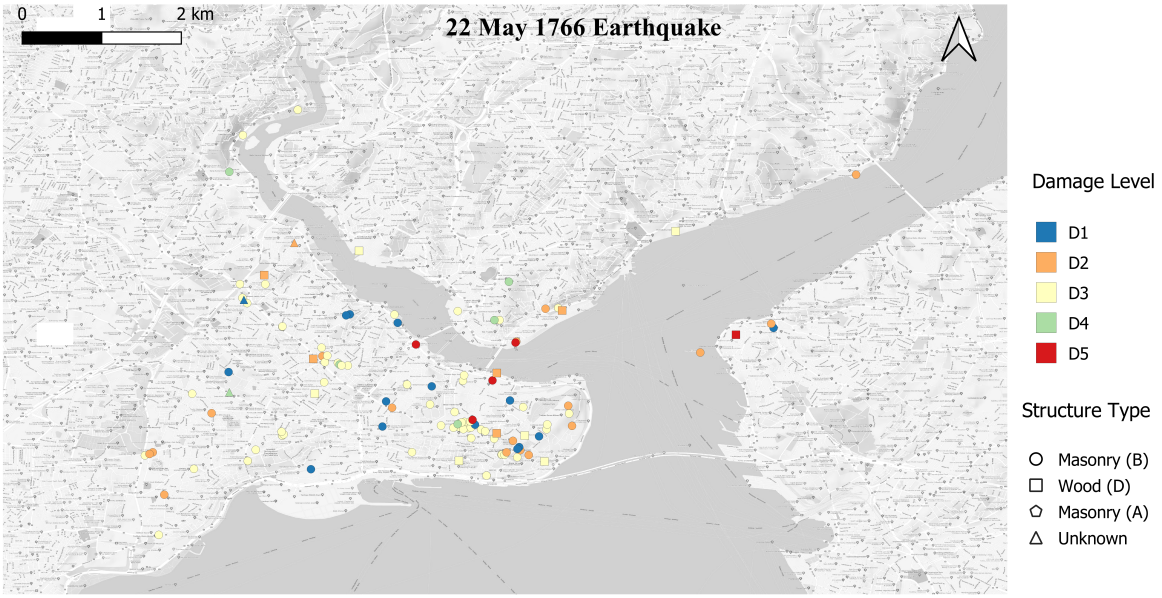

Figure 3.7. Damage distribution map of the 1766 earthquake.

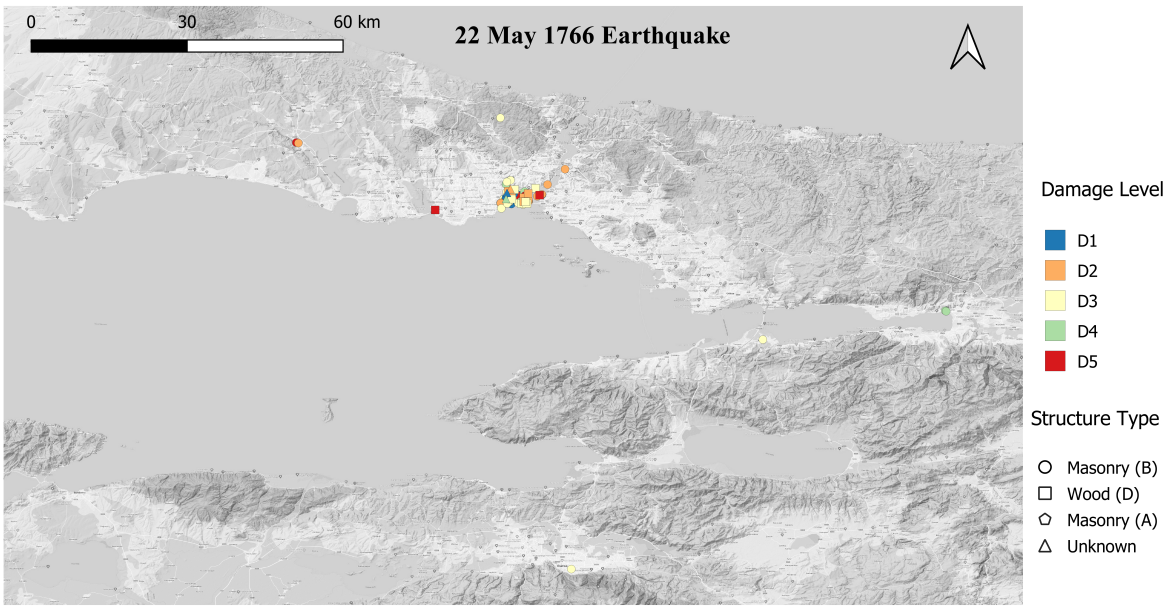

Figure 3.8. Damage distribution map of the 1766 earthquake.

3.3. Intensity Maps

3.3.1. 10 July 1894 Earthquake

The estimated intensity distribution of the 1894 earthquake is presented in Figure 3.11 while Figure 3.12 compares the same with the isoseismal map of Eginitis. The

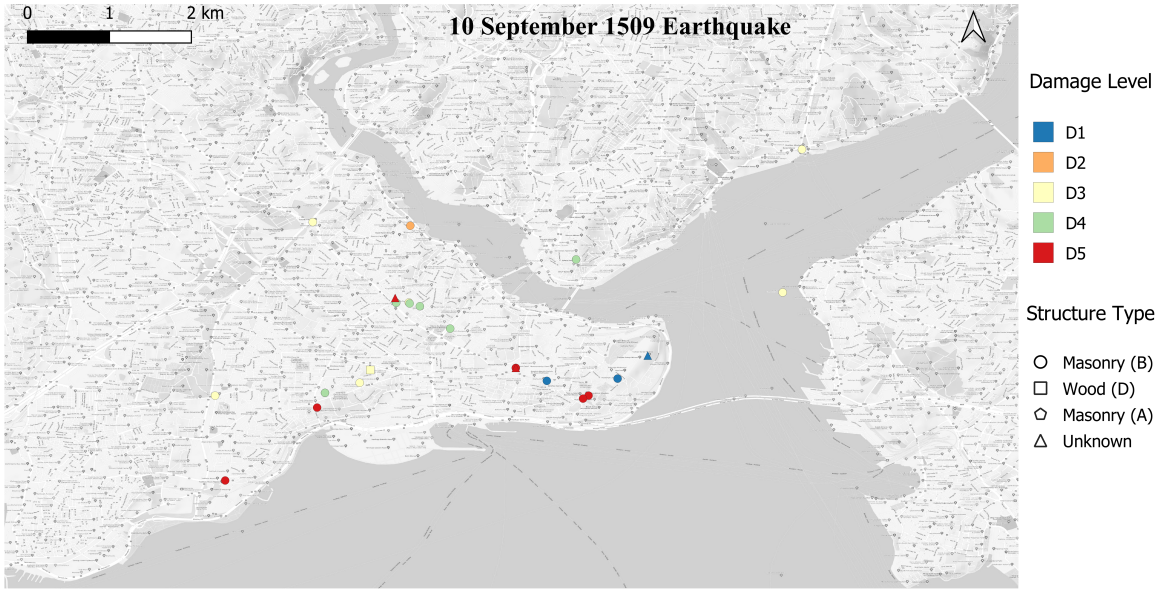

Figure 3.9. Damage distribution map of the 1509 earthquake.

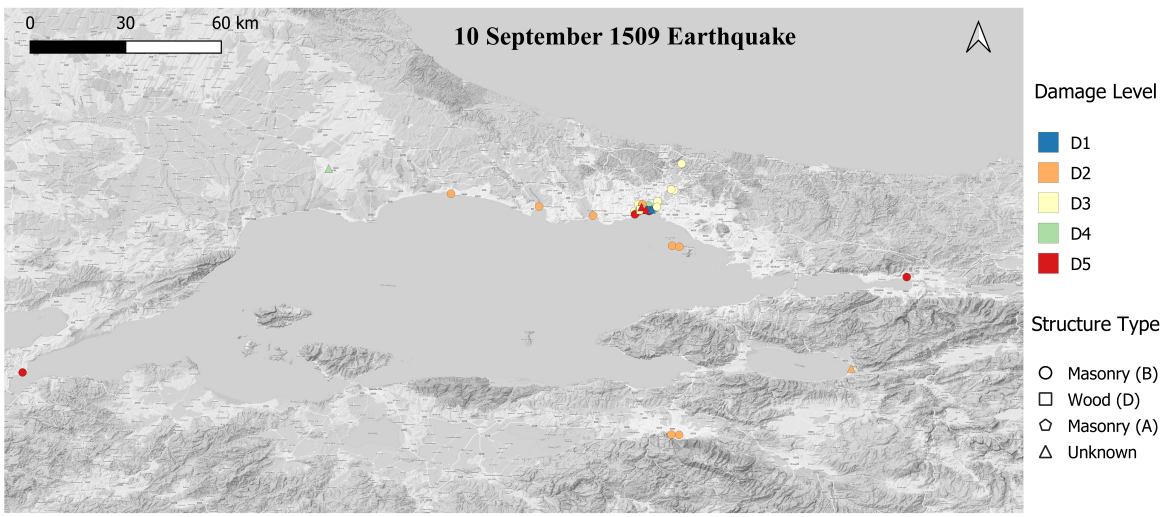

Figure 3.10. Damage distribution map of the 1509 earthquake.

maximum intensity is assigned as IX and our intensity distribution is in accord with the isoseismal contour lines drawn by Eginitis (Figure 3.12).

3.3.2. 22 May 1766 Earthquake

Figure 3.13 shows the intensity distribution of the 1766 event. We appraise the maximum intensity of the 1766 earthquake as IX.

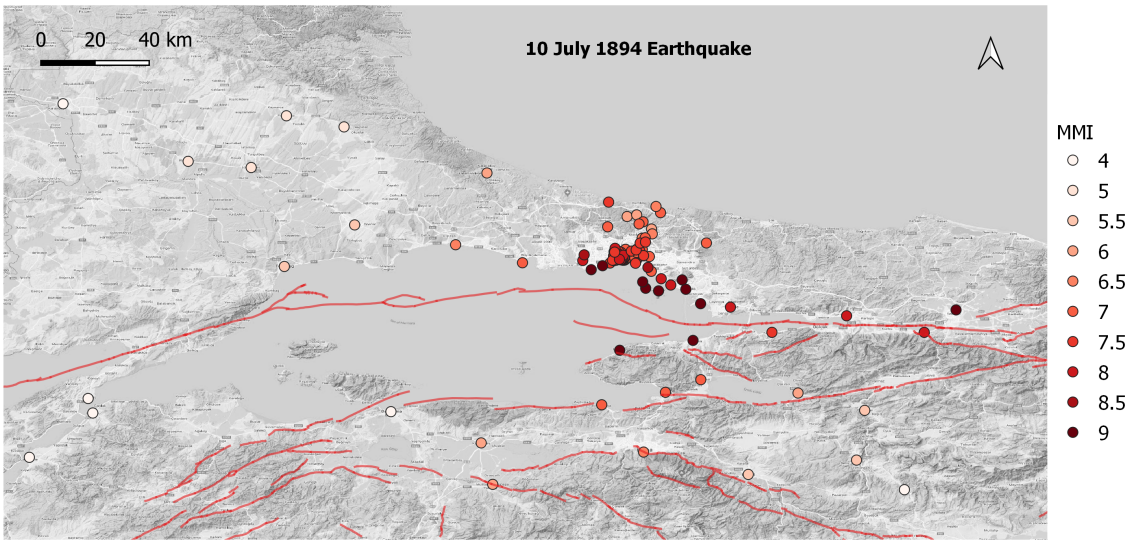

Figure 3.11. Intensity distribution of the 1894 earthquake.

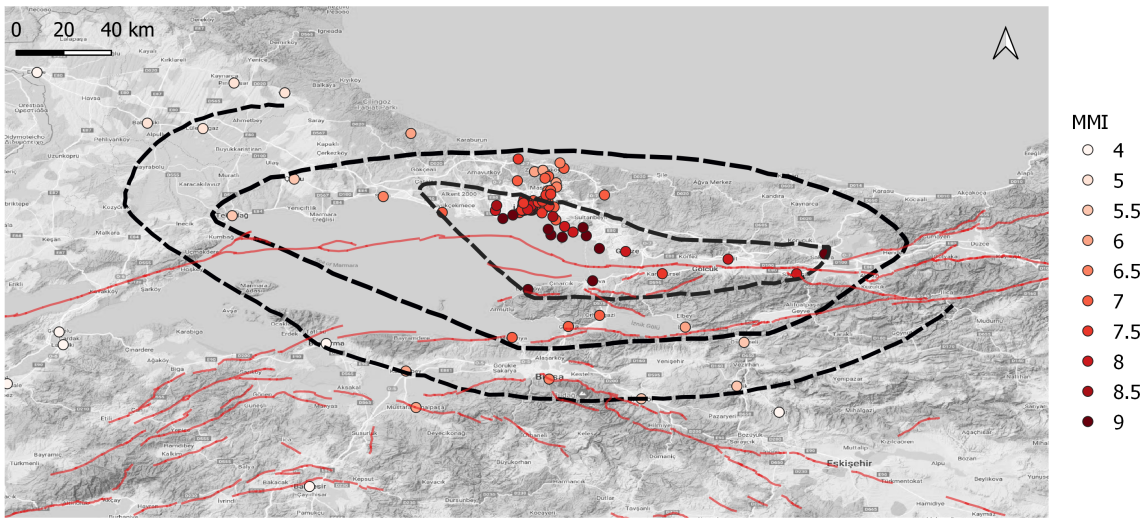

Figure 3.12. Comparison of the obtained intensity distribution of the 1894 earthquake to isoseismals of Eginitis.

3.3.3. 10 September 1509 Earthquake

After the 1509 earthquake, the degree of damage was severe in the heart of the city. Since intensity scale is the best imprecise representation of the destructiveness of the earthquake, we assigned X for the city center (Figure 3.14).

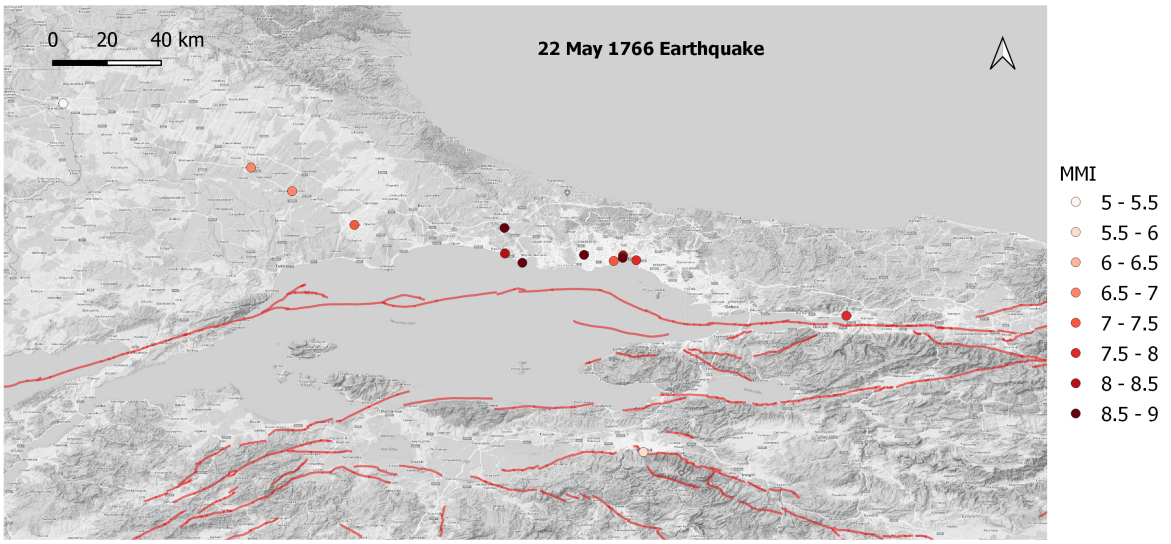

Figure 3.13. Intensity distribution map of the 1766 earthquake.

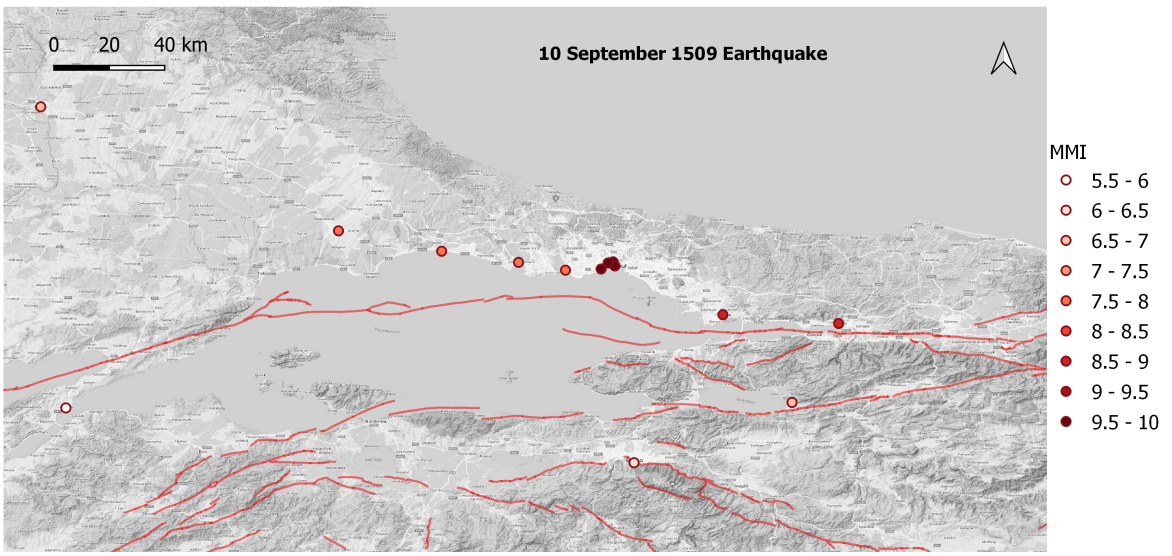

Figure 3.14. Intensity distribution map of the 1509 earthquake.

3.4. Determination of magnitude and epicenter

In order to estimate magnitude and associated faulting of the historical earthquakes, we have used the Boxer method developed by Gasperini et al. (1999, 2010). Although the first version of the method was proposed for Italy only, the latest version can be utilized for any region since it allows to define user calibration. Boxer method was applied to estimate earthquake parameters in Europe such as the 1904 Oslofjord (Norway and Sweden) earthquake, the 1909 Benavente (Portugal) earthquake, the 1983 Stord-Bømlo (Norway) earthquake, the 1356 Basel (Switzerland) earthquake, and the

1858 Setúbal (Portugal) earthquake (Gomez-Capera et al., 2015) as well as in Eastern Iran (Amini et al., 2017). These researchers reported that their calculated magnitudes and earthquake locations by Boxer are consistent with the current catalogues. Detailed information on the Boxer code is given in Section 3.4.1.

3.4.1. The Boxer Method

The method utilizes barycenter of the spatial distribution of intensities to compute magnitude and epicenter of earthquake with their uncertainties. As a location of the earthquake, Boxer creates a rectangular region from the intensity distribution (a box, hence the name of the method) and the epicenter is located in the center. Dimensions of the rectangle are calculated with the Wells and Coppersmith (1994) relation. Boxer uses all the intensity points to estimate magnitude, while epicenter is computed with the highest intensity points which makes the location calculation independent from both magnitude and regional features. The epicenter is calculated using at least three highest intensity coordinates, in case there are less, Boxer considers the second highest macroseismic data points (MDPs). In the Boxer method, a magnitude for each each intensity class is calculated based on the relation given by Sibol et al., (1987) as:

$$M_i = a + b * log^2(A_i) + c * I_0^2 \tag{3.4}$$

where M_i is a magnitude for the ith intensity class, A_i is the ith intensity isoline area that is calculated from the radius of the average distance from the epicenter to the site, I_0 is the epicentral intensity, and a, b, c are the coefficients (Gasperini and Ferrari, 1995). In this equation, the coefficients a, b, and c is determined from the calibration the known instrumental magnitudes and accurate distributions of the MDPs. The Boxer coefficients are produced from the separate least square regression for each intensity level. At the end, the magnitude of the earthquake is computed from the weight of the number of MDPs which are used in each M_i values (Gasperini et al., 1999). Detailed information on the Boxer code methodology can be found on the reference papers.

3.4.2. Examining The Boxer method in Istanbul

Assessing the earthquake moment magnitude (Mw) and location of the Istanbul earthquakes, we have examined barycenter location method (Method 0) by using the last release of Boxer Code (Version 4.1). The regression coefficients a, b and c of the Boxer Code have been taken directly from Şeşetyan et al., (unpublished work), which provides region specific coefficients by using data from 18 earthquakes occurred in Turkey. These coefficients are represented in Table 3.1.

Table 3.1. Calibrated coefficients of Boxer Code for Turkey (N_{EQ} is number of earthquakes used in the corresponding intensity, σ is standard deviation of the model; R^2 is percentage of the coefficient of variation).

Intensity	**a**	**b**	**c**	$\boldsymbol{\sigma}$	$\boldsymbol{R^2}$**%**	$\mathbf{N}_{EQ}$
5	5.70779	0.05645	-	0.3557	29.2857	5
6	4.82687	0.12269	-	0.4591	44.2857	5
7	5.47766	0.09498	-	0.5307	25.0000	5
8	5.56309	0.11833	-	0.1865	36.4000	3

Before starting calculations using the historical earthquakes, we evaluated the Boxer code to estimate the parameters of the 26 September 2019 Silivri M5.8 earthquake. Figure 3.15 shows the estimated barycentre box vertices by Boxer Code. Estimated rectangular area is very close to the fault projection found by Karabulut et al., (2020). Table 3.2 presents the comparision of the estimations with Boxer to the findings by Karabulut et al., (2020). Fault coordinates are not defined in the input file. That's why its estimated extensions are located in the northern region. Clearly for this moderate size earthquake, the Boxer code provides reasonable estimations of the calculations.

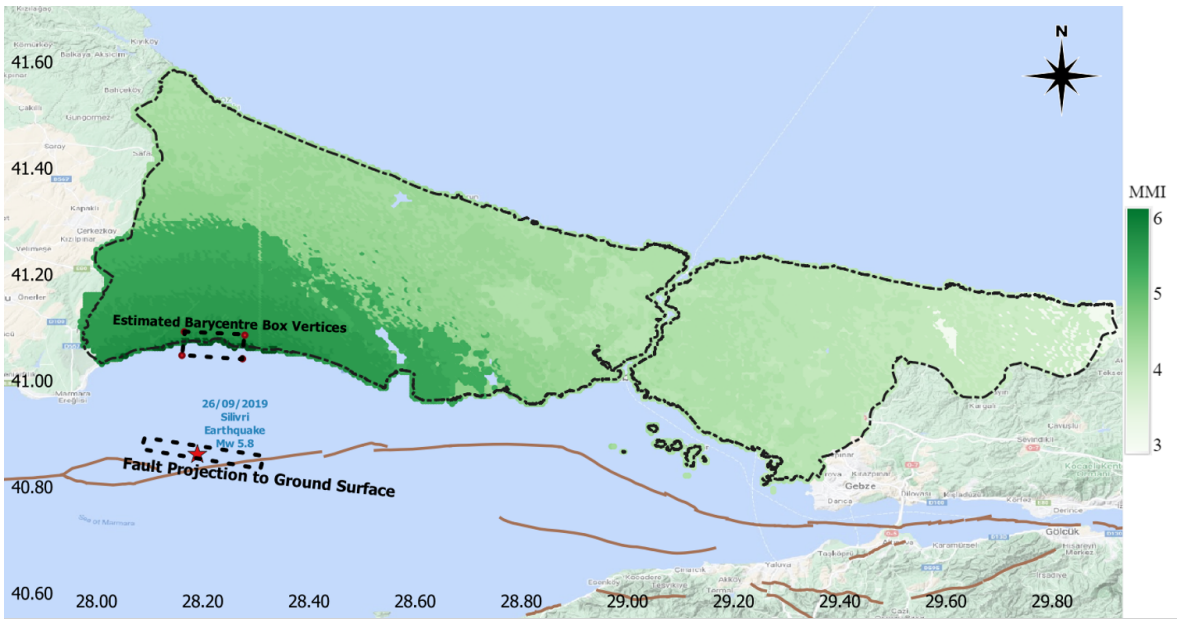

Figure 3.15. Rupture estimation with Boxer for the 26 September 2019 Silivri Earthquake and fault projection calculated by Karabulut et al. (2020) on the simulation based intensity map. Epicenter is represented with the red star.

Table 3.2. Comparison of the source parameters estimated by Boxer to the findings by Karabulut et al., (2020) for the 26 September 2019 Silivri Earthquake.

	Lat	**Long**	**L (km)**	**W (km)**	$\mathbf{M}_w$
Boxer	41.065	28.220	9.6	7.0	5.8
Karabulut et al., (2020)	40.860	28.190	8.0	6.0	5.8

3.4.3. Findings for the Historical Earthquakes with Boxer

Epicenter and magnitude determination for a historical earthquake depends on the available damage information. For the 10 July 1894 earthquake, 11 MDPs are utilized by Boxer with maximum intensity (IX) as Bakırköy, Yeşilköy, Eminönü, Beykoz, Kadıköy, Büyükada, Zeytinburnu, Küçükçekmece, Pendik, Tuzla, Yakacık, Çınarcık, Yalova, and Adapazarı. Boxer estimated moment magnitude as 6.78 ± 0.18 and located the epicenter at 40.8663 (Lat), 29.1344 (Lon) (with uncertainties as 3.13 km x 17.52

km, respectively) and 44.1 km x 16.0 km fault length and width as given in Figure 3.16. Since we have more MDPs in Istanbul comparing to other neighborhood, the rectangular area locates north parallel of the Adalar segment and covers some part of the Izmit Bay extension of the North Anatolian Fault (NAF).

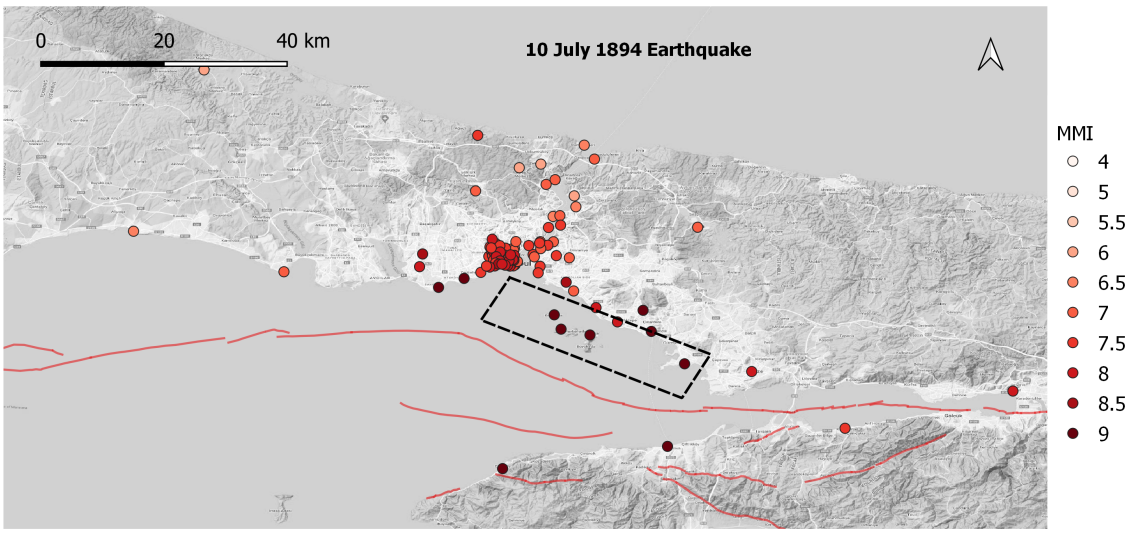

Figure 3.16. The 1894 Earthquake Intensity Map and rupture estimation with Boxer

For the 22 May 1766 earthquake, we used 12 MDPs and the 4 highest intensity data came from Eminönü, Küçükçekmece, Büyükçekmece and Çatalca. Boxer computes Mw 7.39 ± 0.71, and the length and width of the rectangular fault as 82.9 km x 22.6 km. Figure 3.17 shows the epicenter and corresponding rectangular area for the 1766 event. According to the location of the rectangle, associated fault segmentation was estimated on the Central Marmara Fault (CMF).

The 10 September 1509 earthquake has only 9 MDPs for the magnitude calculation and 5 highest intensities (X) came from Eminönü and Galata and the second highest intensity (IX) came from Izmit, Gebze and Çorlu. With this input data, Boxer estimated fault dimensions as 123.7 km x 28.1 km (Figure 3.18) . Since our regional calibration coefficients defined up to intensity IX, Boxer could not compute the moment magnitude for this earthquake. Using the magnitude from I_0, magnitude was estimated as **M** 7.55± 0.54 for the 1509 earthquake.

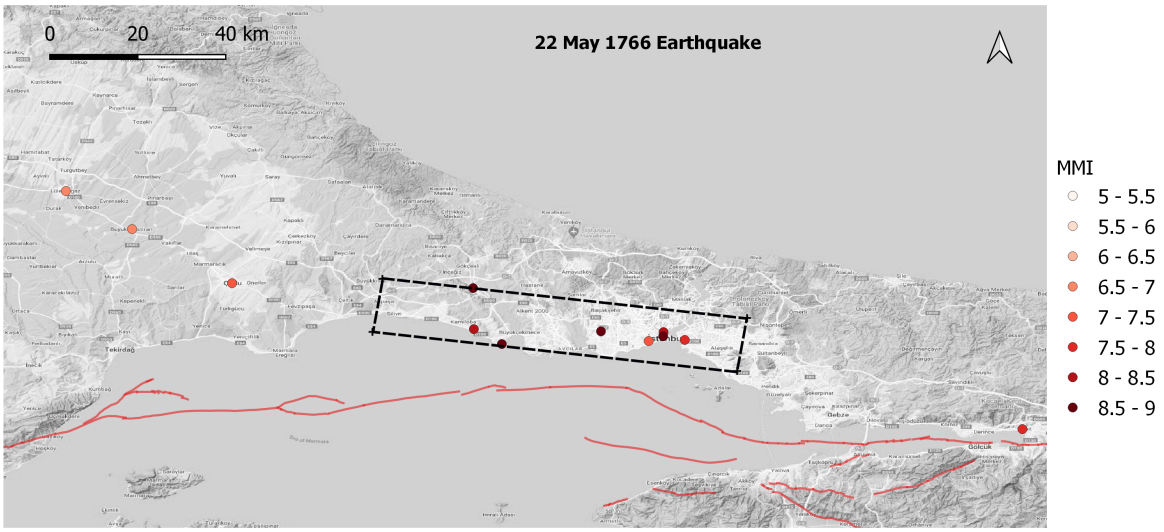

Figure 3.17. The 1766 Earthquake Intensity Map and rupture estimation with Boxer

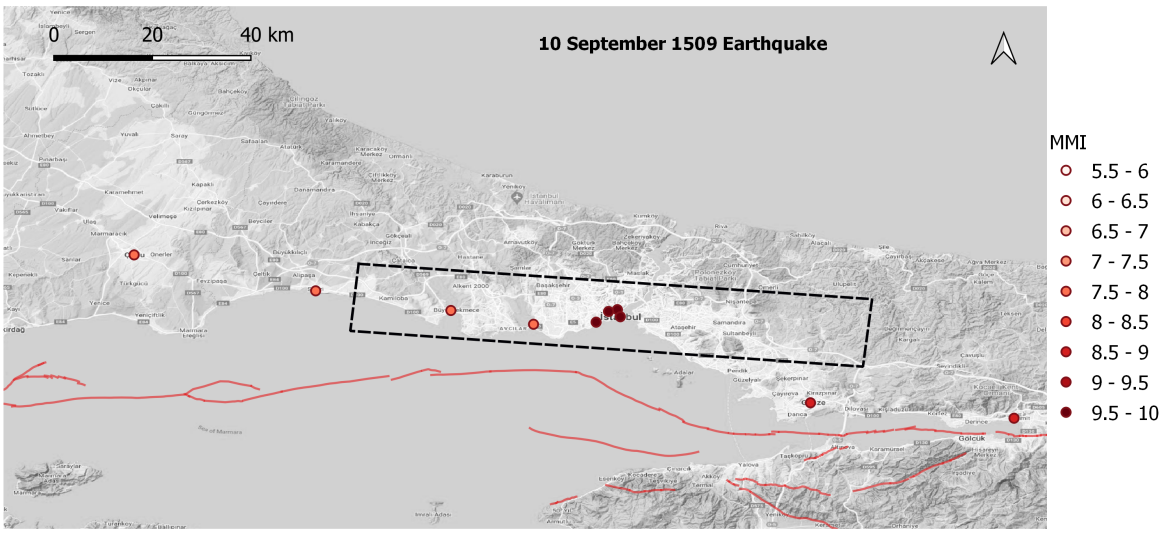

Figure 3.18. The 1509 Earthquake Intensity Map and rupture estimation with Boxer

4. STOCHASTIC APPROACH TO FINITE FAULT GROUND MOTION MODELING AND CREATING OUR MODEL; Mw 5.8 SILIVRI (ISTANBUL) CASE AND Mw 7.4 KOCAELİ CASE

4.1. Stochastic Approach to Finite Fault Ground Motion Modeling

There are two approaches to generate synthetic ground motions; theoretical approach and stochastic approach. In the stochastic approach relatively simplified, evidence based presentations of source, path and site effects are used. Accelerations are sensitive to relatively small size irregularities and heterogeneities associated with faulting and wave propagation path which are unpredictable properties. Therefore, the incoherent behavior of ground motions in high frequencies (>1 Hz) can be represented by using stochastic models.

Stochastic ground motion synthesis with finite fault modeling allows generating specific source effects associated with extended faults and prediction of resulting ground motion. In the stochastic approach of Boore (2003), the incoherent character of high frequency ground motion is modeled by using a band-limited Gaussian noise signal which has uniformly distributed, random phase characteristics. To produce realistic time-series, a window function (coda) is applied to the noise signal in the time domain. The normalization of the noise spectrum is applied to simulate the windowed random phase in the frequency domain. At the end, the random noise spectrum is multiplied by the deterministic target shape of the amplitude spectrum and converted back to the time domain.

In this work, the stochastic finite fault simulation technique with a dynamic corner frequency method developed by Motazedian and Atkinson (2005) has been applied. In this approach, the rectangle representing a fault segment is divided into small, equal area subfaults, which are considered as point sources in simulations. The total energy

produced is constant and independent from the subfault size. Fault rupture begins at the hypocenter of the earthquake and spreads uniformly throughout the fault. For each subsource, the sum of the source duration and the path duration composes the total duration of the motion. The total ground motion at the site is computed as the sum of the subevent motions. In order to generate a comprehensive model to describe the observed seismic motion, the optimum combination of a reliable source model with a suitable path propagation model and a proper site effect model should be used. The accuracy and reliability of simulation models for the prediction of ground motions depend entirely on the ability to quantify source, path, and site effects.

$$Y(M_0, R, f) = E(M_0, f) * P(R, f) * G(f) * I(f) \tag{4.1}$$

$Y(M_0, R, f)$ = Target Fourier Amplitude Spectrum

$E(M_0, f)$ = Earthquake Source

P(R,f) = Propagation Path

G(f) = Site Response

I(f) = Type of motion

where M_0 indicates the seismic moment, R denotes the distance and f is the frequency (Boore, 2003). The required parameters for operating finite fault simulations can be categorized under three main groups as follows.

4.1.1. Source Parameters

Source parameters include magnitude, location of the hypocenter, fault orientation as strike and dip angles, fault dimensions as length and width, and source kinematic parameters as stress drop, rupture velocity, slip model. It is calculated as follows: $\mathrm{E}(\mathrm{M}_0, f) = C.M_0.S(M_0, f)$

where C represents a constant depends on the radiation pattern, shear wave energy, effect of the free surface, density, shear vave velocity and a reference distance), M0 is the seismic moment, and $\mathrm{S}(\mathrm{M}_0$,f) is displacement seismic source spectrum (Boore, 2003). The fault geometry is assumed planar and rectangular and the fault area is divided into identical, small subsources. Each subsource is modeled as a point source with a ω^{-2} spectrum. Ground motions are simulated by summing the contributions coming from the subsources.

4.1.2. Regional Crustal Properties (Path Properties)

Path properties are geometric spreading, inelastic attenuation, shear wave velocity, and density of the medium. The path effects are simply modeled as the multiplication of geometrical spreading with Q functions as Equation 4.2:

$$P(R, f) = Z(R).exp(\frac{-\pi.f.R}{Q_{(f)}.c_Q}) \tag{4.2}$$

where Z(R) represents geometrical spreading, f is frequency, R is the closest distance, Q_f is a frequency-dependent quality factor, c_Qs the S wave velocity that is used in the derivation of seismic attenuation Q model, Q(f). The geometrical spreading Z(R) is simply defined by Boore (2003) as inversely proportional with the closest distance to the rupture surface as given in Equation 4.2:

$$Z(R) = \begin{cases} \frac{R_0}{R}, R \leqslant R_1 \\ Z(R_1)(\frac{R_1}{R})^{p_1}, R_1 \leqslant R \leqslant R_2 \\ . \\ . \\ . \\ Z(R_n)(\frac{R_n}{R})^{p_n}, R_n \leqslant R \end{cases} \tag{4.3}$$

A frequency-dependent, empirical Q model, which represents anelastic scattering and attenuation, is defined in a form as $Q_0 f^{\alpha}$ (Boore, 2003; Aki, 1980).

The radiated energy is assumed as randomly distributed over a duration coming from the source duration, T_0. The path duration model which is a function of the path and the source is defined as:

$$T = \frac{1}{f_c} + bR \tag{4.4}$$

Here, f_c represents the lower corner frequency which is reciprocal of the source duration, and bR is a distance-dependent term that accounts for dispersion where b coefficient controls the increase of duration with distance (Herrmann, 1985; Atkinson and Boore, 1995).

4.1.3. Site Effects

Site effects involve the site and crustal amplifications, and the site-specific high-frequency decay, kappa.

In addition to the source and path effects, ground motion data are significantly affected by local site conditions. For that reason, the site effect has an important role in simulations, and no doubt that it also affects the pattern of isoseismic contours. Site effect, G(f), can be defined by multiplying the amplification and the attenuation as:

$$G(f) = A(f)D(f) \tag{4.5}$$

Here, A(f) represents the amplification function which is usually relative to the source, and D(f) is the path independent attenuation function.

If generated site amplification functions are not available for the recording site, some alternative approaches can be used. To make a rough estimation of the unattenuated generic site amplification, the site amplification factors produced by Boore and Joyner (1997) can be used with respect to the site class of the stations. The main handicap of this method is ignoring the soil nonlinearities.

To add the path independent, high-frequency energy loss, the relationship given by Anderson and Hough (1984) as:

$$D(f) = exp(-\pi\kappa_0 f) \tag{4.6}$$

can be applied, where κ_0 represents zero distance intercept of the high-frequency decay, and f is frequency.

4.2. Stochastic Ground Motion Simulation of the 26 September 2019 Mw 5.8 Silivri (Istanbul) Earthquake

In this section, stochastic simulations are performed for the recordings of the 26 September 2019 Silivri, Istanbul earthquake, using a finite fault simulation approach

with a dynamic corner frequency. The main target of this study is to enlighten possible source uncertainties of the event and to create a valid synthetic model database with consistent source, path, and site parameters in the region. In calibration, we have used the recordings at 59 widely distributed stations located on different site conditions with epicentral distances ranging from 23 to 101 km. Four different frequency-dependent Q models were tested to obtain the best fit with the observations. With the comparison of the generated ground motions to the observed ones, optimum source parameters and crustal characteristics of the region have been estimated. The calibrated model parameters have been obtained from the set of best-fit data with observed ground motion in frequency domain. Synthetic PGAs have been compared with the NGA-West2 Ground Motion Models (GMMs). Furthermore, spatial distributions of the ground motion intensity parameters were obtained and compared with the available damage observations. In conclusion, the results of the simulation were in good agreement with the recorded ones, both in time and frequency domains. The results indicate that the stochastic model proposed herein can be used to simulate ground motion distributions in Istanbul from past and future events in the region.

4.2.1. Background

Although ruptured by several large magnitude earthquakes in the history, the Main Marmara Fault has been relatively quiet in the 20th century. The largest earthquake of recent decades in the region occurred on 26 September 2019 at 13:59 GMT+3, in the Marmara Sea, to the south of Silivri, a western district of Istanbul. The Mw 5.8 earthquake was strongly felt in the Marmara region, and especially in Istanbul, causing damage to public and private buildings and leading to an about two-hour interruption of mobile communication.

In this section, stochastic ground motion simulations are performed on the recordings of the 26 September 2019 Silivri earthquake, using a finite fault simulation approach with a dynamic corner frequency. Our main target is validating the source, path, and site parameters and creating a valid synthetic model database for Istanbul. By comparing synthetic ground motions with the observed ones, optimal regional source

parameters and crustal characteristics are proposed. The calibrated model parameters are inferred from the goodness of fit tests performed in the frequency domain.

The stochastic finite fault simulation approach has been commonly used to generate strong ground motions in the frequency band of engineering concern all over the world. In this study, the last modified version of EXSIM12 (Motazedian and Atkinson, 2005; Assatourians and Atkinson, 2012; Boore, 2009), which is a FORTRAN based stochastic finite fault ground motion simulation algorithm, has been utilized to simulate high-frequency ground motions. EXSIM12 divides the fault plane into smaller subfaults, which act as point sources in the stochastic model. Summation of contributions from individual point sources by properly delaying them in time to account for rupture propagation over the fault plane yields the synthetic ground motion at a specified location. More detailed information can be found in Atkinson and Assatourians, (2015).

A number of studies used stochastic and hybrid (combining deterministic simulations at low frequencies [0.1-1 Hz] with stochastic simulations at high frequencies [1-10Hz]) approaches to create synthetic ground motions for Istanbul (Pulido et al., 2004; Sørensen et al., 2007; Zengin and Cakti, 2012; Akinci et al., 2012). Pulido et al. (2004) used the hybrid simulation technique to generate bedrock level ground motion synthetics for a Mw 7.5 scenario earthquake. Sørensen et al. (2007) investigated the effect of uncertainties due to source and attenuation parameters using the same methodology with Pulido et al., (2004). Zengin and Cakti (2012) applied the stochastic approach to calibrate source and path related parameters using the 25 July 2011, MI5.1 Marmara Sea Earthquake and provided synthetic ground motion distributions for Mw=7.5 scenario events. Akinci et al., (2012) simulated broadband time histories taking a hybrid approach for the most probable Istanbul earthquake scenarios with magnitudes larger than 7. Except for the work of Zengin and Cakti (2012), these studies used source and path parameters from the literature and did not attempt to validate their models against recorded data. In the present work, making use of strong ground motion stations distributed in Istanbul and their recordings from the 26 September 2019 earthquake, we examine the performance of available models and parameter val-

ues. The model calibrated and validated against real data will help to simulate ground motion accelerations for past and future events in Istanbul.

4.2.2. The Earthquake

The 26 September 2019 earthquake took place offshore Silivri, Istanbul (Figure 4.1). Main source parameters are reported by various sources as KOERI, AFAD, Harvard CMT, EMSC, USGS, and Karabulut et al., (2020) in Table 4.1. Estimations for Mw varied between 5.6 and 5.8. Reported focal depths changed between 7-13 km. The earthquake took place close to the Central Marmara segment of the North Anatolian Fault, on which no significant seismic activity has been observed for a long time. This earthquake was the first M5+ event associated with this segment since the 24 April 1988, M_b=5.0 earthquake and it was the largest event in the Marmara Sea since the Mw 6.3 Çınarcık earthquake of 1963.

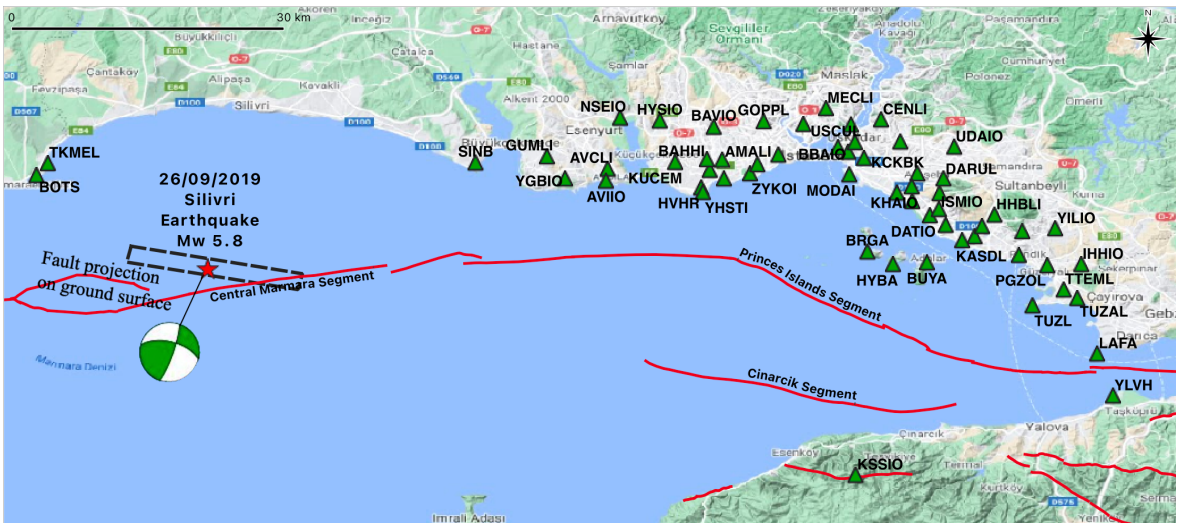

Figure 4.1. 26.9.2019 Silivri earthquake. The red star corresponds to the epicenter of the mainshock. Stations of the Istanbul Earthquake Rapid Response and Early Warning System that recorded the earthquake are indicated with green triangles. Red lines represent the fault segmentation in the Marmara Sea. Fault projection on ground surface and beach ball representation are also included. The fault map is compiled from Active Fault Maps of Turkey, MTA (Mineral Research and Exploration General Directorate (Emre et al., 2013).

Table 4.1. Source Parameters of the 26 September 2019 Silivri Event

Parameters:	**KOERI**	**AFAD**	**HARVARD CMT**	**EMSC**	**USGS**	**Karabulut et al., (2020)**
Magnitude	ML 5.7, Mw 5.6	Mw 5.8	Mw 5.7, Ms 5.7	M 5.7	Mw 5.71	Mw 5.8
Lat., Lon.	40.8832, 28.2110	40.8718, 28.1928	40.8400, 28.2500	40.8700, 28.1900	40.9040, 28.1500	40.8600, 28.1900
Focal Depth (km)	13	6.99	12	7	11.5	Between 9-13
Strike/ Dip/Rake	276/55/145	263/35/129	273/49/144	-	86/64/123	281/60/165

There were slight differences in reported epicentral coordinates of the earthquake (Table 4.1). The focal mechanism was given as dominantly thrust faulting by seismological agencies. More recently, based on a re-analysis of main and aftershock data, Karabulut et al., (2020) have suggested that the event did not take place directly on the Central Marmara segment but was associated with a 60° north dipping fault slightly to the north of the main segment. The causative strand was an oblique strike-slip fault and had a strike-slip displacement with some thrust component (rake angle of 165°). According to the proposed slip model maximum slip was 1 m and occurred close to the hypocenter. The slip was concentrated in a single patch that extended between depths of 9 km to 13 km. The size of the model is 8 km x 6km, along the strike and dip directions, respectively. The source parameters as per Karabulut et al., (2020) can be seen in Table 4.1. The proposed slip model is shown in Figure 4.2.

4.2.3. Recorded Ground Motion Data

The earthquake was recorded by 59 stations of the Istanbul Earthquake Rapid Response and Early Warning System. Recording stations are at 23 km$\leq R_{epi} \leq$101 km from the earthquake (Repi is epicentral distance). The sampling rate is 0.01 s. The acceleration data have been uniformly filtered using a 0.5-25 Hz bandpass filter after removing the mean. The largest accelerations were registered at stations SINB, TKMEL and HVHR, where peak ground accelerations (PGA) were 145.52 / 82.98 / 82.85 cm/s2 in East-West (EW), and 73.90 / 63.45 / 67.38 cm/s2 in North-South (NS) directions, respectively. Table 4.2 summarizes the station information and the peak

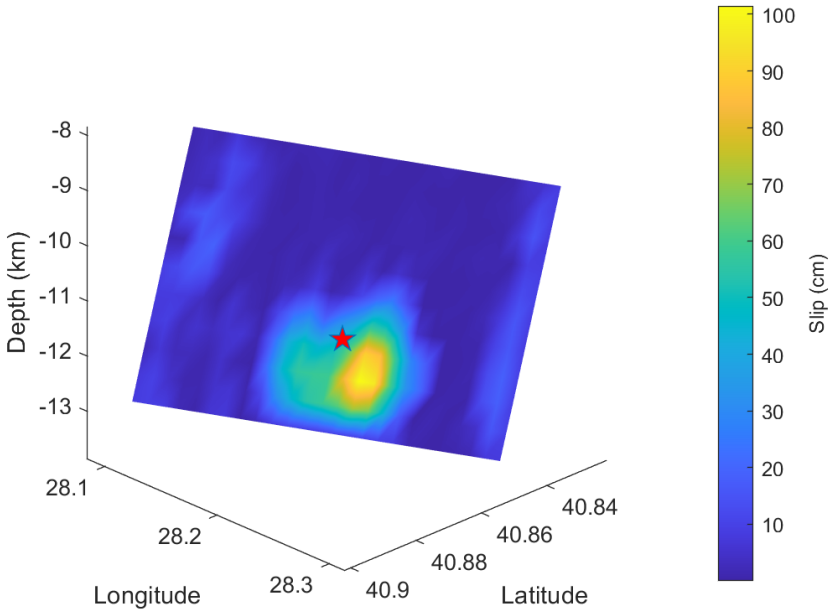

Figure 4.2. Slip Distribution proposed by Karabulut et al., (2020). The red star represents the hypocenter of the 26 September 2019 Silivri earthquake.

ground motion values. Figure 4.3 indicates station specific distribution of PGAs.

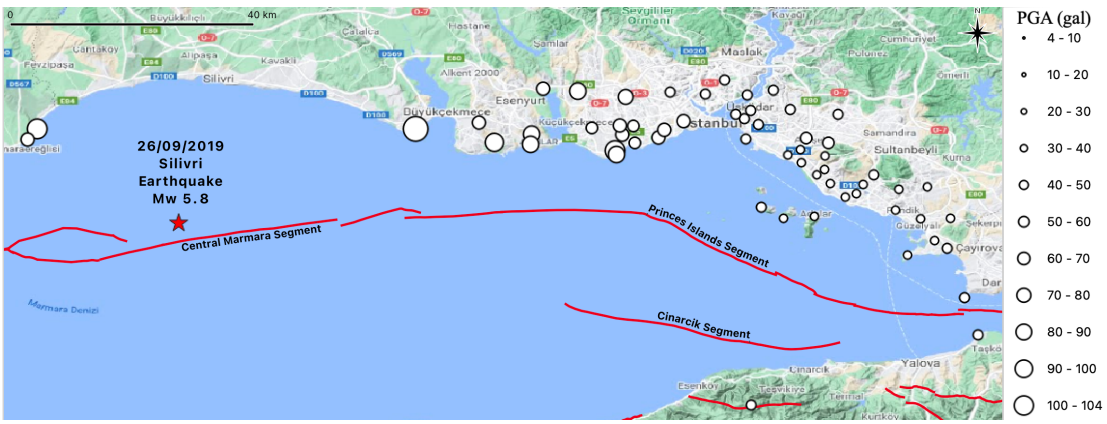

Figure 4.3. Station specific PGA distribution. PGAs (white circles) estimated from the geometric mean of two horizontal components are shown. The red star represents the epicenter.

Site classes of the stations are estimated from the Vs30 Soil Classification Map of Istanbul (IBB-OYO-KOERI, 2009) and included in Table 2. Vs30 information for stations BOTS, KISSIO, LAFA, TKMEL, and YLVH is not available as they are located

outside the municipal boundaries of Istanbul. Site classes of these five stations are estimated from regional geology maps (QTM - Quaternary, Tertiary, Mesozoic) provided by MTA (Mineral Research and Exploration General Directorate), (MTA, 2004).

Table 4.2: Station information (Repi is epicentral distance; B, C, and D are NEHRP soil classes, GS is generic soil, and GR is generic rock).

Station name	**Station code**	**Lat**	**Long**	**Repi (km)**	**Site Class**	**PGA (EW) (cm/s^2)**	**PGA (NS) (cm/s^2)**
Ataköy	AKUKO	40.990	28.845	56.86	GS	24.48	41.65
Bahçelievler	AMALI	41.003	28.861	58.60	GS	27.31	24.29
Ataköy	ATAIO	40.978	28.863	58.10	GS	19.77	33.98
Avcılar	AVCLI	40.991	28.711	46.16	D	54.34	64.20
Avcılar	AVIIO	40.976	28.709	45.52	D	38.44	77.55
Bahçelievler	BAHHI	41.004	28.841	57.00	GS	30.54	35.12
Bağcılar	BAVIO	41.046	28.850	59.16	C	38.31	62.79
Baglarbası	BBAIO	41.014	29.025	72.19	B	24.04	8.16
Botaş	BOTS	40.983	27.967	23.23	C	33.10	48.28
Burgazada	BRGA	40.883	29.050	72.38	GR	11.20	10.96
Buyukada	BUYA	40.870	29.128	78.88	C	8.32	7.60
Çengelköy	CENLI	41.056	29.068	76.91	B	11.63	11.96
Kayışdağı	DARUL	40.978	29.149	81.68	C	24.04	27.41
Maltepe	DATIO	40.931	29.132	79.57	B	7.37	12.66
Kartal	EHAIO	40.903	29.190	84.22	B	3.70	5.80
Fatih	FBZMD	41.010	28.935	64.72	GS	33.33	28.10
G.O.P.	GOPPL	41.053	28.915	64.55	C	14.92	13.54
Gürpınar	GUMLI	41.008	28.633	40.64	GS	55.14	27.55
H. Hatice Byrktr Lis.	HHBLI	40.931	29.216	86.63	C	13.21	14.86
Hava Harp Okulu	HVHR	40.967	28.834	55.36	GS	82.85	67.38

Heybeliada	HYBA	40.867	29.083	75.13	C	4.65	8.14
Halkalı	HYSIO	41.054	28.779	54.00	GR	68.39	49.68
Tuzla	IHHIO	40.867	29.329	95.79	C	5.87	5.19
Maltepe	ISMIO	40.939	29.143	80.60	B	7.08	5.13
Kılıç Ali Paşa İ.Ö. O	KAPIO	41.049	29.029	73.50	C	14.69	15.00
Kartal Soğanlık	KARSO	40.917	29.200	85.15	B	7.28	7.81
Kartal	KASDL	40.898	29.174	82.84	B	7.28	4.61
Küçükbakkalköy	KCKBK	40.985	29.116	79.02	C	21.69	26.36
Kadıköy	KHAIO	40.968	29.108	78.10	B	7.82	7.43
29 Ekim İlkokulu	KSSIO	40.592	29.035	77.19	C	11.25	17.35
Küçükçekmece	KUCEM	41.000	28.800	53.56	GS	24.02	25.83
Lafarge	LAFA	40.750	29.350	98.40	C	12.81	10.97
Maltepe	MBNIO	40.918	29.152	81.16	C	8.72	9.36
Mecidiyeköy	MECLI	41.071	28.996	71.62	B	16.97	15.25
Küçükyalı Merkez	MMZIO	40.949	29.109	77.83	B	7.56	10.01
Kadıköy Moda	MODAI	40.984	29.027	71.65	B	13.40	21.77
Maltepe	MYMIO	40.959	29.144	80.94	B	6.21	9.47
Avcılar	NSEIO	41.058	28.728	50.26	GR	42.26	22.20
Beyoğlu Okmeydanı	OKCIO	41.050	28.967	68.55	B	16.40	16.05
Pendik	PGZOL	40.866	29.285	92.10	B	4.85	6.23
Pendik	PTMLI	40.879	29.248	88.95	B	4.57	4.71
Pendik	PVBIO	40.910	29.253	89.49	B	7.50	7.93
Sinanoba	SINB	40.999	28.540	33.20	GS	145.52	73.90
Kadiköy-Suadiye	SMKIO	40.960	29.089	76.36	B	6.43	7.23

Trakya Marmara Ereğlisi	TKMEL	40.999	27.981	23.39	C	82.98	63.45
Tuzla	TTEML	40.834	29.306	93.92	B	3.82	4.33
Tuzla	TUZAL	40.823	29.324	95.51	C	10.71	16.66
Tuzla	TUZL	40.813	29.266	90.66	GR	9.80	6.75
Ümraniye	UACPI	41.027	29.093	78.10	B	12.98	12.43
Ümraniye	UDAIO	41.020	29.163	83.67	C	12.39	18.73
Kadıkoy	UMSBI	41.005	29.046	73.71	B	11.29	17.30
Üsküdar	USCUL	41.026	29.034	73.24	GR	25.77	14.62
Üsküdar	USKPL	41.020	29.012	71.27	B	28.47	9.81
Yakuplu	YGBIO	40.979	28.656	41.31	GS	75.77	56.91
Yeşilköy	YHSTI	40.961	28.836	55.44	GS	44.08	57.60
Kurtköy	YILIO	40.913	29.295	93.12	B	4.66	5.18
Yalova	YLVH	40.695	29.370	101.07	GS	21.50	16.22
Zeytinburnu	ZYKOI	40.986	28.898	61.07	D	30.20	34.76
Zeytinburnu	ZYTAL	40.997	28.907	62.10	GS	30.61	33.24

4.2.4. Model Parameters and Sensitivity of Results to Parameter Values

The essence of validation of model parameters is about selecting the parameter values properly and comparing the synthetics against recorded ground motion data. Selection of the parameter values can be either based on previously published information, on information that is inferred from the analysis of recorded data available at the time of simulation, or both. Table 4.3 summarizes the input parameters required by EXSIM12. It also includes preferred parameter values that we used in the simulations of the September 26, 2019 Silivri earthquake. In this section, we will discuss how and why the values in Table 4.3 are selected.

The goodness of fit between observed and simulated ground motions, also called model bias is calculated with the help of an error function E(f) defined as in Equation

4.7:

$$E(f) = \frac{1}{n}\sum_{i=1}^{n} log\left(\frac{A_i(f)_{observed}}{A_i(f)_{simulated}}\right) \tag{4.7}$$

where n is the number of modeled stations, and A_i is the Fourier Amplitude Spectra of acceleration time histories in the ith the station for both recorded (observed) and generated (simulated) ground motions. It can be a measure of the performance of a single station or the general model performance when averaged over all stations used. In this section model bias will be occasionally utilized to discuss the effect of selection of different parameter values on simulated ground motion. In the next section, we will use it to evaluate the simulation results.

Starting from the source, we defined the slip distribution as per the model proposed by Karabulut et al., (2020) (Figure 4.2). The rectangular fault plane, which is 8 km long and 5.5 km wide, is divided into 10 subfaults along the strike and 11 subfaults along the dip directions. The dimensions of individual subfaults are 0.8 km x 0.5 km. The slip distribution shown in Figure 4.2 has been converted to slip weights and used as such in EXSIM12. We have used amplification factors of Boore and Joyner, (1997) corresponding to NEHRP site classes D and C for stations with Vs30 values of 156 - 296 m/s and 405 - 574 m/s respectively. For a narrow band of Vs30 for 297 - 404 m/s, we assigned amplification factors corresponding to Generic Soil, and for 575 -724 m/s those corresponding to Generic Rock.

In our case, sites with Vs30 value for 725 m/s and up correspond to B site class. Few if any studies on ground motion simulation of rock sites available in the literature used generic site amplifications provided by Boore and Joyner (1997) for very hard rock sites (Vs30=2900m/s) or NEHRP B/C boundary site class (Vs30=760m/s) provided by Atkinson and Boore (2006). On the other hand, according to the Vs30 profile,

Istanbul has a firm to hard rock site (up to Vs30=1400 m/s). In simulations, site amplification provided by the former resulted in underestimated simulation data for rock sites while the latter caused overestimation. Figure 4.4 represents the effect of generic site amplification on time domain and frequency domain at randomly selected B site station, KARSO. Clearly, the first two models are not enough to represent B site conditions in Istanbul region. This effect was especially more dramatic on intensity parameters. Figure 4.5 illustrates the impact of the selected site amplification model on PGA distribution at B site stations while all the other parameters remained the same. For that reason, we used generic site amplifications adopted by Pischiutta et al. (2021) for the Italian soft rock class (Vs30=1163m/s).

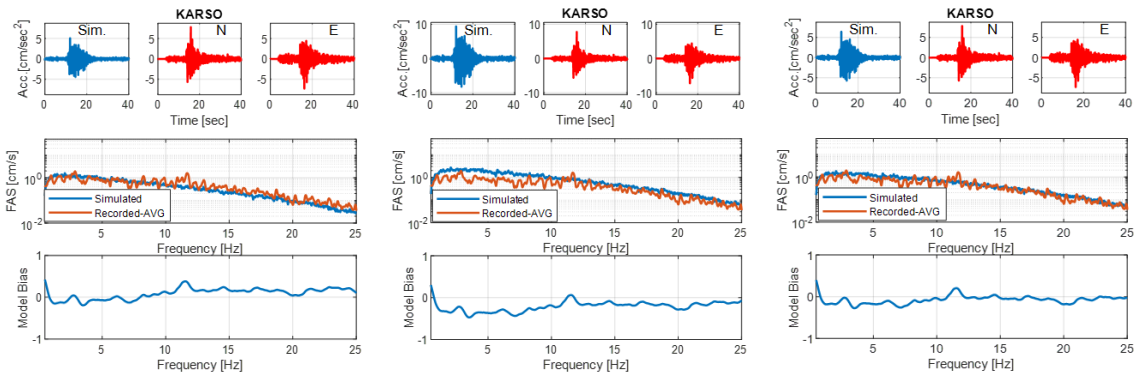

(a) (b) (c)

Figure 4.4. Effect of generic site amplification models on B site at representative station KARSO by using (a) Boore and Joyner, (1997) (Vs30=2900 m/s) (b) Atkinson and Boore, (2006) (Vs30=760 m/s) (c) Pischiutta et al., (2021) (Vs30=1163m/s).

The total duration of the simulated ground motions expresses using a sum of source duration and path duration. In this paper, firstly we evaluated a simple and widely used generic duration model defined by Herrmann (1985) as $T = T_0 + 0.05R$ where T_0 is source duration and R is the closest source to site distance. When this model was used, while the simulations might seem to match the recorded motions in terms of their FAS, the comparison of the waveforms does not support this match. The waveforms of simulated ground motions (Figure 6a and Figure 6b) seem quite different than recordings in terms of their amplitudes and durations. To handle this problem, stochastic simulation duration was expressed with the model developed by

Table 4.3. Input Model Parameters and Parameter Values Used in the Simulation of the 26 September 2019 Silivri Earthquake by EXSIM12

Parameters		**Parameter Value**
Event		The 26 September 2019, Silivri
Source Parameters	Lat. and Lon. of upper edge of fault	Latitude: 40.83N, Longitude: 28.31E
	Moment magnitude	5.8
	Fault orientation (Strike/Dip)	281°/60°
	Fault depth to upper edge (km)	9.0
	Fault length and width (km)	8x5.5
	Sub-fault dimensions (km)	0.8x0.5
	Stress drop (bar)	50
	Rupture velocity (km/s)	0.8 x (shear wave velocity)
	Slip Distribution	Karabulut et al., (2020)
	Pulsing percentage Windowing-function	50 Saragoni-Hart
Path Properties	Crustal density (g/cm3)	2.8
	Attenuation, Q(f)	$Q(f)=50f^{1.09}$, Horasan et al., (1998)
	Crustal shear wave velocity (km/s)	3.8
	Geometric spreading	1/R (R $\leq$ 30 km) $1/R^{0.4}$ (30 km <R<60 km) $1/R^{0.6}$(60 km $\leq$R<90 km) $1/R^{0.8}$ (90 km $\leq$R<100 km) $1/R^{0.5}$ (R$\geq$100 km) Ansal et al., (2009)
	Empirical Amplification	-
	Duration Model	Boore and Thompson, (2014)
Site Effects	Site amplification	GS, GR, NEHRP D and C: Boore and Joyner, (1997) NEHRP B site class: Pischiutta et al., (2021)
	Crustal amplification	-
	Kappa Factor	Site specific kappa; Süleyman, (2018) Constant kappa; Durukal and Çatalyürekli, (2014)

Boore and Thompson (2014) which gives significantly longer durations and provides a better match with the recordings (Figure 4.6c and Figure 4.6d).

Figure 4.7 displays a comparison of simulated and observed ground motions in terms of Arias intensity and effective duration versus epicentral distance and Vs30 values. Observations are estimated as the geometric mean of two horizontal components. Simulated values are represented by a mean of 30 iterations. Effective duration corre-

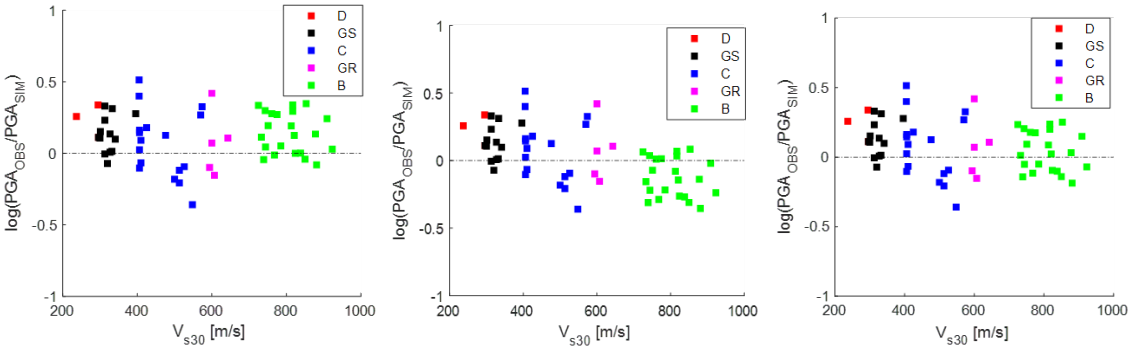

(a) (b) (c)

Figure 4.5. Effect of generic site amplification models on PGA distribution at all of the rock stations (green color) by using (a) Boore and Joyner, 1997 (Vs30=2900 m/s) (b) Atkinson and Boore, 2006 (Vs30=760 m/s) (c) Pischiutta et al., 2021 (Vs30=1163m/s).

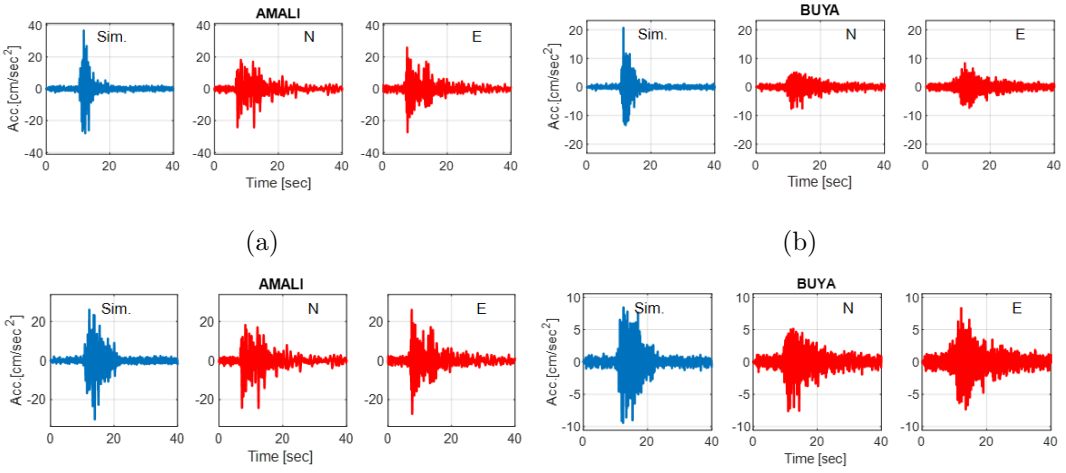

(a) (b)

(c) (d)

Figure 4.6. Evaluation of duration models at two randomly selected representative stations AMALI, and BUYA for path duration models (a) by Herrmann, (1985) for stations AMALI, and (b) BUYA, (c) by Boore and Thompson, (2014) for stations AMALI, and (d) BUYA. (Blue color is for simulated motion, red color is for recordings in the N and E directions)

sponds to the time interval between 5% to 75% (D75) and between 5% to 95% (D95) of the cumulative integral of the squared ground accelerations (Arias intensity). In our calculations for D95, we applied the effective duration formula provided by Boore and Thompson, (2014) as $D_{95}{}' = 2.0(D_{80} - D_{20})$. According to Figure 4.7, although

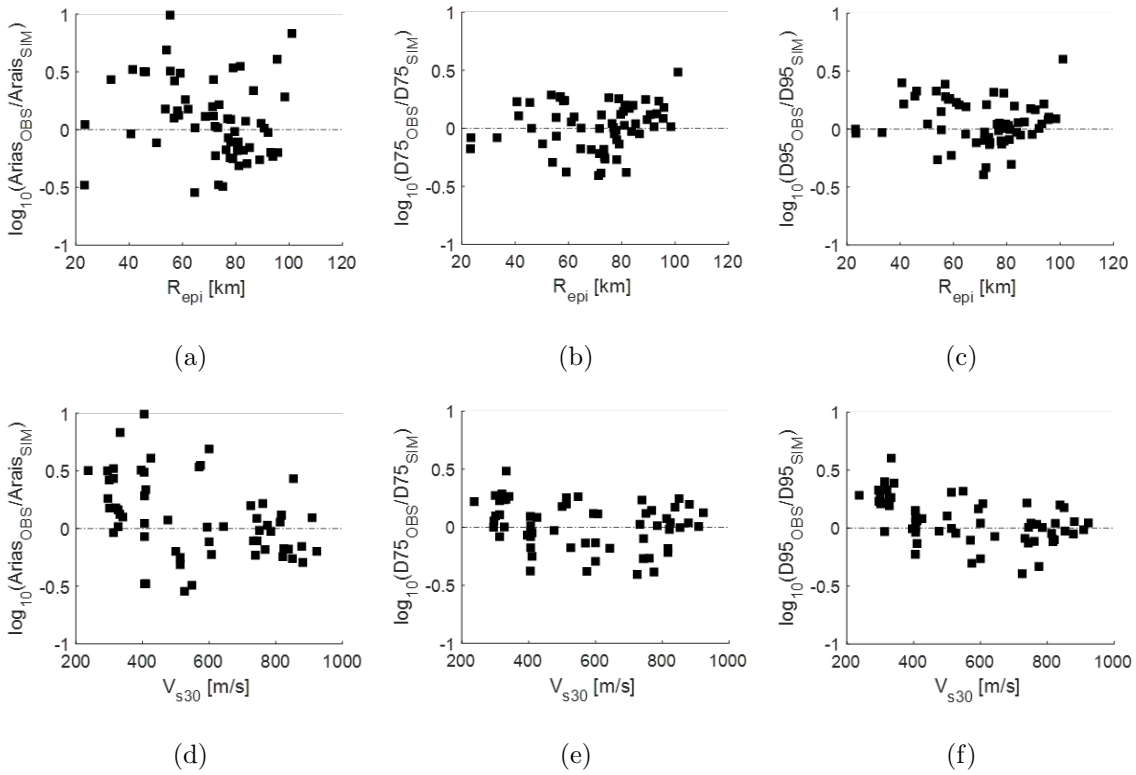

Figure 4.7. Comparing observed and predicted (a) Arias intensity (b) D75 effective duration, (c) D95 effective duration versus epicentral distance and (d) Arias intensity, (e) D75 effective duration, (f) D95 effective duration versus epicentral distance.

Arias intensity comparison shows a wider scattering especially in lower Vs30 values, the model provides an acceptable error range for both D5-75 and D5-95 effective durations.

Our analyses have shown that the results are more sensitive to the stress drop and frequency dependent Q model than other uncertainties, as stated earlier by Sørensen et al., (2007). Stress drop is an important variable that affects the amplitude of the waveform in both low and high frequency ranges. In our model, stress drop was assumed as 50 bar which minimized the error distribution in the frequency range of interest. We have examined four different frequency dependent empirical quality factors: The regional Q model by Akinci et al., (2006) as $Q(f) = 180f^{0.45}$ caused overestimation of FAS levels for frequencies up to 5-6 Hz. This was observed especially at the stations with higher Vs30 values and could not be adjusted with multiple sets of changes in the source, path, and site parameters. Even though it gives better results at D and generic soil site stations, all synthetics were underestimating the observations at high

frequencies (18-25 Hz). When another regional Q model given by Süleyman (2018) as $Q(f) = 45f^{0.92}$ was chosen, it was found that the fit in the range between 1 Hz and 10 Hz is quite reasonable. The model, however, slightly underestimated the spectral levels for frequencies larger than about 10 Hz. To handle this problem, which was also mentioned by Ugurhan and Askan, (2010), we used the Q model defined by Boore, (1984) as $Q(f) = 88f^{0.9}$ derived based on worldwide data. This model resulted in better fits in the high frequency range. However, it performed not well for frequencies smaller than about 10Hz, clearly overestimating recorded ground motion levels. Finally, we examined the Q model by Horasan et al., (1998) given as $Q(f) = (50 \pm 1.7)f^{(1.09\pm0.05)}$ which was derived using data from the Marmara Region. We have observed that this model provides a better overall fit across the stations and in the frequency band of interest. Figure 4.8 shows the effect of the use of different Q models on FAS at station BBAIO.

Station specific kappa values estimated from the slope fitted to the high-frequency part of horizontal Fourier amplitude spectra (FAS) provided by Süleyman, (2018) are used, except at eight stations which are not available in the cited study. For these stations (AMALI, AVIIO, DARUL, HHBLI, NSEIO, TUZL, YGBIO, and ZYKOI) we assigned kappa as 0.050, 0.055, and 0.065 s based on their Vs30 values.

The effect of using different values for the high frequency decay parameter, kappa, on the synthesized ground motion is represented in Figure 4.9 for selected stations GOPPL, KAPIO, and MODAI. Other parameters being the same, at station GOPPL, station specific kappa has resulted in a 74.5% overestimation of PGA, while kappa=0.054 s has caused 24% underestimation of PGA (geometric mean of the two recorded horizontal PGAs is compared with the PGA of simulations). Similarly, at station KAPIO station specific kappa and using constant kappa (the details are given in the following paragraph) caused 44.3% and 16.6% overestimation, respectively. Using station specific kappa resulted in 59.5% underestimation at station MODAI, while constant kappa creates 44% underestimation. In addition, the use of constant kappa has shown higher consistency between simulated and recorded levels.

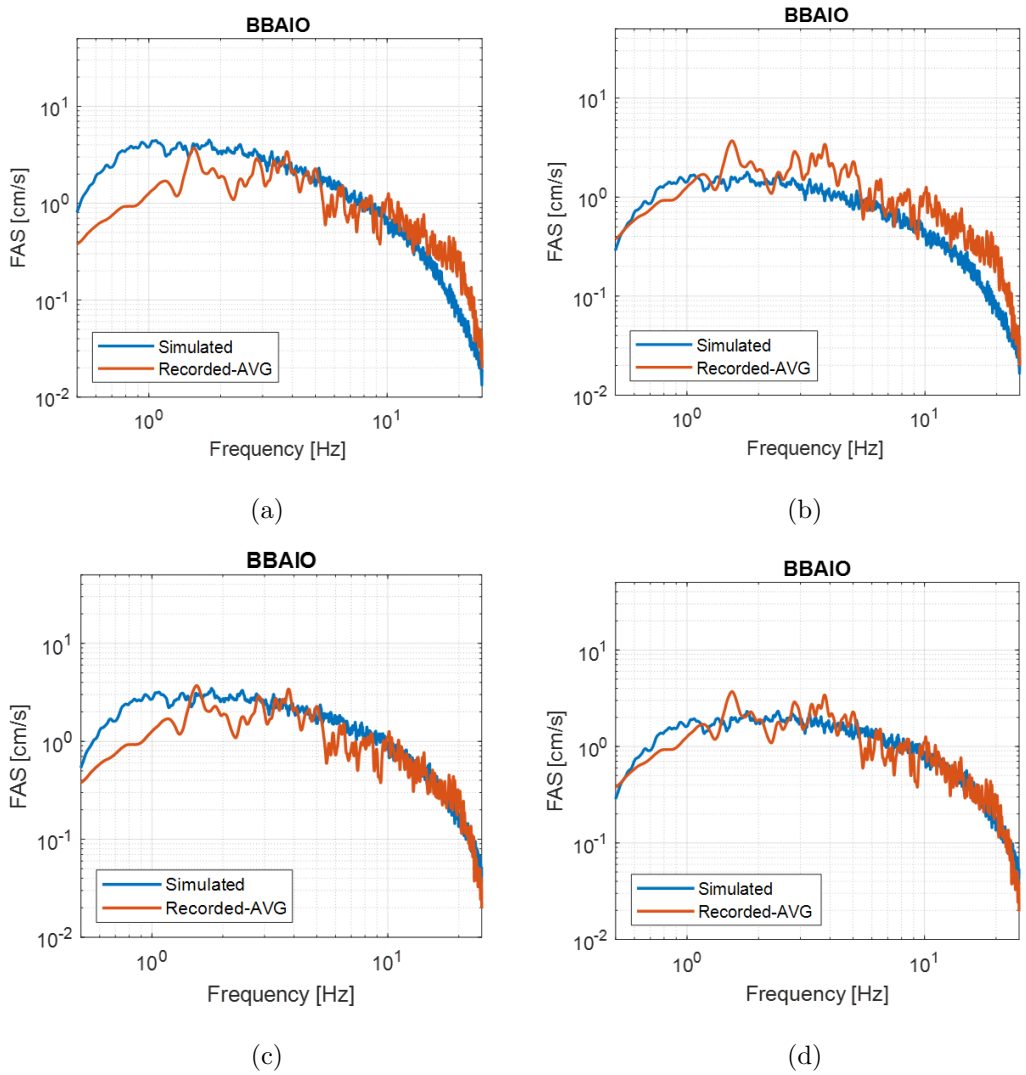

Figure 4.8. Effect of different Q models. Synthetic FAS simulated using four Q models are compared with recorded FAS for station BBAIO. (a) Akinci et al., (2006) (b) Süleyman, (2018) (c) Boore, (1984) (d) Horasan et al., (1998). The models are indicated in the sub-figure captions. Qmin is taken as 60 in all models, other variables are kept the same.

Figure 4.10 explores how the fit between observed and predicted PGAs varies as a function of epicentral distance, Repi, and Vs30. Based on Figures 10a and 10b, it can safely be stated that our estimated PGAs do not show any systematic variation with distance and Vs30. They are contained roughly within +/-0.5. In simulations that formed the basis of Figure 4.10a and 4.10b, station specific kappa values derived from earlier recordings are used. To investigate if the use of fixed kappa values affects the PGA estimates we turned to Durukal (2002), and Durukal and Çatalyürekli (2004).

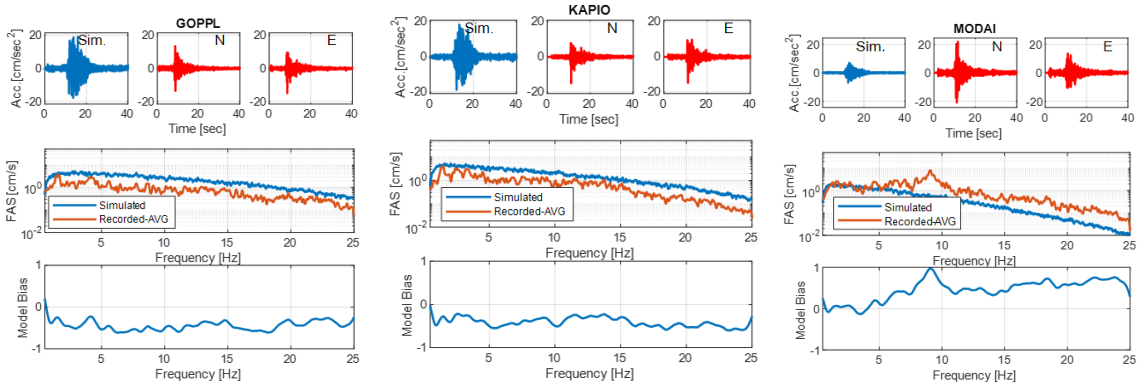

(a) Kappa : 0.035s
PGA Simulated : 21.79 cm/s^2

(b) Kappa : 0.041 s
PGA Simulated : 21.41 cm/s^2

(c) Kappa= 0.071 s
PGA Simulated : 6.93 cm/s^2

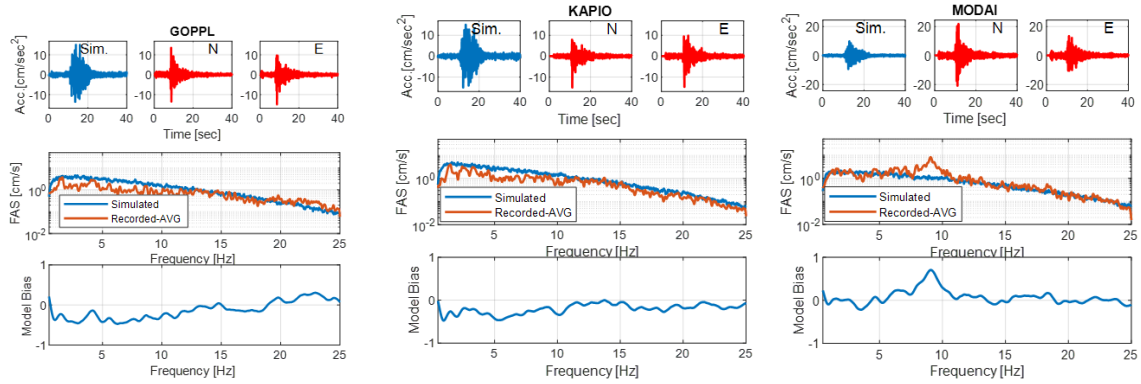

(d) Kappa= 0.054 s
PGA Simulated : 17.63 cm/s2

(e) Kappa= 0.054 s
PGA Simulated : 17.30 cm/s2

(f) Kappa= 0.048 s
PGA Simulated : 9.57 cm/s2

Figure 4.9. Effect of the high frequency decay parameter, kappa, at stations GOPPL, KAPIO, and MODAI for station specific kappa (upper part), and constant kappa (below).

Based on analysis of the mainshock and the main aftershock data of the 1999 Kocaeli and Düzce earthquakes, Durukal (2002) suggested average horizontal kappa values as 0.072-0.073 s for D type soils, and 0.048-0.054 s for B and C type soils. Later Durukal and Çatalyürekli (2004) estimated horizontal kappa values as 0.041 s and 0.056 s for C and D soil classes respectively using the 1999 Kocaeli and Düzce earthquakes' aftershock sequence data. Using kappa values estimated by Durukal (2002), we have achieved better fits between observed and simulated PGAs, and used those when plotting Figures 4.10c and 4.10d. The exercise did not affect the general observations we made on Figures 4.10a and 4.10b. However, it was interesting to note that the scat-

ter around the zero line became more contained when constant kappa values assigned based on station site class are used instead of station specific kappas derived from the previous recordings. In the comparisons presented in Figure 4.9 and discussed in this paragraph the Q model by Horasan et al., (1998) is used. When we repeat the same exercise using the Q model by Süleyman (2018) we have observed a slight systematic upward shift in all subfigures (not included herewith), indicating, that the Q model affects the peak ground values as well.

Simulations using two rupture velocities as 0.7 x shear wave velocity and 0.8 x shear wave velocity, two shear wave velocities as 3.6 km/s and 3.8 km/s and two crustal densities as 2.7 g/cm^3 and 2.8 g/cm^3 revealed negligible sensitivity on the results and the latter ones have been chosen.

The number of iterations in EXSIM12 was chosen as thirty, as the effect of using a higher number of iterations was indistinguishable. In this paper, while time histories were represented by a randomly picked iteration, all frequency domain plots were represented by averaging individual Fourier spectra of the iterations. Similarly, all ground motion intensity measures, peak ground acceleration (PGA), peak ground velocity (PGV), and spectral accelerations (SA) were calculated using the mean value of the iterations.

4.2.5. Comparison and Validation of Simulation Results with Recorded Data

Using input models and parameters discussed in the previous section, we have simulated acceleration time histories at 59 stations in Istanbul. Simulated ground motions are uniformly compared with the recordings in time and frequency domains. For each station, we provide synthetic acceleration time histories, observed accelerations in two horizontal components (NS and EW), average FAS of recorded accelerations, and FAS of synthetic accelerations. All data, recorded and simulated, are filtered between 0.5-25 Hz, and FAS are smoothed. The comparison for 59 stations is available in the electronic supplement file. Herewith we discuss our findings in two groups. The first

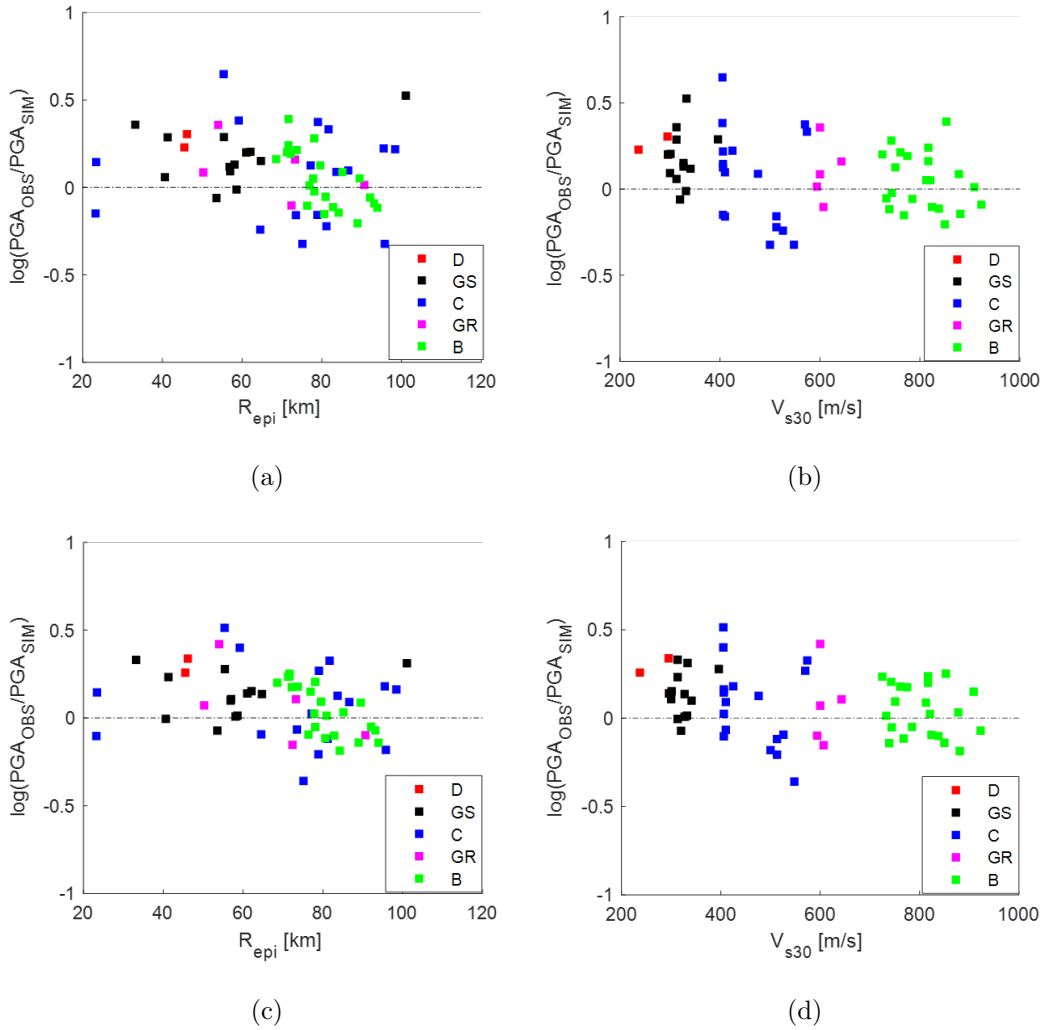

Figure 4.10. Comparing observed and predicted PGAs (a) versus epicentral distance using station specific kappa values, (b) versus Vs30 using station specific kappa values, (c) versus epicentral distance using constant kappa values, (d) versus Vs30 using constant kappa values, (colors represent NEHRP site classes). Following constant kappa values are used: B= 0.048, GR= 0.048, C=0.054, GS=0.054, and D=0.072. Observed PGAs are estimated as the geometric mean of two horizontal components.

group is selected from stations at which minimum bias between recorded and simulated accelerations is achieved. The second group is a selection of stations at which the simulations could not satisfactorily represent recorded ones.

In Figure 4.11 six selected stations are shown at which the model bias was min-

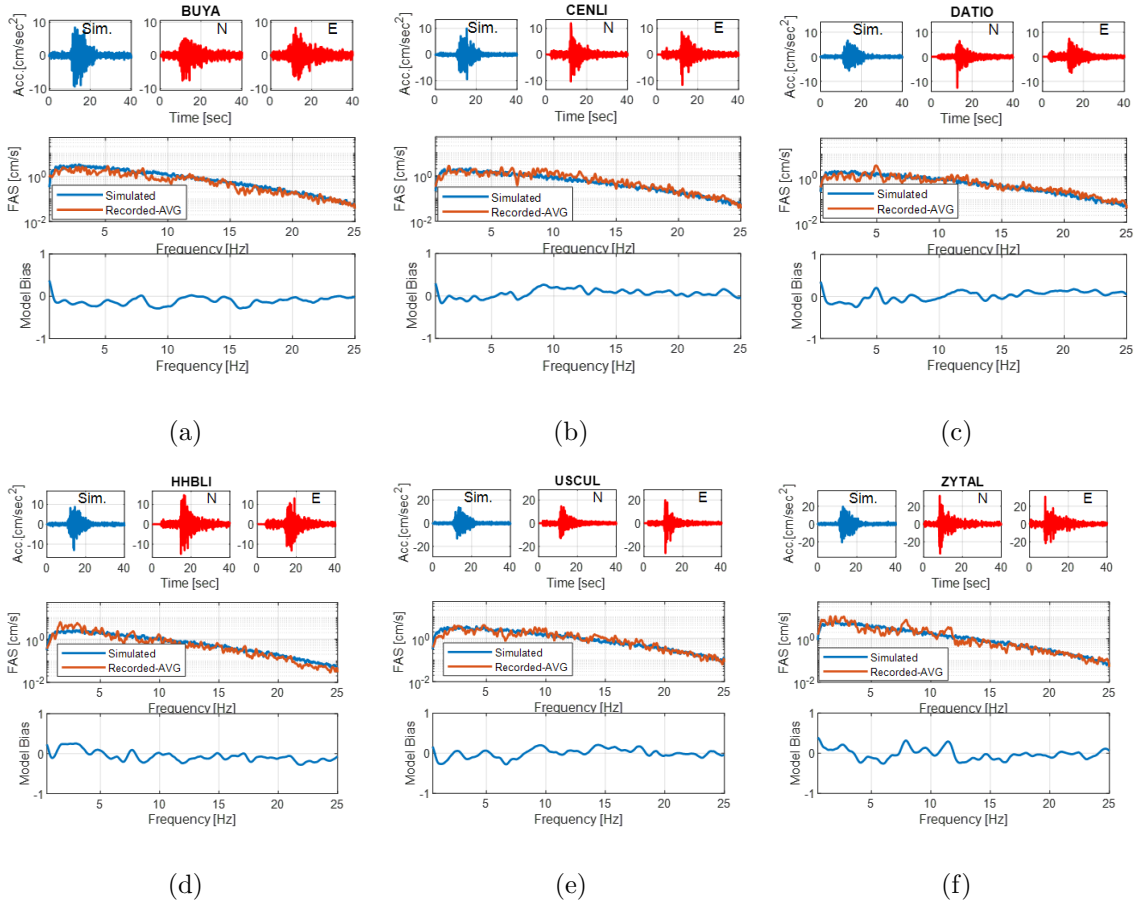

Figure 4.11. Comparison of observed and simulated acceleration-time histories and FAS for selected stations at different site conditions (BUYA and HHBLI are C site class, CENLI and DATIO are B site class, USCUL is GR class, and ZYTAL is GS class)

imum. If model bias is negative, it means that simulation overestimates observation, whereas positive model bias indicates that the estimation tends to underestimate observation. In frequency domain, we had the best fits between the simulated and observed FAS at stations BBAIO, BUYA, CENLI, DATIO, EHAIO, HHBLI, ISMIO, KARSO, KSSIO, MMZIO, MYMIO, OKCIO, PGZOL, PVBIO, SMKIO, TTEML, UACPI, UDAIO, USCUL, and ZYTAL where model biases are within -0.2 / +0.2 log units. We observed a satisfactory consistency at stations AVCLI, FBZMD, GOPPL, KASDL, KHAIO, LAFA, MECLI, NSEIO, SINB, UMSBI, USKPL, and YILIO where model biases are within -0.4 / +0.4 log units.

The worst fits were observed at stations ATAIO, BOTS, HVHR, HYBA, HYSIO,

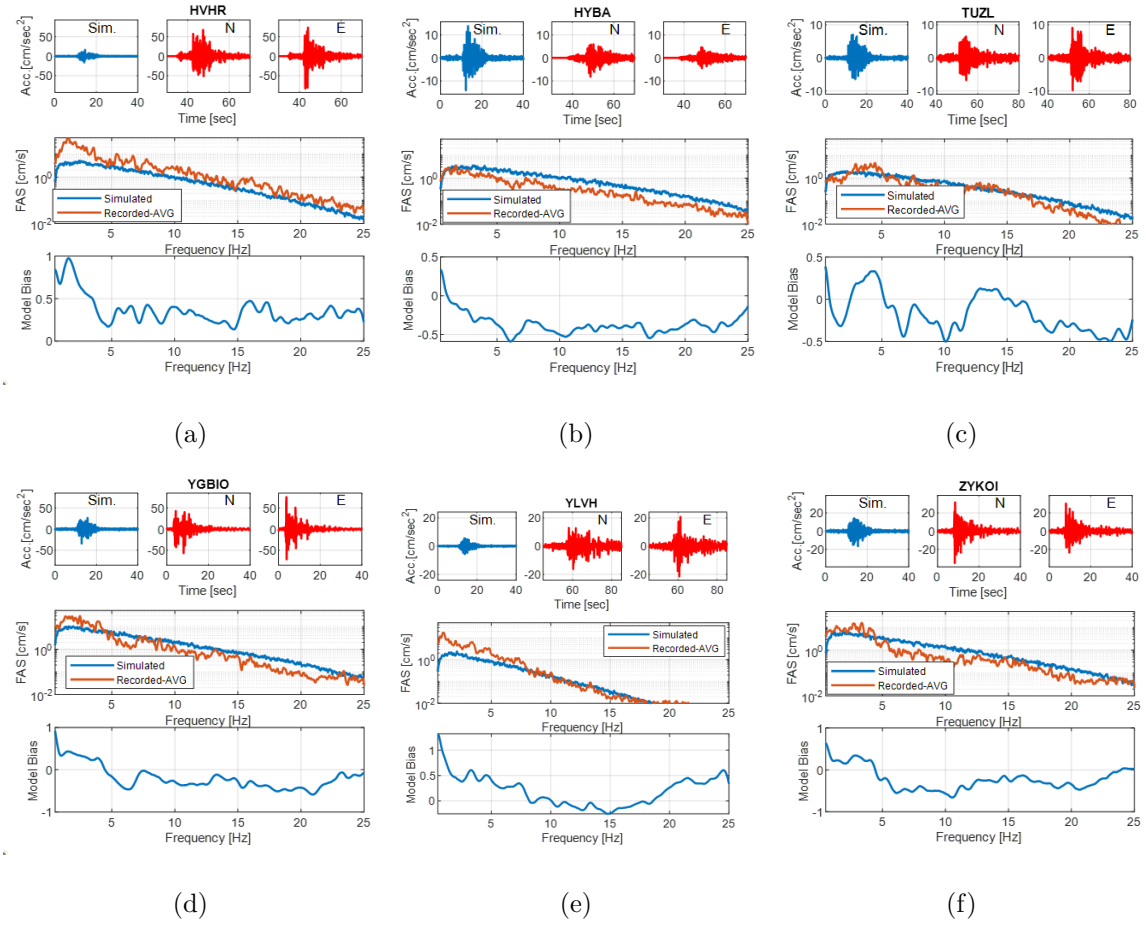

Figure 4.12. Comparison of acceleration-time histories and FAS of the simulated and recorded data for the worst estimated stations.

MODAI, PTMLI, TUZAL, TUZL, YGBIO, YLVH, and ZYKOI (Figure 4.12). In ATAIO and PTMLI, the inconsistency at high frequencies may indicate a kappa estimation problem. Misfit at HVHR station could not be fixed even by defining higher site amplification factors. At BOTS and HYBA stations, synthetics became higher than the observations at almost all frequency ranges. Stations HYSIO, MODAI, and TUZAL have local irregularities at some frequencies. As mentioned previously, due to lack of information, we made estimations for kappa values at YGBIO and ZYKOI stations and for site classification of YLVH. It should be recalled that we used generic site amplification factors, which could explain the mismatch observed over the frequency domain and in the peak values. Besides, mismatches may originate from the complexity of the nature of wave propagation.

There are a number of stations that deserve specific discussion. Station BOTS is at the closest epicentral distance (Figure 4.1, Figure 4.3), where the mean recorded PGA is 39.9 cm/s^2, while simulated PGA is 50.68 cm/s^2. As this is considerable, although likely difference, we wanted to check a nearby off-line station, TKMEL. Station TKMEL is located on similar site conditions with BOTS and just 2.1 km to the northeast. Recorded PGAs at TKMEL were 82.98 cm/s^2 and 63.45 cm/s^2 in EW and NS directions, respectively. The discrepancy between peak and simulated values at station BOTS can therefore be related to an instrumental problem, which we double checked and could not confirm, or it can be related to site amplification factors. As already stated before, the site condition of the station BOTS was taken from QTM data which can be different than seismic microzonation studies. At this station, using lower site amplification factors can provide better matches.

To see if there is a systematic variation in bias ranges concerning a stations' soil conditions and their geographical distribution, we have categorized the stations into three groups (i.e. three bias ranges) and showed them against the Vs30 map (Figure 4.13). In figure, green triangles illustrate the stations where synthetics match well with the recordings (up to $\pm$0.4 misfit level in log10), orange triangles are the stations the model bias of which are found to be moderately good (between $\pm$0.5), and purple ones represent the stations which are evaluated as the worst fitting group (beyond $\pm$0.5). The comparison shows no clear dependency between the model biases of stations and their locations or their general site conditions.

Figure 4.14 represents the model bias of all stations in terms of their epicentral distances and Vs30 values at three randomly selected frequencies as 2 Hz, 6 Hz, and 13 Hz. At high frequencies, since station misfits are randomly distributed regardless of frequencies and there is not any distance dependent bias, we can claim that our path effect modeling is successful. On the other hand, at 2 Hz, simulations underpredict observations until about 60 km, while at larger distances model bias seems to be random. Similarly, at 2 Hz, the synthetics underestimate the recordings at the stations with Vs30 less than 400 m/s. Checking station specific spectra, we identified the relevant frequency range for this observation as 1 Hz - 2.5 Hz. Therefore, which suggests a

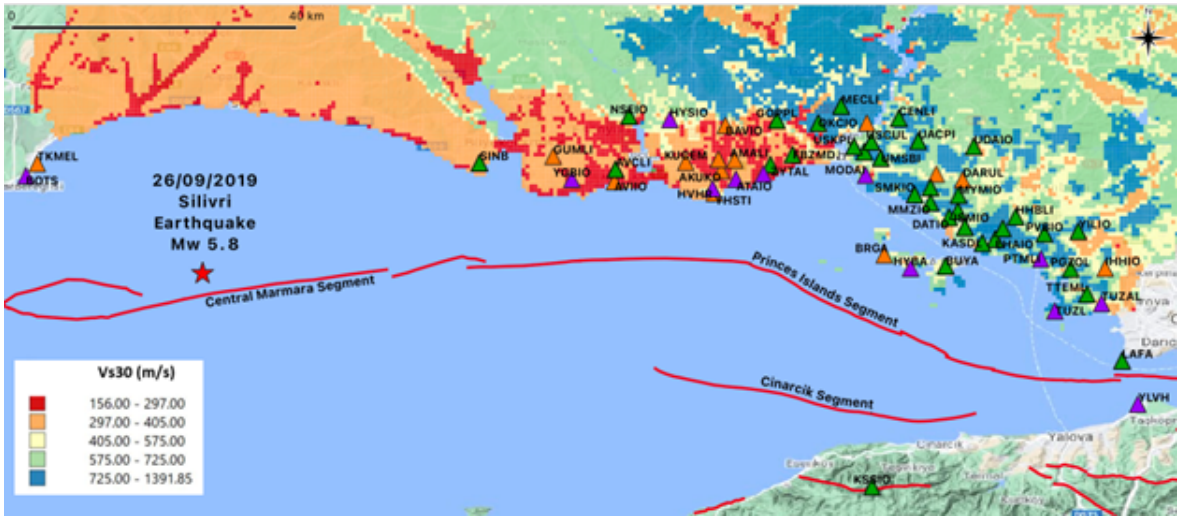

Figure 4.13. Station based misfits. Stations are illustrated with triangles. Colors indicate model bias ranges: green stations are less than ± 0.4; orange stations are ± 0.5, purple stations are beyond ± 0.5. The base map is the Vs30 Map for Istanbul (IBB-OYO-KOERI, 2009). The faults are compiled from the Active Fault Map of Turkey, MTA (Mineral Research and Exploration General Directorate (Emre et al., 2013).

potential for improvement of the Q model in this frequency range.

The misfits calculated using Equation 4.7 and averaged over 59 stations are shown in Figure 4.15. According to these plots, we can say that there is no systematic mismatch in both rock and soil site stations. Overall, the synthetics are in good agreement with the recorded data between 0.5-25 Hz frequency band.

Zengin and Cakti (2012) had applied the stochastic approach to calibrate source and path related parameters for the 25 July 2011, MI 5.1 Marmara Sea earthquake using a similar data set. The earthquake had taken place on NAF further to the west. When parameter values proposed for use by Zengin and Caktı (2012) and by the present study are compared the following can be noted: both use the same crustal shear wave velocity and crustal density; there are however differences in preferred attenuation models, rupture velocities, and duration models (Table 4.4).

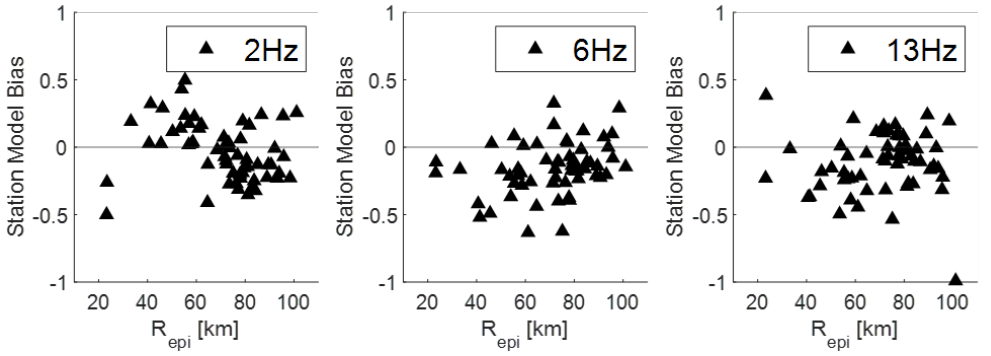

(a)

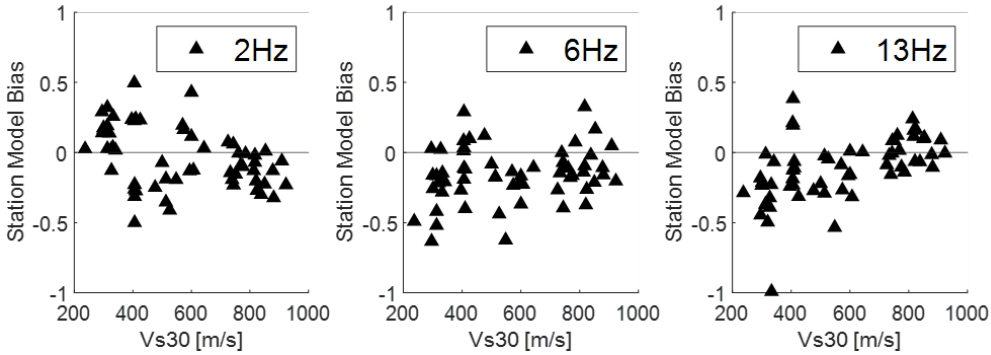

(b)

Figure 4.14. Station misfits (ratios of observed to simulated spectra) at three frequencies, 2 Hz, 6 Hz, and 13 Hz versus (a) epicentral distance and (b) Vs30.

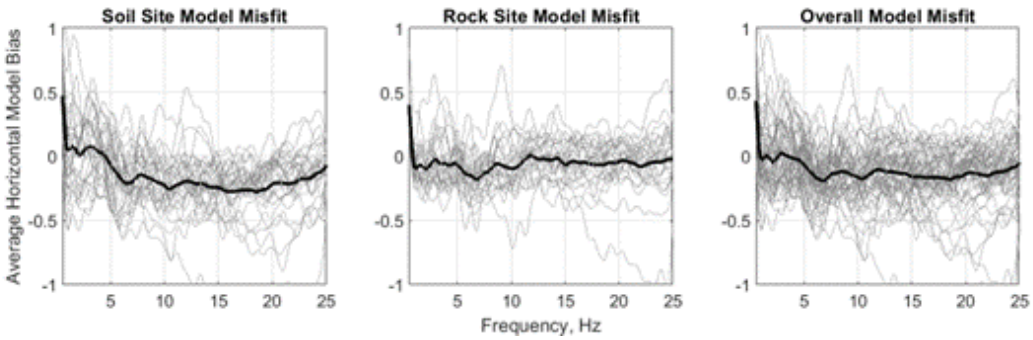

Figure 4.15. Averaged model misfit obtained from the error functions of 59 stations in frequency domain. Grey lines represent 59 stations independently while the bold black line corresponds to the overall misfit.

Figure 4.16 illustrative of results of three representative stations located on different NEHRP site classifications using both model sets used by Zengin and Çaktı (2012) and created in this study. In these comparison plots, all the parameters remained the same except the different ones mentioned in Table 4.4. Figure 4.17 illustrates model

Table 4.4. Differences in Parameter Values between this study and Zengin and Çaktı, (2012)

Parameters	**Zengin and Çaktı, (2012)**	**This study**
Rupture velocity (km/s)	0.7 x (shear wave velocity)	0.8 x (shear wave velocity)
Attenuation, Q(f)	$Q(f)=180f^{0.45}$	$Q(f)=50f^{1.09}$
Duration Model	To+0.07R	Boore and Thompson, (2014)
Site Model	NEHRP D: Boore and Joyner (1997)	NEHRP D and C: Boore and Joyner, (1997) GR and GS: Boore and Joyner, (1997) NEHRP B: Pischiutta et al., (2021)
Kappa	0.05	Durukal and Çatalyürekli, (2004)

bias in the recorded and simulated PGAs versus both epicentral distance and Vs30. Clearly, the former model sets caused higher PGAs and a high range of misfits in frequency domain compared to the parameter sets created in this study. Although the former model can give tolerable simulation results for soft soils up to Vs30=400m/s and epicentral distance less than 65 km, it is considerably poor to represent ground motions in a firm to hard rock sites and longer distances. Besides, their path duration model was not enough to represent the recordings. Since our study involves improved descriptions of site classes and station specific kappa values and a more rigorous check on simulation parameters, we can suggest that it can be more reliable for use in region specific studies.

4.2.6. Regional Simulation and Comparison with Damage

One of the purposes of the present exercise is to show that the model can be used for uniform regional simulation of ground motion time histories and consequently for regional estimation of important engineering parameters. We prepared maps showing spatial distributions of simulated PGAs, peak ground velocities (PGV), and spectral accelerations (SA) at 0.2 s and 1.0 s for two cases. The first case is the area within the municipal boundaries of Istanbul. The second case is the wider Marmara region. The grid sizes used for the two cases are 0.005 and 0.012 degrees, respectively.

The reason for using two geographical scales is twofold. The first reason is as-

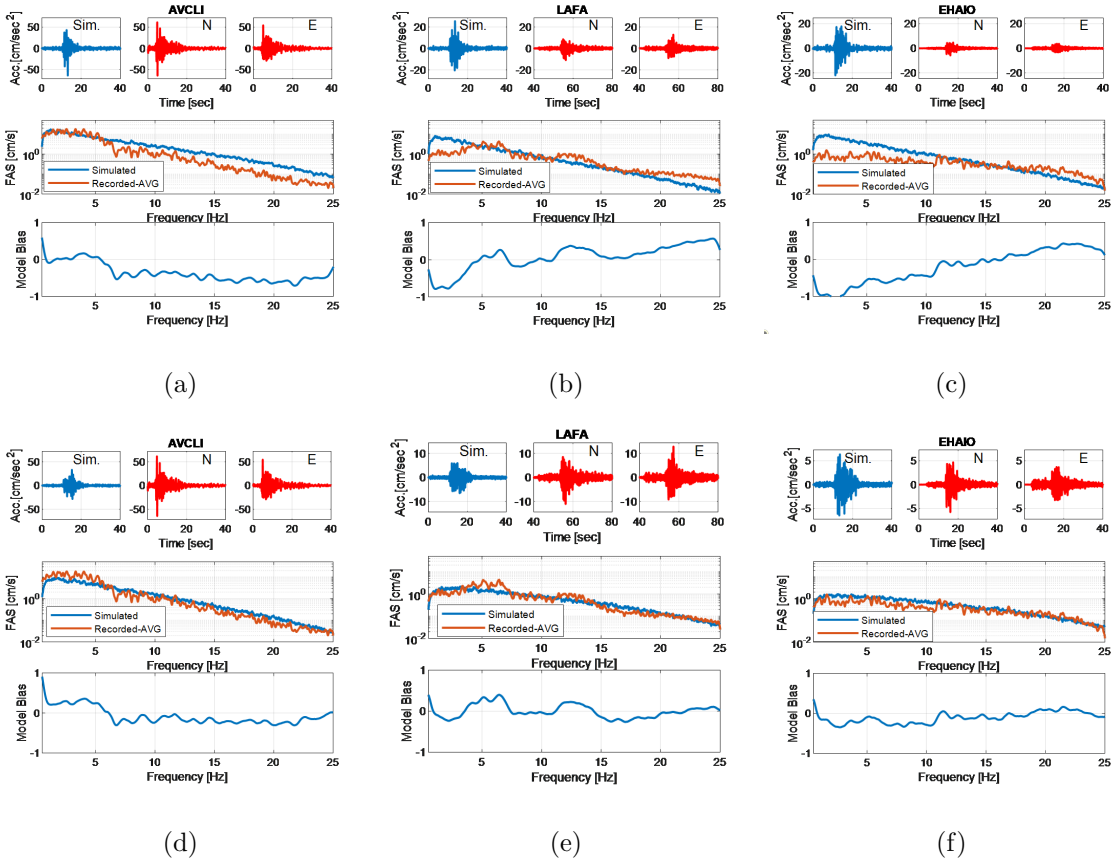

Figure 4.16. Comparison of the simulated and recorded fround motions with sets of model parameters used by study of Zengin and Çaktı (2012) (upper part) and created in this study (below part) for stations AVCLI (NEHRP D site class), LAFA (NEHRP C site class), and EHAIO (NEHRP B site class).

sociated with available information regarding soil conditions. Within the municipal boundaries of Istanbul, a relatively detailed site classification based on the Vs30 Soil Classification Map is available. For the region beyond, site classes assigned by QTM information exists. Therefore, Istanbul specific regional simulations were carried out using site classes assigned on the basis of Vs30, while regional simulation covering the Marmara region (inclusive of Istanbul) used classes assigned from QTM maps. This provided an opportunity for comparing the use of two different but similar site class sets for Istanbul. At the same time, it provided an insight on the use of our model for simulations in a larger scale, as we prepare for applying it in simulations of past and future events, the effects of which are regional and not necessarily Istanbul specific.

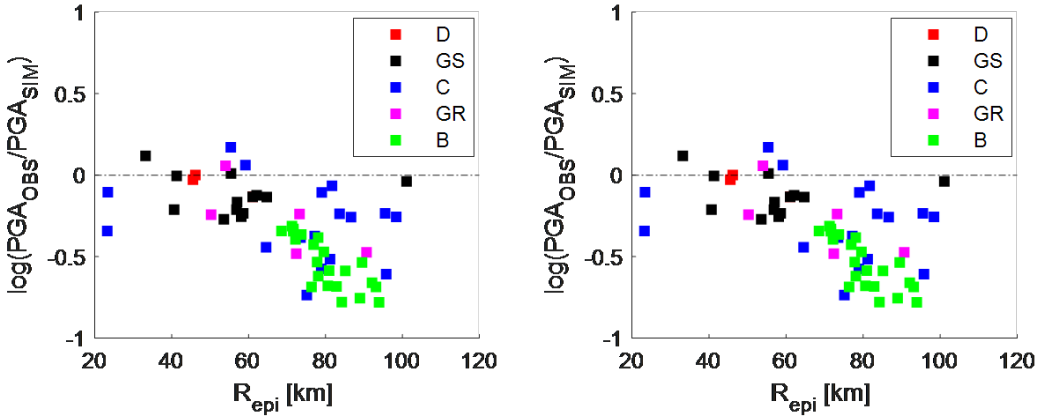

(a) (b)

Figure 4.17. Comparison of observed and predicted PGAs in the model set used by Zengin and Çaktı (2012) (a) versus epicentral distance and (b) versus Vs30, (colors represent NEHRP site classes). Observed PGAs are estimated as the geometric mean of two horizontal components.

According to site classifications, we assumed constant kappa values as: Site Class B= 0.048, GR= 0.048, C=0.054, GS=0.054, and D=0.072 (Figure 4.9). Since the QTM model provides Vs30 values of 333 m/s, 406 m/s, and 589 m/s, the Marmara Region maps include site effects for classes GS, C and GR.

The use of two sets of site classes resulted in some variations in ground motion distributions. Generally, lower peak values were predicted when QTM based site classes are used. For example, maximum PGAs were up to 6.60 (g%) when QTM was used, it was 7.63 (g%) with the latter. Likewise, predicted PGVs were up to 4.90 cm/s using Istanbul specific Vs30 map, while QTM data ended up with up to 4.33 cm/s PGVs. The highest spectral acceleration estimations were 17.48 and 7.46 (g%) with Istanbul soil classification map, 15.96 and 5.64 (g%) with QTM map at periods 0.2 and 1.0 seconds, respectively. In terms of geographical distribution, a similar conclusion can be made. It is evident from Figure 4.18 and Figure 4.19, that larger parts of Istanbul having similar parameter values are affected when Vs30 based site classes are used. All figures are drawn to the same scale.

As a last step of validation, we compare simulated and observed PGAs, PGVs,

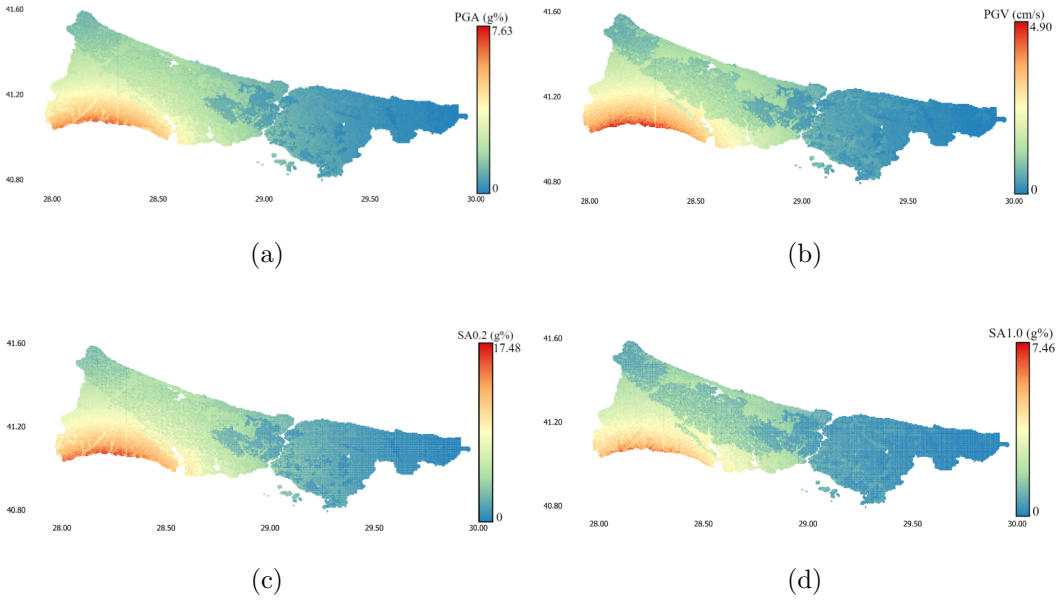

Figure 4.18. Simulation based regional distribution in terms of (a) PGAs (g%), (b) PGVs (cm/s), (c) SA at T=0.2 s (g%) (d) and SA at T=1.0 s (g%) using calibrated model parameters and Vs30 Soil Classification Map of Istanbul.

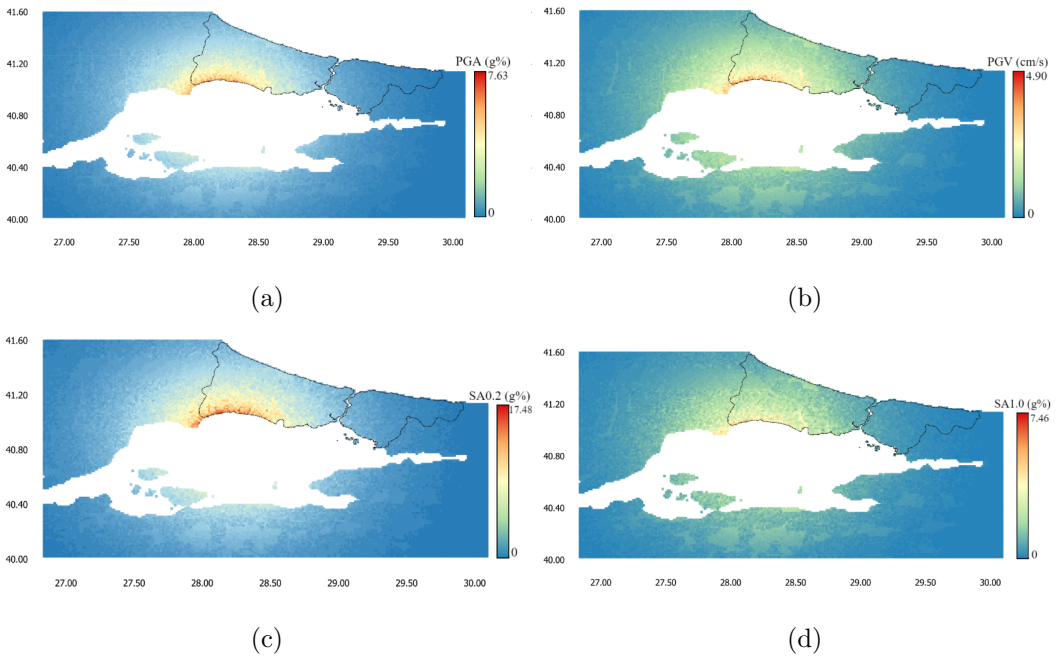

Figure 4.19. Simulation based regional distribution in terms of (a) PGAs (g%), (b) PGVs (cm/s), (c) SA at T=0.2 s (g%) (d) and SA at T=1.0 s (g%) using calibrated model parameters and regional geology maps, QTM.

and SAs at 0.2 sec and 1.0 sec with NGA-West2 Ground Motion Models (GMMs) (Figure 4.20). We select GMMs defined by Akkar et al., (2014), and Chiou and Youngs (2014). GMMs were plotted with their median and ± 1 standard deviation for Generic Rock (including GR and B) and Generic Soil (including D, GS, and C) type soils. We observed a good agreement in rock sites and only a few of the stations stayed out of the median lines. In soil sites, synthetics are slightly below the median similar to the recordings. Figure 20 suggests a satisfactory match between our simulations and predictions by the GMMs for both rock and soil stations. On the same figure, we also plot grid-based synthetic intensity measures using site classes based on Vs30. It can be observed that the grid-based simulations closely follow the station-based predictions as expected and are within the ± 1 standard deviation boundaries, although some GMM specific differences exist. Grid based synthetics resulted in significantly biased low values than GMM median predictions beyond 100 km distance which is a sign of fast attenuation over a certain distance. Also, it is not an appropriate distance level to make a comparison with predictions because it is not captured by NGA-West2 GMMs. It should be reminded that since there is no station over 101 km distances, we couldn't make a comparison by real records. It is interesting to note that the use of grid-based synthetic PGAs based on QTM, would probably yield a distribution slightly lower than those shown in Figure 4.20, would however be in general agreement with the GMMs.

Silivri earthquake led to structural damages in Istanbul. As we have no access to the official damage information, we compiled damages reported by various sources, as summarized in Table 4.5. Based on compiled information we estimate the number of heavily damaged buildings as about 250 and slightly damaged buildings as about 750. No estimation could be made regarding the number of moderately damaged buildings. The locations with damages are indicated in Figure 4.21 which also shows the regional distribution of simulated PGAs.

Department of Earthquake Engineering of Kandilli Observatory and Earthquake Research Institute – Bogazici University, published estimated damage distribution maps for this earthquake (Figure 4.22) (`https://eqe.boun.edu.tr/sites/che.boun.edu.tr/files/26-09-2019-silivri_depremi_eng.pdf`). The damage infor-

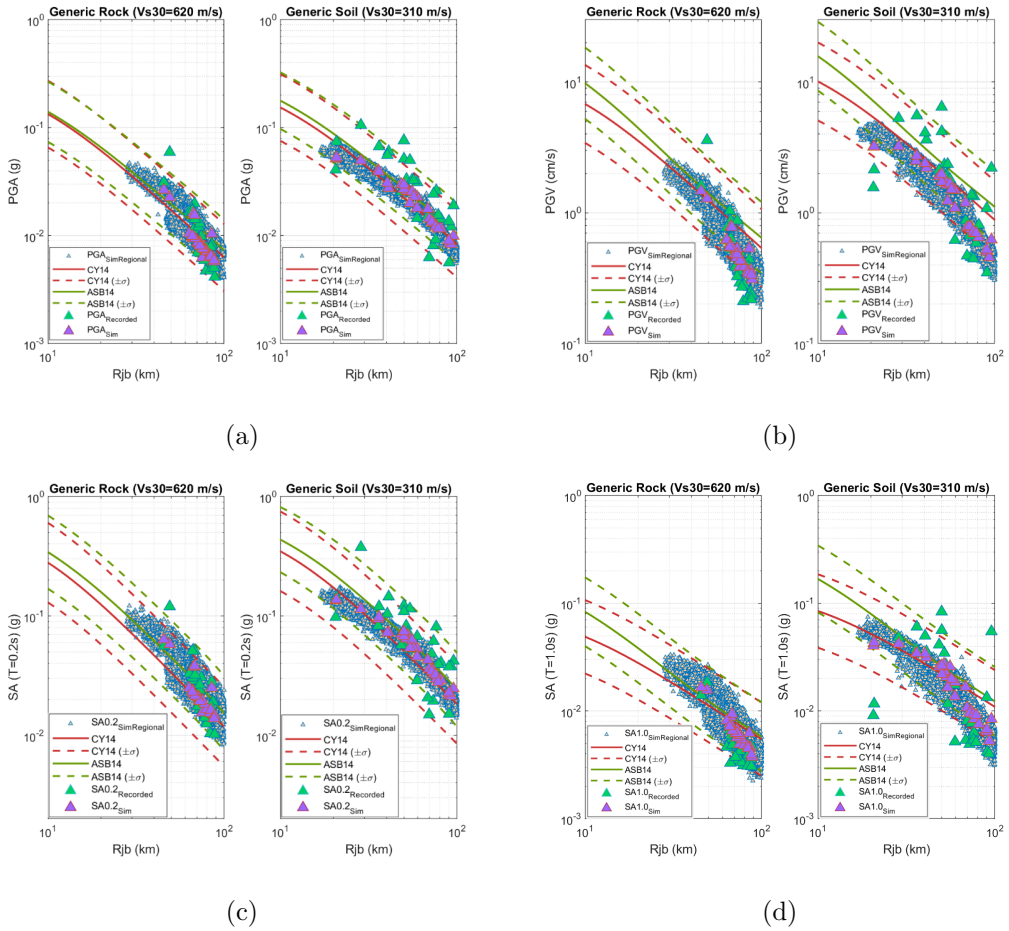

Figure 4.20. Comparison of the synthetics and recordings with Akkar et al., (2014) and Chiou and Youngs (2014). GMMs in terms of PGAs (g), PGVs (cm/s), and SAs at periods 0.2 and 1.0 seconds versus Boore and Joyner closest distances for generic rock and generic soil. Recordings are in terms of the geometric mean of the horizontal components.

mation is provided by ELER (ELER, 2010). using ground motion data coming from the Istanbul Earthquake Rapid Response System and the building inventory of Istanbul (KOERI, 2019). It was estimated that 60 buildings would be in a heavy damage state, about 800 buildings would be moderately damaged and 5000 buildings would receive light damage. It is important to note that the number of heavily damaged buildings (about 250, our estimate based on compiled data) is four times of those estimated by ELER. On the other hand, the number of slightly damaged buildings that we could compile from informal sources (about 750) is much less than those estimated. It would be reasonable to expect that the actual number of slightly damaged buildings in Istan-

Table 4.5. Reported damages for the 26 September 2019 Silivri earthquake

Damage level	**Number of affected buildings**	**Locality**	**Source**
Slight	Many, exact number not given	Avcılar, Bağcılar, Bahçelievler, Bakırköy, Beyoğlu, Büyükçekmece, Esenyurt, Eyüp, Fatih (Çapa), Sarıyer, Silivri, Şişli, Sultangazi	[1-4]
	One minaret	Sarıyer	[3]
	20 schools, one hospital, one public building, and one mosque	Arnavutköy, Avcılar, Beykoz, Büyükçekmece, Eyüp, Fatih, Gaziosmanpaşa, Güngören, Küçükçekmece, Maltepe, Pendik, Sarıyer, Sancaktepe, Silivri, Sultangazi, and Üsküdar.	[4, 5]
	724	throughout Istanbul	[6]
Moderate	One building tilted	Şirinevler	[1]
Heavy	One minaret	Avcılar	[1, 3, 7]
	Three mosques	Avcılar, Silivri	[6]
	Several buildings	Bahçelievler, Balat, Büyükçekmece, Silivri, and Sultangazi	[1, 3, 8-10]
	9 schools, 4 public buildings, one hospital administration unit	Bahçelievler, Büyükçekmece, Çatalca, Gaziosmanpasa, Pendik, and Sancaktepe	[5]
	224	throughout Istanbul	[6]

bul were significantly larger than our estimated figure of 750, as this level of damage tends to remain relatively anonymous.

An independent source for checking the order of damages can be the Turkish Catastrophe Insurance Pool (TCIP). From the TCIP 2019 report (DASK, 2019a) and press releases (DASK, 2019b) we understand that the number of claims made following this earthquake was somewhere between 10,000 and 12,555. In 2019 TCIP made payments to 4,723 individuals out of 15,222 claims Turkey-wide, indicating that about 31% of the claims were related to earthquake induced damages. With this ratio in mind, in Istanbul the number of insured who received compensation should be between 3,100 – 3,900. The penetration of compulsory earthquake insurance in Istanbul was 67% in

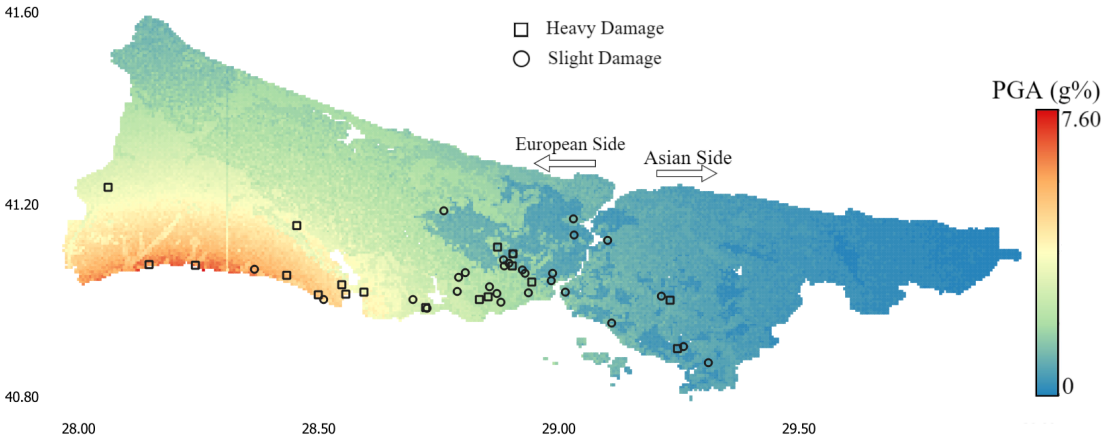

Figure 4.21. Neighborhoods where damages were reported. Squares represent locations of heavily damaged buildings while circles show slight damage. Regional simulated PGAs (g%) given in colors.

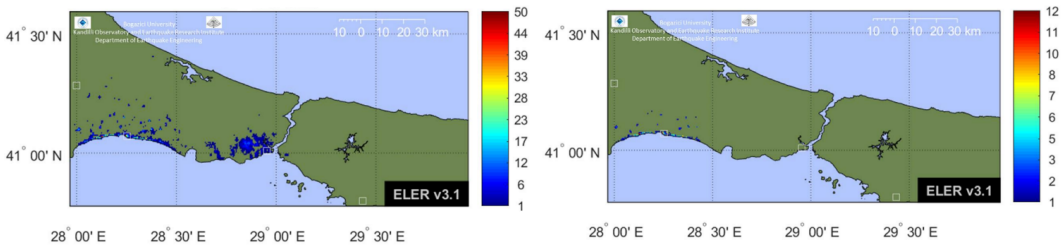

(a) (b)

Figure 4.22. Estimated damages for the 26 September 2019 Silivri earthquake by ELER, (ELER, 2010). On the left: distribution of slightly damaged buildings (about 5,000 in total); on the right: distribution of moderately damaged buildings (about 800 in total). Number of heavily damaged buildings are estimated about 60.

2019 (DASK, 2019a). Therefore we can estimate that the total number of damages were somewhere between 4,627 – 5,820. As the damage states were not disclosed, this number includes all types and is in close agreement with the damage figures by ELER, which was about 5,860 for all damage types. It would be reasonable to expect that the internal distribution is close to ELER estimations with slight damages dominating. The geographical distribution of damages was not disclosed as well, but we can expect that it would be very close to that of ELER (Figure 4.22).

4.3. Stochastic Simulation of the 17 August 1999 Mw 7.4 Kocaeli Earthquake

In this section, we aimed to test our stochastic simulation model developed by using the September 26, 2019 Silivri earthquake on a Marmara region earthquake with magnitude larger than 7. In this complementary work, we simulated the 17 August 1999 Mw 7.4 Kocaeli, Marmara earthquake using our parameters.

Previously, Yalçınkaya et al., (2012) generated a suitable stochastic model by performing EXSIM12 for the 1999 Kocaeli earthquake. Yalçınkaya et al., (2012) (from now on called Yalçınkaya) evaluated the performance of the model by using six different, already available rupture models and they compared the findings to their own model. They used random slip distribution generated by EXSIM12 and obtained satisfactory results when compared with those produced by using other rupture models, observing better estimations in some cases. For that reason, we will compare the performance of our model with the model constrained by Yalçınkaya.

Original recordings from 19 widely distributed stations of the 1999 earthquake were obtained from PEER NGA-West2 ground motion database. Table 4.6 lists locations, site classes and recorded PGA values of these stations. Figure 4.3 illustrates their spatial distributions and exemplifies the selected fault model.

Table 4.6: Station information of the 1999 Kocaeli earthquake (Repi is epicentral distance; B, C, and D are NEHRP soil classes, GS is generic soil, and GR is generic rock).

Station name	**Station code**	**Lat**	**Long**	**Repi (km)**	**Site Class**	**PGA (H1) (cm/s^2)**	**PGA (H2) (cm/s^2)**
Darıca Arcelik	1148	40.8300	29.3600	50.6	GS	205.6	125.4
Atakoy	1149	40.9890	28.8490	96.5	D	95.7	163.1
Cekmece	1157	40.9700	28.7000	109.1	GS	170.2	131.2
Fatih	1160	41.0200	28.9500	89.4	D	173.1	157.1

Havaalanı DHM	1163	40.9820	28.8200	98.7	GS	87.1	77.3
Istanbul	1164	41.0810	29.0070	87.5	B	41.8	54.6
Maslak	1169	41.1040	29.0100	88.3	B	48.6	37.1
Mecidiyekoy	1170	41.0650	28.9900	88.1	B	51.4	63.9
Yarimca	1176	40.7630	29.7610	16.4	GS	226.0	293.7
Zeytinburnu	1177	40.9860	28.9080	91.7	D	109.5	112.6
Iznik Karayollari 147. Sube Sefligi	1612	40.4416	29.7169	40.3	D	126.9	90.5
Istanbul Merkez Bayindirlik Ve Iskan Mudurlugu	3401	41.0582	29.0095	86.3	GR	42.7	55.7
Istanbul K.Cekmece Nukleer Santral Binasi	3403	41.0265	28.7587	105.0	D	85.0	124.7
Kocaeli Merkez Meteoroloji Istasyon Mudurlugu	4101	40.7665	29.9172	3.4	B	227.4	160.9
Kocaeli Gebze Tubitak Marmara Arastirma Merkezi	4106	40.7863	29.4500	42.7	GR	138.6	240.7
Sakarya Merkez Bayindirlik Ve Iskan Mudurlugu	5401	40.7371	30.3801	35.9	C	363.8	363.8

Tekirdag Merkez Valilik Binasi	5902	40.9793	27.5150	206.7	C	33.4	31.8
Marmara Ereglisi Kaymakamlik Binasi	5903	40.9730	27.9503	170.3	GS	103.3	90.2
Düzce Merkez Meteoroloji	8101	40.8439	31.1481	100.9	D	360.0	318.0

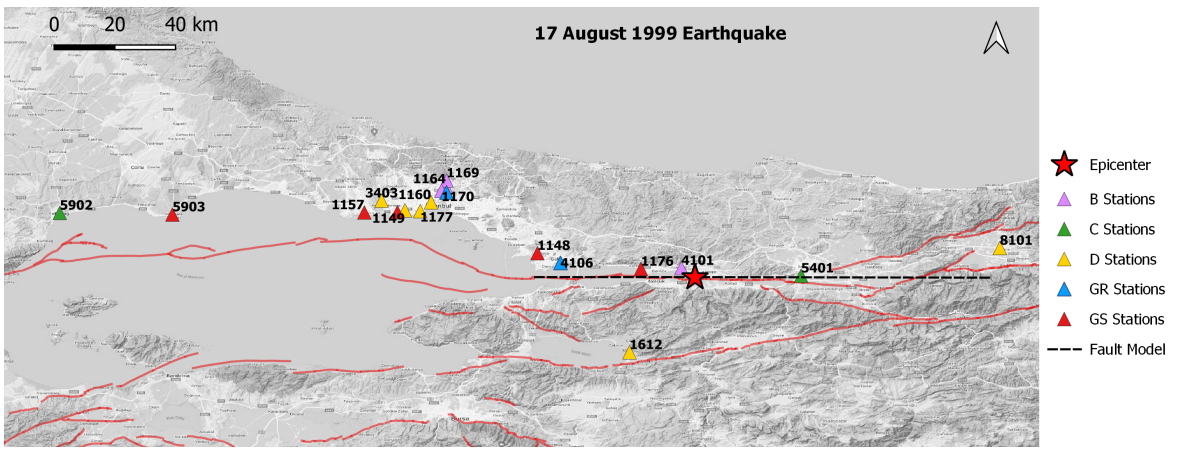

Figure 4.23. Locations of 19 stations and their site classes, shown as colored triangles. The red star represents the epicenter. Dashed line corresponds to used fault model in this study.

Table 4.7 lists a comparison of model parameters used in this study with those of Yalçınkaya. If a parameter was not specified in Yalçınkaya, it was left blank. We kept all parameters the same with the Silivri case in order to test our model in a larger earthquake. The only exception was the slip model. The slip model we adopted for the Silivri earthquake simulation was produced specifically for this particular earthquake.

Table 4.7: Input Model Parameters and Parameter Values Used in the Simulations of the 17 August 1999 Kocaeli Earthquake by EXSIM12.

Parameters	**Our Model**	**Yalçınkaya**

Epicenter	Latitude: 40.73, Longitude: 29.97	The same
Lat. and Lon. of upper edge of fault	Latitude: 40.73, Longitude: 31.11	The same
Moment magnitude	7.4	The same
Fault orientation (Strike/Dip)	270°/90°	The same
Fault depth to upper edge (km)	2.0	
Fault length and width (km)	150x20	The same
Hypocentral Depth (km)	17	The same
Sub-fault dimensions (km)	5x3	50x6
Stress drop (bar)	95	40
Rupture velocity (km/s)	0.8 x (shear wave velocity)	The same
Slip Distribution	Random	Random
Pulsing percentage Windowing-function	50 Saragoni-Hart	The same The same
Crustal density (g/cm3)	2.8	The same
Attenuation, Q(f)	$Q(f)=50f^{1.09}$, Horasan et al., (1998)	$Q(f)=180f^{0.45}$, Akinci et al., (2006)
Crustal shear wave velocity (km/s)	3.8	3.5
Geometric spreading	$1/R$ ($R \leq 30$ km) $1/R^{0.4}$ (30 km $<R<60$ km) $1/R^{0.6}$ (60 km $\leq R<90$ km) $1/R^{0.8}$ (90 km $\leq R<100$ km) $1/R^{0.5}$ ($R \geq 100$ km) Ansal et al., (2009)	$1/R$ ($R \leq 30$ km) $1/R^{0.75}$ (30 km $<R<100$ km) $1/R^{0.1}$ ($R \geq 100$ km)

Empirical Amplification	-	-
Duration Model	Boore and Thompson, (2014)	0.1*R
Site amplification	Generic Soil, Generic Rock, NEHRP D and C: Boore and Joyner, (1997) NEHRP B site class: Pischiutta et al., (2021)	Station dependent (H/V)
Crustal amplification	-	Margaris and Boore, 1998
Kappa Factor	Constant kappa parameters; Durukal and Çatalyürekli, (2004)	Station dependent

Figures 4.24 and 4.25 show three best- and three worst performing stations. Both groups are located in Istanbul region. The poorly performing stations are 1149 (Ataköy), 1160 (Fatih), and 1163 (Yeşilköy) which are located on soft soil and known for their high site amplification characteristics.

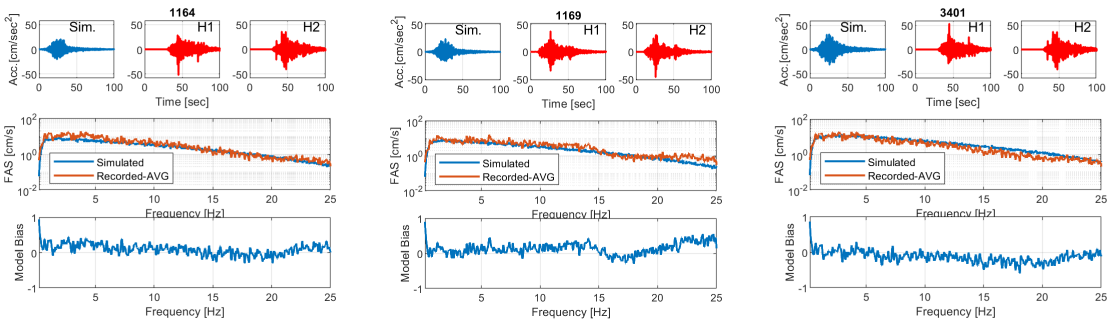

(a) (b) (c)

Figure 4.24. Comparison of acceleration-time histories and FAS of the simulated and recorded data for the best estimated stations.

Figure 4.26 demonstrates PGA comparison of simulated and recorded ground motions with two GMMs. After about 20 km distance, estimated PGAs generally

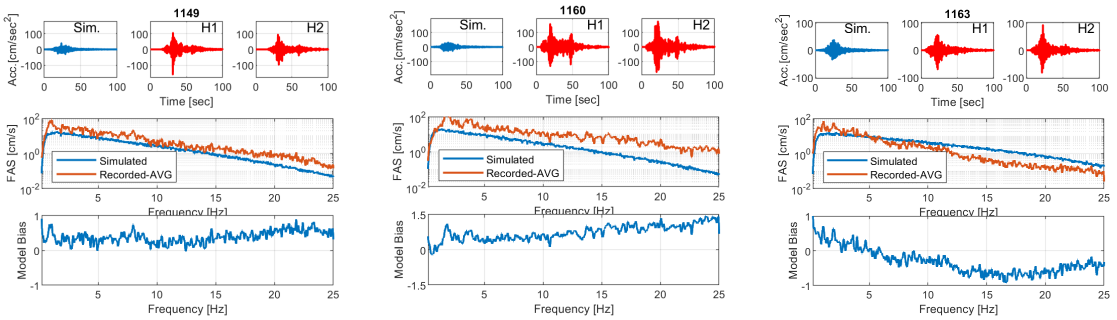

(a) (b) (c)

Figure 4.25. Comparison of acceleration-time histories and FAS of the simulated and recorded data for the worst estimated stations.

have become lower than those of recordings. This difference was more clear at larger distances and was independent of site class. A similar observation was also made by Yalçınkaya and they concluded that this earthquake can be characterized as a low PGA earthquake (Yalçınkaya et al., 2012). In our model, estimated PGAs were generally closer to the -SD lines of adopted GMMs with the exception of a few cases.

Figure 4.27 shows misfits for each station and average model bias over 19 stations. By looking at these figures, it can be noted that rock stations are modeled better than the soil stations. Although our model results in relatively larger misfits at higher frequencies, especially over 20Hz, overall all stations stayed $\pm$ 0.5 bounds.

In the next step, we compared the intensities as a further verification of the results. Intensity estimation for the synthetics and real recordings was performed on their FAS with the Sokolov method (Section 3.1.5). Figure 4.28 compares intensities estimated from synthetic and real records. In this figure the 45 degree line is shown in black, while the red dashed line represents the trend of our comparison. The proximity of the two lines allows us to check the performance of the model and the results. It can be observed that there is a general agreement between synthetic and real intensities. Synthetic intensities are lower than the real intensities by about 0.2-0.3 as indicated by the two trend lines, which is found reasonable. However there is a certain scatter in our results. In particular at stations 1148 (Darıca), 1157 (Çekmece) and 5903 (Tekirdağ) the discrepancy between the real and synthetic intensities is up to 2 intensity units.

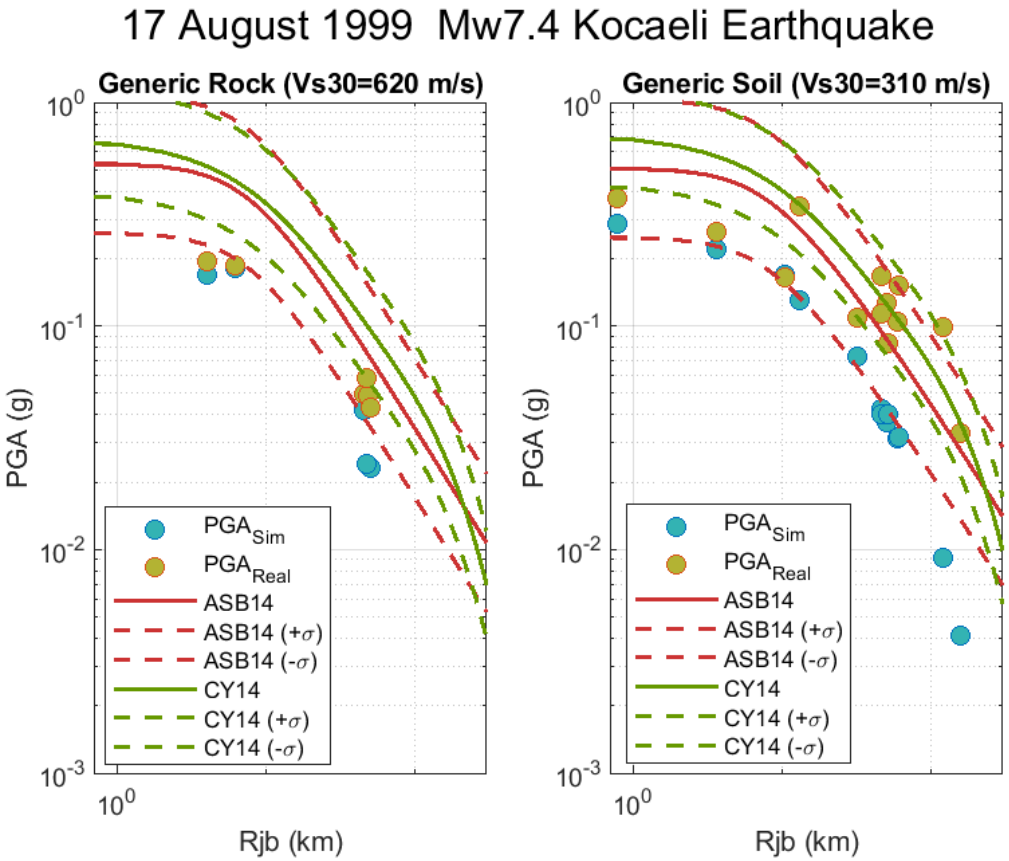

Figure 4.26. Comparison of the synthetic and recorded PGAs with Akkar et al., (2014), and Chiou and Youngs (2014).

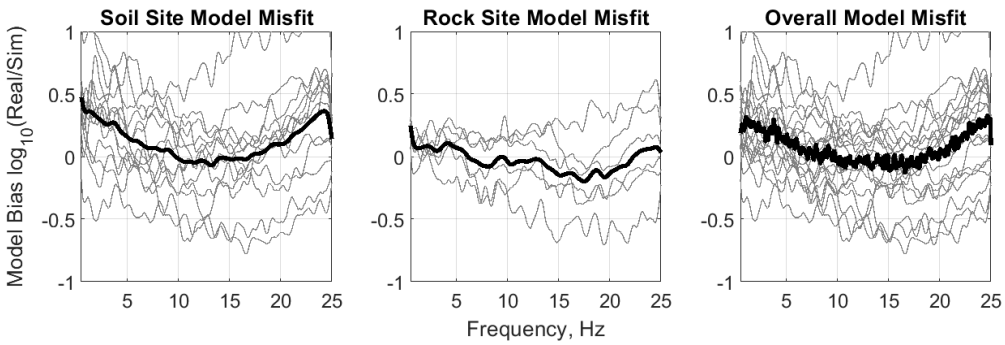

Figure 4.27. Averaged model misfit obtained from the error functions of 19 stations. Grey lines represent 19 stations while the bold black line corresponds to average misfit.

There are distant stations located at 90-170 epicentral distance. It was concluded that the model performed reasonably well, but at distances beyond about 90 km the findings need to evaluated with more caution.

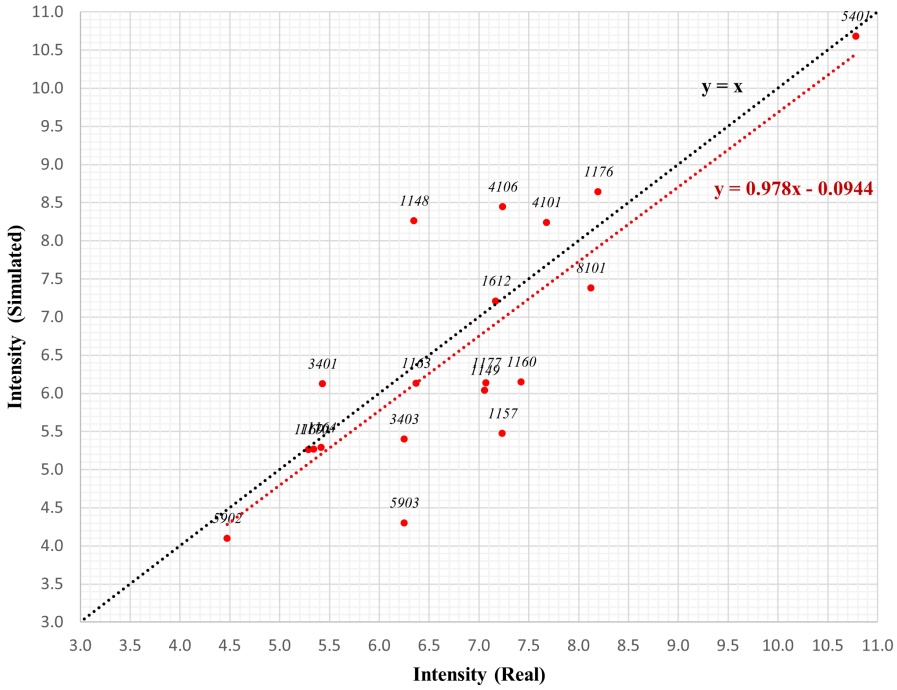

Figure 4.28. Comparison of intensities estimated from real (horizontal axis) and synthetic recordings (vertical axis) for the 1999 Kocaeli earthquake.

Lastly, we compared the performance of our model with the Yalçınkaya's. Figure 4.29 shows the comparison of two models in terms of model bias of 6 stations; 1148 (Darıca), 1164 (Istanbul), 4101 (Kocaeli), 4106 (Gebze), 5401 (Sakarya) and 8101 (Duzce). It should be pointed out that we did not run Yalçınkaya's model to make this comparison, but we digitized the random slip model bias figure given in their paper (Figure 5). The average model bias of our model is acceptably similar with Yalçınkaya's model, although the performance of individual stations differ for the two models. Our model yield relatively larger biases for these stations and they are not among of our best modeled stations.

4.4. Chapter Discussions

In this chapter, firstly, the 26 September 2019 Silivri earthquake (Mw 5.8) has been simulated with a commonly used technique,namely the stochastic finite fault approach. The synthetics were performed using the last version of EXSIM12 software. We utilized data from 59 widely distributed stations of the KOERI Earthquake Rapid Re-

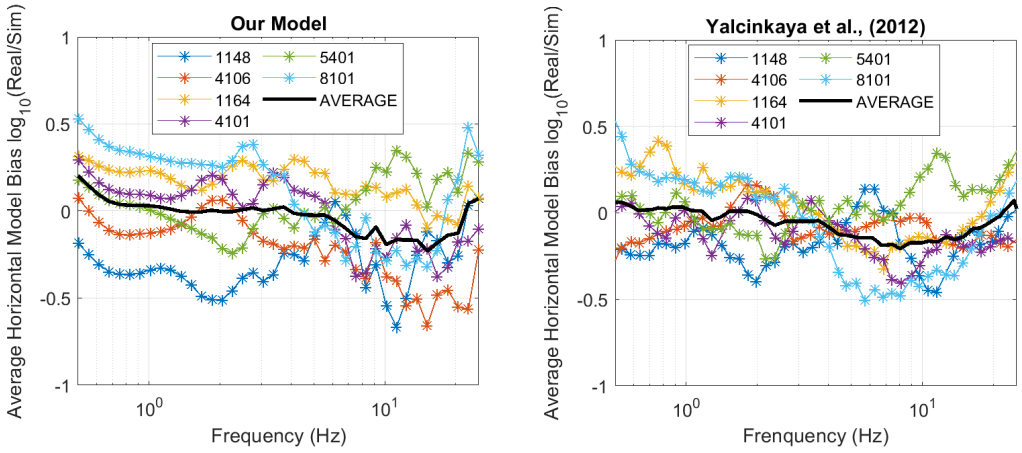

(a) (b)

Figure 4.29. Model misfit comparison with Yalçınkaya in terms of six stations and their average model bias.

sponse and Early Warning System network. We used an event-specific slip distribution model.

Required input parameters for path and site effects were obtained from previous studies. We have tried four different frequency dependent quality models in our simulations and compared them with recordings in frequency range. High consistency has been obtained with the Q model produced by Horasan et al., (1998). We employed different kappa selections as both a station specific and constant value and evaluated the effect. Comparison of the intensity values obtained from the geometric mean of the horizontal components of the recordings to the value of the synthetics, as well as an analysis of the discrepancies with respect to epicentral distances and site classes did not yield any systematic trend, meaning that our model was successful to define path and site effects.

The validity of the method and the model calibration have been tested by comparing synthetic ground motions with the recordings. Error functions in the frequency domain remained within a ± 0.5 in log10 units or lower in many stations. Few stations were out of this range fluctuating between $\pm$ 0.6 and ± 1. Most probably unpredictable site properties and other uncertainties caused these local differences. Testing model biases for three randomly selected representative frequencies with respect to station

Vs30 values and epicentral distances revealed no dependency.

Furthermore, we checked simulated amplitudes against two NGA-West2 ground motion models, Akkar et al., (2014) and Chiou and Youngs (2014), all simulations remaining within ± 1 standard deviation bounds of the models.

The validated model parameters have been used to obtain spatial distributions of PGAs, PGVs, and SAs in Istanbul and Marmara Region, separately. Here we utilized two different soil classification maps, the Istanbul specific grid-based Vs30 distribution and an estimated Vs30 distribution from QTM maps in a larger area. Verified constant kappa values have been used for regional simulations with the created model. A comparison of the obtained regional PGAs with the available damage information after the earthquake yielded a reasonable geographic fit.

In Section 4.3, we aimed to test our model on larger Marmara earthquakes for validation of its abilities. For this purpose, we simulated the 17 August 1999 Mw 7.4 Kocaeli earthquake. In this complementary case, we kept all the parameters the same excluding the earthquake source parameters. We used recordings from 19 widely distributed regional stations. Our findings were validated with the recordings in terms of time histories and in frequency domain. We compared our estimations with the Yalçınkaya et al., (2012) over six stations. There were some discrepancies, however the two models compared reasonably well, yielding results in similar bias ranges. The results from all the stations are included in Appendix B.

Overall, the model misfit calculations have resulted in an acceptable error range for the moderate and large earthquakes we selected for use. With this study, we improved the model created by Zengin and Çaktı (2012) for stochastic simulation in Istanbul by suggesting a different attenuation model and a duration model. By this change, the model became more suitable for varying site classes and kappa values in the wider region and we have obtained reasonable source, path, and site model datasets for future ground motion simulations in the region.

5. GROUND MOTION SIMULATION FOR THE 1894, 1766 and 1509 EARTHQUAKES

We followed a simulation strategy similar to 26 September 2019 Silivri and the 17 August 1999 earthquakes, as discussed in detail in Section, in generating he synthetics for the historical earthquakes 4.2 and 4.3.

For the historical earthquakes, the associated fault was determined by using the Boxer code as we described earlier. Strike and dip angles were obtained from MTA. Since EXSIM12 uses a simplified version of the fault, in case of deflection in the fault direction (like Çınarcık Fault and CMF), we defined an approximate strike angle that represents the real fault orientation as much as possible. For the rupture length, initially Boxer estimation was used if the segment is sufficiently long. Because the magnitude versus rupture length model of Wells and Coppersmith (1994) used by BOXER is rather outdated, magnitude - fault dimension relations defined by Leonard (2010) have been evaluated as well. The upper bound of rupture area was controlled by the geometry of the segments. Because hypocenters have depths around 10 km in the Sea of Marmara (Maede et al., 2002; Engintav et al., 2007), rupture width was kept as 10 km. The upper edge of the fault started at 2 km below ground surface.

We performed stochastic simulations by changing only one parameter incrementally in each run. After obtaining the best value for a parameter, which provides the lowest RMSE in our comparison, we moved on to the next parameter and repeated the same process. At the end, we estimated the most suitable epicenter, magnitude, rupture length and stress drop for each scenario. This approach allowed us to assess the influence of each variable independently.

Even though several studies provide equations between seismic moment (or magnitude) and stress drop, a stress drop correlation for the Marmara region does not exist. Köseoğlu et al., (2014) studied 174 small to moderate regional earthquakes from

the western part of Turkey including the Marmara Region and estimated stress drops to range between 0.017 bar and 647.6 bar. Parolai et al., (2017) used 523 aftershock recordings ($0.5 < ML < 5.9$) of the 1999 Kocaeli earthquake and estimated stress drops as varying between 0.02 bar and 400 bar. Irmak et al., (2020) investigated source parameters by using 77 small to moderate earthquakes that occurred in the Marmara Region and found no clear dependence between seismic moment and stress drop. They used broadband regional recordings of $3.5 < ML < 5.2$ earthquakes. Estimated stress drops were in a range of 1-1360 bar. These studies considered only small to moderate events due to lack of large magnitude data. We have varied magnitude and stress drop in a wide range by increasing them incrementally. We didn't define any lower bound, because our simulations provided a better match with the actual value at a higher magnitude and stress drop. Their upper bound was determined when the estimated intensity at any point exceeds the value of I_0.

The remaining parameter values were the same as with the Silivri earthquake simulation input set. As an example, input parameters to simulate the 1894 earthquake along the PIS were tabulated in Table 5.1. For other scenarios of this earthquake and for the other historical earthquakes, all parameters were kept the same excluding the strike and dip angle, upper edge of fault, epicentral location and fault dimensions.

We evaluated the scenarios by comparing the synthetics to the observations in terms of their intensities. As discussed earlier, observed damage information was converted to corresponding intensities by following the definitions given in EMS-98, while intensities of the synthetics have been estimated with the Sokolov method which uses FAS of synthetic recordings. A comparison of the forecast intensity with its actual value was done by using root-mean-square error (RMSE) for each intensity point. In order to see the performance of the simulation input set in different geographical areas, we categorized the overall RMSEs in terms of their spatial distribution and calculated their average RMSE (RMSE_R). This allows us to assess errors and/or best estimations in different zones separately.

We started our analysis with the 1894 event since we have relatively more damage

information for this particular earthquake. Also, the pictures taken after the event provided us a better understanding of the strength of shaking and an opportunity for the evaluation of repetitive expressions in the sources. A similar approach was followed for the 1766 and 1509 earthquakes as well.

5.1. 10 July 1894 Earthquake

Input parameters used in the simulation of the 1894 earthquake were listed in Table 5.1. For the 1894 earthquake, we defined eight different zones as represented in Figure 5.1. Intensity distribution indicated that this earthquake could be associated with either the PIS or the Izmit Segment (Figures 3.11 and 5.2). For that reason, we started our simulations with the PIS. To determine the epicenter, we increased the its location by 3 km incrementally along the fault by starting at its northwest edge (Marked as S1 in Figure 5.2a). We tried 17 scenarios up until the endpoint of the segment. In this initial simulation set, we kept magnitude, stress drop, and all other parameters the same, except epicentral location. Table 5.2 lists intensity comparison results over different epicentral locations in terms of their RMSEs for a magnitude of Mw 7.0, 90 bar stress drop and 5 km seismological depth. The best estimations in many regions were obtained when the epicenter was 21-24 km away from the northwest corner of the segment. Besides, the lowest regional RMSE was obtained when the epicenter was at the midpoint of the segment. Also near its southeast edge which represented with S3 in Figure 5.2a, provided lower errors. For that reason, we moved on to further simulations by constraining epicenter locations to these two points, S2 and S3.

In order to assess the upper limits of magnitude and stress drop, we started with the constant stress drop as 90 bar and increased only earthquake magnitude for an epicenter located 22 km away from the northwest corner. The findings were listed in Table 5.3. In this evaluation, we obserded that our S2 better estimations at higher magnitudes. Then, we kept the magnitude the same (Mw 7.0) and changed only the stress drop. Resulting RMSEs are given in Table 5.4. The RMSE scatter plot for eight different regions is shown in Figure 5.3. We noticed that while the stress drop increased, the difference between the estimated and actual intensities decreased. In other words,

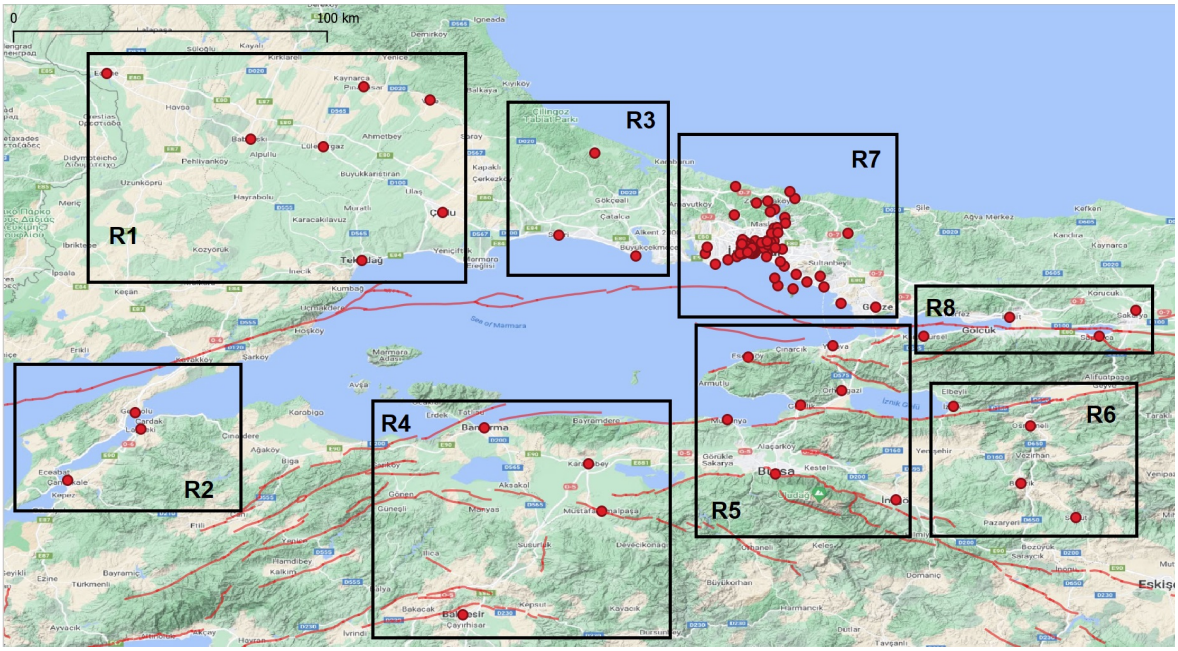

Figure 5.1. RMSE Regions of the 1894 Earthquake

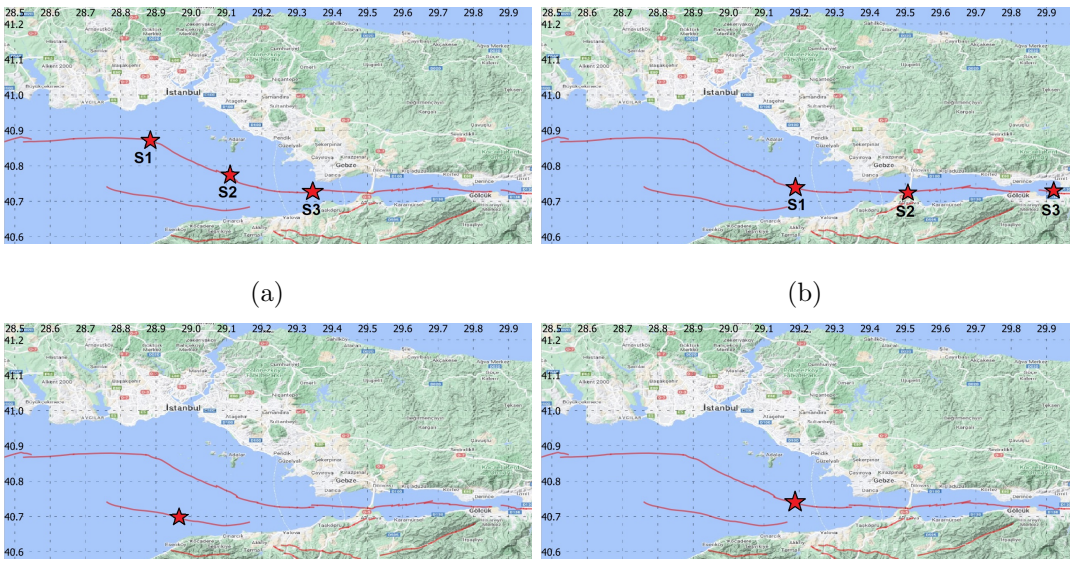

(a) (b)

(c) (d)

Figure 5.2. Representation of estimated epicenter locations for the 1894 Earthquake (a) the PIS (b) Izmit Segment (c) Çınarcık Fault (d) Combined Rupture Scenario

lower RMSEs were associated with higher stress drops and larger magnitudes. We set intensity upper bound as the value at which estimated intensity of any point becomes equal and higher than I=X since the maximum intensity is estimated as Io=IX for this

event and we judged higher intensities as unrealistic. With this approach, we started to change both magnitude and stress drop at the same time until lowest errors were found. These results were listed in Table 5.5 and also illustrated in Figure 5.4.

Table 5.1. Input model parameters Used in the Simulation of the 10 July 1894 Earthquake

Parameters	**Parameter Value**
Event	The 10 July 1894
Lat. and Lon. of upper edge of fault	40.874, 28.873
Moment magnitude	Mw 6.7-7.4
Fault orientation (Strike/Dip)	120°/70°
Depth of fault upper edge (km)	2.0
Fault length and width (km)	42x10
Sub-fault dimensions (km)	5x3
Stress drop (bar)	Increased incrementally
Rupture velocity (km/s)	0.8 x (shear wave velocity)
Slip Distribution	Random Slip RupGEN
Pulsing percentage	50
Windowing-function	Saragoni-Hart
Crustal density (g/cm3)	2.8
Attenuation, Q(f)	$Q(f) = 50f^{1.09}$, Horasan et al., (1998)
Crustal shear wave velocity (km/s)	3.8
Geometric spreading	Ansal et al., (2009)
Empirical Amplification	-
Duration Model	Boore and Thompson, (2014)
Site amplification	Boore and Joyner, (1997) Pischiutta et al., (2021)
Crustal amplification	-
Kappa Factor	Durukal and Çatalyürekli, (2004)

Table 5.2. The 1894 Earthquake Epicenter Assessment Along the PIS

Fault	Mw	Epicenter	Depth (km)	$\Delta\sigma$ (bar)	RMSE	R1	R2	R3	R4	R5	R6	R7	R8	RMSE_R
PIS	7	S1 0 km	5	90	0.9265	0.9429	0.3961	0.8517	0.5889	0.7089	0.5285	0.7607	3.1520	1.2949
	7	S1 3 km	5	90	0.9142	0.9413	0.3964	0.8601	0.6016	0.7093	0.5367	0.7614	3.0220	1.2574
	7	S1 6 km	5	90	0.9212	0.9424	0.3964	0.8642	0.6115	0.7073	0.5345	0.7724	3.0194	1.2582
	7	S1 9 km	5	90	0.9212	0.9424	0.3964	0.8642	0.6115	0.7073	0.5345	0.7724	3.0194	1.2582
	7	S1 12 km	5	90	0.9344	0.9436	0.3987	0.8604	0.6077	0.7258	0.5307	0.7705	3.1548	1.2997
	7	S1 15 km	5	90	0.9344	0.9436	0.3987	0.8604	0.6077	0.7258	0.5307	0.7705	3.1548	1.2997
	7	S1 18 km	5	90	0.9380	0.9424	0.3972	0.8756	0.5995	0.7048	0.5161	0.7762	3.1652	1.3017
	7	S1 21 km	5	90	0.9119	0.9455	0.3967	0.8606	0.6019	0.6902	0.5215	0.7588	3.0235	1.2560
	7	S1 22 km	5	90	0.9119	0.9455	0.3967	0.8606	0.6019	0.6902	0.5215	0.7588	3.0235	1.2560
	7	S1 23 km	5	90	0.9119	0.9455	0.3967	0.8606	0.6019	0.6902	0.5215	0.7588	3.0235	1.2560
	7	S1 24 km	5	90	0.9119	0.9455	0.3967	0.8606	0.6019	0.6902	0.5215	0.7588	3.0235	1.2560
	7	S1 27 km	5	90	0.9322	0.9480	0.3962	0.8485	0.5945	0.7263	0.5372	0.7697	3.1401	1.2941
	7	S1 30 km	5	90	0.9322	0.9480	0.3962	0.8485	0.5945	0.7263	0.5372	0.7697	3.1401	1.2941
	7	S1 33 km	5	90	0.9310	0.9465	0.3947	0.8649	0.6094	0.7121	0.5340	0.7654	3.1553	1.2993
	7	S1 36 km	5	90	0.9310	0.9465	0.3947	0.8649	0.6094	0.7121	0.5340	0.7654	3.1553	1.2993
	7	S1 39 km	5	90	0.9152	0.9431	0.3917	0.8412	0.5995	0.7016	0.5255	0.7637	3.0262	1.2559
	7	S1 42 km	5	90	0.9136	0.9414	0.3975	0.8563	0.6030	0.7144	0.5302	0.7608	3.0192	1.2563

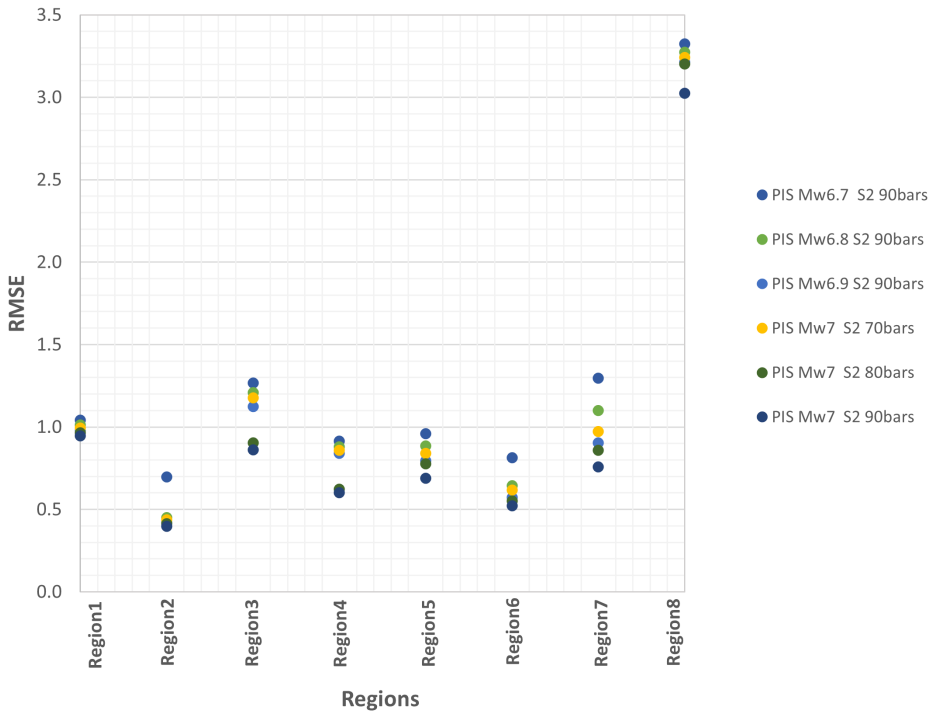

Figure 5.3. The 1894 Earthquake PIS S2 Scenario First Assessment

Table 5.3. The 1894 Earthquake Magnitude Assessment for S2 Scenario on the PIS

Fault	Mw	Epicenter	$\Delta\sigma$ (bar)	RMSE	R1	R2	R3	R4	R5	R6	R7	R8	RMSE_R	Comment
PIS	6.7	S2	90	1.3480	1.0414	0.6972	1.2664	0.9143	0.9598	0.8129	1.2960	3.3233	1.5131	-
	6.8	S2	90	1.1917	1.0111	0.4497	1.2077	0.8786	0.8846	0.6431	1.1005	3.2730	1.4394	-
	6.9	S2	90	1.0433	0.9789	0.4215	1.1241	0.8404	0.7953	0.5722	0.9038	3.2137	1.3789	-
	7	S2	90	0.9119	0.9455	0.3967	0.8606	0.6019	0.6902	0.5215	0.7588	3.0235	1.2560	-
	7.1	S2	90	0.8321	0.9141	0.3716	0.5841	0.5651	0.8537	0.5153	0.6630	2.8325	1.1774	Intensity > X

Table 5.4. The 1894 Earthquake Stress Drop Assessment for S2 Scenario on the PIS

Fault	Mw	Epicenter	$\Delta\sigma$ (bar)	RMSE	R1	R2	R3	R4	R5	R6	R7	R8	RMSE_R	Comment
PIS	7	S2	70	1.0961	0.9940	0.4360	1.1771	0.8586	0.8402	0.6185	0.9722	3.2427	1.4075	-
	7	S2	80	1.0001	0.9659	0.4133	0.9038	0.6237	0.7775	0.5515	0.8577	3.2007	1.3322	-
	7	S2	90	0.9119	0.9455	0.3967	0.8606	0.6019	0.6902	0.5215	0.7588	3.0235	1.2560	-
	7	S2	100	0.8744	0.9241	0.3829	0.8200	0.5896	0.9078	0.5200	0.7083	2.8881	1.2226	Intensity > X

Table 5.5. The 1894 Earthquake Magnitude Stress Assessment for S2 Scenario on the PIS

Fault	Mw	Epicenter	$\Delta\sigma$ (bar)	RMSE	R1	R2	R3	R4	R5	R6	R7	R8	RMSE_R	Comment
PIS	6.7	S2	140	0.9756	0.9572	0.4026	0.8753	0.6131	0.7494	0.5501	0.8263	3.1856	1.3189	-
	6.7	S2	150	0.9270	0.9483	0.3891	0.8651	0.5957	0.7336	0.5424	0.7794	3.0210	1.2609	-
	6.7	S2	160	0.8972	0.9372	0.3914	0.8282	0.5974	0.8868	0.5181	0.7408	2.9130	1.2330	Intensity > X
	6.8	S2	140	0.8667	0.9273	0.3860	0.8101	0.5824	0.7007	0.5223	0.7154	2.8698	1.1998	-
	6.8	S2	150	0.8280	0.9153	0.3753	0.7846	0.5731	0.5879	0.5112	0.6698	2.8323	1.1726	-
	6.8	S2	160	0.8161	0.9009	0.3645	0.5734	0.5653	0.8544	0.3078	0.6468	2.8122	1.1589	Intensity > X
	6.9	S2	100	0.9689	0.9605	0.4061	0.8905	0.6044	0.7381	0.5414	0.8177	3.1762	1.3153	-
	6.9	S2	110	0.9070	0.9447	0.3878	0.8348	0.6005	0.6947	0.5348	0.7533	3.0118	1.2504	-
	6.9	S2	120	0.8575	0.9225	0.3815	0.7972	0.5881	0.5952	0.5129	0.7058	2.8872	1.1953	Intensity > X
	7	S2	80	1.0001	0.9659	0.4133	0.9038	0.6237	0.7775	0.5515	0.8577	3.2007	1.3322	-
	7	S2	90	0.9119	0.9455	0.3967	0.8606	0.6019	0.6902	0.5215	0.7588	3.0235	1.2560	-
	7	S2	100	0.8744	0.9241	0.3829	0.8200	0.5896	0.9078	0.5200	0.7083	2.8881	1.2226	Intensity > X
	7.1	S2	70	0.9736	0.9620	0.4077	0.8831	0.6179	0.7572	0.5504	0.8219	3.1843	1.3203	-
	7.1	S2	80	0.8913	0.9344	0.3900	0.8276	0.5922	0.6077	0.5131	0.7368	3.0064	1.2387	-
	7.1	S2	90	0.8321	0.9141	0.3716	0.5841	0.5651	0.8537	0.5153	0.6630	2.8325	1.1774	Intensity > X
	7.2	S2	50	1.0899	0.9925	0.4221	1.1463	0.8501	0.8283	0.5686	0.9660	3.2376	1.3975	-
	7.2	S2	60	0.9692	0.9587	0.4039	0.8932	0.6138	0.7332	0.5455	0.8168	3.1850	1.3183	-
	7.2	S2	70	0.8776	0.9260	0.3839	0.8179	0.5855	0.6162	0.5153	0.7206	2.9772	1.2270	Intensity > X
	7.3	S2	60	0.8534	0.9216	0.3818	0.7886	0.5950	0.5957	0.5266	0.7033	2.8603	1.1874	-
	7.4	S2	50	0.8770	0.9287	0.3880	0.8099	0.5815	0.6884	0.5105	0.7178	2.9619	1.2262	-

In an attempt to assess the influence of hypocentral depth, we varied it up to 20 km. Even though the best fits, i.e. the lowest RMSEs were observed in the depth range of 7 km to 10 km, its effect was not significant. Findings are listed in Table 5.6. Since the hypocentral depth did not create an essential difference in the S3 scenario as well, we listed the findings only for the S2 and in the next steps kept it constant at 5 km.

The effect of slip distribution was also examined. EXSIM12 allows use of three different options: uniform slip, random slip and user defined slip. It internally produces a random slip model by distributing seismic moments on the sub-sources. In addition to random slip, we generated a synthetic slip distribution by running the MATLAB version of the RUPGEN tool, which produces a random slip distribution for assigned source

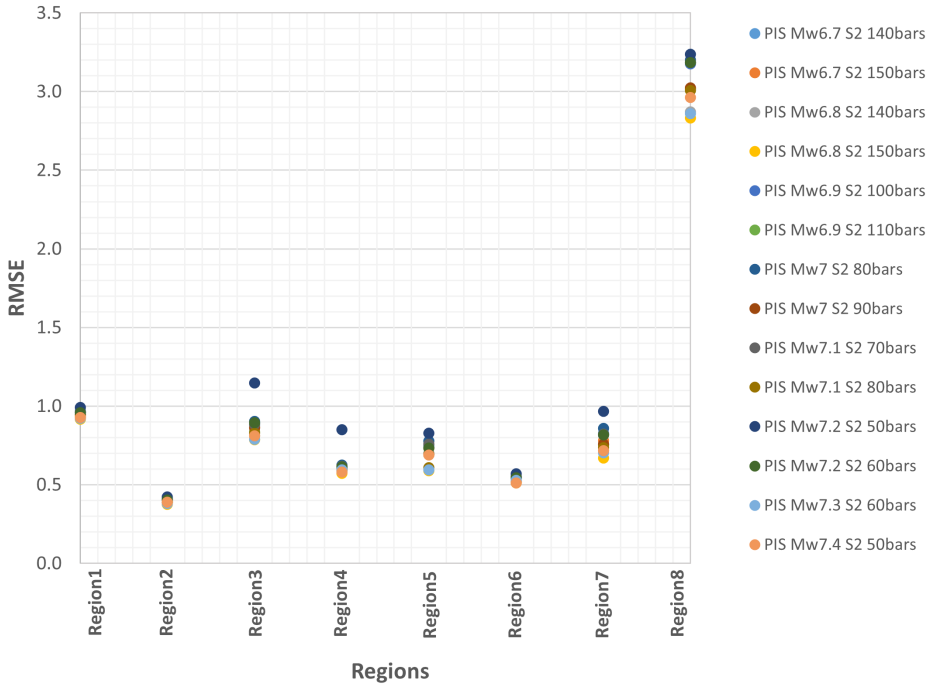

Figure 5.4. The 1894 Earthquake PIS S2 Scenario Magnitude and Stress Assessment

parameters (`http://equake-rc.info/cers-software/rupgen/`). We transformed slip distribution into a weighted form which is required by EXSIM12. The synthetic slip produced by RUPGEN for the PIS (L=42 km, W=10 km) is demonstrated in Figure 5.5. Even though specialized slip distribution performed better in some cases, EXSIM12's internal random slip option also performed well. Findings are listed in Table 5.7 and demonstrated in Figure 5.6 for the S2 scenario.

Table 5.6. The 1894 Earthquake Hypocentral Depth Assessment for the S2 Scenario on the PIS

Fault	Mw	Epicenter	Depth	$\Delta\sigma$ (bar)	RMSE	R1	R2	R3	R4	R5	R6	R7	R8	RMSE_R
PIS	7	S1	5	90	0.9119	0.9455	0.3967	0.8606	0.6019	0.6902	0.5215	0.7588	3.0235	1.2560
	7	S1	7	90	0.9315	0.9449	0.3867	0.8466	0.5994	0.7192	0.5429	0.7653	3.1635	1.3002
	7	S1	9	90	0.9417	0.9473	0.3898	0.8470	0.6091	0.9211	0.5494	0.7668	3.1579	1.3157
	7	S1	11	90	0.9417	0.9473	0.3898	0.8470	0.6091	0.9211	0.5494	0.7668	3.1579	1.3157
	7	S1	13	90	0.9358	0.9438	0.3956	0.8777	0.6109	0.7065	0.5356	0.7726	3.1583	1.3014
	7	S1	15	90	0.9358	0.9438	0.3956	0.8777	0.6109	0.7065	0.5356	0.7726	3.1583	1.3014
	7	S1	17	90	0.9381	0.9492	0.3984	0.8517	0.5979	0.7285	0.5312	0.7761	3.1562	1.3000

The best synthetic results were obtained from the S2 scenario earthquake with magnitude Mw=6.8 and 150 bar stress drop on the PIS.

We applied the same strategy for the S3 scenario, in which the epicenter is located

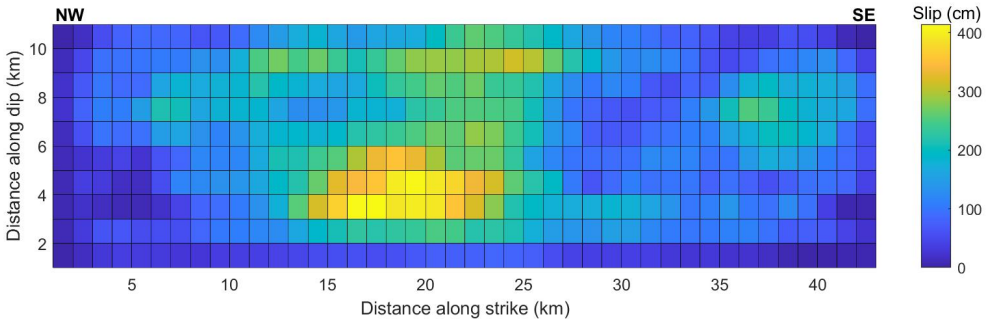

Figure 5.5. Slip distribution generated by RUPGEN along the PIS

Table 5.7. The 1894 Earthquake Slip Assessment for the S2 Scenario on the PIS

Fault	Mw	Epicenter	$\Delta\sigma$ (bar)	Slip	RMSE	R1	R2	R3	R4	R5	R6	R7	R8	RMSE_R	Comment
PIS	6.7	S2	150	Random	0.9270	0.9483	0.3891	0.8651	0.5957	0.7336	0.5424	0.7794	3.0210	1.2609	-
	6.7	S2	150	RupGEN	1.0565	0.9736	0.4144	1.1136	0.6128	0.7359	0.5299	0.9425	3.1676	1.3453	-
	6.8	S2	140	RupGEN	0.9481	0.9528	0.3912	0.8962	0.5929	0.6014	0.5101	0.8416	2.8631	1.2116	-
	6.8	S2	150	Random	0.8280	0.9153	0.3753	0.7846	0.5731	0.5879	0.5112	0.6698	2.8323	1.1726	-
	6.8	S2	150	RupGEN	0.9195	0.9412	0.3877	0.8604	0.5825	0.8622	0.3110	0.7901	2.8534	1.2105	Intensity > X
	6.9	S2	110	Random	0.9070	0.9447	0.3878	0.8348	0.6005	0.6947	0.5348	0.7533	3.0118	1.2504	-
	6.9	S2	110	RupGEN	1.0281	0.9660	0.3951	1.1011	0.5970	0.7055	0.5287	0.9064	3.1494	1.3311	-
	7	S2	90	Random	0.9119	0.9455	0.3967	0.8606	0.6019	0.6902	0.5215	0.7588	3.0235	1.2560	-
	7	S2	90	RupGEN	1.0333	0.9699	0.4053	0.9149	0.6187	0.7045	0.5275	0.9192	3.1508	1.3168	-
	7.1	S2	80	Random	0.8913	0.9344	0.3900	0.8276	0.5922	0.6077	0.5131	0.7368	3.0064	1.2387	-
	7.1	S2	80	RupGEN	0.9955	0.9613	0.3963	0.8995	0.5974	0.7074	0.5275	0.8840	3.0125	1.2690	-
	7.2	S2	60	Random	0.9692	0.9587	0.4039	0.8932	0.6138	0.7332	0.5455	0.8168	3.1850	1.3183	-
	7.2	S2	60	RupGEN	1.0921	0.9831	0.4148	1.1258	0.8219	0.7405	0.5331	0.9859	3.1745	1.3676	-

on the southeast edge of the Prince Island segment (Figure 5.2a). Table 5.8 lists RMSEs for different magnitude and stress drop combinations associated with the S3 scenario. Findings are also demonstrated in Figure 5.7.

In the S3 scenario, in addition to the former process we also tried to see the effect of different rupture lengths and widths on our results. Rupture length and width were estimated with the equation given by Leonard (2010). Rupture length was taken as up to 42 km which is the physical limit of the segment. Our results indicate that there is a significant correlation between magnitude, stress drop and rupture length. Findings are listed in Table 5.9 and also shown in Figure 5.8.

We tested the effect of slip distribution for the S3 scenario and noticed that scenarios with user defined slip distributions provided lower RMSEs. These findings are tabulated in Table 5.10 and represented in Figure 5.9.

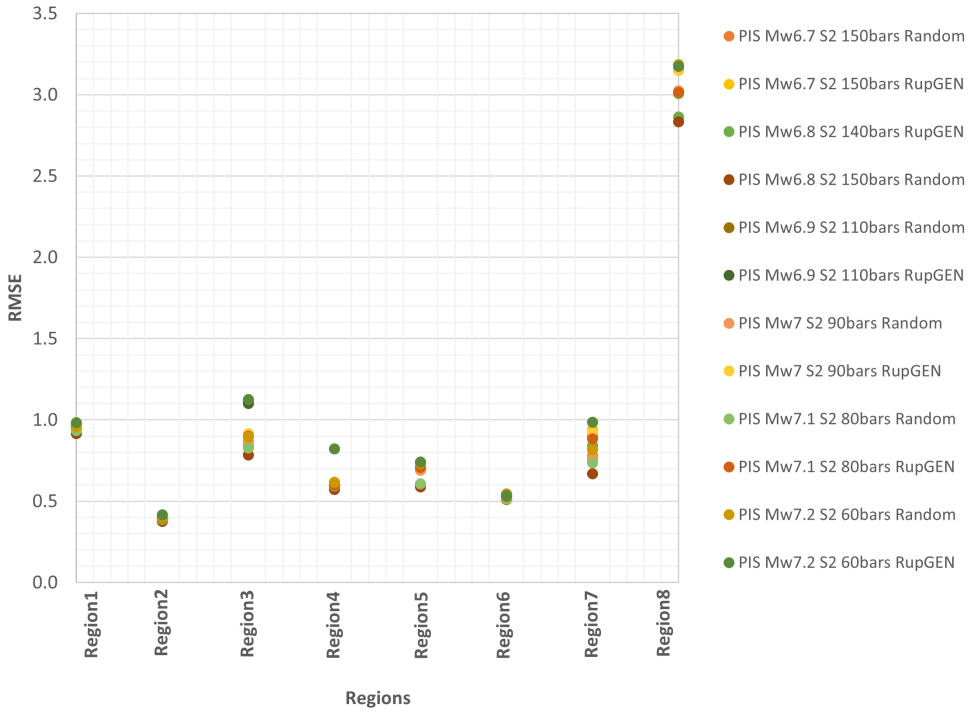

Figure 5.6. The 1894 Earthquake PIS S2 Scenario Slip Assessment

Table 5.8. The 1894 Earthquake Magnitude and Stress Drop Assessment for S3 Scenario on the PIS

Fault	Mw	Epicenter	$\Delta\sigma$ (bar)	RMSE	R1	R2	R3	R4	R5	R6	R7	RMSE_R	Comment
PIS	6.7	S3	140	0.9736	0.9555	0.4072	0.8840	0.6189	0.7678	0.5469	0.8222	1.3198	-
	6.7	S3	150	0.9178	0.9413	0.3940	0.8592	0.5945	0.7083	0.5290	0.7688	1.2546	-
	6.7	S3	160	0.8882	0.9290	0.3868	0.8255	0.5884	0.6816	0.5196	0.7308	1.2370	-
	6.7	S3	170	0.8571	0.9204	0.3858	0.6214	0.5764	0.8841	0.3017	0.7017	1.1816	Intensity > X
	6.8	S3	120	0.9558	0.9531	0.3974	0.8814	0.6187	0.7557	0.5225	0.7986	1.3106	-
	6.8	S3	130	0.9164	0.9349	0.3925	0.8418	0.6090	0.7029	0.5216	0.7474	1.2892	-
	6.8	S3	140	0.8673	0.9230	0.3815	0.8101	0.5931	0.8650	0.5121	0.7077	1.2056	Intensity > X
	6.9	S3	90	1.0366	0.9712	0.4122	0.9288	0.8400	0.7879	0.5616	0.9025	1.3570	-
	6.9	S3	100	0.9659	0.9555	0.4043	0.8872	0.5958	0.7562	0.5331	0.8137	1.3131	-
	6.9	S3	110	0.9132	0.9417	0.3915	0.8400	0.5935	0.9244	0.5121	0.7469	1.2667	Intensity > X
	7	S3	80	0.9997	0.9641	0.4097	0.9107	0.8298	0.7584	0.5510	0.8524	1.3425	-
	7	S3	90	0.9136	0.9414	0.3975	0.8563	0.6030	0.7144	0.5302	0.7608	1.2563	-
	7	S3	100	0.8617	0.9225	0.3813	0.7946	0.5932	0.8589	0.3064	0.7027	1.1980	Intensity > X
	7.1	S3	70	0.9739	0.9608	0.3998	0.8892	0.6075	0.9340	0.5498	0.8104	1.3321	Intensity > X
	7.1	S3	80	0.8895	0.9384	0.3853	0.8200	0.5807	0.6948	0.5205	0.7292	1.2422	-
	7.1	S3	90	0.8325	0.9095	0.3726	0.7861	0.5644	0.8702	0.3025	0.6614	1.1840	Intensity > X
	7.2	S3	50	1.0916	0.9874	0.4286	1.1516	0.8494	0.8292	0.5712	0.9673	1.4009	-
	7.2	S3	60	0.9631	0.9566	0.4051	0.8956	0.6086	0.7611	0.5434	0.8083	1.3144	-
	7.2	S3	70	0.8754	0.9308	0.3896	0.7963	0.5801	0.8545	0.5200	0.7135	1.2189	Intensity > X
	7.3	S3	60	0.8669	0.9251	0.3812	0.8009	0.5742	0.8910	0.5189	0.6983	1.2188	Intensity > X
	7.3	S3	50	0.9664	0.9589	0.4038	0.8943	0.6104	0.7346	0.5414	0.8128	1.3174	-
	7.4	S3	50	0.8588	0.9240	0.3820	0.8183	0.5853	0.6145	0.5194	0.7099	1.1912	-

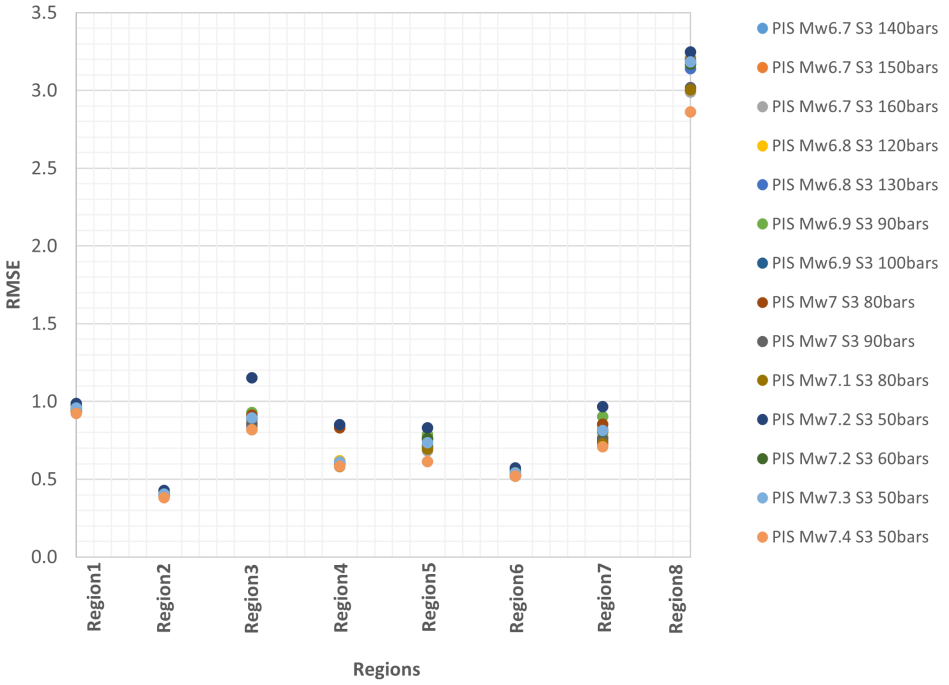

Figure 5.7. The 1894 Earthquake PIS S3 Scenario Magnitude and Stress Assessment

Table 5.9. The 1894 Earthquake Different Rupture Dimensions for S3 Scenario on the PIS

Fault	Mag.	Epicenter	L(km) x W(km)	$\Delta\sigma$ (bar)	RMSE	R1	R2	R3	R4	R5	R6	R7	R8	RMSE_R	Comment
PIS	6.7	S3	33x17	160	0.9444	0.9045	0.3748	0.6105	0.5758	0.9180	0.5588	0.7742	3.2077	1.3089	-
	6.7	S3	42 x10	160	0.8882	0.9290	0.3868	0.8255	0.5884	0.6816	0.5196	0.7308	2.9887	1.2370	-
	6.7	S3	33 x17	170	0.9169	0.8937	0.3653	0.5017	0.5823	0.8788	0.5472	0.7415	3.1797	1.2872	-
	6.7	S3	42x20	170	0.8982	0.9147	0.3690	0.7896	0.5659	0.5808	0.3162	0.7616	2.9819	1.2158	-
	6.7	S3	42x10	170	0.8571	0.9204	0.3858	0.6214	0.5764	0.8841	0.3017	0.7017	2.8442	1.1816	Intensity > X
	6.8	S3	38x19	130	0.9611	0.9253	0.3784	0.8258	0.5831	0.6810	0.5299	0.8172	3.1644	1.2965	-
	6.8	S3	42x10	130	0.9164	0.9349	0.3925	0.8418	0.6090	0.7029	0.5216	0.7474	3.1405	1.2892	-
	6.8	S3	38x19	140	0.9021	0.9108	0.3724	0.6291	0.5711	0.5873	0.5230	0.7634	3.0055	1.2209	-
	6.8	S3	42x20	140	0.9191	0.9203	0.3748	0.8111	0.5632	0.5797	0.5175	0.7863	2.9943	1.2324	-
	6.8	S3	42x10	140	0.8673	0.9230	0.3815	0.8101	0.5931	0.8650	0.5121	0.7077	2.8480	1.2056	Intensity > X
	6.9	S3	42x10	100	1.0294	0.9509	0.3993	0.8728	0.5866	0.7785	0.5378	0.9076	3.1852	1.3245	-
	6.9	S3	42x10	100	0.9659	0.9555	0.4043	0.8872	0.5958	0.7562	0.5331	0.8137	3.1713	1.3131	-
	6.9	S3	42x10	110	0.9647	0.9340	0.3887	0.8496	0.5795	0.7066	0.5220	0.8413	3.0214	1.2595	-
	6.9	S3	42x10	110	0.9132	0.9417	0.3915	0.8400	0.5935	0.9244	0.5121	0.7469	3.0106	1.2667	Intensity > X
	7	S3	42x22	90	1.0093	0.9367	0.3829	0.8535	0.5751	0.6974	0.5438	0.8859	3.1749	1.3101	-
	7	S3	42x10	90	0.9136	0.9414	0.3975	0.8563	0.6030	0.7144	0.5302	0.7608	3.0192	1.2563	-
	7	S3	42x22	100	0.9232	0.9147	0.3730	0.7934	0.5710	0.6211	0.5172	0.7945	2.9716	1.2271	-
	7	S3	42x20	100	0.9019	0.9228	0.3774	0.6318	0.5721	0.5851	0.5141	0.7791	2.8965	1.1897	-
	7	S3	42x10	100	0.8617	0.9225	0.3813	0.7946	0.5932	0.8589	0.3064	0.7027	2.8594	1.1980	Intensity > X
	7.1	S3	42x24	80	0.9788	0.9253	0.3779	0.8209	0.5793	0.6658	0.5211	0.8443	3.1725	1.2991	-
	7.1	S3	42x10	80	0.8895	0.9384	0.3853	0.8200	0.5807	0.6948	0.5205	0.7292	3.0033	1.2422	-
	7.1	S3	42x24	90	0.9026	0.9045	0.3643	0.6173	0.5568	0.6125	0.5096	0.7663	2.9951	1.2163	-
	7.1	S3	42x20	90	0.8635	0.9003	0.3700	0.5977	0.5636	0.5542	0.3097	0.7383	2.8399	1.1530	-
	7.1	S3	42x10	90	0.8325	0.9095	0.3726	0.7861	0.5644	0.8702	0.3025	0.6614	2.8329	1.1840	Intensity > X

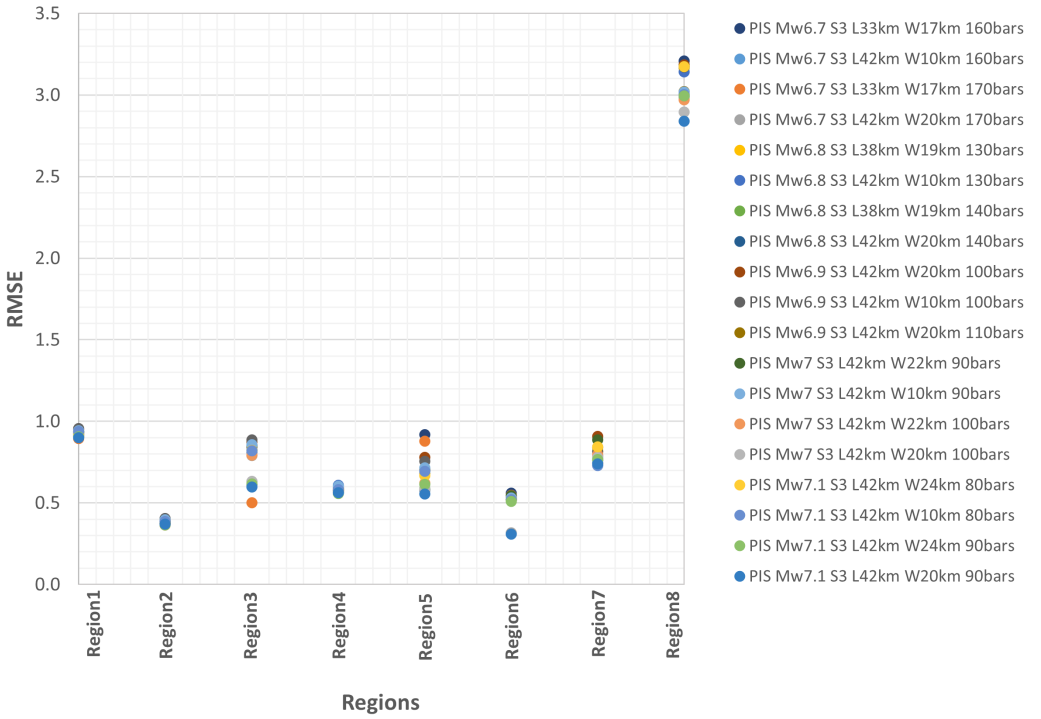

Figure 5.8. The 1894 Earthquake PIS S3 Different Rupture Dimensions

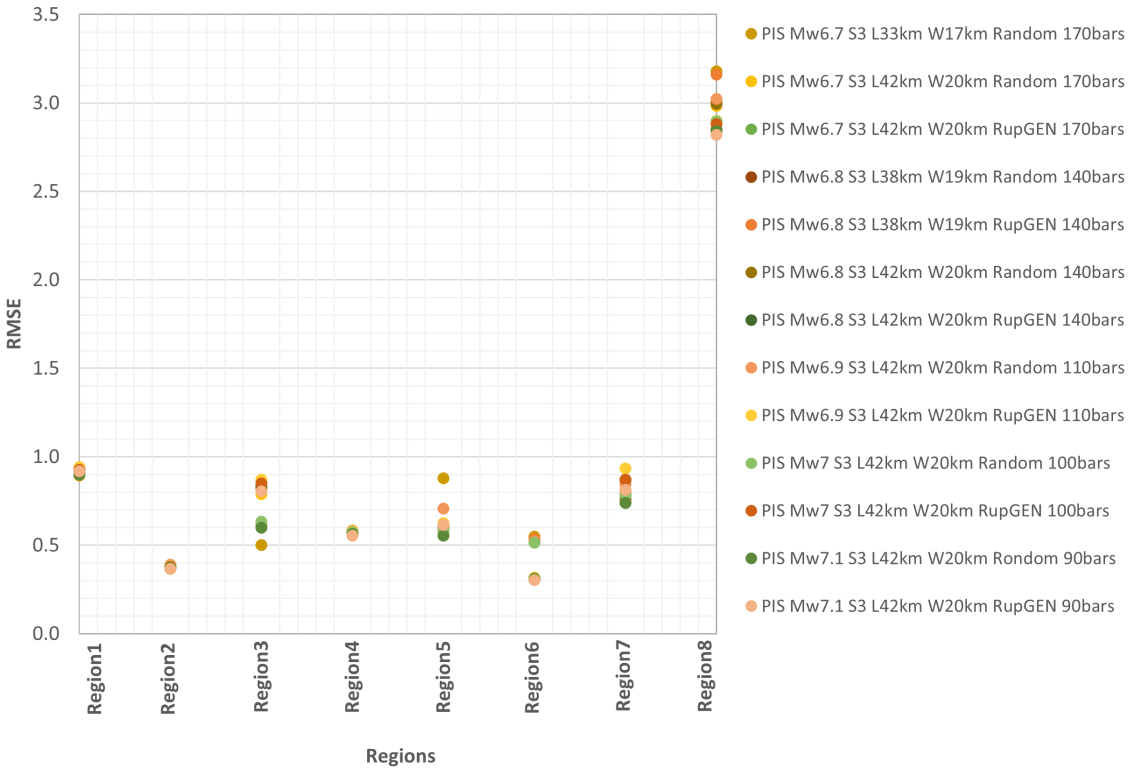

Figure 5.9. The 1894 Earthquake PIS S3 Slip Assessment

Table 5.10. The 1894 Earthquake Slip Assessment for S3 Scenario on the PIS

Fault	Mw	Epicenter	L(km) x W(km)	Slip	$\Delta\sigma$ (bar)	RMSE	R1	R2	R3	R4	R5	R6	R7	R8	RMSE_R	Comment
PIS	6.7	S3	33x17	Random	170	0.9169	0.8937	0.3653	0.5017	0.5823	0.8788	0.5472	0.7415	3.1797	1.2872	-
	6.7	S3	33x17	RupGEN	170	0.8623	0.9057	0.3684	0.5958	0.5756	0.6696	0.5410	0.6682	3.1591	1.2654	Intensity > X
	6.7	S3	42x20	Random	170	0.8982	0.9147	0.3690	0.7896	0.5659	0.5808	0.3162	0.7616	2.9819	1.2158	-
	6.7	S3	42x20	RupGEN	170	0.9545	0.9248	0.3757	0.8301	0.5618	0.6020	0.3088	0.8626	2.8435	1.1879	-
	6.8	S3	38x19	Random	140	0.9021	0.9108	0.3724	0.6291	0.5711	0.5873	0.5230	0.7634	3.0055	1.2209	-
	6.8	S3	38x19	RupGEN	140	0.9468	0.9058	0.3691	0.6085	0.5769	0.6127	0.5355	0.8072	3.1595	1.2726	-
	6.8	S3	42x20	Random	140	0.9191	0.9203	0.3748	0.8111	0.5632	0.5797	0.5175	0.7863	2.9943	1.2324	-
	6.8	S3	42x20	RupGEN	140	0.9613	0.9285	0.3786	0.8299	0.5648	0.6095	0.3062	0.8711	2.8487	1.1912	-
	6.9	S3	42x20	Random	110	0.9647	0.9340	0.3887	0.8496	0.5795	0.7066	0.5220	0.8413	3.0214	1.2595	-
	6.9	S3	42x20	RupGEN	110	1.0114	0.9418	0.3801	0.8692	0.5769	0.6245	0.3043	0.9332	2.8986	1.2183	-
	7.0	S3	42x20	Random	100	0.9019	0.9228	0.3774	0.6318	0.5721	0.5851	0.5141	0.7791	2.8965	1.1897	-
	7.0	S3	42x20	RupGEN	100	0.9632	0.9256	0.3755	0.8485	0.5622	0.6137	0.3067	0.8694	2.8793	1.2016	-
	7.1	S3	42x20	Rondom	90	0.8635	0.9003	0.3700	0.5977	0.5636	0.5542	0.3097	0.7383	2.8399	1.1530	-
	7.1	S3	42x20	RupGEN	90	0.9166	0.9180	0.3659	0.8044	0.5543	0.6137	0.3026	0.8116	2.8190	1.1729	-

According to these evaluations, for the S3 scenario on the PIS, Mw 7.4 and stress drop 50 bar provided lowest errors. Mw 6.7 and 160 bar stress drop resulted in low RMSEs as well.

For the Izmit segment, we have evaluated three different scenarios by changing epicentral location; S1 and S3 are for an epicenter located on the two edges of the segment (60 km total distance), S2 is for an epicenter located in between S1 and S3, 27 km away from the western edge (Figure 5.2b).

For the Izmit segment, we followed the same steps as we did with the Prince Islands. We started our assessments by changing magnitude and stress drop at three different epicentral locations. Results were tabulated in Table 5.11 and Figure 5.10 illustrates their RMSEs. In this first simulation set on the Izmit segment, we noticed that even though these scenarios provided better estimations for Region 8 (includes, Adapazari, Karamursel, Sapanca and Izmit), forecasts were underestimated for Istanbul (Region 7) which is an essential region in our evaluation and where more intensity points were available compared to to other regions. Since Scenario S1 provided lower errors in Region 7, we decided to consider only Scenario S1 for the next steps.

In the next step, we changed the rupture length and width as we did for the PIS. These findings are listed in Table 5.12 and RMSE distributions over the regions are demonstrated in Figure 5.11. According to this Table, magnitude Mw 7.1-7.2 and rupture length around 57-60 km provided better estimations. On the other hand,

Table 5.11. The 1894 Earthquake Magnitude, Stress Drop and Epicenter Assessment Along the Izmit Fault

Fault	Mw	Epicenter	L(km) x W(km)	$\Delta\sigma$ (bar)	RMSE	R1	R2	R3	R4	R5	R6	R7	R8	RMSE_R	Comment
	6.8	S1	60x10	100	1.7256	1.2543	0.8370	1.8622	1.1739	1.3943	0.4935	1.8091	2.2036	1.4763	-
	6.8	S1	60x10	110	1.6231	1.2318	0.8116	1.8533	1.1476	1.3481	0.6777	1.6965	1.9785	1.4141	Intensity > X
	6.9	S1	60x10	90	1.6662	1.2436	0.8228	1.8606	1.1577	1.3660	0.4963	1.7479	1.9861	1.4203	Intensity > X
	6.9	S1	60x10	80	1.7741	1.2688	0.8452	1.8904	1.1754	1.4191	0.4727	1.8676	2.1852	1.4908	-
	7	S1	60x10	90	1.5520	1.2053	0.7768	1.8091	1.1270	1.2977	0.7325	1.5936	2.3435	1.4514	Intensity > X
	7	S1	60x10	80	1.5972	1.2320	0.8076	1.8457	1.1428	1.3370	0.6914	1.6644	1.9866	1.4082	-
	7.1	S1	60x10	60	1.7067	1.2549	0.8281	1.8746	1.1727	1.3885	0.4846	1.7861	2.1911	1.4707	-
	7.1	S1	60x10	70	1.5787	1.2241	0.7968	1.8250	1.1414	1.3315	0.7013	1.6430	1.9798	1.3987	Intensity > X
	7.2	S1	60x10	50	1.7246	1.2543	0.8282	1.8799	1.1761	1.3957	0.4723	1.8084	2.1846	1.4744	-
	7.2	S1	60x10	60	1.5636	1.2186	0.7924	1.8185	1.1357	1.3293	0.7082	1.6231	2.0159	1.3998	Intensity > X
	7.3	S1	60x10	50	1.5831	1.2223	0.7948	1.8349	1.1339	1.3352	0.7170	1.6468	2.0083	1.4063	Intensity > X
	7.3	S1	60x10	40	1.7711	1.2708	0.8461	1.8889	1.1801	1.4153	0.4670	1.8632	2.1997	1.4926	-
	7.4	S1	60x10	40	1.6200	1.2363	0.8073	1.8429	1.1556	1.3434	0.6807	1.6919	1.9941	1.4150	Intensity > X
	7.4	S1	60x10	30	1.9148	1.4346	0.8735	1.9098	1.1947	1.5207	0.4382	2.0265	2.2063	1.5562	-
	6.8	S2	60x10	110	1.6420	1.2430	0.8159	1.8506	1.1519	1.3642	0.6807	1.7070	2.2134	1.4620	-
	6.8	S2	60x10	120	1.5813	1.2204	0.7948	1.8281	1.1315	1.3231	0.7036	1.6282	2.3380	1.4623	Intensity > X
	6.9	S2	60x10	90	1.6622	1.2432	0.8190	1.8577	1.1615	1.3722	0.5150	1.7425	1.9843	1.4203	Intensity > X
	6.9	S2	60x10	80	1.7755	1.2697	0.8469	1.8909	1.1733	1.4229	0.4656	1.8690	2.1853	1.4913	-
	7	S2	60x10	70	1.7381	1.2587	0.8369	1.8762	1.1705	1.4039	0.4787	1.8236	2.2059	1.4818	-
	7	S2	60x10	80	1.6207	1.2372	0.8139	1.8425	1.1494	1.3578	0.6831	1.6920	1.9929	1.4166	Intensity > X
Izmit	7.1	S2	60x10	70	1.5824	1.2249	0.7975	1.8228	1.1457	1.3415	0.5264	1.6461	1.9982	1.3942	Intensity > X
	7.1	S2	60x10	60	1.7212	1.2598	0.8290	1.8712	1.1670	1.4016	0.4760	1.8033	2.1962	1.4750	-
	7.2	S2	60x10	60	1.5700	1.2188	0.7961	1.8198	1.1404	1.3345	0.7111	1.6314	1.9986	1.3997	Intensity > X
	7.2	S2	60x10	50	1.7378	1.2560	0.8361	1.8734	1.1733	1.3955	0.4848	1.8246	2.1888	1.4776	-
	7.3	S2	60x10	50	1.5718	1.2204	0.7963	1.8287	1.1476	1.3347	0.6947	1.6327	2.0074	1.4028	Intensity > X
	7.3	S2	60x10	40	1.7748	1.2713	0.8435	1.8839	1.1770	1.4245	0.4569	1.8677	2.1982	1.4925	-
	7.4	S2	60x10	40	1.6309	1.2314	0.8118	1.8393	1.1458	1.3504	0.6802	1.6965	2.1846	1.4495	Intensity > X
	7.4	S2	60x10	30	1.9268	1.4352	0.8724	1.9301	1.1940	1.5215	0.4320	2.0441	2.1257	1.5480	-
	6.8	S3	60x10	100	1.7174	1.2555	0.8296	1.8690	1.1607	1.4006	0.4909	1.7993	2.1902	1.4723	-
	6.8	S3	60x10	110	1.6181	1.2399	0.8136	1.8517	1.1425	1.3487	0.6954	1.6721	2.3225	1.4759	Intensity > X
	6.9	S3	60x10	100	1.5810	1.2201	0.7978	1.8159	1.1415	1.3255	0.7082	1.6461	1.9910	1.3990	Intensity > X
	6.9	S3	60x10	90	1.6497	1.2432	0.8192	1.8418	1.1586	1.3755	0.5014	1.7273	1.9870	1.4154	-
	7	S3	60x10	80	1.6043	1.2280	0.8039	1.8330	1.1442	1.3452	0.6962	1.6732	1.9896	1.4087	Intensity > X
	7	S3	60x10	70	1.7337	1.2568	0.8313	1.8728	1.1637	1.3930	0.4802	1.8195	2.1973	1.4766	-
	7.1	S3	60x10	60	1.7103	1.2570	0.8340	1.8665	1.1630	1.3965	0.4958	1.7912	2.1763	1.4685	-
	7.1	S3	60x10	70	1.5768	1.2239	0.7978	1.8312	1.1439	1.3409	0.7147	1.6392	1.9919	1.4036	Intensity > X
	7.2	S3	60x10	50	1.7130	1.2601	0.8264	1.8739	1.1717	1.3962	0.4730	1.7933	2.1945	1.4731	-
	7.2	S3	60x10	60	1.5665	1.2210	0.7985	1.8152	1.1269	1.3258	0.7201	1.6270	2.0132	1.3995	Intensity > X
	7.3	S3	60x10	50	1.5993	1.2250	0.7922	1.8406	1.1479	1.3595	0.6986	1.6758	1.7763	1.3754	-
	7.4	S3	60x10	40	1.6519	1.2383	0.8104	1.8539	1.1532	1.3731	0.5028	1.7380	1.8084	1.3868	-

findings were poor compared to those for the PIS scenarios. Besides giving higher RMSEs in Region 7, these scenarios were still not good enough to model the intensity definitions described in the damage sources.

In addition to the Prince Islands and Izmit segments, we evaluated Çınarcık Fault as well. It should be noted that historically no major earthquake was associated with this fault before. Furthermore the seismicity along this fault is relatively low in the instrumental period (Figure 1.1). Mw 6.3 Çınarcık earthquake of 1963 was the biggest

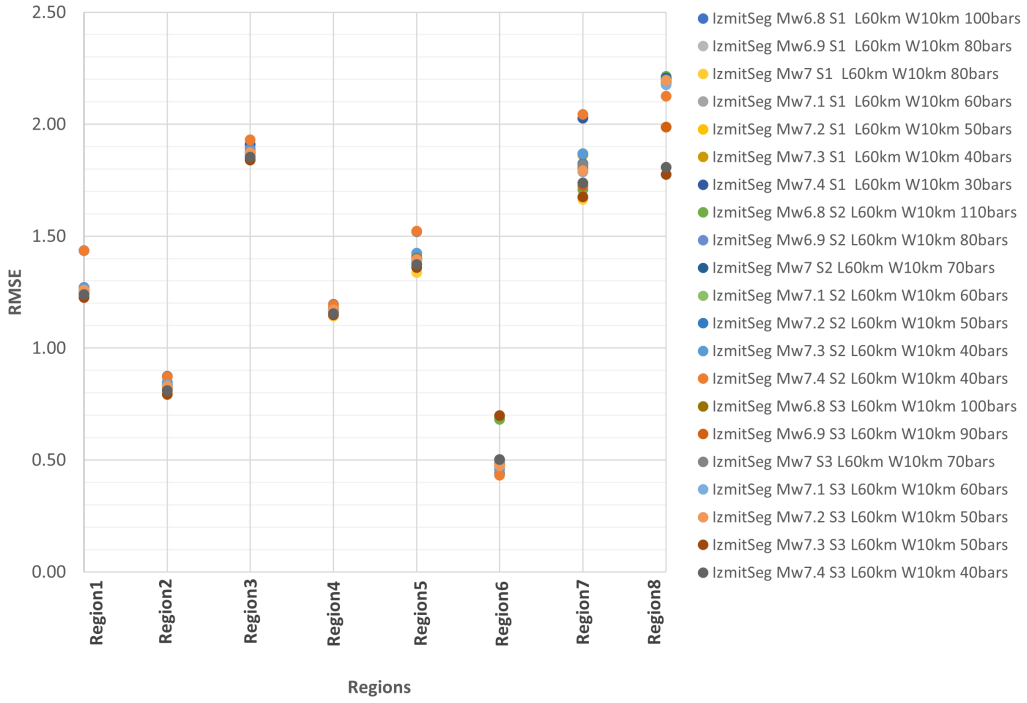

Figure 5.10. The 1894 Earthquake Izmit Segment Magnitude and Stress Assessment

Table 5.12. The 1894 Earthquake Izmit Segment Rupture Dimension Assessment

Fault	Mw	Epicenter	L(km x W(km)	$\Delta\sigma$ (bar)	RMSE	R1	R2	R3	R4	R5	R6	R7	RMSE_R	Comment
Izmit	6.8	S1	60x20	140	1.5089	1.1985	0.7608	1.7777	1.1127	1.2938	0.8851	1.5621	1.3654	-
	6.8	S1	38x19	110	1.5462	1.1956	0.7654	1.7827	1.1129	1.3057	0.4453	1.5831	1.4486	Intensity > X
	6.8	S1	38x19	100	1.5815	1.2196	0.7896	1.8241	1.1421	1.3315	0.4184	1.6214	1.4746	-
	6.9	S1	60x20	120	1.4984	1.1906	0.7637	1.7690	1.1039	1.2872	0.7485	1.5537	1.3478	-
	6.9	S1	43x20	100	1.5370	1.1965	0.7698	1.7788	1.1303	1.2980	0.4726	1.5790	1.4230	Intensity > X
	6.9	S1	43x20	90	1.5681	1.2153	0.7864	1.8147	1.1339	1.3435	0.4379	1.6107	1.4504	-
	7	S1	60x20	100	1.5020	1.1885	0.7570	1.7720	1.1086	1.3040	0.7514	1.5571	1.3508	-
	7	S1	50x22	100	1.4684	1.1671	0.7370	1.7385	1.0957	1.2541	0.7187	1.5045	1.3817	Intensity > X
	7	S1	50x22	90	1.5144	1.1905	0.7615	1.7734	1.1143	1.2921	0.5100	1.5559	1.4005	-
	7.1	S1	60x20	90	1.4671	1.1781	0.7455	1.7496	1.0983	1.2794	0.8986	1.5124	1.3489	-
	7.1	S1	57x24	90	1.4372	1.1626	0.7350	1.7205	1.0830	1.2393	0.8962	1.4795	1.3294	-
	7.1	S1	57x24	100	1.3849	1.0600	0.7012	1.5146	1.0545	1.1571	0.9495	1.4316	1.2671	Intensity > X
	7.2	S1	60x20	70	1.5077	1.1897	0.7613	1.7701	1.1143	1.2992	0.7491	1.5643	1.3522	-
	7.2	S1	66x27	70	1.5186	1.1907	0.7686	1.7895	1.1225	1.3190	0.7507	1.5789	1.3505	-
	7.2	S1	66x27	80	1.4723	1.0782	0.7367	1.7361	1.0866	1.1900	0.9250	1.5277	1.3354	Intensity > X

earthquake recorded on this fault. Because of its tectonic potential to create events up to Mw 7.0, we decided to evaluate different magnitudes and stress drops by locating the epicenter in the midpoint as shown in Figure 5.12. Results are listed in Table 5.13. According to these findings, we can claim that a scenario with Mw 6.9 and 90 bar stress drop provides the best estimations for this fault.

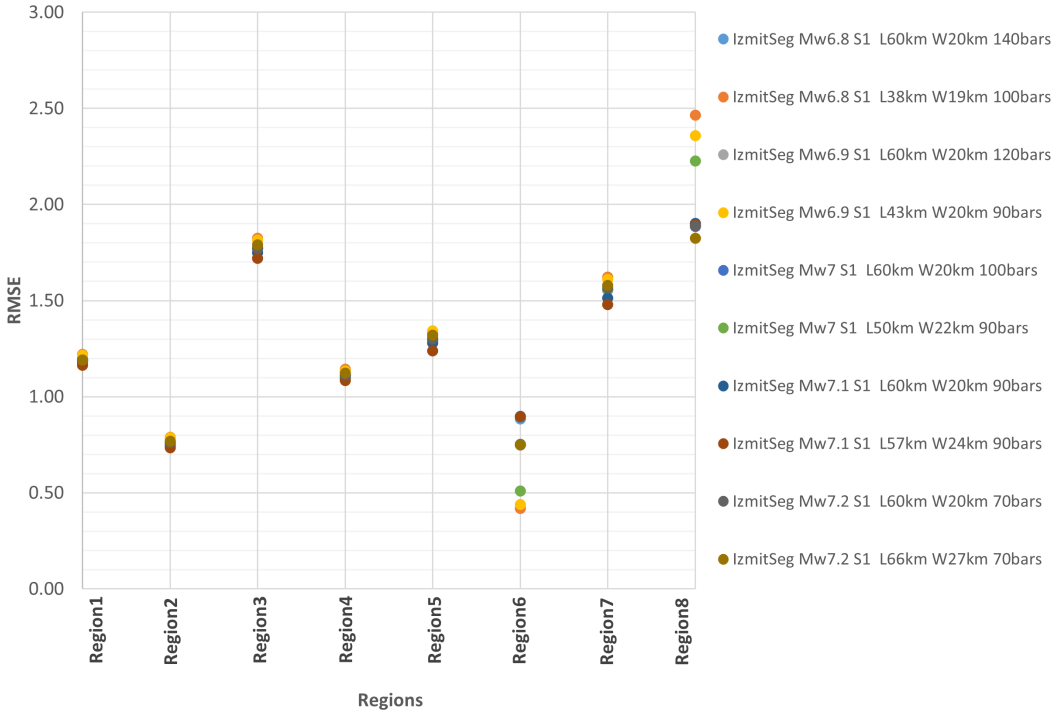

Figure 5.11. The 1894 Earthquake Izmit Segment Rupture Dimension Assessment

Table 5.13. The 1894 Earthquake Çınarcık Scenario

Fault	Mw	$\Delta\sigma$ (bar)	RMSE	R1	R2	R3	R4	R5	R6	R7	R8	RMSE_R	Comment
Çınarcık	6.8	100	1.4732	0.9719	0.3996	1.1597	0.5838	0.9093	0.7743	1.4779	3.3110	1.4732	Intensity > X
	6.8	90	1.4921	0.9960	0.4138	1.2042	0.5990	0.8167	0.7973	1.5449	3.3389	1.4921	-
	6.9	90	1.3929	0.9667	0.3842	1.1282	0.5722	0.7176	0.7705	1.3894	3.2904	1.4382	-
	6.9	110	1.1749	0.9200	0.3563	0.8575	0.7262	0.6897	0.6030	1.1124	3.2372	1.3598	Intensity > X
	7	60	1.5541	1.0032	0.4240	1.2325	0.6111	0.8625	0.8163	1.5820	3.3535	1.5099	-
	7	70	1.4772	0.9793	0.3991	1.1599	0.5835	0.9247	0.7890	1.4872	3.3149	1.4783	Intensity > X
	7.1	60	1.4526	0.9779	0.3934	1.1452	0.5747	0.7821	0.7698	1.4616	3.3164	1.4617	-
	7.2	50	1.4692	0.9758	0.3957	1.1518	0.5913	0.7685	0.7693	1.4838	3.3129	1.4639	-
	7.2	60	1.2848	0.9373	0.3752	1.0900	0.7227	0.6851	0.5625	1.2514	3.2735	1.4052	Intensity > X

According to Aochi and Ulrich (2015), ruptures on the CMF can jump on the PIS and can continue on the Izmit segment. In the 1999 Kocaeli earthquake, a combination of different segments of the NAFZ ruptured and resulted in a 150 km total rupture length. Combining the Prince Islands and Izmit segments without changing the starting and end points, i.e. assuming the segments are fully ruptured can result in the possibility of earthquakes over the M7 range. In our simulations, we decided to evaluate the possibility of a combined rupture of the PIS with some part of Izmit segment. In this scenario, the hypocenter was located at the intersection point of the

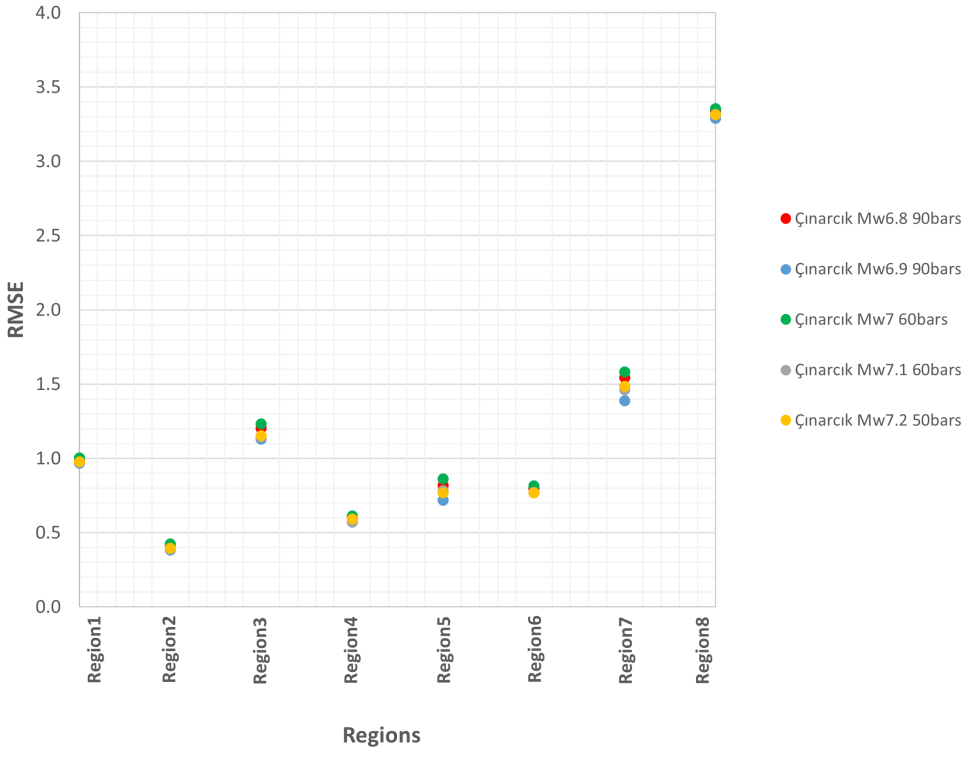

Figure 5.12. The 1894 Earthquake Çınarcık Fault Assessment

two segments. We estimated two scenarios as Case1 (a 42 km rupture on the PIS and a 18 km rupture along the Izmit segment, total rupture length 60 km) and Case2 (20 km rupture on both PIS and the Izmit segment, total rupture length 40 km). We increased stress drop incrementally in both cases. Estimations in terms of RMSEs were listed in Tables 5.14 and 5.15. Findings from the combined scenarios were also illustrated in Figure 5.13. In the 40 km combined rupture scenario, Mw 7.0 and 50 bar stress drop scenario resulted in the lowest RMSEs. For the 60 km combined rupture scenario, the best estimations were obtained with Mw 6.9 and 90 bar stress drop.

Table 5.14. The 1894 Earthquake Combined Scenario 60 km Rupture Length

Fault	Mw	L(km x W(km)	$\Delta\sigma$ (bar)	RMSE	R1	R2	R3	R4	R5	R6	R7	RMSE_R	Comment
Combined	6.7	(42+18) x 10	130	0.8368	0.9849	0.6695	0.9432	1.0614	1.1606	0.5419	0.5804	1.2966	Intensity > X
	6.7	(42+18) x 10	120	0.8746	1.0023	0.6813	1.1547	1.0795	1.2614	0.5525	0.6160	1.3441	-
	6.8	(42+18) x 10	110	0.8321	0.9866	0.4524	0.9357	1.0646	1.1578	0.5422	0.5773	1.2851	Intensity > X
	6.8	(42+18) x 10	100	0.8791	1.0052	0.6894	1.1589	1.0862	1.2616	0.5577	0.6212	1.3488	-
	6.9	(42+18) x 10	90	0.8306	0.9921	0.6736	0.9455	0.9163	1.1588	0.5520	0.5758	1.2863	-
	6.9	(42+18) x 10	100	0.7802	0.9695	0.4360	0.8971	0.8954	0.9726	0.5326	0.5257	1.2321	Intensity > X
	7	(42+18) x 10	70	0.8981	1.0072	0.6885	1.1639	1.0867	1.2646	0.5595	0.6294	1.3879	-
	7	(42+18) x 10	80	0.8026	0.9832	0.4452	0.9264	0.9121	0.9899	0.5350	0.5581	1.2464	Intensity > X
	7.1	(42+18) x 10	60	0.8775	1.0013	0.6840	1.1664	1.0776	1.2650	0.5598	0.6191	1.3474	-
	7.1	(42+18) x 10	70	0.7908	0.9709	0.4418	0.9115	0.9033	0.9751	0.5275	0.5446	1.2352	Intensity > X

Table 5.15. The 1894 Earthquake Combined 40 km Rupture Length

Fault	Mw	L(km) x W(km)	$\Delta\sigma$ (bar)	RMSE	R1	R2	R3	R4	R5	R6	R7	R8	RMSE_R	Comment
Combined	6.7	(20+20) x 10	120	1.1376	1.0419	0.7160	1.2866	1.0879	1.1549	0.5460	1.0404	2.8269	1.3758	Intensity > X
	6.7	(20+20) x 10	110	1.2380	1.0657	0.7331	1.3249	1.1024	1.2592	0.5596	1.1655	2.8677	1.4197	-
	6.8	(20+20) x 10	90	1.2660	1.0705	0.7379	1.4663	1.1071	1.2883	0.5655	1.1859	2.9759	1.4709	-
	6.8	(20+20) x 10	100	1.1414	1.0494	0.7156	1.2859	1.0765	1.0016	0.5505	1.0555	2.8380	1.3647	Intensity > X
	6.9	(20+20) x 10	90	1.0728	1.0346	0.7019	1.2724	1.0714	0.9772	0.5306	0.9641	2.8113	1.3416	Intensity > X
	6.9	(20+20) x 10	80	1.1981	1.0568	0.7243	1.3142	1.0923	1.2474	0.5540	1.1140	2.8492	1.4046	-
	7	(20+20) x 10	80	1.0188	1.0240	0.6890	1.2508	0.9082	0.9644	0.5293	0.8977	2.7853	1.3080	Intensity > X
	7	(20+20) x 10	70	1.1415	1.0502	0.7133	1.2900	1.0864	1.1637	0.5413	1.0430	2.8428	1.3817	-
	7.1	(20+20) x 10	50	1.3526	1.1706	0.7528	1.5122	1.1244	1.3152	0.5740	1.2800	3.1296	1.5403	-
	7.1	(20+20) x 10	60	1.1187	1.0490	0.7134	1.2884	1.0752	1.0864	0.5506	1.0175	2.8341	1.3682	Intensity > X

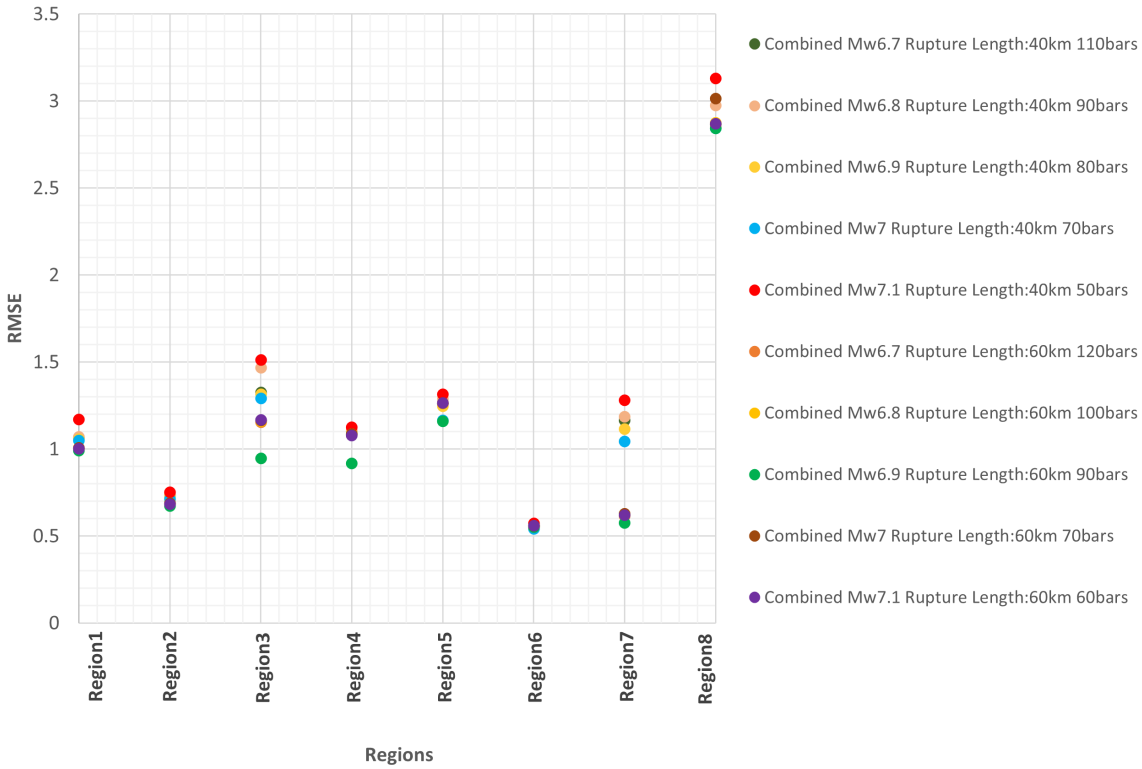

Figure 5.13. The 1894 Earthquake Combined Rupture Assessment

Findings from all scenarios with different epicentral locations, fault segments, rupture lengths, magnitudes and stress drops were summarized in Figure 5.14. The lowest RMSEs for the majority of the regions were obtained in the scenario with Mw 6.8 and the epicenter located at 22 km away from the NW edge of the PIS (S2). For the combined rupture scenarios, minimum errors were obtained in a 60 km total rupture with Mw 6.9 (Figure 5.13) which is consistent with the S2 scenario on the PIS.

As the last step, we estimated distribution of intensities in Istanbul and Marmara

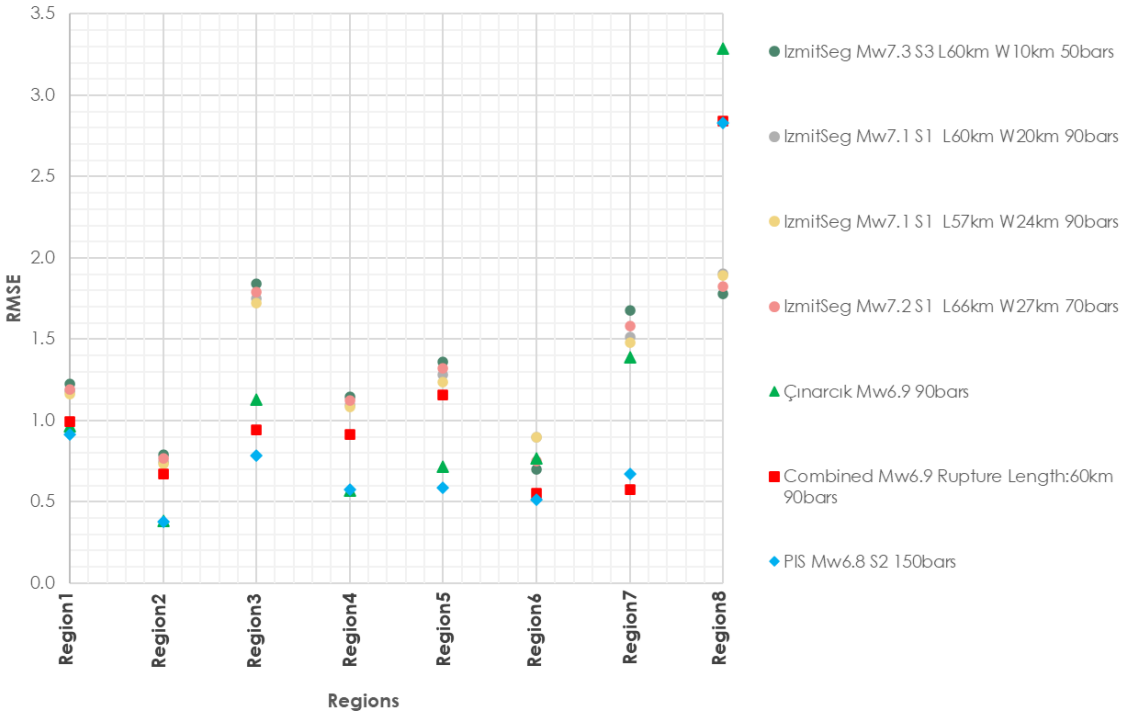

Figure 5.14. The 1894 Earthquake Final Assessment

region by performing a grid-based simulation. It must be recalled that two different types of Vs30 information were available. Vs30s for Istanbul were obtained from a microzonation study (IBB-OYO-KOERI, 2009). The second Vs30 set was estimated from QTM and covers the Marmara region (MTA, 2004). Figures 5.15 and 5.16 represent estimated intensities for the Mw 6.8, S2 scenario on the PIS and the Mw 6.9 combined scenario (60 km rupture length). Figure 5.15 shows the intensity distribution estimated using 24,164 simulations, while Figure 5.16 was obtained from 21,461 simulations. Moreover, in each simulation, results were averaged over three iterations to reduce variability. It should be mentioned that we did thirty iterations in the RMSE evaluations, but preferred three iterations when producing grid based intensity maps to reduce the calculation time.

Grid-based simulation results for the 1894 earthquake demonstrated that Istanbul was exposed to high intensity levels which was consistent with damage inventories. The intensity range was estimated as 3.3 - 11. For the Prince Islands scenario, large intensities were evident around Çınarcık as well as in Prince Islands. This situation

originated from the definition of simplified segment extension as 42 km total rupture with 120 strike angle which approached Çınarcık region more than in reality. The overall consistency between our intensity estimations and the intensities obtained from the damage observations validated our simulation methodology in the study region.

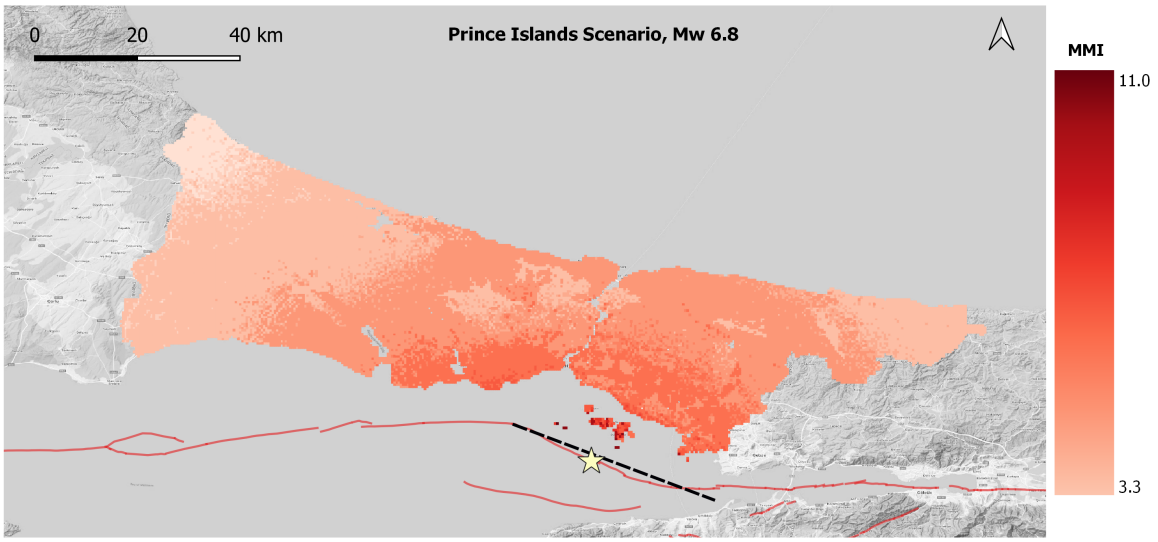

(a)

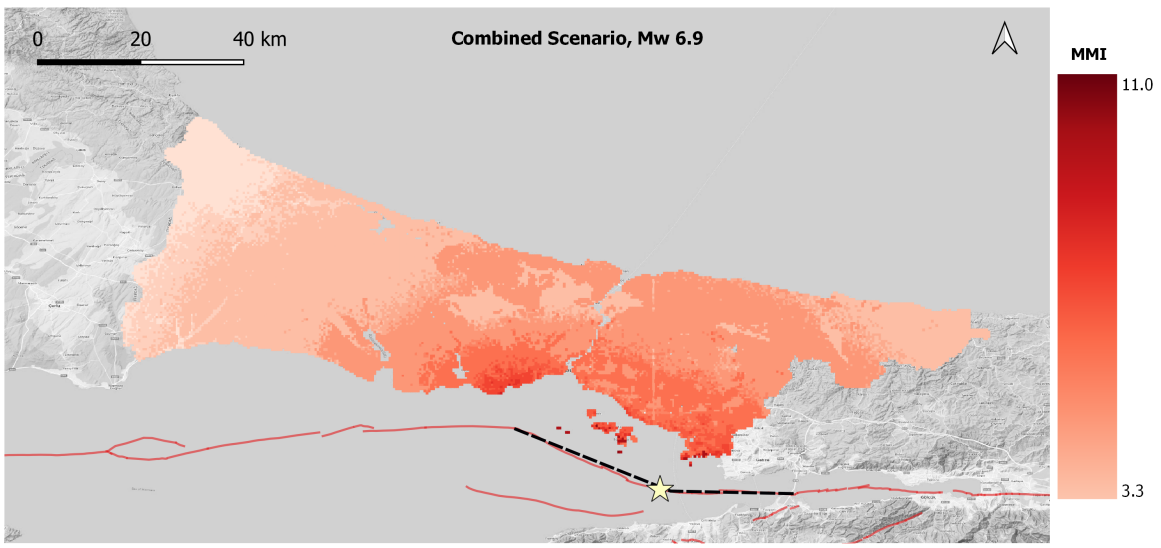

(b)

Figure 5.15. The 1894 Earthquake Stochastic Based Intensity Distribution for (a) the Prince Islands Scenario, (b) Combined Rupture Scenario

Intensity level at Adapazarı was calculated in a range of I=[4.4-6.1] with all the scenarios. This intensity level is significantly lower than our first estimation. We believe that it originated from inadequate modeling of the directivity effect in stochastic

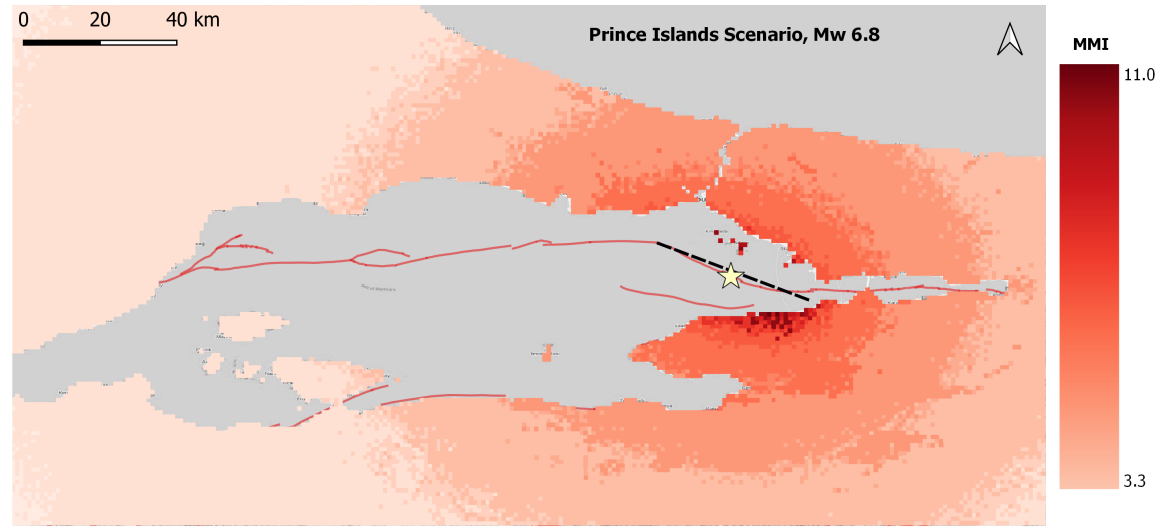

(a)

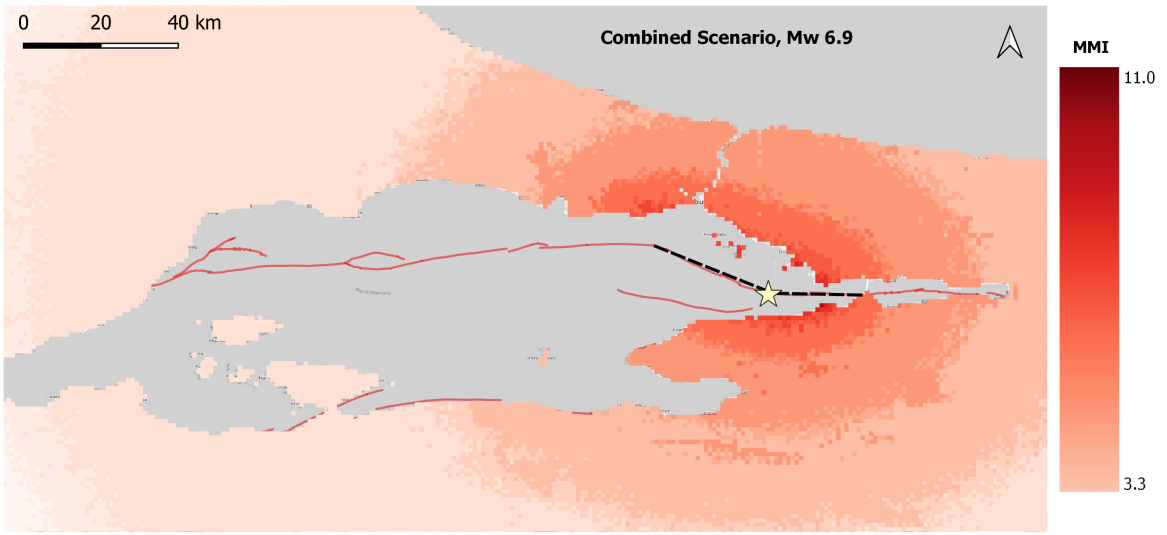

(b)

Figure 5.16. The 1894 Earthquake Stochastic Based Intensity Distribution for (a) the Prince Islands Scenario, (b) the Combined Rupture Scenario

simulation. Even though stochastic simulation tools cannot take into account the rupture directivity effect, EXSIM12 tries to model rupture propagation by dividing the fault into sub-faults. To verify the efficiency of directivity modelling of EXSIM12, we performed two simulations with different epicenters located on the two edges of the Price Islands Segment. In this comparison, we kept all the parameters the same (Mw 6.8, Stress drop: 90 bar, and 42 km total rupture length) except for the epicentral location. These two simulations resulted in small, negligible differences in the intensities.

For example, when the epicenter was located on the southeast edge of the segment the intensity level in Büyükçekmece (I=6.23), Küçükçekmece (I=7.04) and Silivri (I=5.30), which are localities in the forward directivity region, were higher than those when the epicenter was located on the northwest edge (I=6.22, 6.48 and 5.29, respectively). Similarly, intensities in Kartal (I=7.23), Izmit (I=5.33) and Yalova (8.70) decreased in the former scnario compared to the case in which the epicenter is at the northwest edge (7.25, 5.35, and 9.25). Despite the change in Yalova and Küçükçekmece, it was almost negligible in other localities. For that reason, it was concluded that the directivity effect can be insufficiently modelled in EXSIM12.

Another reason for this underestimation in the eastern towns could be the difference between the extensions of the faults in reality and as defined in EXSIM12. EXSIM12 allows for defining linear fault segments represented with constant parameters, whereas in reality fault segments are geometrically irregular entities which results in varying source parameters such as rupture velocity, rise time, dip angle and strike, and therefore synthetics may yield lower intensities.

In addition, although every effort was made to check the accounts, the possibility of exaggeration of damage in the inventory sources may have led to the inconsistency in the simulation outputs. As mentioned before, official damage records from surrounding cities were rare. Also, even with the rupture scenario starting in the Gulf of Izmit, we could not provide outputs for all regions consistent with intensity level described in the sources.

As the final step for validating our findings, we compared the results of the best scenarios with two NGA-West2 GMMs, Akkar et al., (2014) and Chiou and Youngs (2014) in Figure 5.17. Based on this comparison we could claim that estimated PGA values taken for the best Izmit scenarios showed inconsistency with the GMMs because synthetics were underestimating the medians and their lower band standard deviations. Even though the synthetics of the Çınarcık fault somehow stayed around the lower band standard deviation lines, they underestimated the medians. The best overlaps were obtained in the Prince Islands scenarios S2 and S3. These comparison plots had

consistency with the RMSE scatter plots and validated our conclusion for the 1894 event.

5.2. 22 May 1766 Earthquake

Steps similar to those for the 1894 earthquake were followed for the 1766 event. Regions were identified based on the density and distribution of intensity points. These regions were more or less similar to the former case, except some which were removed due to lack of damage information. Figure 5.18 shows RMSE regions utilized for the 1766 event.

In agreement with the estimated intensity distribution, the CMF was associated with the 1766 earthquake (see: Section 3.4.3). Initially, we located the epicenter at the intersection point of the CMF with the PIS (labeled as S1 in Figure 5.19a). Even though the total rupture length was estimated up to 80 km, we evaluated the effect of different rupture lengths. For the CMF, we also considered the possibility of a more distant epicenter location from Istanbul (40 km away) which was marked as S2 in Figure 5.19a. Similar to the 1894 earthquake, we also considered the possibility of a combined fault rupture along the CMF and the PIS. The epicenter location of this scenario was illustrated in Figure 5.19b.

We incrementally increased magnitude and stress drop. In these estimations, total rupture length was taken as 80 km. Findings were listed in Tables 5.16 and 5.17 for the S1 and S2 scenarios, respectively. These tables were also illustrated in Figures 5.20 and 5.21. In these first evaluations, we noticed that the stress drop is much higher than in the 1894 event. The best magnitude and stress drop pairs were obtained as Mw 7.0, 240 bar and Mw 7.1, with 200 bar for the S1 scenario. For S2, Mw 7.1 with 210 bar stress drop provided the best results.

As the second step, we tested the influence of the rupture length for scenarios S1 and S2. Findings are represented in Tables 5.18 and 5.19. Besides they are shown in Figures 5.22 and 5.23 for two scenarios respectively. In this analysis, the best result for

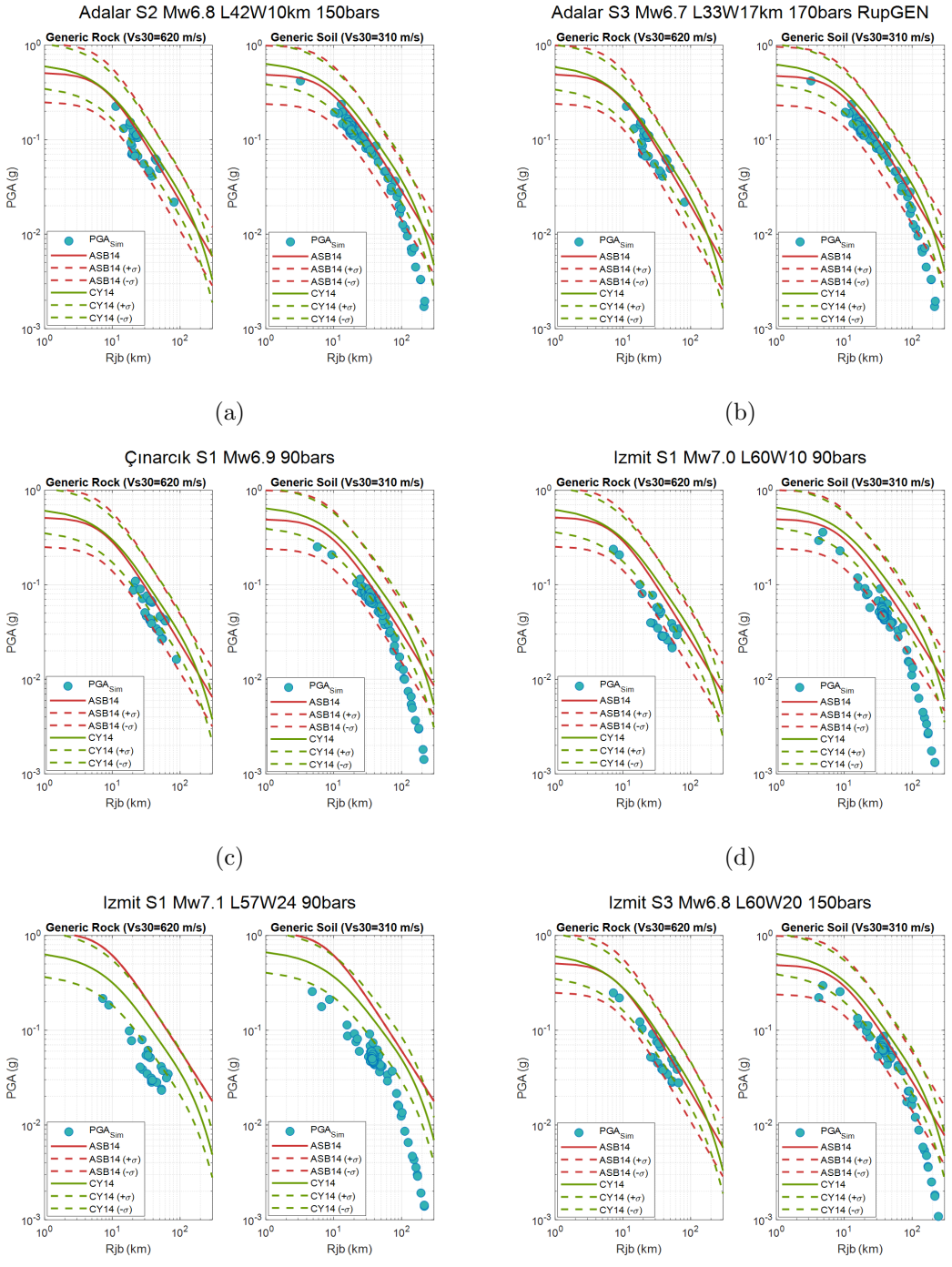

Figure 5.17. Comparison of the best estimated simulation scenarios with GMMs for the 1894 Earthquake (a) the PIS, S2 Scenario with Mw 6.8 (b) the PIS, S3 Scenario with Mw 6.7 (c) Çınarcık Fault Scenario, with Mw 6.9 (d) Izmit Segment, S1 Scenario with Mw 7.0 (e) Izmit Segment, S1 Scenario with Mw 7.1 (f) Izmit Segment, S3 Scenario with Mw 6.8

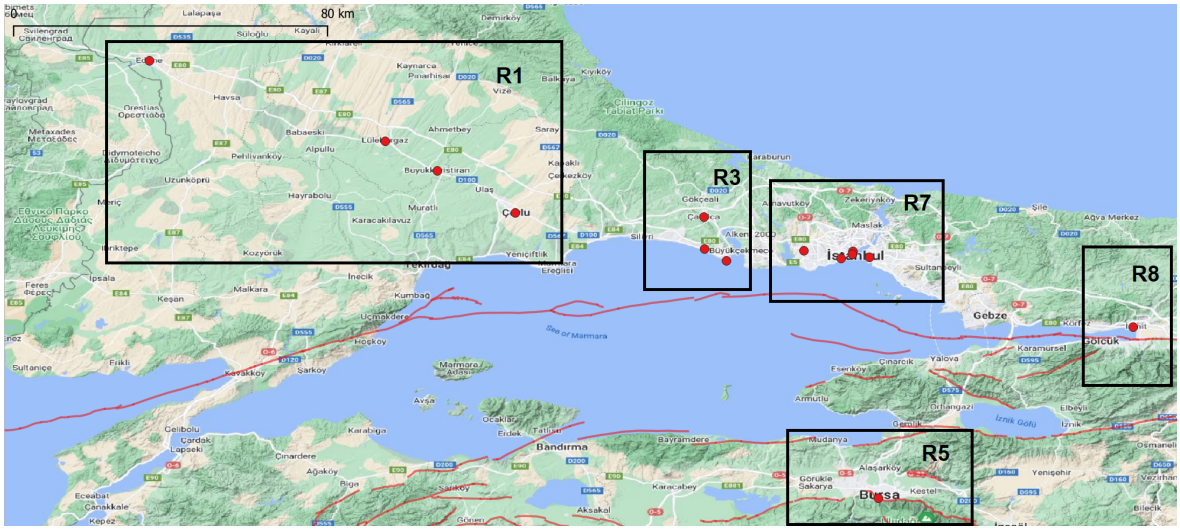

Figure 5.18. RMSE Regions of the 1766 Earthquake

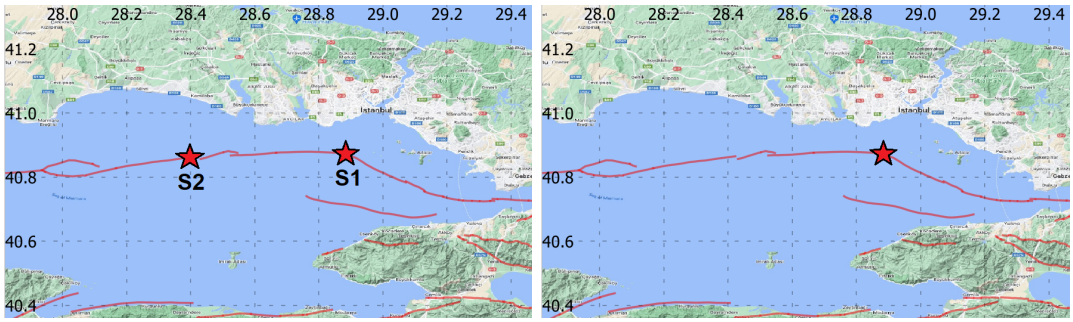

(a) (b)

Figure 5.19. Representation of estimated epicenter locations for the 1766 Earthquake (a) the CMF Scenarios (b) Combined Rupture Scenario

the S1 scenario was obtained with Mw 6.9 and 200 bar stress drop for a 43 km rupture length. For S2, Mw 7.2 and 160 bar stress drop along a 66 km rupture provided lowest RMSEs.

Next, we assessed the effect of slip distribution for this earthquake by comparing the random slip generated by EXSIM12 to the random slip generated by RUPGEN. These results are expressed in Tables 5.20 and 5.21; and illustrated in Figures 5.24 and 5.25 for scenarios S1 and S2. According to these results, EXSIM12 generated random slip resulted in better estimations for the S1 scenario while specialized slip for Mw 7.4 with 110 bar stress drop and 80 km rupture gives lower RMSEs for scenario S2.

Table 5.16. The 1766 Earthquake Magnitude and Stress Drop Assessment for the CMF S1 Scenario

Fault	Mw	Epicenter	$\Delta\sigma$ (bar)	RMSE	R1	R3	R5	R7	R8	RMSE_R	Comment
CMF	6.9	S1	100	2.0058	1.7376	1.8550	1.4257	1.9264	3.6520	2.2601	-
	6.9	S1	150	1.6532	1.4037	1.3056	0.7644	1.5713	3.5127	1.9528	-
	6.9	S1	260	1.2441	0.9974	0.9524	0.5323	1.1834	2.7719	1.5013	-
	6.9	S1	270	1.1768	0.9730	0.9330	0.5523	1.0142	2.7463	1.4624	-
	6.9	S1	280	1.2165	0.9665	0.9281	0.5042	1.1569	2.7296	1.4724	Intensity >9.5
	7	S1	100	1.8654	1.6681	1.7720	0.8268	1.7052	3.5976	2.1193	-
	7	S1	150	1.5284	1.2252	1.1916	0.6868	1.4185	3.4506	1.8608	-
	7	S1	230	1.2276	0.9752	0.9377	0.5322	1.1561	2.7734	1.4928	-
	7	S1	240	1.0686	0.9003	0.8326	0.1060	0.8432	2.6641	1.3655	-
	7	S1	250	1.1225	0.9395	0.9537	0.4590	0.8562	2.7398	1.4312	Intensity >9.5
	7.1	S1	100	1.6747	1.4217	1.3200	0.7956	1.5960	3.5473	1.9762	-
	7.1	S1	190	1.1818	0.9814	0.9369	0.4967	1.0202	2.7598	1.4659	-
	7.1	S1	200	1.1369	0.9605	0.9620	0.4920	0.8740	2.7506	1.4436	-
	7.1	S1	210	1.2300	0.9512	1.2941	0.4725	0.9901	2.7227	1.4964	Intensity >9.5
	7.2	S1	100	1.5543	1.2317	1.2365	0.7259	1.4437	3.4955	1.8908	-
	7.2	S1	150	1.5087	1.0127	0.9576	0.5186	1.1957	2.7819	1.5087	-
	7.2	S1	160	1.2350	0.9946	0.9313	0.5317	1.1629	2.7837	1.4994	-
	7.2	S1	170	1.1312	0.9673	0.9335	0.5170	0.8749	2.7320	1.4355	Intensity >9.5
	7.3	S1	130	1.2521	1.0097	0.9443	0.5467	1.1874	2.8012	1.5144	-
	7.3	S1	140	1.1669	0.9837	0.9281	0.4638	0.9789	2.7573	1.4564	-
	7.3	S1	150	1.1222	0.9527	0.9527	0.4646	0.8550	2.7216	1.4261	Intensity >9.5
	7.4	S1	110	1.2495	1.0045	0.9380	0.5464	1.1910	2.7913	1.5098	-
	7.4	S1	120	1.1739	0.9736	0.9466	0.5222	0.9913	2.7614	1.4645	-
	7.4	S1	130	1.1240	0.9354	0.9465	0.4507	0.8702	2.7406	1.4312	Intensity >9.5

For the assessment of combined rupture scenarios, we modelled two different ruptures as Case 1 (80 km total rupture; 60 km rupture along the CMF and 20 km on the PIS) and Case 2 (40 km rupture along the CMF and 40 km rupture along the PIS, a total of 80 km rupture). Findings are listed in Table 5.22 for the first case, and Table 5.23 for the latter. Figures 5.26 and 5.27 express RMSE calculations.

In the 20 km + 60 km rupture case, even though we observed lower errors in many regions for Mw 7.4 and 100 bar stress drop scenario, it created a high error range for Region 8 by underestimating intensity levels in the Eastern Marmara. In the 40km+40km case, Mw 7.3 and 140 bar stress drop provided the best intensity estimations.

Table 5.17. The 1766 Earthquake Magnitude and Stress Drop Assessment for the CMF S2 Scenario

Fault	Mw	Epicenter	$\Delta\sigma$ (bar)	RMSE	R1	R3	R5	R7	R8	RMSE_R	Comment
CMF	6.9	S2	270	1.2288	0.9939	0.9439	0.5143	1.1433	2.7775	1.4943	-
	6.9	S2	280	1.1753	0.9794	0.9343	0.5001	1.0011	2.7609	1.4634	-
	6.9	S2	290	1.2461	0.9841	1.2851	0.4866	1.0083	2.7554	1.5143	Intensity >9.5
	7	S2	220	1.1837	0.9799	0.9760	0.4796	1.0058	2.7621	1.4686	-
	7	S2	230	1.2347	0.9944	0.9259	0.5198	1.1782	2.7577	1.4906	-
	7	S2	240	1.1837	0.9799	0.9760	0.4796	1.0058	2.7621	1.4686	Intensity >9.5
	7.1	S2	200	1.1707	0.9797	0.9312	0.4971	0.9934	2.7505	1.4578	Intensity >9.5
	7.1	S2	210	1.1394	0.9753	0.9691	0.4580	0.8829	2.7286	1.4370	-
	7.1	S2	220	1.1881	0.9339	1.2874	0.4314	0.8597	2.7240	1.4748	Intensity >9.5
	7.2	S2	170	1.4639	0.9784	0.9573	0.4918	0.9859	2.7617	1.4639	Intensity >9.5
	7.2	S2	160	1.2356	0.9973	0.9474	0.5449	1.1618	2.7668	1.4963	-
	7.2	S2	150	1.2632	1.0165	0.9532	0.5680	1.2098	2.7999	1.5210	-
	7.3	S2	130	1.2464	1.0002	0.9439	0.5379	1.1813	2.7942	1.5089	-
	7.3	S2	140	1.1785	0.9805	0.9366	0.4972	1.0027	2.7736	1.4686	-
	7.3	S2	150	1.1324	0.9649	0.9773	0.4648	0.8550	2.7373	1.4371	Intensity >9.5
	7.4	S2	100	1.3118	1.1228	0.9843	0.5795	1.2479	2.8317	1.5583	-
	7.4	S2	110	1.1988	1.0140	0.9673	0.5575	1.0180	2.7759	1.4844	-
	7.4	S2	120	1.2437	0.9759	1.2917	0.4964	1.0089	2.7391	1.5092	Intensity >9.5

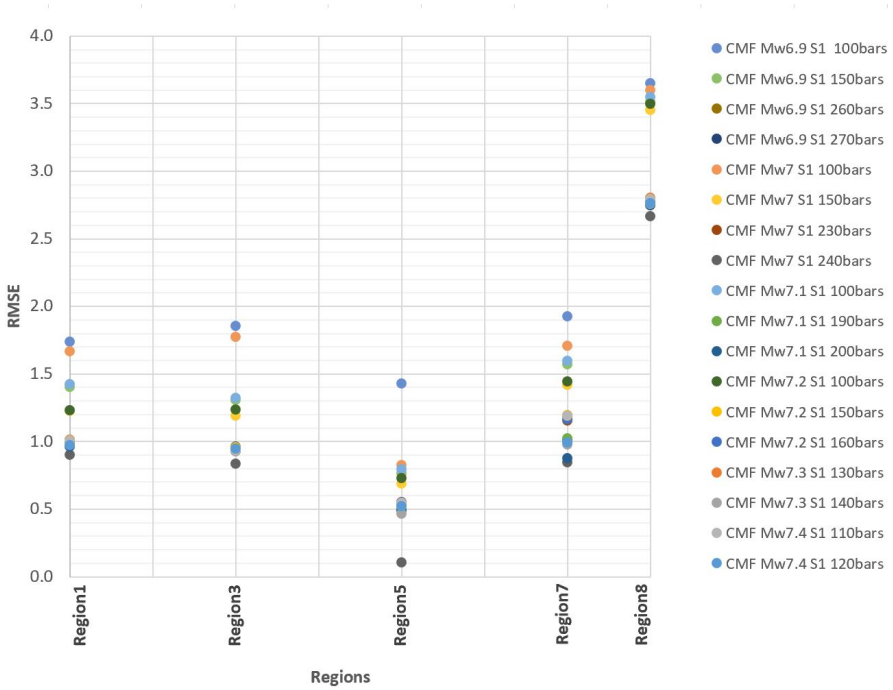

Figure 5.20. The 1766 Earthquake CMF S1 Scenario Magnitude and Stress Drop Assessment

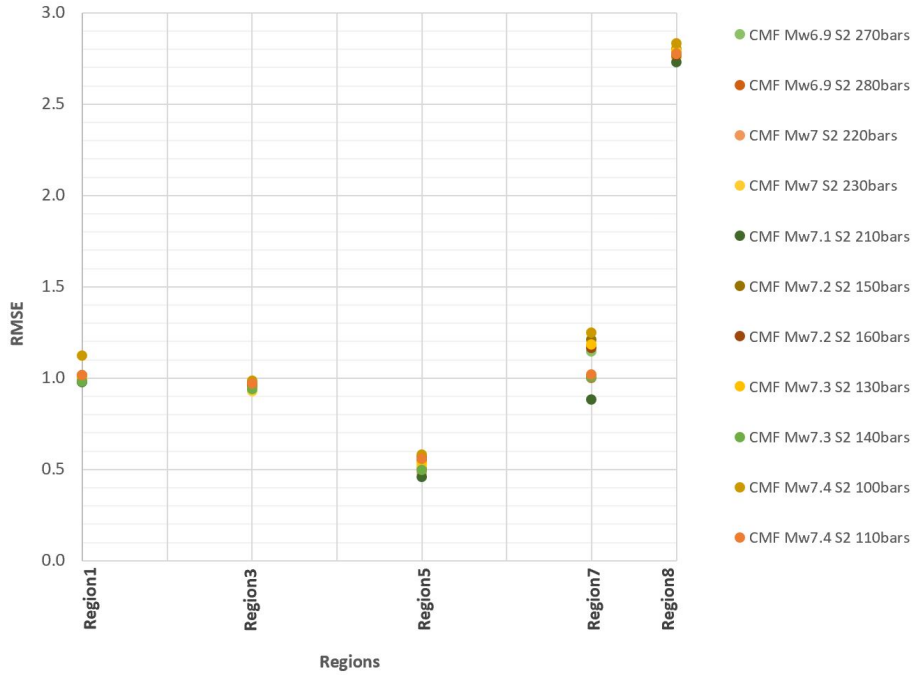

Figure 5.21. The 1766 Earthquake CMF S2 Scenario Magnitude and Stress Drop Assessment

Table 5.18. The 1766 Earthquake Rupture Length Assessment for the CMF S1 Scenario

Fault	Mw	Epicenter	L(km) x W(km)	$\Delta\sigma$ (bar)	RMSE	R1	R3	R5	R7	R8	RMSE_R	Comment
CMF	6.9	S1	43x10	190	1.4554	1.6956	1.0295	0.5607	1.1571	2.8221	1.6464	-
	6.9	S1	43x10	200	1.3633	1.6743	0.9951	0.5518	0.8822	2.7647	1.5824	-
	6.9	S1	43x10	210	1.3778	1.6524	0.9846	0.5224	0.9884	2.7547	1.5836	Intensity >9.5
	7	S1	50x10	140	1.4908	1.7175	1.0632	0.6432	1.2069	2.8680	1.6838	-
	7	S1	50x10	150	1.4762	1.6999	1.0270	0.6112	1.2230	2.8164	1.6581	-
	7	S1	50x10	160	1.5031	1.6666	1.2902	0.5888	1.2071	2.8094	1.6816	Intensity >9.5
	7.1	S1	57x10	140	1.3877	1.4290	0.9928	0.6120	1.2155	2.8411	1.6095	-
	7.1	S1	57x10	150	1.3877	1.4290	0.9928	0.6120	1.2155	2.8411	1.6095	-
	7.1	S1	57x10	160	1.2542	1.2485	0.9573	0.5207	0.9914	2.8021	1.5219	Intensity >9.5
	7.2	S1	66x10	140	1.2975	1.1760	0.9464	0.5577	1.1899	2.8214	1.5470	-
	7.2	S1	66x10	150	1.5225	1.1534	0.9376	0.5486	1.1690	2.7772	1.5225	-
	7.2	S1	66x10	160	1.1743	1.1330	0.9584	0.5023	0.8538	2.7420	1.4630	Intensity >9.5
	7.3	S1	75x10	100	1.3487	1.2084	1.0025	0.6269	1.2586	2.8802	1.5961	-
	7.3	S1	75x10	110	1.3279	1.1751	0.9829	0.5996	1.2513	2.8421	1.5716	-
	7.3	S1	75x10	120	1.3021	1.1371	0.9804	0.5641	1.2108	2.8339	1.5537	Intensity >9.5

For the 1766 earthquake, we illustrated best scenarios in Figure 5.28, where it is clearly seen that all CMF scenarios remained deficient in modelling the eastern Marmara Region, and synthetic intensities significantly underestimated the assessed intensities. On the other hand, not all combined scenarios were adequate to represent

Table 5.19. The 1766 Earthquake Rupture Length Assessment for the CMF S2 Scenario

Fault	Mw	Epicenter	L(km) x W(km)	$\Delta\sigma$ (bar)	RMSE	R1	R3	R5	R7	R8	RMSE_R	Comment
CMF	6.9	S2	43x10	190	1.4699	1.7122	1.0311	0.6164	1.1852	2.8160	1.6558	-
	6.9	S2	43x10	200	1.4527	1.6905	1.0210	0.5619	1.1693	2.7994	1.6383	-
	6.9	S2	43x10	210	1.4446	1.6804	0.9919	0.5579	1.1748	2.7853	1.6283	-
	7	S2	50x10	140	1.6038	1.7279	1.0895	0.7166	1.2927	3.4117	1.8972	-
	7	S2	50x10	180	1.4440	1.6374	1.0077	0.5621	1.2030	2.8049	1.6326	-
	7	S2	50x10	160	1.4887	1.6767	1.0273	0.6330	1.2778	2.8378	1.6705	-
	7.1	S2	57x10	140	1.4612	1.6341	1.0234	0.6380	1.2183	2.8709	1.6644	-
	7.1	S2	57x10	150	1.4092	1.4452	1.0007	0.6264	1.2584	2.8522	1.6248	-
	7.1	S2	57x10	160	1.3768	1.4054	1.0032	0.5796	1.2141	2.8131	1.5941	-
	7.2	S2	66x10	140	1.3372	1.2260	0.9979	0.6071	1.2328	2.8401	1.5782	-
	7.2	S2	66x10	150	1.5466	1.1904	0.9808	0.5401	1.2014	2.8011	1.5466	-
	7.2	S2	66x10	160	1.2900	1.1768	0.9641	0.5658	1.1761	2.7811	1.5331	-
	7.3	S2	75x10	100	1.5943	1.2177	1.2116	0.7287	1.5689	3.5232	1.9160	-
	7.3	S2	75x10	110	1.5351	1.1734	1.0641	0.6847	1.5255	3.4618	1.8595	-
	7.3	S2	75x10	120	1.4708	1.1380	1.0161	0.6708	1.4006	3.4279	1.8160	-

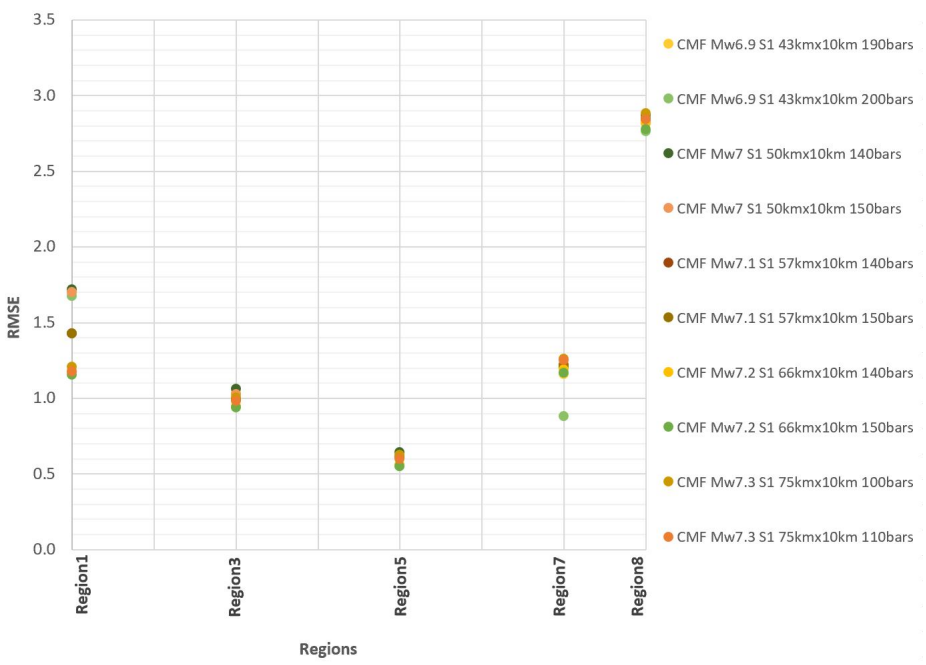

Figure 5.22. The 1766 Earthquake CMF S1 Scenario Rupture Length Assessment

western parts of Marmara, like for example Regions 1 and 2. This situation can be a clear sign of insufficient directivity modeling in EXSIM12.

If we did not take Region 8 into consideration, which might be exposed to higher intensities due to directivity, we could conclude that the best scenarios were obtained

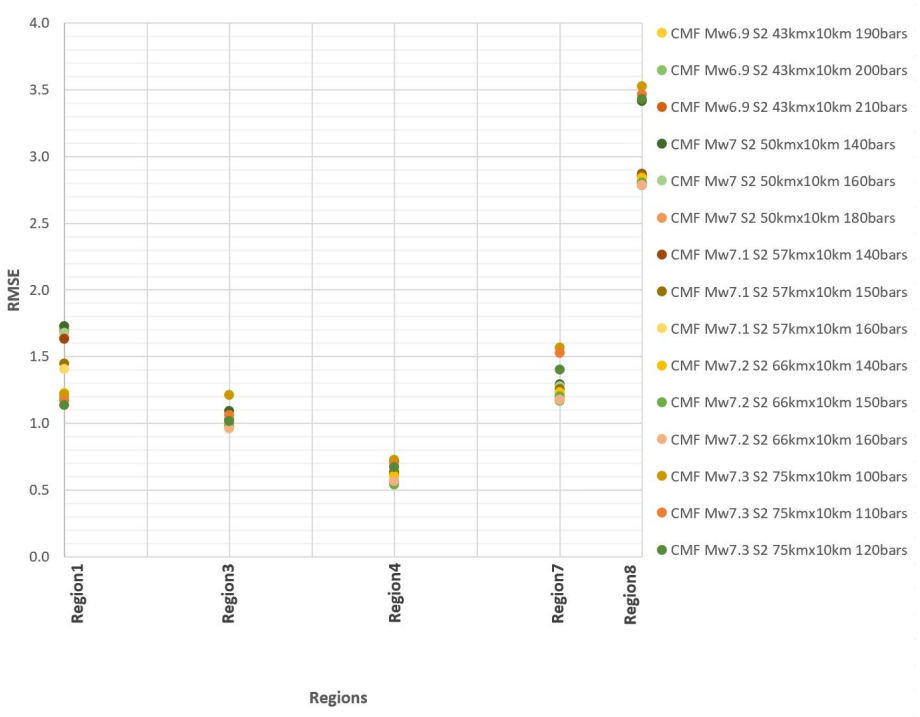

Figure 5.23. The 1766 Earthquake CMF S2 Scenario Rupture Length Assessment

Table 5.20. The 1766 Earthquake Slip Assessment for the CMF S1 Scenario

Fault	Mw	Epicenter	$\Delta\sigma$ (bar)	Slip	RMSE	R1	R3	R5	R7	R8	RMSE_R	Comment
CMF	6.9	S1	260	RupGEN	1.2590	0.9441	0.9492	0.5407	1.2478	2.8012	1.5158	-
	6.9	S1	270	Random	1.1768	0.9730	0.9330	0.5523	1.0142	2.7463	1.4624	-
	6.9	S1	270	RupGEN	1.2901	0.9303	1.2483	0.5236	1.1957	2.7827	1.5408	Intensity >9.5
	7	S1	230	RupGEN	1.2261	0.9150	0.9123	0.5085	1.2037	2.7744	1.4883	-
	7	S1	240	Random	1.0686	0.9003	0.8326	0.1060	0.8432	2.6641	1.3655	-
	7	S1	240	RupGEN	1.2122	0.9131	0.9270	0.4794	1.1713	2.7512	1.4740	Intensity >9.5
	7.1	S1	190	RupGEN	1.2209	0.9347	0.9183	0.5053	1.1754	2.7713	1.4855	-
	7.1	S1	200	Random	1.1369	0.9605	0.9620	0.4920	0.8740	2.7506	1.4436	-
	7.1	S1	200	RupGEN	1.2130	0.9067	0.9347	0.4902	1.1657	2.7670	1.4799	Intensity >9.5
	7.2	S1	160	Random	1.2350	0.9946	0.9313	0.5317	1.1629	2.7837	1.4994	-
	7.2	S1	160	RupGEN	1.2367	0.9269	0.9378	0.5159	1.2196	2.7629	1.4917	-
	7.3	S1	140	Random	1.1669	0.9837	0.9281	0.4638	0.9789	2.7573	1.4564	-
	7.3	S1	140	RupGEN	1.2087	0.9010	0.8967	0.4766	1.1753	2.7677	1.4754	-
	7.4	S1	120	Random	1.1739	0.9736	0.9466	0.5222	0.9913	2.7614	1.4645	-
	7.4	S1	120	RupGEN	1.2028	0.9097	0.8883	0.4869	1.1556	2.7679	1.4731	-

on the CMF with Mw 7.0 and 240 bar stress drop of scenario S1. For scenario S2, Mw 7.1 and 210 bar yielded good estimations.

To validate our estimations, we compared our best estimations with two NGA-West2 GMMs. Figure 5.29 represents this comparison for six best scenarios on the CMF. According to these plots, for the S1 scenario, we can say that Mw 6.9 and 43

Table 5.21. The 1766 Earthquake Slip Assessment for the CMF S2 Scenario

Fault	Mw	Epicenter	$\Delta\sigma$ (bar)	Slip	RMSE	R1	R3	R5	R7	R8	RMSE_R	Comment
CMF	6.9	S2	270	RupGEN	1.2326	0.9294	0.9306	0.4961	1.2048	2.7773	1.4927	-
	6.9	S2	280	Random	1.1753	0.9794	0.9343	0.5001	1.0011	2.7609	1.4634	-
	6.9	S2	280	RupGEN	1.2094	0.8946	0.9076	0.4940	1.1712	2.7751	1.4792	Intensity >9.5
	7	S2	230	Random	1.2347	0.9944	0.9259	0.5198	1.1782	2.7577	1.4906	-
	7	S2	230	RupGEN	1.2258	0.9194	0.9128	0.5154	1.1902	2.7939	1.4945	-
	7.1	S2	200	RupGEN	1.2180	0.9045	0.9238	0.4953	1.1911	2.7561	1.4786	-
	7.1	S2	210	Random	1.1394	0.9753	0.9691	0.4580	0.8829	2.7286	1.4370	-
	7.1	S2	210	RupGEN	1.2117	0.9033	1.2605	0.4485	0.9852	2.7330	1.4863	Intensity >9.5
	7.2	S2	160	RupGEN	1.4872	0.9211	0.8985	0.5334	1.2042	2.7693	1.4872	-
	7.2	S2	160	Random	1.2356	0.9973	0.9474	0.5449	1.1618	2.7668	1.4963	-
	7.3	S2	140	Random	1.1785	0.9805	0.9366	0.4972	1.0027	2.7736	1.4686	-
	7.3	S2	140	RupGEN	1.2120	0.9155	0.9046	0.5028	1.1719	2.7634	1.4778	-
	7.4	S2	110	Random	1.1988	1.0140	0.9673	0.5575	1.0180	2.7759	1.4844	-
	7.4	S2	110	RupGEN	1.1928	1.1981	0.9232	0.5146	0.8657	2.7581	1.4771	-

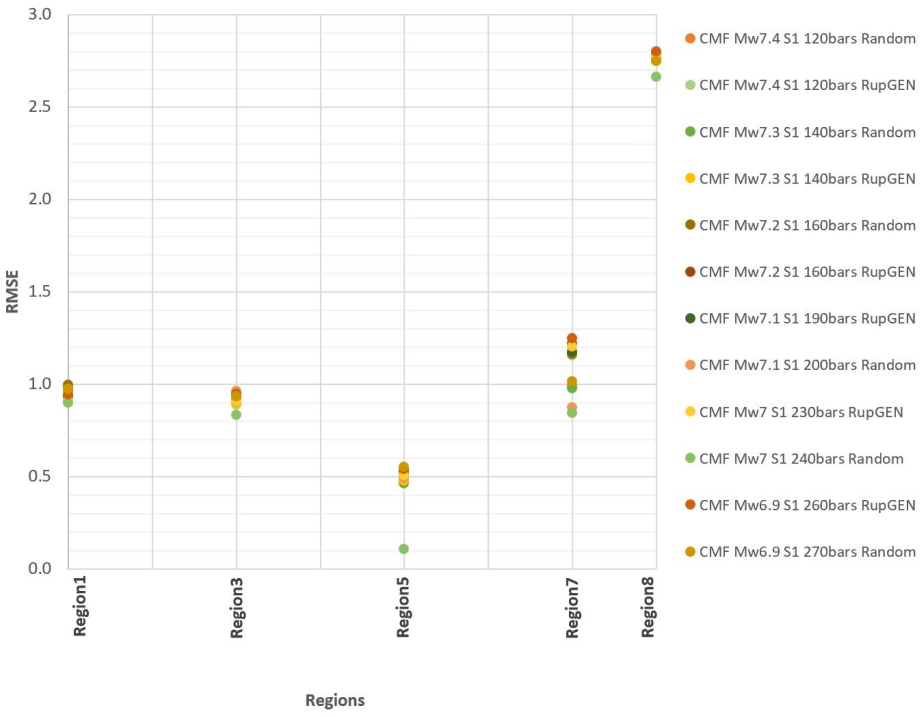

Figure 5.24. The 1766 Earthquake CMF S1 Scenario Slip Assessment

km rupture length scenario caused PGAs above the medians, while the Mw 7.1 and 80 km rupture scenario resulted in low PGAs. The best fits were obtained with the Mw 7.0 and 240 bar stress drop scenario. For the epicenter located at S2, even though all the synthetics are over the lower standard deviation bound, they are still lower than the medians.

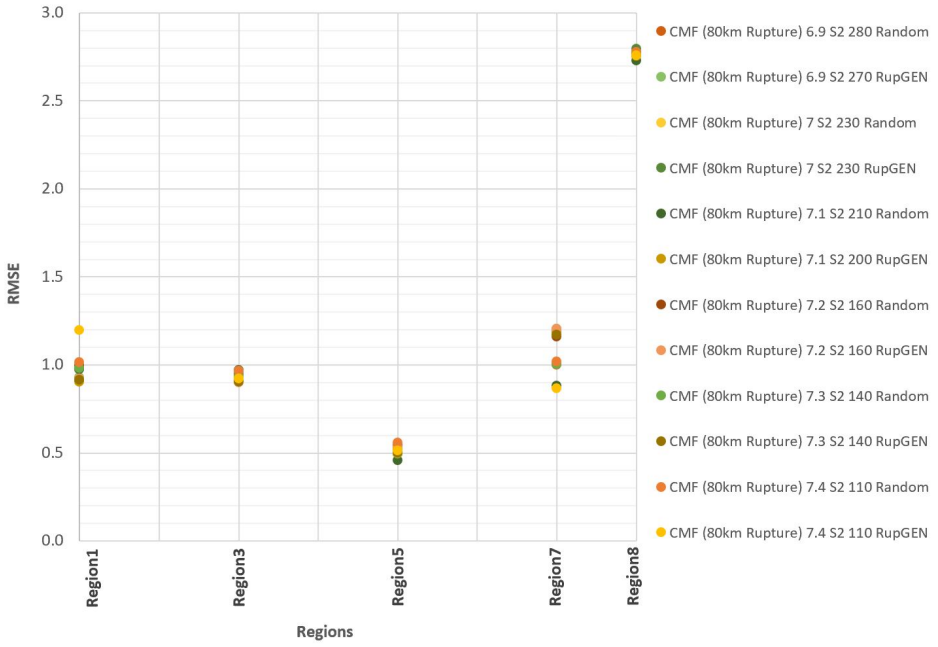

Figure 5.25. The 1766 Earthquake CMF S2 Scenario Slip Assessment

Table 5.22. The 1766 Earthquake Combined Scenario Assessment for Case 1

Fault	Mw	Epicenter	L(km) x W(km)	$\Delta\sigma$ (bar)	RMSE	R1	R3	R5	R7	R8	RMSE_R	Comment
Combined	6.9	S1	(20+60)x10	260	1.2993	1.6675	1.0292	0.1937	0.8088	2.4546	1.4530	-
	6.9	S1	(20+60)x10	280	1.2020	1.4640	0.9891	0.2422	0.9992	1.9153	1.2528	-
	6.9	S1	(20+60)x10	300	1.3261	1.4396	0.9669	0.2800	1.4139	1.8574	1.3065	IIntensity >9.5
	7	S1	(20+60)x10	220	1.2782	1.6582	1.0331	0.2042	0.9961	1.9156	1.3054	-
	7	S1	(20+60)x10	240	1.1941	1.4519	0.9707	0.2566	1.0056	1.8927	1.2417	-
	7	S1	(20+60)x10	260	1.3808	1.4247	1.2642	0.2624	1.4338	1.8518	1.3551	Intensity >9.5
	7.1	S1	(20+60)x10	200	1.1978	1.4644	0.9874	0.2269	0.9930	1.8981	1.2458	-
	7.1	S1	(20+60)x10	220	1.1959	1.4260	0.9543	0.2882	1.0660	1.8415	1.2292	-
	7.1	S1	(20+60)x10	240	1.3090	1.3878	0.9349	0.3321	1.4312	1.8194	1.2860	Intensity >9.5
	7.2	S1	(20+60)x10	140	1.3481	1.7014	1.1837	0.1379	0.8312	2.4877	1.4963	-
	7.2	S1	(20+60)x10	160	1.2703	1.6431	0.9944	0.2217	0.9998	1.9438	1.3050	-
	7.2	S1	(20+60)x10	180	1.2993	1.4331	0.9574	0.2848	1.3975	1.8538	1.2993	Intensity >9.5
	7.3	S1	(20+60)x10	120	1.3450	1.6945	1.1838	0.1707	0.8306	2.4811	1.4932	-
	7.3	S1	(20+60)x10	140	1.1943	1.4634	0.9875	0.2242	0.9782	1.9083	1.2462	-
	7.3	S1	(20+60)x10	160	1.3150	1.4196	0.9496	0.3166	1.4138	1.8300	1.2934	Intensity is greater than 9.5
	7.4	S1	(20+60)x10	100	1.3533	1.7071	1.1810	0.1468	0.8434	2.4943	1.5009	-
	7.4	S1	(20+60)x10	120	1.1977	1.4560	0.9886	0.2340	0.9988	1.9047	1.2472	-
	7.4	S1	(20+60)x10	140	1.3265	1.3879	0.9263	0.3393	1.4797	1.8148	1.2948	Intensity >9.5

In the last step, we plotted grid-based intensity distributions for best S1 and S2 scenarios. Figure 5.30 represents estimated intensities for Istanbul and Figure 5.31 illustrates the intensity distribution in the Marmara region. By looking at these figures, we can easily see that the location of the epicenter did not create significant differences in the intensity distribution. As discussed before, this situation stemmed from the inadequate directivity modelling in stochastic simulation and needs to be improved in

Table 5.23. The 1766 Earthquake Combined Scenario Assessment for Case 2

Fault	Mw	Epicenter	L(km) x W(km)	$\Delta\sigma$ (bar)	RMSE	R1	R3	R5	R7	R8	RMSE_R	Comment
Combined	6.9	S1	(40+40)x10	300	1.2816	1.7123	0.9970	0.3544	1.0129	1.7407	1.2734	-
	6.9	S1	(40+40)x10	320	1.2635	1.6881	1.0004	0.4015	0.9923	1.6927	1.2539	-
	6.9	S1	(40+40)x10	340	1.5690	1.6675	0.9641	0.4332	1.8740	1.6760	1.4296	Intensity >9.5
	7	S1	(40+40)x10	240	1.3386	1.8599	1.0113	0.3797	0.9917	1.7660	1.3212	-
	7	S1	(40+40)x10	260	1.2722	1.6940	1.0059	0.4077	1.0026	1.7181	1.2653	-
	7	S1	(40+40)x10	280	1.3917	1.6822	0.9714	0.4227	1.4123	1.6773	1.3236	Intensity >9.5
	7.1	S1	(40+40)x10	200	1.2939	1.7421	1.0166	0.3362	0.9919	1.7788	1.2907	-
	7.1	S1	(40+40)x10	220	1.2723	1.7013	0.9836	0.3862	1.0016	1.7368	1.2673	-
	7.1	S1	(40+40)x10	240	1.3939	1.6670	0.9846	0.4359	1.4245	1.6852	1.3272	Intensity >9.5
	7.2	S1	(40+40)x10	180	1.2679	1.7097	1.0012	0.3911	0.9949	1.7232	1.2679	-
	7.2	S1	(40+40)x10	200	1.2705	1.6809	0.9515	0.4293	1.0527	1.6895	1.2552	-
	7.2	S1	(40+40)x10	220	1.5578	1.4639	0.9660	0.5037	1.9800	1.6578	1.4141	Intensity >9.5
	7.3	S1	(40+40)x10	140	1.2838	1.7459	1.0055	0.3415	0.9589	1.7704	1.2829	-
	7.3	S1	(40+40)x10	160	1.2724	1.6887	0.9882	0.3929	1.0230	1.7156	1.2627	-
	7.3	S1	(40+40)x10	180	1.3952	1.6493	0.9723	0.4759	1.4547	1.6517	1.3218	Intensity >9.5
	7.4	S1	(40+40)x10	120	1.3326	1.8624	1.0219	0.3466	0.9658	1.7525	1.3143	-
	7.4	S1	(40+40)x10	140	1.2672	1.6828	0.9729	0.4225	1.0262	1.6936	1.2553	-
	7.4	S1	(40+40)x10	160	1.5917	1.6419	0.9415	0.5025	1.9600	1.6012	1.4311	Intensity >9.5

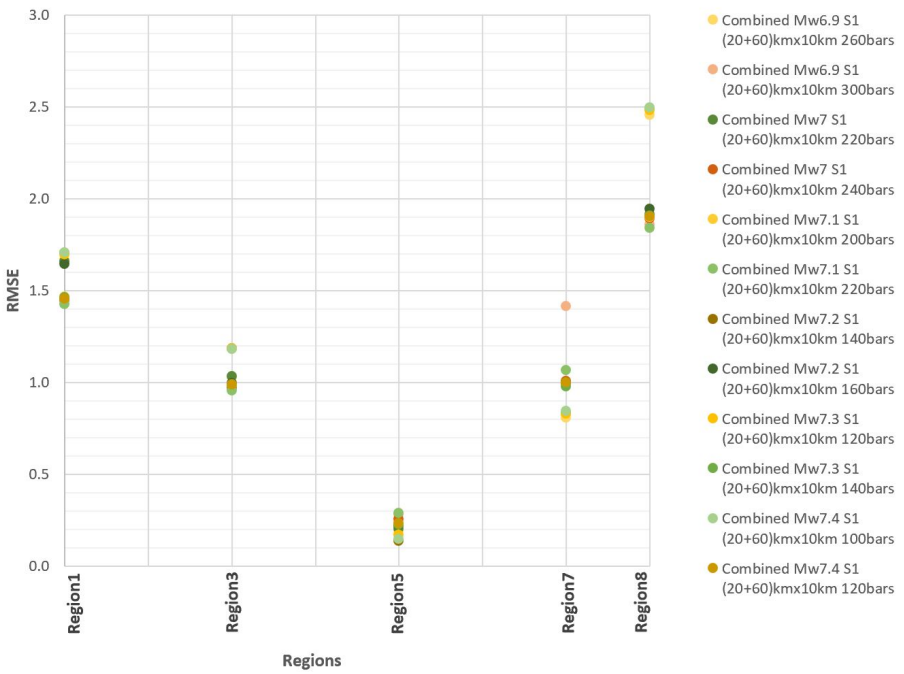

Figure 5.26. The 1766 Earthquake Combined Scenario Case 1 Assessment

future developments.

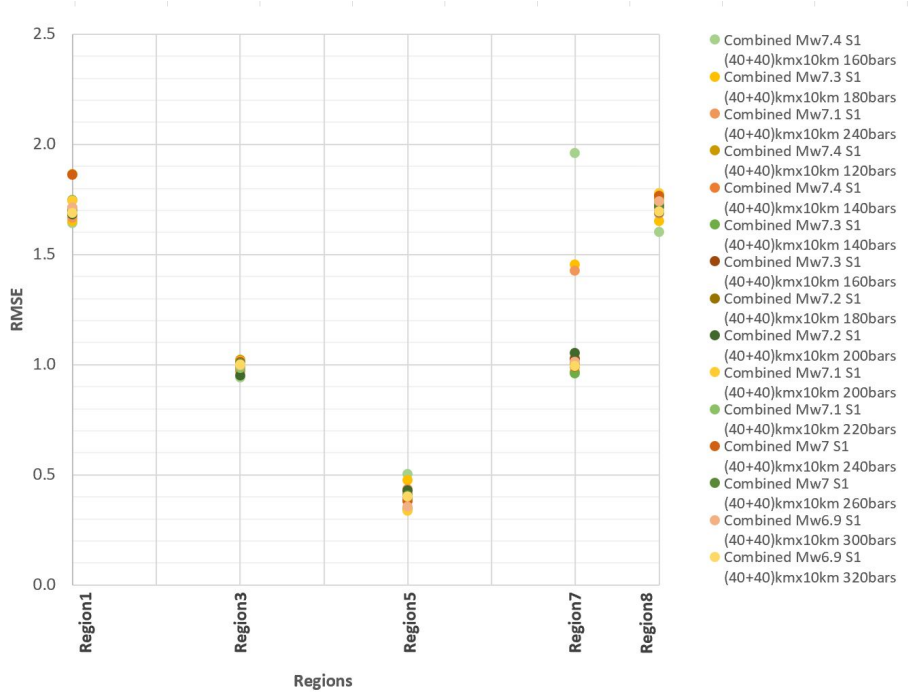

Figure 5.27. The 1766 Earthquake Combined Scenario Case 2 Assessment

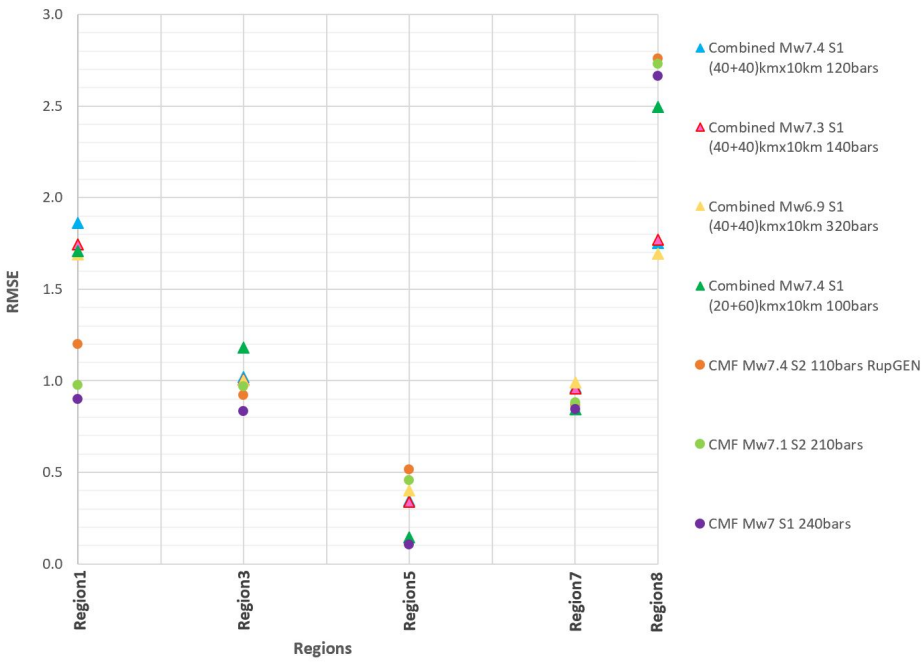

Figure 5.28. The 1766 Earthquake Final Assessment

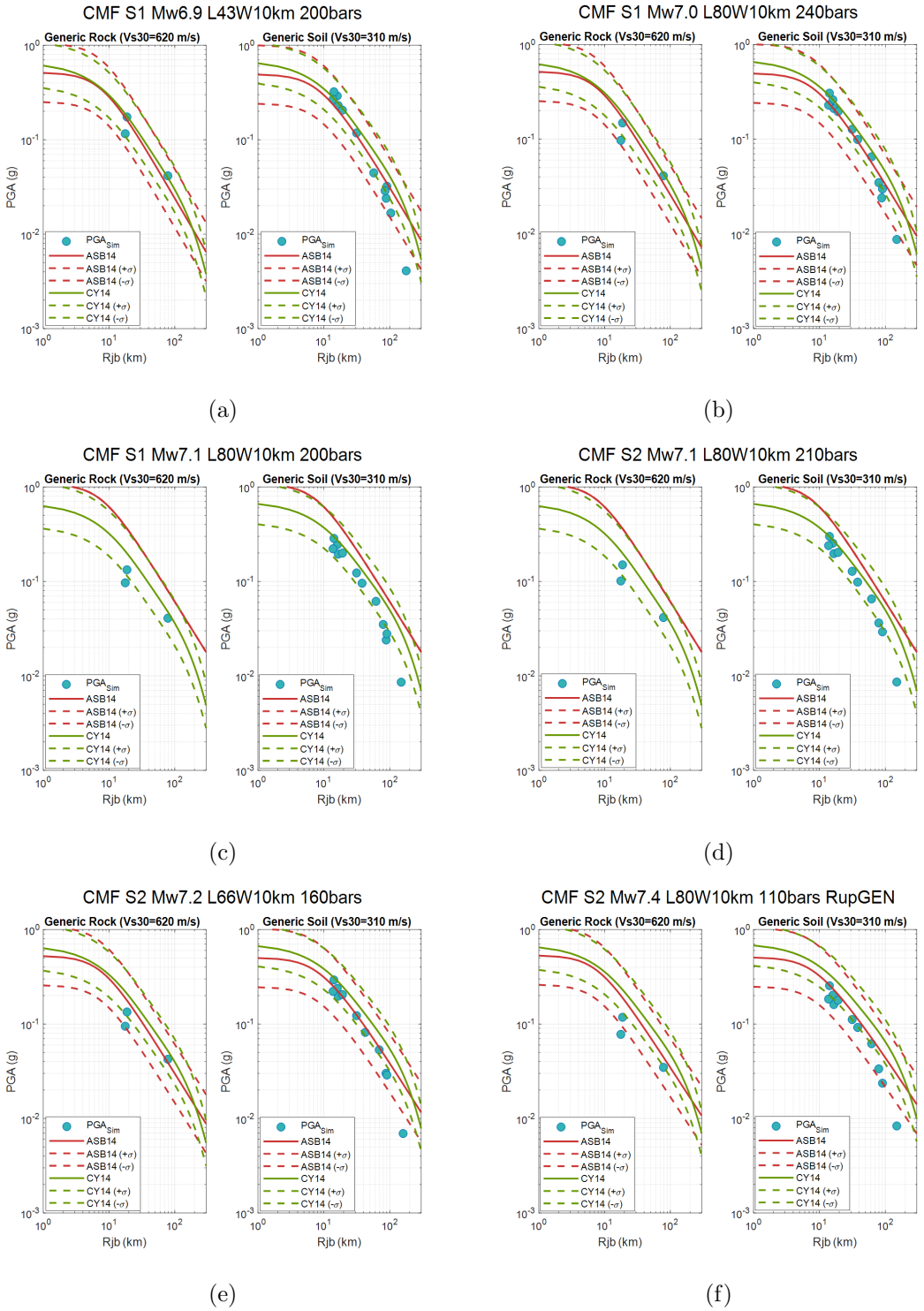

Figure 5.29. Comparison of the best estimated simulation scenarios with GMMs for the 1766 Earthquake for the CMF (a) S1 Scenario with Mw 6.9 (b) S1 Scenario with Mw 7.0 (c) S1 Scenario, with Mw 7.1 (d) S2 Scenario with Mw 7.1 (e) S2 Scenario with Mw 7.2 (66 km Rupture) (f) S2 Scenario with Mw 7.4 RupGEN

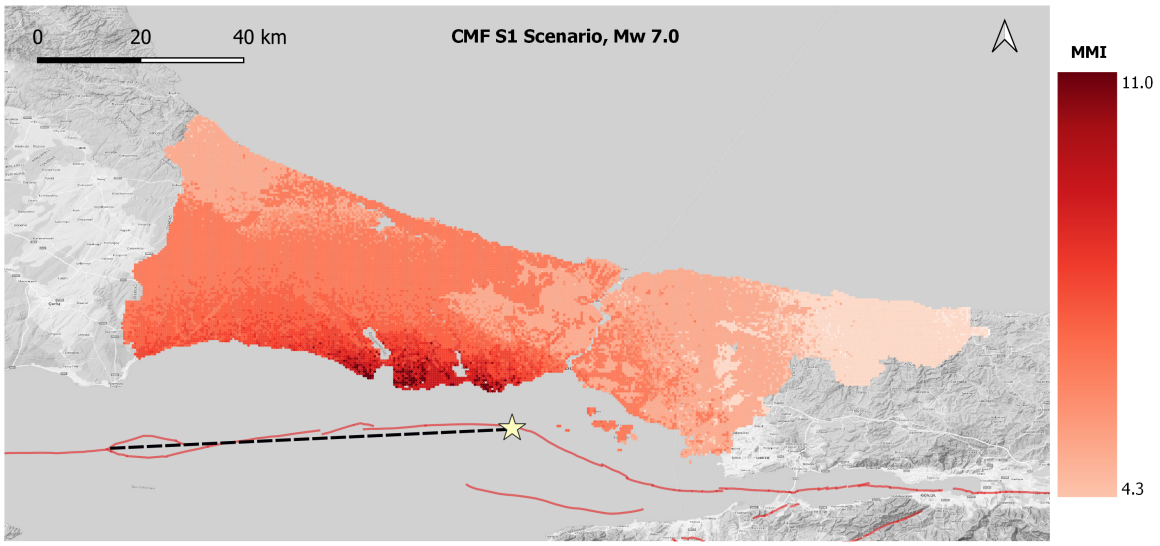

(a)

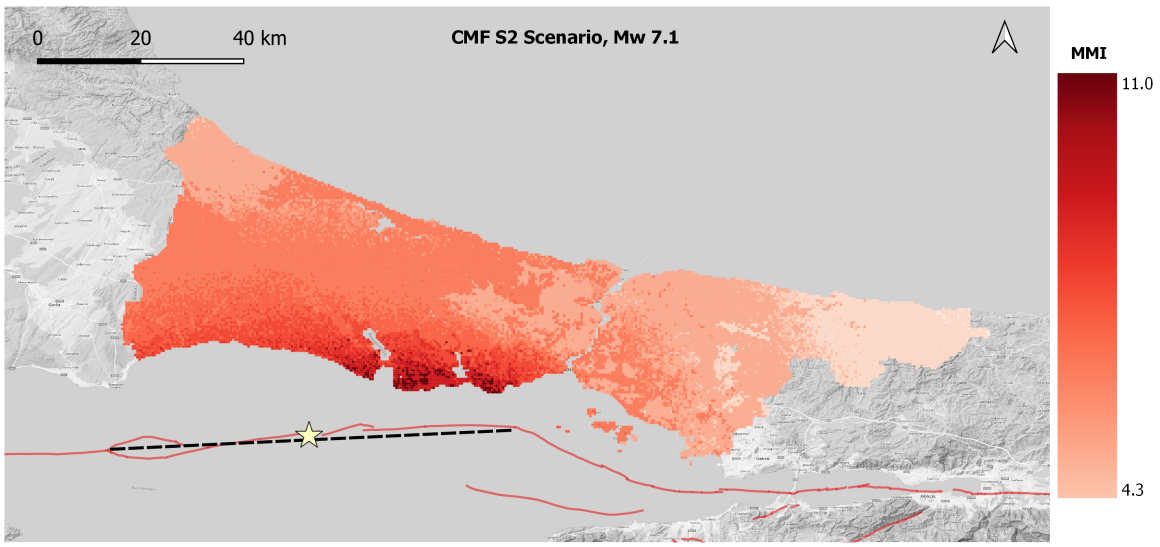

(b)

Figure 5.30. The 1766 Earthquake Stochastic Based Intensity Distribution for the CMF (a) S1 Scenario, (b) S2 Scenario

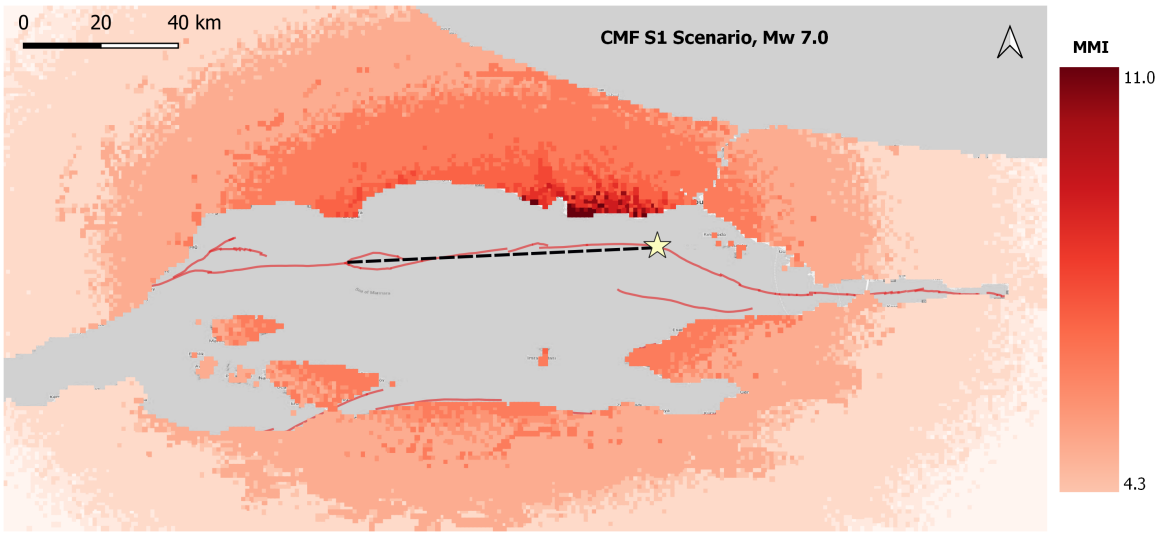

(a)

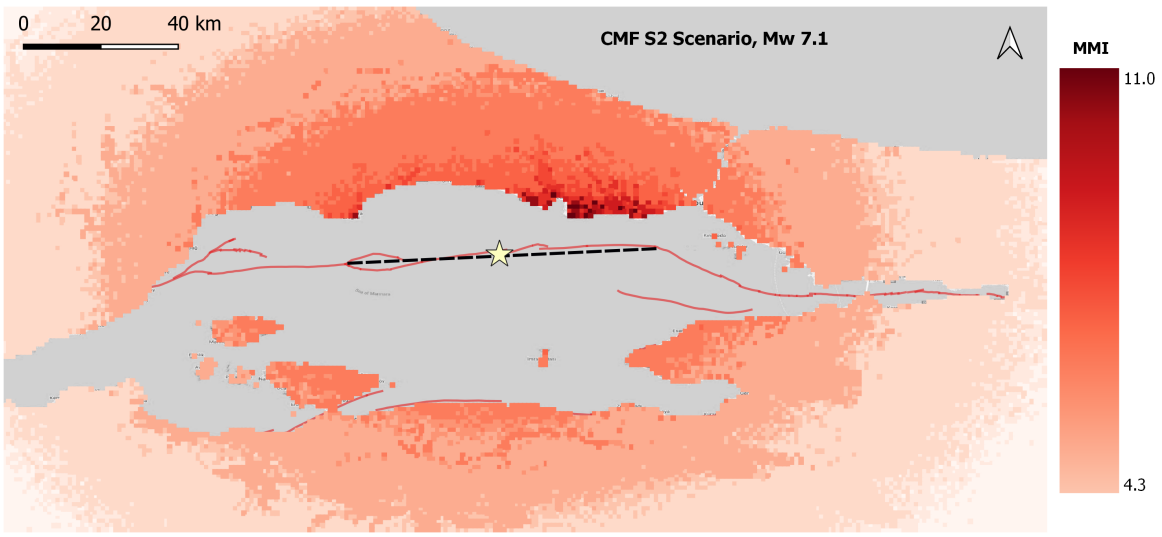

(b)

Figure 5.31. The 1766 Earthquake Stochastic Based Intensity Distribution for the CMF (a) S1 Scenario, (b) S2 Scenario

5.3. 10 September 1509 Earthquake

Seven different regions were formed for the 1509 earthquake as visualized in Figure 5.32. The number of intensity points for the 1509 earthquake was small due to the scarcity of damage information. For that reason, in Regions 2, 5, and 6 there was only one intensity point; in Regions 1 and 8 there were two intensity points; in Region 3 there was three and in Region 7 (Istanbul) there was four intensity points.

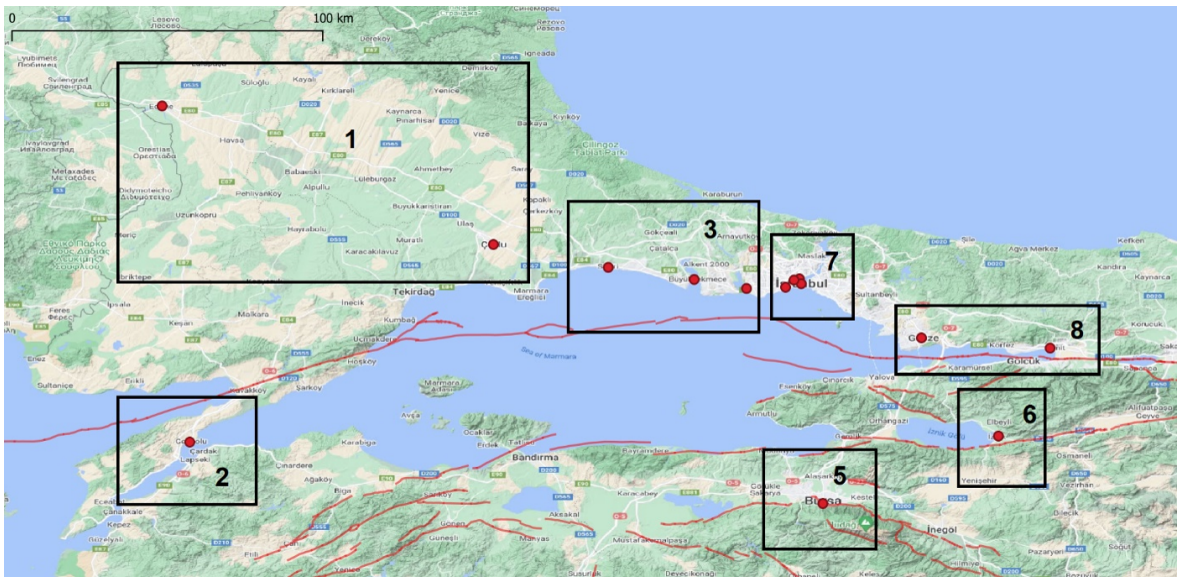

Figure 5.32. RMSE Regions of the 1509 Earthquake

As discussed before, the faults that the 1509 earthquake was most likely associated with, were estimated to be the CMF and the PIS. We started our analysis with two likely epicenters along the CMF, represented as S1 and S2. They were located 80 km away from each other. We also evaluated the combined rupture of CMF and the PIS. Figure 5.33 visualizes these scenarios.

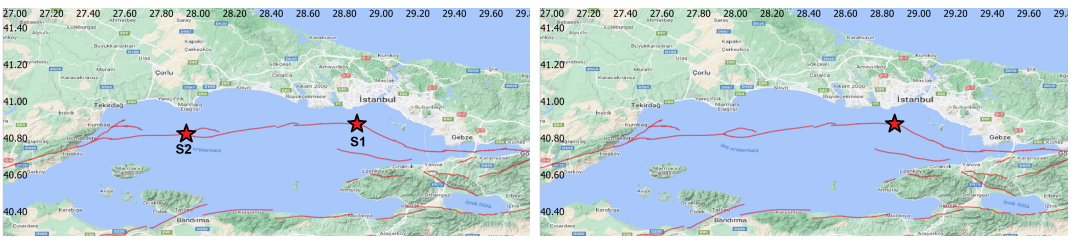

(a) (b)

Figure 5.33. Representation of Estimated Epicenter locations for the 1509 Earthquake (a) the CMF Scenarios (b) Combined Scenario

For scenarios S1 and S2, we kept the rupture length as 80 km. Fault width was 10 km. We increased magnitudes and stress drops incrementally. As might be remembered from previous analyses, the RMSE systematically decreased with increasing magnitudes and stress drops. Moreover we stopped the analysis and any further increment when the intensity at any point exceeded 10.5. Table 5.24 and Figure 5.34 represent the results for scenario S1. Table 5.25 lists RMSEs for scenario S2 and Figure 5.35 is their illustration. For scenario S1, Mw 7.3 and 170 bar stress drop combination resulted in the lowest errors. For scenario S2, we had the best estimations with Mw 7.4 and 140 bar stress drop. On the other hand, we observed that their error estimations were almost the same. Similar to the 1894 earthquake, the effect of the epicenter was not dominant in our model. Therefore we decided to move on to the next step with only scenario S1.

Table 5.24. The 1509 Earthquake Magnitude and Stress Drop Assessment for Scenario S1 on the CMF

Fault	**Mw**	**Epicenter**	**$\Delta\sigma$ (bar)**	**RMSE**	**R1**	**R2**	**R3**	**R5**	**R6**	**R7**	**R8**	**RMSE_R**	**Comment**
CMF	7.6	S1	80	2.2950	2.0345	1.0526	1.0856	1.0381	1.7177	2.6769	3.3807	2.0371	-
	7.6	S1	90	2.2014	1.9918	1.0023	1.1862	0.9711	1.6577	2.4502	3.3269	1.9691	-
	7.6	S1	100	2.1936	1.9719	0.9632	1.7691	0.3878	1.6274	2.2546	3.2659	1.9454	Intensity > X
	7.5	S1	100	2.2164	2.0075	1.0381	1.1461	0.9800	1.6826	2.4776	3.3497	1.9846	-
	7.5	S1	110	2.2012	2.0000	0.9998	1.2408	0.9829	1.6710	2.4313	3.3140	1.9709	-
	7.5	S1	120	2.2064	1.9653	0.9571	1.7800	0.9135	1.6048	2.2453	3.2838	1.9705	Intensity > X
	7.4	S1	120	2.1296	2.0054	1.0349	1.1596	0.9990	1.6886	2.4618	3.3356	1.9811	-
	7.4	S1	130	2.1984	1.9932	1.0256	1.2797	0.9288	1.6377	2.4260	3.3041	1.9643	-
	7.4	S1	140	2.2067	1.9677	0.9265	1.7991	0.4048	1.6206	2.2775	3.2753	1.9520	Intensity > X
	7.3	S1	160	2.1406	1.9812	0.9587	1.3028	0.9151	1.6285	2.2513	3.3123	1.9299	-
	7.3	S1	170	2.1172	1.9745	0.9329	1.2923	0.8940	1.6287	2.2244	3.2673	1.9091	-
	7.3	S1	180	2.1856	1.9537	0.9160	1.8985	0.3647	1.5758	2.1851	3.2476	1.9346	Intensity > X
	7.2	S1	190	2.1848	1.9758	0.9690	1.2580	0.9491	1.6447	2.4054	3.3024	1.9538	-
	7.2	S1	200	2.1227	1.9598	0.9678	1.3070	0.8946	1.6045	2.2397	3.2706	1.9114	-
	7.2	S1	210	2.1830	1.9625	0.9370	1.8225	0.3746	1.5968	2.2109	3.2528	1.9350	Intensity > X
	7.1	S1	190	2.2918	2.0155	1.0272	1.1052	1.0209	1.7163	2.6810	3.3688	2.0306	-
	7.1	S1	200	2.2821	2.0086	1.0300	1.1694	0.9905	1.6931	2.6503	3.3560	2.0212	-
	7.1	S1	210	2.2854	1.9921	1.0080	1.7130	1.0085	1.6803	2.4554	3.3307	2.0312	Intensity X

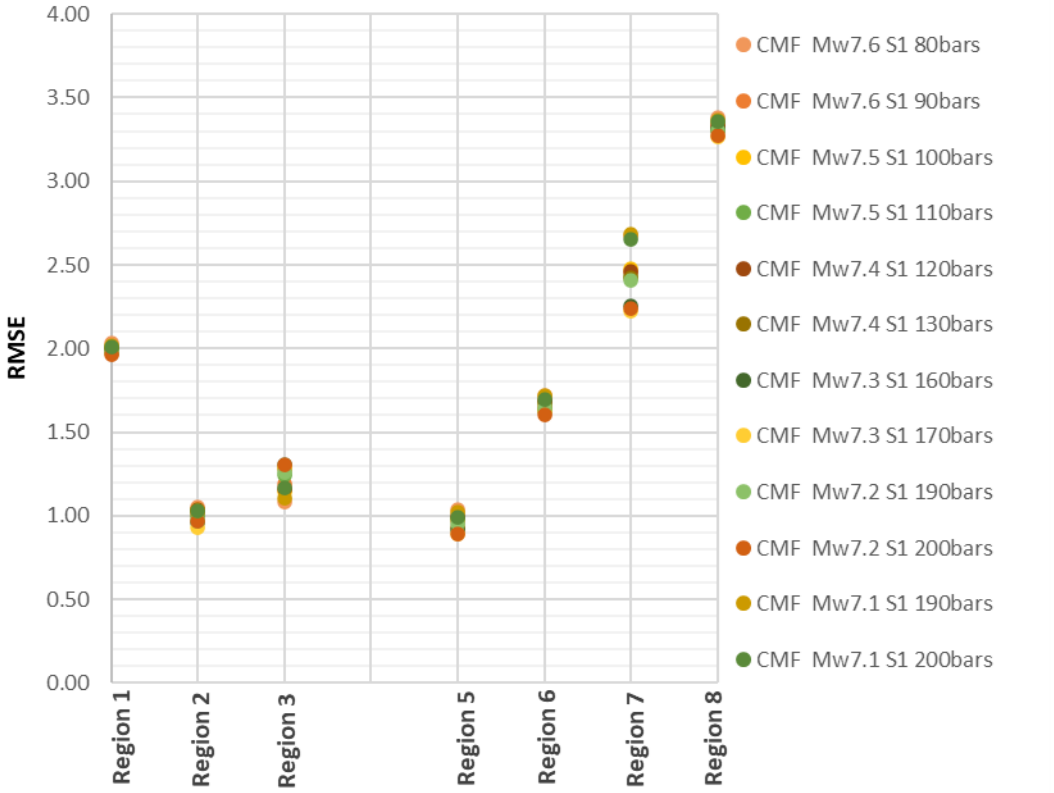

Figure 5.34. The 1509 Earthquake, Scenario S1 on the CMF, Magnitude and Stress Drop Assessment

Table 5.25. The 1509 Earthquake Magnitude and Stress Drop Assessment for Scenario S2 on the CMF

Fault	Mw	Epicenter	$\Delta\sigma$ (bar)	RMSE	R1	R2	R3	R5	R6	R7	R8	RMSE_R	Comment
CMF	7.6	S2	80	2.2912	2.0203	1.0232	1.1176	1.0163	1.7007	2.6783	3.3665	2.0287	-
	7.6	S2	90	2.1988	1.9932	0.9849	1.1820	0.9745	1.6660	2.4486	3.3191	1.9668	-
	7.6	S2	100	2.2121	1.9656	0.9453	1.8129	0.9100	1.6229	2.2442	3.2806	1.9750	Intensity > X
	7.5	S2	100	2.2734	2.0099	1.0118	1.1509	0.9922	1.6829	2.6314	3.3615	2.0153	-
	7.5	S2	110	2.1445	1.9748	0.9837	1.2336	0.9599	1.6409	2.2881	3.3088	1.9342	-
	7.5	S2	120	2.1815	1.9629	0.9274	1.7847	0.3708	1.6110	2.2239	3.2580	1.9343	Intensity > X
	7.4	S2	130	2.1101	1.9940	1.0043	1.2244	0.9439	1.6513	2.4185	3.3064	1.9597	-
	7.4	S2	140	2.1227	1.9646	0.9455	1.2637	0.9285	1.6132	2.2523	3.2723	1.9122	-
	7.4	S2	150	2.1876	1.9586	0.9336	1.8705	0.3491	1.6060	2.2048	3.2424	1.9377	Intensity > X
	7.3	S2	150	2.1949	1.9868	1.0077	1.1943	0.9422	1.6849	2.4306	3.3228	1.9663	-
	7.3	S2	160	2.1241	1.9724	0.9809	1.2839	0.3886	1.6430	2.2630	3.2885	1.9006	-
	7.3	S2	170	2.2849	1.9676	0.9296	2.2204	0.4097	1.6032	2.2503	3.2771	2.0074	Intensity > X
	7.2	S2	160	2.2833	2.0128	1.0356	1.1466	1.0163	1.7021	2.6515	3.3617	2.0248	-
	7.2	S2	170	2.2101	1.9985	1.0156	1.1668	0.9711	1.6760	2.4645	3.3426	1.9779	-
	7.2	S2	180	2.3342	1.9861	0.9915	2.0633	0.9223	1.6530	2.4295	3.3160	2.0586	Intensity > X
	7.1	S2	170	2.3341	2.0364	1.0568	0.8815	1.0674	1.7461	2.8175	3.4017	2.0612	-
	7.1	S2	180	2.2917	2.0298	1.0356	0.9196	1.0431	1.7252	2.7060	3.3964	2.0340	-
	7.1	S2	190	2.3452	2.0098	1.0057	1.6049	1.0103	1.6913	2.6522	3.3662	2.0658	Intensity > X

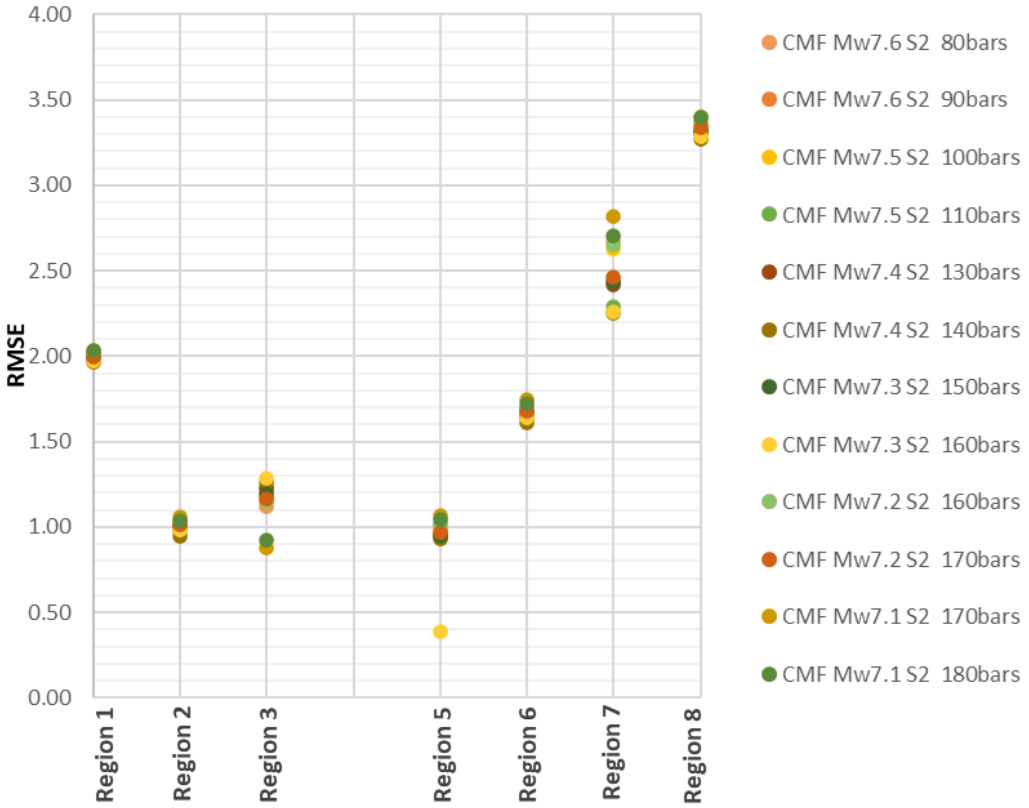

Figure 5.35. The 1509 Earthquake, Scenario S2 on the CMF, Magnitude and Stress Drop Assessment

In the next step, we considered different rupture lengths as we did in the previous simulations. We correlated the magnitudes and rupture lengths with the relation given by Leonard (2010) while stress drop was increased incrementally. The epicentral location was kept as illustrated with S1 in Figure 5.33a. We first considered only the CMF. Findings were summarized in Table 5.26 and the errors were shown in Figure 5.36. In this scenario, the best estimations were obtained with the magnitude Mw 7.6 and rupture length 115 km along the CMF, in a rupture starting at S1 and travelling to the west. This scenario resulted in lower errors than the previous 80 km rupture scenarios. The best-modelled Regions were 1, 2 and 5, which corresponded to western and southeastern regions. This analysis showed that the 1509 earthquake had a longer rupture than the 1766 event, the rupture length of which we estimated as 80 km along the CMF.

Table 5.26. The 1509 Earthquake, Different Rupture Dimensions for Scenario S1 on the CMF

Fault	Mw	Epicenter	L(km)x W(km)	$\Delta\sigma$ (bar)	RMSE	R1	R2	R3	R5	R6	R7	R8	RMSE_R	Comment
CMF	7.6	S1	115x10	90	2.3840	1.8985	0.2010	0.8740	1.0770	1.7388	2.8607	3.7030	2.0870	-
	7.6	S1	80x10	90	2.2014	1.9918	1.0023	1.1862	0.9711	1.6577	2.4502	3.3269	1.9691	-
	7.6	S1	115x10	130	2.0586	1.7880	0.0496	1.3039	0.3436	1.6122	2.2206	3.2520	1.8175	-
	7.5	S1	100x10	110	2.2599	1.9374	0.3512	1.1570	1.0048	1.6966	2.6686	3.3447	1.9789	-
	7.5	S1	80x10	110	2.2012	2.0000	0.9998	1.2408	0.9829	1.6710	2.4313	3.3140	1.9709	-
	7.5	S1	100x10	120	2.1675	1.9143	0.3140	1.2486	0.9389	1.6350	2.4271	3.3056	1.9159	-
	7.4	S1	87x10	130	2.0765	1.9749	0.9502	1.2394	0.9777	1.6644	2.3088	3.3172	1.9420	-
	7.4	S1	80x10	130	2.1984	1.9932	1.0256	1.2797	0.9288	1.6377	2.4260	3.3041	1.9643	-
	7.4	S1	87x10	140	2.1021	1.9489	0.3875	1.2326	0.9103	1.6086	2.2408	3.2892	1.8794	-
	7.3	S1	80x10	140	2.2029	2.0081	1.0482	0.9826	0.9839	1.7143	2.4764	3.3608	1.9796	-
	7.3	S1	75x10	130	2.2847	2.0442	1.0777	1.1275	1.0301	1.6968	2.6424	3.3655	2.0305	-
	7.3	S1	75x10	140	2.2155	2.0336	1.0559	1.1877	1.0035	1.6773	2.4632	3.3241	1.9856	-
	7.2	S1	80x10	180	2.1541	1.9901	0.9630	1.1798	0.9794	1.6714	2.3175	3.3214	1.9433	-
	7.2	S1	66x10	180	2.1413	2.0342	1.0538	1.2812	0.9285	1.6281	2.2476	3.2844	1.9362	-
	7.2	S1	66x10	170	2.2292	2.0482	1.0729	1.7070	0.9618	1.6581	2.2684	3.3211	2.0039	Intensity > X
	7.1	S1	80x10	180	2.3318	2.1869	1.0446	1.0951	1.0377	1.7347	2.6978	3.4081	2.0720	-
	7.1	S1	57x10	180	2.1918	2.2520	1.1628	1.2616	0.9700	1.6592	2.2769	3.2980	1.9918	-
	7.1	S1	57x10	170	2.2123	2.2846	1.1764	1.1871	1.0075	1.6626	2.3224	3.3334	2.0106	-

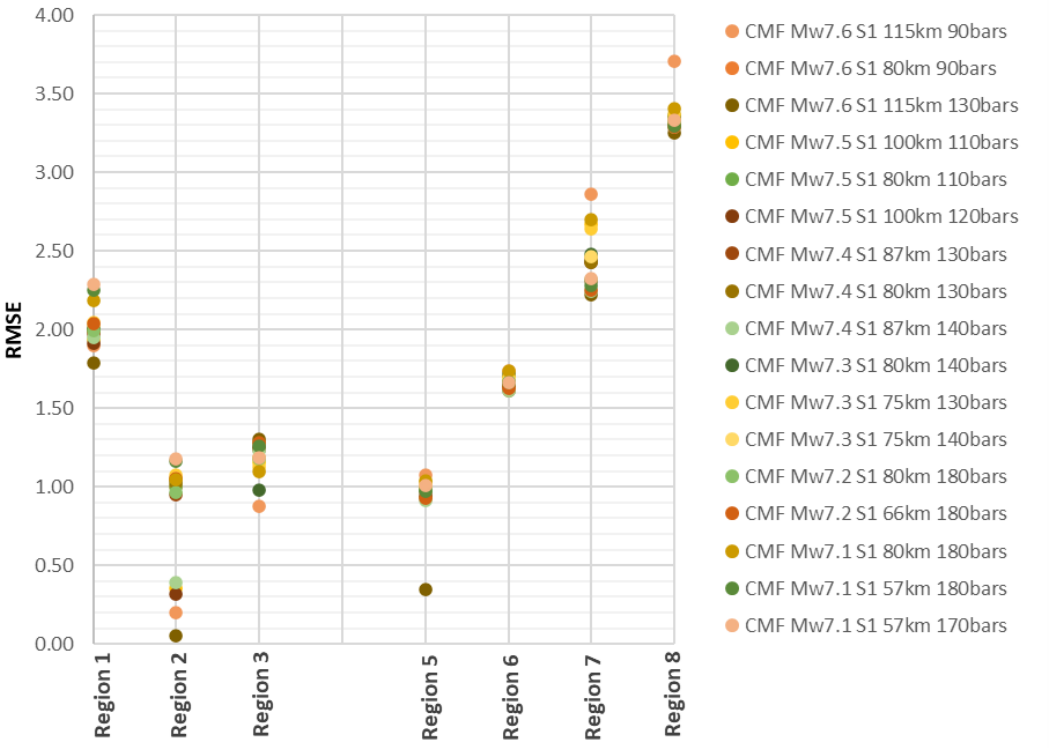

Figure 5.36. The 1509 Earthquake Rupture Dimension Assessment

Up to this point, slip distribution was defined as random as per EXSIM12. In order to test its effect, RupGEN generated slips were also implemented. RMSEs for

scenario S1 with a 80 km rupture are given in Table 5.27 and represented in Figure 5.37. We had the lowest errors with RupGEN generated slip distribution for the combination of Mw 7.4 and 140 bar stress drop in 80 km rupture scenario. However there were no significantly large differences among the combinations except in Regions 2 and 5.

Table 5.27. The 1509 Earthquake Slip Assessment for Scenario S1 on CMF

Fault	Mw	Epicenter	$\Delta\sigma$ (bar)	Slip	RMSE	R1	R2	R3	R5	R6	R7	R8	RMSE_R	Comment
CMF	7.6	S1	100	RupGEN	2.1017	1.9201	0.3795	1.2998	0.3926	1.6132	2.2741	3.2708	1.8573	-
	7.6	S1	90	Random	2.2014	1.9918	1.0023	1.1862	0.9711	1.6577	2.4502	3.3269	1.9691	-
	7.6	S1	90	RupGEN	2.1922	1.9472	0.9237	1.1772	0.9414	1.6417	2.4569	3.3281	1.9539	-
	7.5	S1	130	RupGEN	2.0806	1.9006	0.3533	1.4463	0.3629	1.5808	2.1934	3.2232	1.8384	-
	7.5	S1	110	Random	2.2012	2.0000	0.9998	1.2408	0.9829	1.6710	2.4313	3.3140	1.9709	-
	7.5	S1	110	RupGEN	2.2190	1.9446	0.9198	1.2190	0.9171	1.6729	2.5239	3.3186	1.9689	-
	7.4	S1	160	RupGEN	1.9869	1.8870	0.3349	1.3908	0.3406	1.5530	2.1775	3.2202	1.8223	-
	7.4	S1	130	Random	2.1984	1.9932	1.0256	1.2797	0.9288	1.6377	2.4260	3.3041	1.9643	-
	7.4	S1	130	RupGEN	2.1608	1.9336	0.3985	1.2061	0.4018	1.6549	2.4452	3.3076	1.8963	-
	7.3	S1	160	RupGEN	2.1711	1.9369	0.4000	1.2458	0.9258	1.6337	2.4223	3.3138	1.9212	-
	7.3	S1	170	Random	2.1172	1.9745	0.9329	1.2923	0.8940	1.6287	2.2244	3.2673	1.9091	-
	7.3	S1	170	RupGEN	2.0953	1.9212	0.3713	1.2661	0.3920	1.6018	2.2658	3.2780	1.8528	-
	7.2	S1	190	RupGEN	2.2451	1.9392	0.3934	1.7062	0.9350	1.6325	2.4300	3.3135	1.9730	Intensity > X
	7.2	S1	200	Random	2.1227	1.9598	0.9678	1.3070	0.8946	1.6045	2.2397	3.2706	1.9114	-
	7.2	S1	200	RupGEN	2.1023	1.9206	0.3628	1.3035	0.3896	1.5987	2.2692	3.2824	1.8574	-
	7.1	S1	220	RupGEN	2.1764	1.9326	0.4032	1.2144	0.9525	1.6308	2.4422	3.3238	1.9254	-
	7.1	S1	200	Random	2.2821	2.0086	1.0300	1.1694	0.9905	1.6931	2.6503	3.3560	2.0212	-
	7.1	S1	200	RupGEN	2.2731	1.9613	0.9483	1.1263	0.9902	1.7051	2.6617	3.3574	2.0092	-

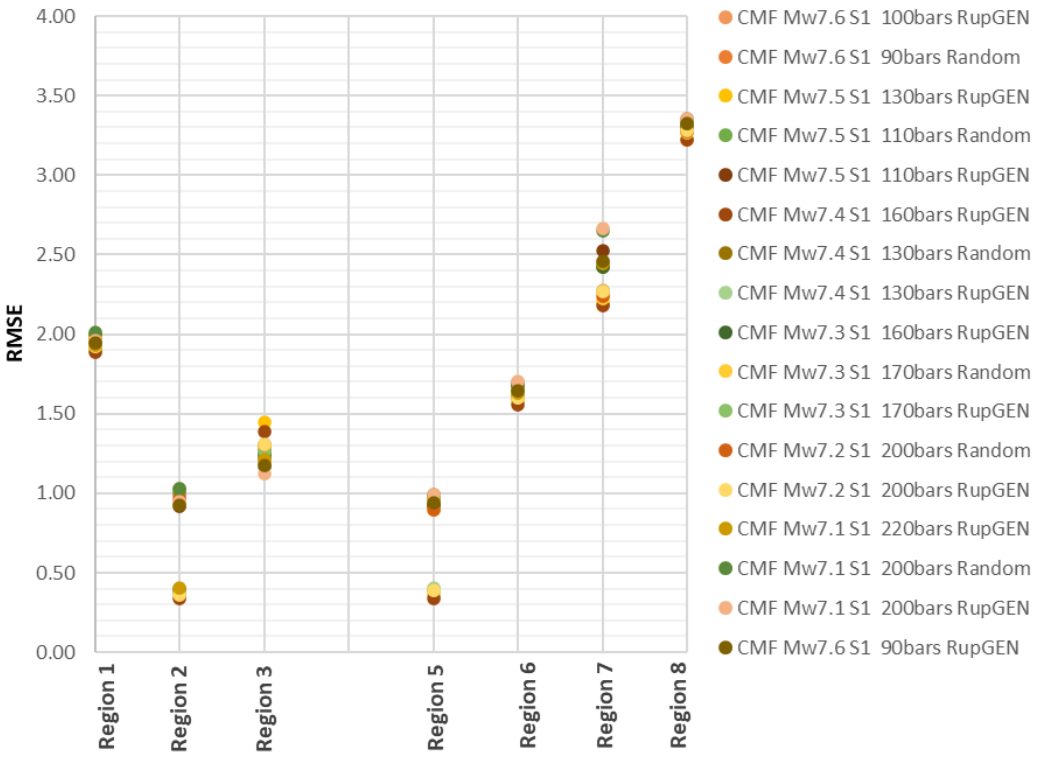

Figure 5.37. The 1509 Earthquake Slip Assessment for Scenario S1 on CMF

Even though better estimations were obtained with random slips for the 115 km rupture, there is no systematic improvement was observed between results obtained using EXSIM12 and RupGEN generated slip distributions. Results are given in Table 5.28 and Figure 5.38.

Table 5.28. The 1509 Earthquake Slip Assessment for Different Rupture Lengths for Scenario S1 on CMF

Fault	Mw	Epicenter	LxW	Slip	$\Delta\sigma$ (bar)	RMSE	R1	R2	R3	R5	R6	R7	R8	RMSE_R	Comment
	7.6	S1	115x10	RupGEN	120	2.1034	1.8507	0.1500	1.2212	0.9283	1.6577	2.2711	3.3114	1.8774	-
	7.6	S1	115x10	RupGEN	130	2.2014	1.9918	1.0023	1.1862	0.9711	1.6577	2.4502	3.3269	1.9691	-
	7.6	S1	115x10	Random	130	2.0891	1.8377	0.0833	1.3037	0.9308	1.6190	2.2402	3.2644	1.8611	-
	7.5	S1	110x10	RupGEN	130	2.2553	1.8839	0.2614	1.1554	0.9760	1.7011	2.6787	3.3471	1.9704	-
	7.5	S1	110x10	RupGEN	120	2.3163	1.9025	0.2900	1.0913	1.0261	1.6989	2.8318	3.3790	2.0096	-
	7.5	S1	110x10	Random	120	2.1675	1.9143	0.3140	1.2486	0.9389	1.6350	2.4271	3.3056	1.9159	-
	7.4	S1	87x10	RupGEN	150	2.1033	1.9114	0.3674	1.2140	0.9111	1.6577	2.4734	3.3183	1.9261	-
	7.4	S1	87x10	RupGEN	140	2.2615	1.9332	0.3924	1.1518	0.9771	1.6717	2.6800	3.3468	1.9767	-
	7.4	S1	87x10	Random	140	2.1021	1.9489	0.3875	1.2326	0.9103	1.6086	2.2408	3.2892	1.8794	-
CMF	7.3	S1	75x10	RupGEN	150	2.1170	1.9178	0.3552	1.4750	0.3488	1.5914	2.2449	3.2742	1.8668	-
	7.3	S1	75x10	RupGEN	140	2.4307	2.0262	1.0662	0.5234	1.0984	1.7868	2.9102	3.7657	2.1569	-
	7.3	S1	75x10	Random	140	2.2155	2.0336	1.0559	1.1877	1.0035	1.6773	2.4632	3.3241	1.9856	-
	7.2	S1	66x10	RupGEN	170	2.1507	2.2042	1.1155	1.2438	0.9364	1.6062	2.2150	3.2746	1.9543	-
	7.2	S1	66x10	Random	180	2.1413	2.0342	1.0538	1.2812	0.9285	1.6281	2.2476	3.2844	1.9362	-
	7.2	S1	66x10	RupGEN	180	2.3112	2.1993	1.1072	2.1822	0.9039	1.5987	2.2119	3.2644	2.0614	Intensity > X
	7.1	S1	57x10	RupGEN	190	2.3239	2.2496	1.1505	1.2038	0.9975	1.7119	2.6597	3.3309	2.0677	-
	7.1	S1	57x10	RupGEN	180	2.3762	2.2609	1.1511	1.1504	0.9786	1.7131	2.8034	3.3581	2.0972	-
	7.1	S1	57x10	Random	180	2.1918	2.2520	1.1628	1.2616	0.9700	1.6592	2.2769	3.2980	1.9918	-

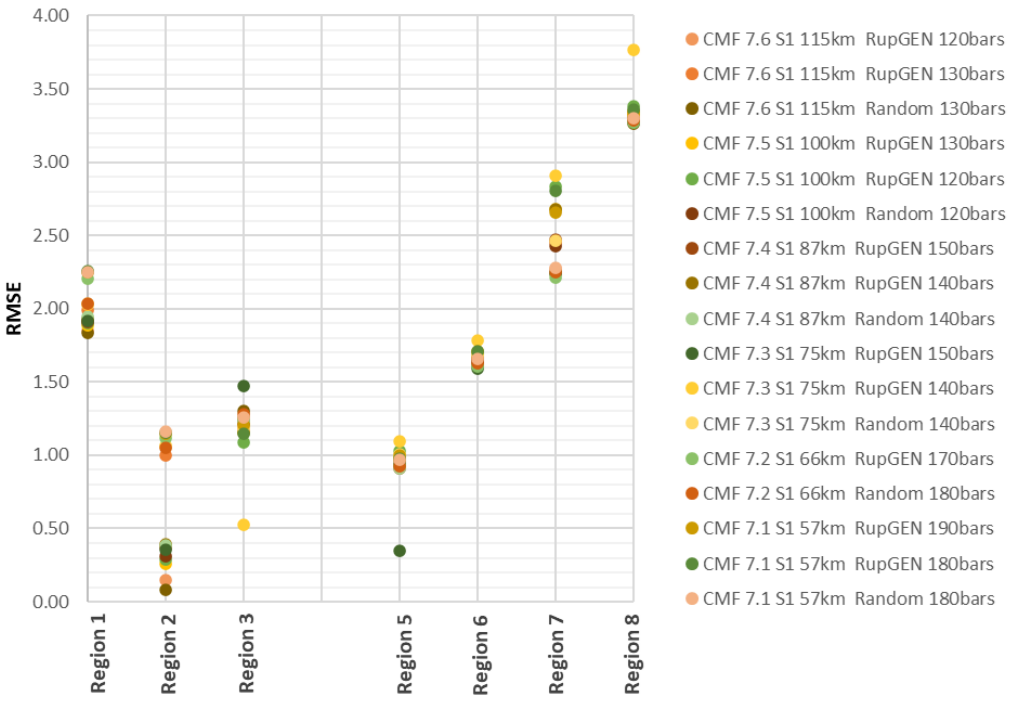

Figure 5.38. The 1509 Earthquake Slip Assessment for Different Rupture Lengths on CMF

For the combined mobilisation of two segments, involving the CMF and the PIS, a 120 km rupture length was considered that is composed of a 80 km rupture along the CMF and a 40 km rupture along the PIS. The epicenter was located at the intersection of these two segments (Figure 5.33b). We evaluated this scenario by changing the magnitudes and stress drops while other parameters were kept constant.

We tabulated the results of the combined rupture scenario in Table 5.29. Figure 5.39 illustrates RMSEs for this scenario. The optimum values were obtained with Mw 7.6 and 120 bar stress drop.

Table 5.29. The 1509 Earthquake Combined Rupture Scenario

Fault	**Mw**	**L(km) x W(km)**	**$\Delta\sigma$ (bar)**	**RMSE**	**R1**	**R2**	**R3**	**R5**	**R6**	**R7**	**R8**	**RMSE_R**	**Comment**
Combined	7.6	(80+40)x 10	100	1.7778	2.2708	1.1423	0.8998	0.1090	0.6201	1.9890	2.3257	1.5599	-
	7.6	(80+40)x 10	120	1.6780	2.2281	1.1113	1.0475	0.0304	0.5118	1.7363	2.2168	1.4875	-
	7.6	(80+40)x 10	140	1.7094	2.0331	1.0587	1.8542	0.0819	0.1036	1.5201	2.1243	1.4896	Intensity > X
	7.5	(80+40)x 10	120	1.7839	2.2788	1.1449	0.9244	0.1148	0.5989	1.9988	2.3192	1.5631	-
	7.5	(80+40)x 10	140	1.7054	2.2343	1.1096	1.1808	0.0328	0.5136	1.7334	2.2502	1.5095	-
	7.5	(80+40)x 10	160	1.7220	2.1817	1.0703	1.7768	0.0553	0.0639	1.5218	2.1382	1.5098	Intensity > X
	7.4	(80+40)x 10	140	1.7167	2.2849	1.1516	0.8857	0.1240	0.6093	1.9939	2.3292	1.5638	-
	7.4	(80+40)x 10	160	1.6950	2.2376	1.1081	1.0050	0.0435	0.5422	1.7776	2.2518	1.5010	-
	7.4	(80+40)x 10	180	1.7529	2.2009	1.0867	1.7757	0.0192	0.0418	1.5747	2.2018	1.5357	Intensity > X
	7.3	(80+40)x 10	160	1.7282	2.2401	1.1128	0.9756	0.1168	0.5965	1.8404	2.3215	1.5285	-
	7.3	(80+40)x 10	180	1.7134	2.2655	1.1331	0.9568	0.0619	0.5709	1.8116	2.2816	1.5189	-
	7.3	(80+40)x 10	200	1.7412	2.2251	1.1008	1.6146	0.0343	0.5229	1.6134	2.2125	1.5373	Intensity > X
	7.2	(80+40)x 10	180	1.9078	2.3056	1.1599	0.8672	0.1523	0.6559	2.1308	2.6894	1.6750	-
	7.2	(80+40)x 10	200	1.7823	2.2763	1.1334	0.9427	0.1187	0.6067	2.0002	2.3017	1.5600	-
	7.2	(80+40)x 10	220	1.7968	2.2550	1.1228	1.5200	0.0446	0.5608	1.8024	2.2690	1.5752	Intensity > X
	7.1	(80+40)x 10	220	1.8327	2.2922	1.1574	0.8832	0.1575	0.6396	2.1183	2.3552	1.5965	-
	7.1	(80+40)x 10	240	1.7791	2.2728	1.1342	0.9367	0.1145	0.5941	1.9873	2.3169	1.5590	-
	7.1	(80+40)x 10	260	1.7990	2.2452	1.1133	1.5351	0.0514	0.5613	1.8049	2.2733	1.5757	Intensity > X

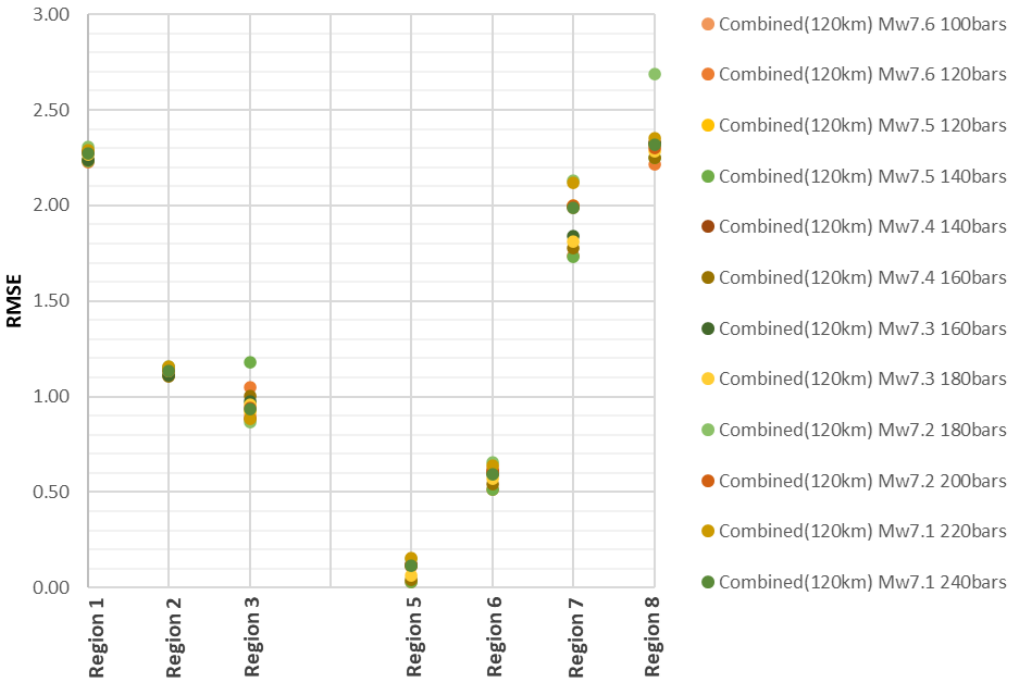

Figure 5.39. The 1509 Earthquake Magnitude and Stress Drop Assessment for the Combined Rupture Scenario

Figure 5.40 shows the RMSEs of the most reasonable scenarios that were discussed above. Apparently, the combined rupture scenario performed better than the others. It resulted in the lowest errors for six regions while yielding higher errors in Regions 1 and 2, which had more than about 100 km rupture distances.

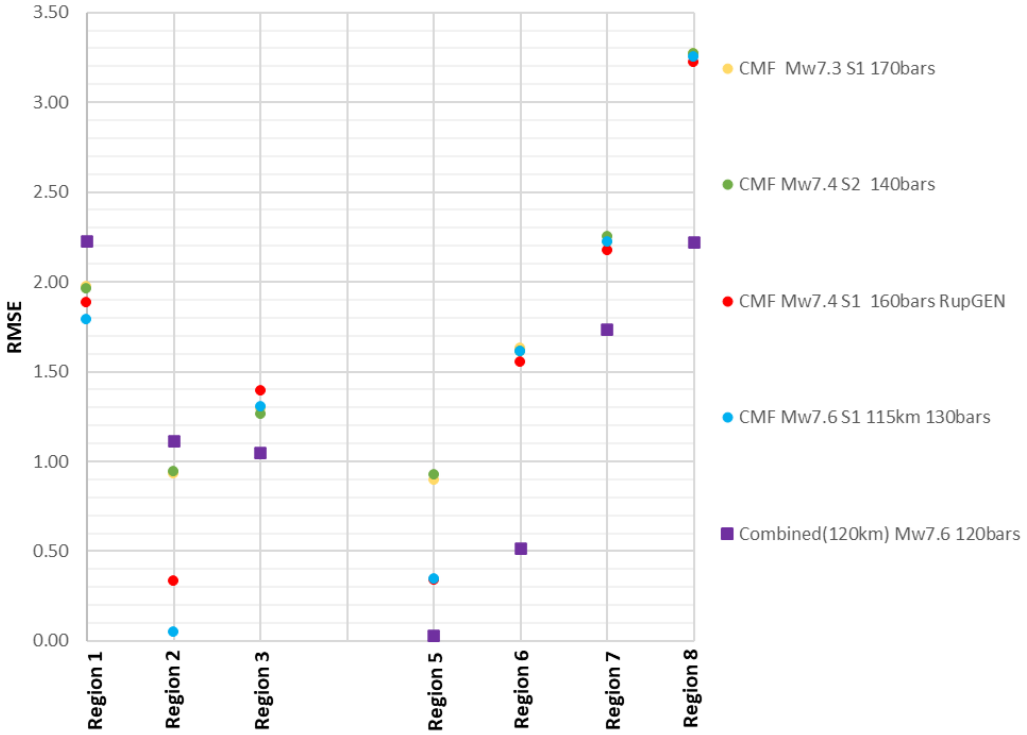

Figure 5.40. The 1509 Earthquake Final Assessment

We also compared our findings from the four best performing CMF scenarios with two ground motion models, namely Akkar et al., (2014) and Chiou and Youngs (2014). Figure 5.41 demonstrates this comparison with the GMMs in terms of PGA. Even though the best fit was associated with the Mw 7.3 scenario, its performance was not significantly different than the larger magnitude scenarios. For that reason, the preference among them was not sufficiently clear.

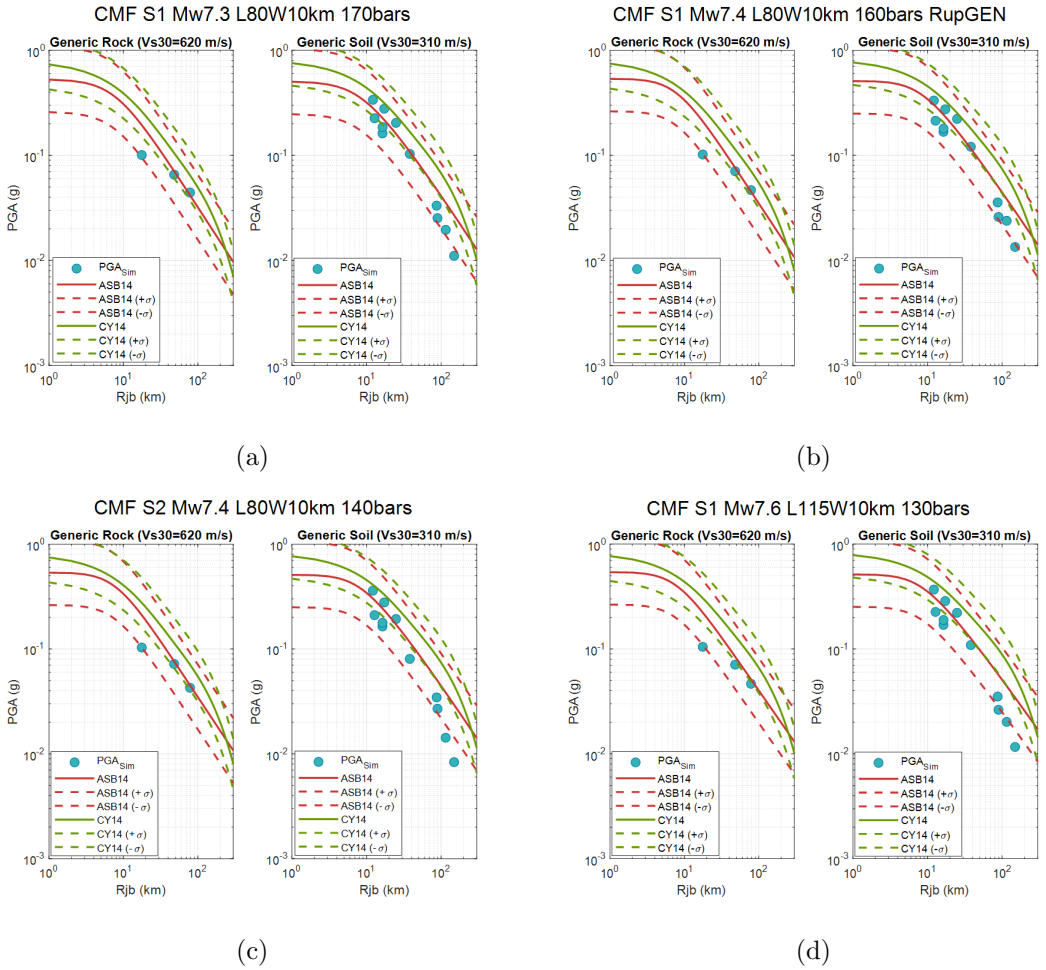

Figure 5.41. Comparison of the best estimating scenarios with GMMs for the 1509 Earthquake for the CMF (a) S1 Scenario with Mw 7.3 (b) S1 Scenario with Mw 7.4 Specialized Slip (c) S2 Scenario, with Mw 7.4 (d) S1 Scenario with Mw 7.6

Lastly, we produced regional intensity maps of the combined rupture scenario for Istanbul and greater Marmara. Findings are illustrated in Figure 5.42. The highest intensity points, which corresponded to 11.2, concentrated in Istanbul, Princes Islands and Çınarcık regions.

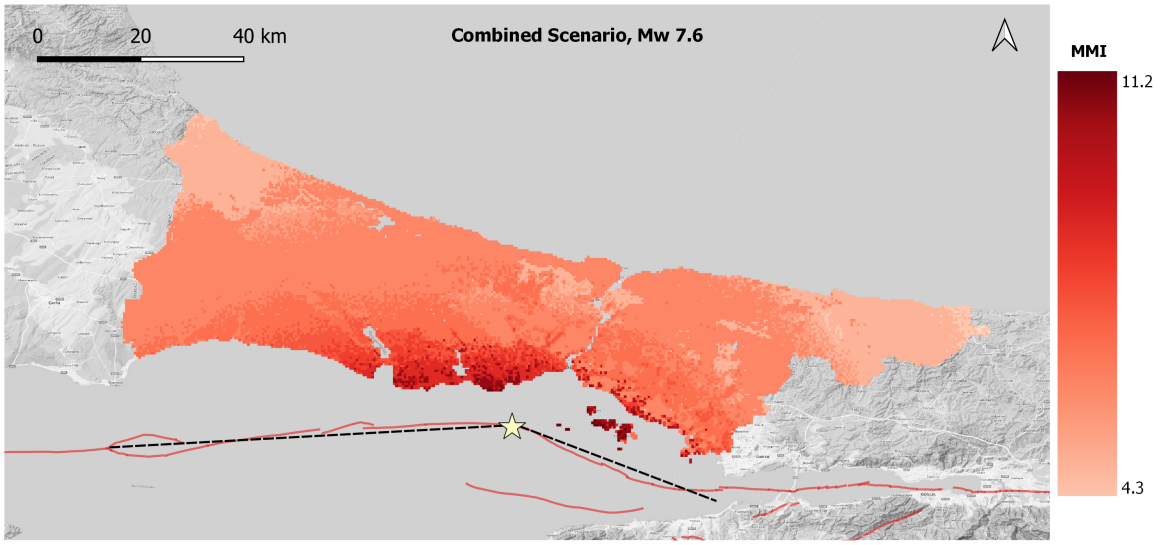

(a)

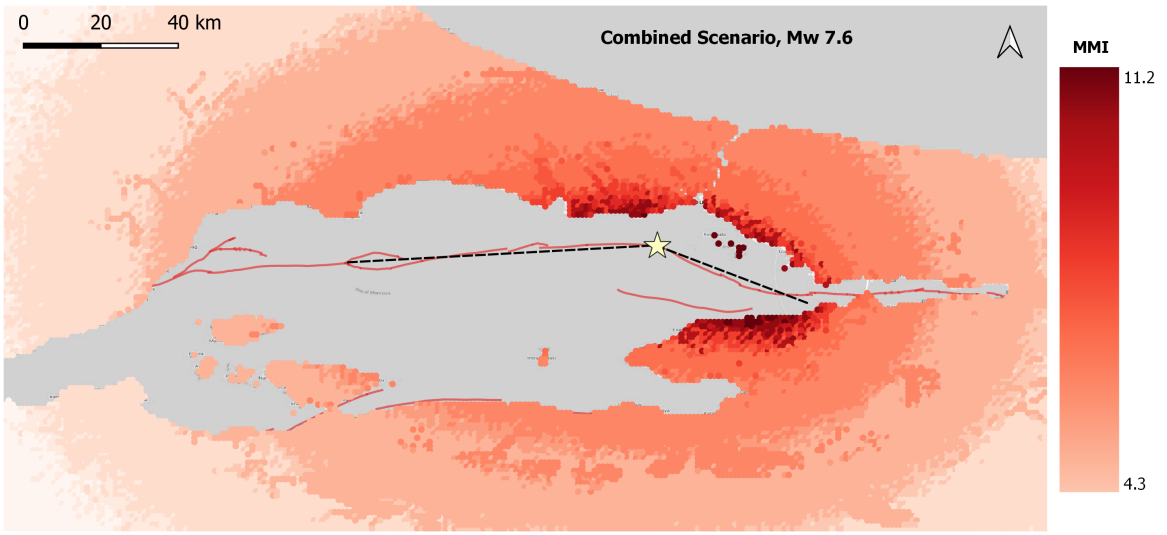

(b)

Figure 5.42. The 1509 Earthquake Synthetic Intensity Distribution for The Combined Rupture Scenario of Mw 7.6 for (a) Istanbul Region, (b) Marmara Region.

5.4. Chapter Results

We compared synthetic intensities obtained from the best performing rupture scenarios with the previously generated intensities by using the damage information (Section 3.2). These two intensity estimations were co-shown on the maps given in Figures 5.43 to 5.45, where the synthetic intensity level was represented in shades of

red, and the intensities obtained from damages were represented with circles.

For the 1894 earthquake, Figure 5.43 shows intensities obtained due to the rupture along the PIS and combined rupture scenarios. It resulted in largest intensities in the southern parts of the Marmara Sea reaching MMI XI at a few locations. On the other hand, the highest intensity was estimated as IX based on evaluation of descriptions of damage in Section 3.3.1. This overestimation must be due to the simplified fault definition, which is oriented more steeper to the south than its actual extension.

In the 1894 earthquake, there were intensity underestimations in the eastern part of the region (Figure 5.43). As previously mentioned, our errors were higher in the east and could not be fixed by changing scenarios or parameters. A similar situation was observed in the 1766 and 1509 earthquakes (Figures 5.44 and 5.45), which could originate from earthquake rupture heterogeneity or directivity and could not be reliably modelled by the approach that we followed.

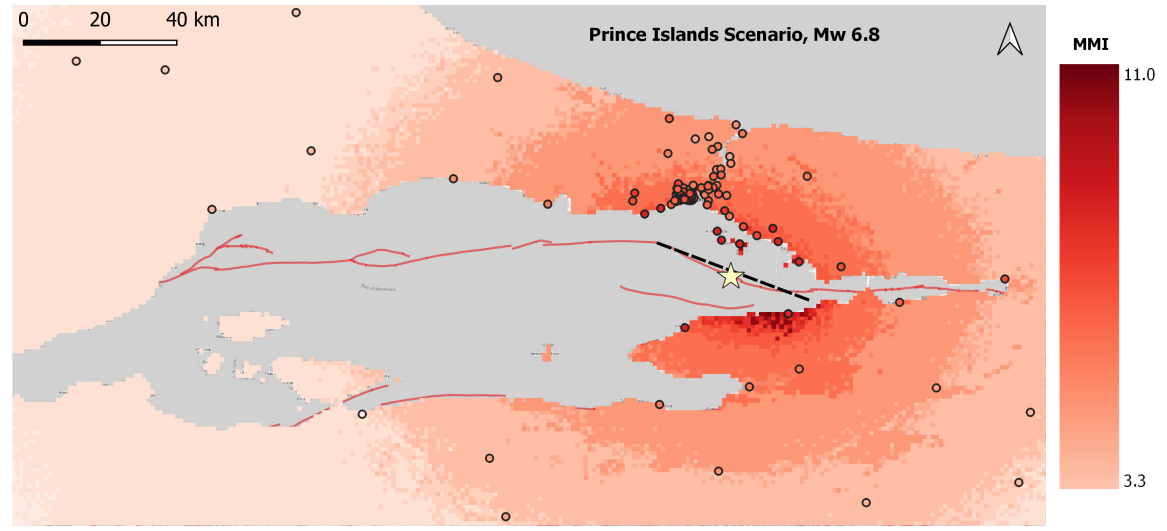

(a)

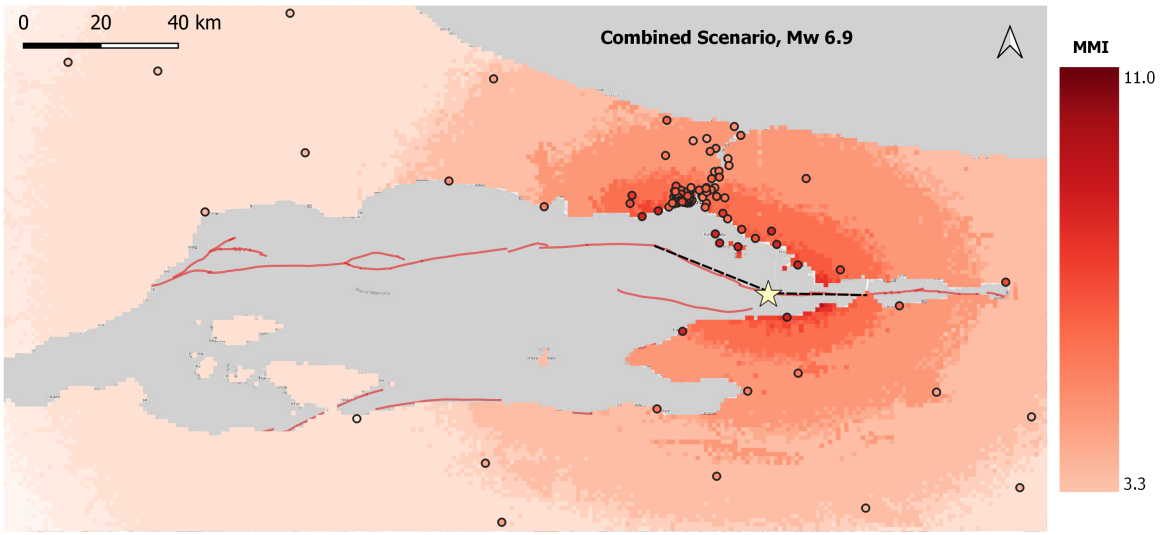

(b)

Figure 5.43. The 1894 Earthquake Synthetic Intensity Distribution for (a) the Prince Islands Scenario, (b) Combined Rupture Scenario (Circles Represent Intensities Estimated Using the Damage Information).

Figure 5.44 illustrates intensity estimations utilizing two well-performing CMF scenarios for the 1766 earthquake. Estimations obtained from the two scenarios along the CMF were not significantly different from each other. A similar observation was made for the 1894 earthquake simulation along the PIS (Section 5.1). This might indicate that the epicentral location might be less effective than variables, like magnitude,

stress drop and rupture length.

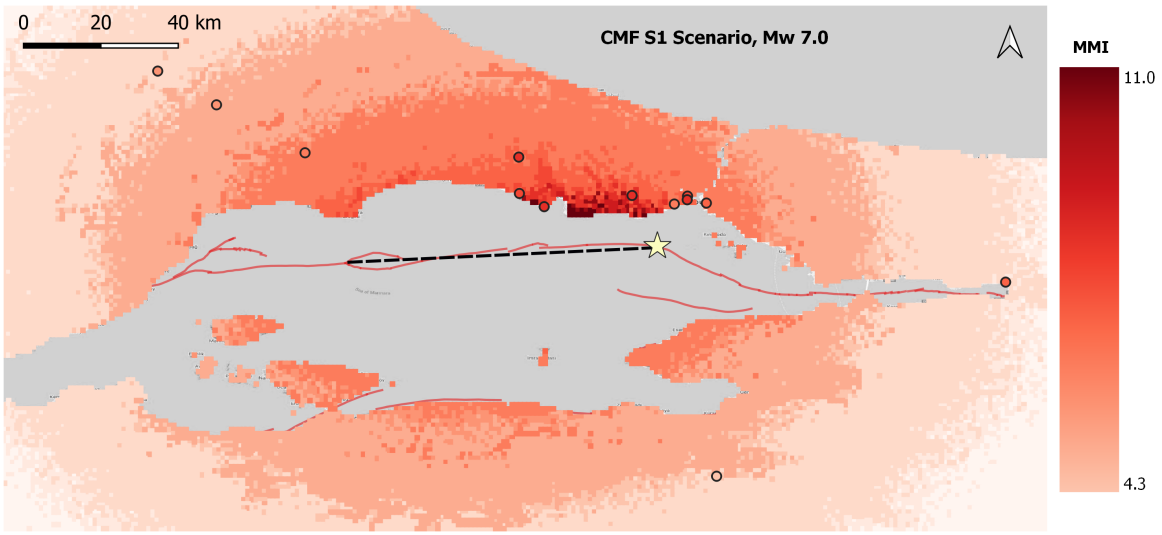

(a)

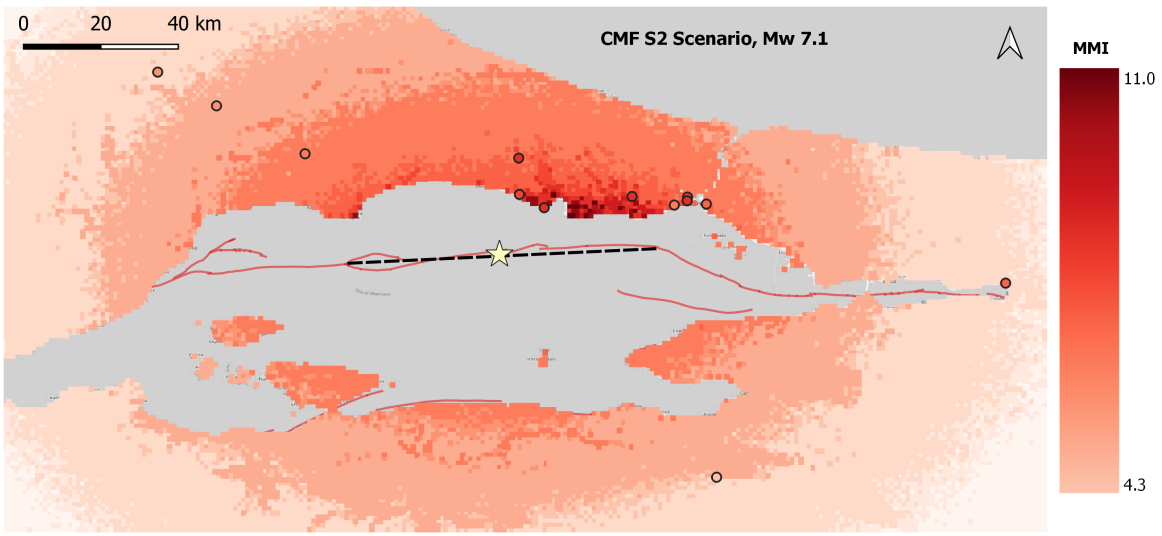

(b)

Figure 5.44. The 1766 Earthquake Stochastic Based Intensity Distribution for (a) the CMF S1 Scenario, (b) the Central Marmara S2 Scenario (Circles Represent Estimated Intensities Using the Damage Distribution Maps).

For the 1509 earthquake the estimations of which are shown in Figure 5.45 the combined rupture scenario yielded the best performance compared to CMF scenarios. Our evaluations showed that this earthquake had X as the highest intensity, Mw 7.6 as the largest magnitude and 120 km as the longest rupture length. It was not a surprise

because previously we had estimated its epicentral intensity as $I_0 = X$ by looking at the massive damage it created in a wide region. According to our calculations, the highest intensities were estimated in Istanbul, Prince Islands, and Çınarcık. These findings were highly consistent with the estimations made from damage information.

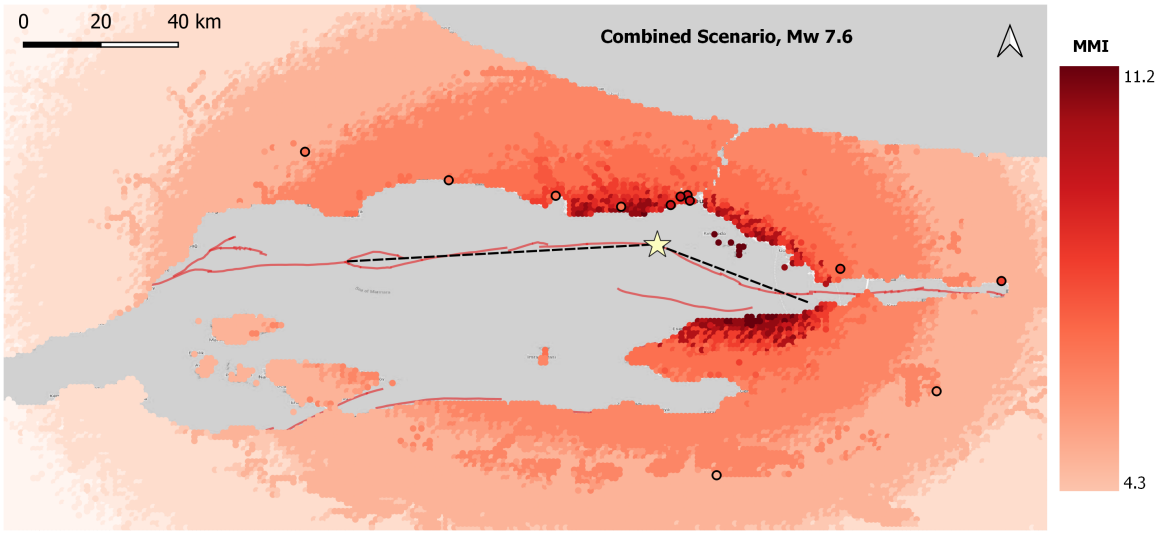

Figure 5.45. The 1509 Earthquake Synthetic Intensity Distribution for The Combined Rupture Scenario with Mw 7.6 for (a) Istanbul Region, (b) Marmara Region (Circles Represent Estimated Intensities Using Damage Information).

Table 5.30 summarizes our findings regarding the source parameters of historical earthquakes of interest in this thesis.

Table 5.30. Obtained Source Parameters

Source Parameters	**10 July 1894**	**22 May 1766**	**10 September 1509**
Moment Magnitude, (Mw)	6.8-6.9	7.0-7.1	7.6
Epicenter (Long., Lat.)	28.88, 40.87 29.11, 40.77	28.88, 40.87 28.43, 40.86	28.88, 40.87
Fault length (km) and width (km)	42x 10 60 x 10	60 x 10	120 x 10
Focal Depth (km)	5	5	5
Stress Drop (bar)	90-150	210-240	120
Fault	The PIS the PIS and Izmit segment	The CMF	the CMF and the PIS

5.5. Discussion on Uncertainties

While proposing source parameters for historical events, it is important to outline possible sources of uncertainties in our findings. In this study, we can classify our uncertainties under epistemic and aleatory. Epistemic uncertainties are common in all historical earthquake studies. In the data collection part, it is required to consider possible exaggeration and false information. Researchers have to make some assumptions about the damaged area, and documents are needed to be read carefully and sometimes with skepticism. After compiling the damage information, we generated the intensity maps by using the definitions given in EMS98. This part is mostly interpretive, because experts may have different judgements by looking at the same data.

In our analysis, we implemented a stochastic simulation approach which inherently includes aleatory uncertainties. This method depends on simplified models, assumptions on the source, site, and path parameters and functions developed by statistical analysis of strong motion data. For example we have to define a simplified fault mechanism on EXSIM12 code but in reality, there is heterogeneity, which may cause variable rupture velocities and rise times. Most of the time, the slips were characterized as random. We compared our estimations with those by specialized slip but we did not observe any systematic bias. We accounted for local site amplification by using two different types of Vs30 information in different grid sizes. Due to lack of sufficient H/V functions in the study area, we preferred generic site amplifications according to site classes. There is no region-wide, grid-based borehole data. Available Vs30 information is either result of interpolation or deduced from surface geology.

6. SUMMARY and CONCLUSIONS

This thesis provided the first detailed earthquake damage assessment in a collective, interdisciplinary effort and was the first attempt to enlighten source properties and assess intensity distributions of historical Istanbul earthquakes by using earthquake engineering tools. We trust that we were able to improve existing knowledge about 1894, 1766 and 1509 earthquakes. We believe that our findings, our model and our approach will be beneficial to researchers and outputs of this work will contribute to the literature.

The study focused on three major Istanbul earthquakes that occurred on 10 July 1984, 22 May 1766 and 10 September 1509. In order to constrain the source properties of these historical earthquakes, we started by compiling damage information from various sources. We compared descriptions of damage with the pictures taken after the 1894 earthquake in order to better interpret the information in written sources. Because of the importance of the city, official damage inventories focused only on Istanbul region, especially on the historical peninsula which was the seat of the Sultans and the administrative center of the Ottoman Empire. Information about the surrounding towns like Sakarya, Izmit, Bursa and Edirne were relatively rare. Given this lack of detailed and extensive damage information but the presence of reports, statements, and other types of materials we could estimate earthquake intensities in these localities.

After compiling damage inventories, known structures were classified by considering their structural material type. Old city maps were used for this purpose. Then, their damage grades were assigned and damage distribution maps were prepared. These maps were converted to intensity maps by following the descriptions given in EMS98. Utilizing the BOXER code, we estimated faults each earthquake was likely associated with by using assigned intensities.

With the help of the BOXER code, we associated the 1894 event with the PIS.

The 1766 and 1509 earthquakes were found to be related to the CMF. A preliminary magnitude assessment could also be made for these three earthquakes.

In the second part of this study, we performed stochastic simulations. We created our region specific simulation model by using recordings of the 26 September Mw 5.8 Silivri, Istanbul earthquake. We checked model bias in the frequency domain and also compared the synthetic PGAs, PGVs, and SAs at 0.2 sec and 1.0 sec with those of real recordings. To obtain intensities from the synthetics, we used Sokolov's method, which calculates intensities from Fourier amplitude spectra. Finally, we generated grid-based intensity maps and compared them with real damage observations collected after the Silivri earthquake. As a further validation, we favourably compared our model with two NGA-West2 GMMs. Because Silivri earthquake is a moderate size earthquake, we tested our model on the 17 August 1999 Kocaeli earhquake, (Mw=7.4) in order to see its performance in case of a larger earthquake as well. We calibrated and validated our source, path and site parameters. We concluded that it was sufficiently well developed and comprehensive enough for regional simulations.

For the simulation of historical earthquakes, we initially tested the effect of epicentral location. Forecasts were compared with previously obtained intensities in terms of their root mean square errors. We grouped our intensity points according to their locations to assess geographical dependencies. A number of magnitude - stress drop combinations and different rupture lengths were checked. We also modeled combined fault rupture scenarios. In addition to EXSIM12 generated random slip distributions, we evaluated specialized slips developed by the RupGEN tool. We noticed that our results were more sensitive to the selected magnitude, stress drop, and rupture length. On the other hand, changing the focal depth did not create a meaningful difference.

Our assessments of the source parameters of 1894, 1766 and 1509 Istanbul earthquakes were summarized in Table 5.30. According to our final assessments for the 1894 earthquake, we can claim that if the earthquake happened in the PIS, its epicenter could be at the midpoint of the segment, its magnitude could be Mw 6.8, and the optimum stress drop with these parameters was 150 bar. In another scenario, if it

occurred as a combined rupture, which included the PIS and some part of the Izmit segment, it could be an earthquake with a total rupture of 60 km, Mw 6.9, and 90 bar stress drop. These results were consistent with the actual damage observations and we checked them against GMMs. Moreover, these results were very close to the Boxer code estimations which provided us another way of validation. At the end, we also provided grid-based intensity maps using two different Vs30 sets and different scales. These maps showed high level of consistency with the observations, excluding the Eastern part of the Marmara. This inconsistency stems from the poor model of directivity and may be solved by future developments.

For the 1766 earthquake, our best estimations were obtained with the Central Marmara Fault scenarios. With the assumption of a 80 km total rupture length, if the earthquake took a place at the intersection point of the CMF with the PIS, its magnitude could be assessed to be Mw 7.0 and the optimum stress drop was 240 bar. If it happened 40 km to the west of the first scenario, in this case, a scenario with Mw 7.1 and 210 bar stress drop provided the lowest root mean square errors. The higher magnitude estimation confirmed that the 1766 earthquake was a larger earthquake than the 1894 event. By looking at its large destructive area and the damage level of well-built monumental structures, we were satisfied with our results.

For the 1509 earthquake, combination of the PIS with the CMF provided the best matches with our initial intensity estimations. According to this scenario, the epicenter of the 1509 earthquake was most likely at the intersection of the two segments and probably caused a 120 km rupture with a magnitude of Mw 7.6.

REFERENCES

Aki, K. (1980). Attenuation of shear-waves in the lithosphere for frequencies from 0.05 to 25 Hz. Physics of the Earth and Planetary Interiors, 21(1), 50-60.

Akıncı, A., Aochi, H., Herrero, A., Pischiutta, M., and Karanikas, D. (2017). Physics Based Broadband Ground Motion Simulations for Probable $Mw \geq 7.0$ Earthquakes in the Marmara Sea Region (Turkey). Bulletin of the Seismological Society of America.

Akıncı, A., Malagnini, L., Herrmann, R. B., Gok, R., and Sørensen, M. B. (2006). Ground motion scaling in the Marmara region, Turkey. Geophysical Journal International, 166(2), 635-651.

Akkar, S., Sandıkkaya, M. A., and Bommer, J. J. (2014). Empirical ground-motion models for point-and extended-source crustal earthquake scenarios in Europe and the Middle East. Bulletin of earthquake engineering, 12(1), 359-387.

Aktepe, M. (1958). İstanbul'un nüfus meselesine dair bazı vesikalar. Tarih Dergisi, 9(13), 1-30.

Âlî, M. (2009). Künhü'l-Ahbâr: Dördüncü Rükn, Osmanlı tarihi.

Alman Mavileri. (1914). "I. Dünya Savaşı Öncesi İstanbul Haritaları (1913).

Ambraseys N.N., Finkel C., (1991). "Long-term seismicity of Istanbul and of the Sea Marmara region", Terra Nova 3 pages 527–539.

Ambraseys, N. N., (2001). The earthquake of 1509 in the Sea of Marmara, Turkey, revisited. Bulletin of the Seismological Society of America, 91(6), 1397-1416.

Ambraseys, N. N., and Finkel, C. F. (1995). The seismicity of Turkey and adjacent areas. A historical review, 1500, 1800.

Ambraseys, N. N., and Jackson, J. A. (2000). Seismicity of the Sea of Marmara (Turkey) since 1500. Geophysical Journal International, 141(3), F1-F6.

Anderson, J. G., and Hough, S. E. (1984). A model for the shape of the Fourier amplitude spectrum of acceleration at high frequencies. Bulletin of the Seismological Society of America, 74(5), 1969-1993.

Ansal, A., Akinci, A., Cultrera, G., Erdik, M., Pessina, V., Tönük, G., and Ameri, G. (2009). Loss estimation in Istanbul based on deterministic earthquake scenarios of the Marmara Sea region (Turkey). Soil Dynamics and Earthquake Engineering, 29(4), 699-709.

Aochi, H., and Ulrich, T. (2015). A probable earthquake scenario near Istanbul determined from dynamic simulations. Bulletin of the Seismological Society of America, 105(3), 1468-1475.

Assatourians, K., and G. Atkinson (2012). EXSIM12: A Stochastic Finite- Fault Computer Program in FORTRAN.

Atkinson, G. M., and Assatourians, K. (2015). Implementation and validation of EXSIM (a stochastic finite [U+2010] fault ground [U+2010] motion simulation algorithm) on the SCEC broadband platform. Seismological Research Letters, 86(1), 48-60.

Atkinson, G. M., and Boore, D. M. (1995). Ground-motion relations for eastern North America. Bulletin of the Seismological Society of America, 85(1), 17-30.

Atkinson, G. M., and Boore, D. M. (2006). Earthquake ground-motion prediction equations for eastern North America. Bulletin of the seismological society of America, 96(6), 2181-2205.

Ayverdi, E. H. (1953), Fatih Devri Mimarisi,İstanbul Fetih Cemiyeti İstanbul Enstitüsü Yayınları, Istanbul.

Ayverdi, E. H. (1958), Fatih Devri Sonlarında İstanbul Mahalleleri, Şehrin İskanı ve Nüfusu, Ankara.

Ayverdi, E. H. (1958). Asırda İstanbul haritası.

Batur A. and Tanyeli G. (1993), "1894 Depremi ve İstanbul'un Tarihi Yapılarındaki Hasar Üzerine Bir Örnekleme Çalışması: Kapalıçarşı", II. Ulusal Deprem Sempozyumu, İstanbul, İMO.

Batur, A. (1994). Yazı Pek Heyecanlı Geçmisti. Bir Depremin Yüzyıl Dönümü," Istanbul Dergisi, 10, 24-32.

Boore, D. M. (1984). Use of seismoscope records to determine ML and peak velocities. Bulletin of the Seismological Society of America, 74(1), 315-324.

Boore, D. M. (2003). Simulation of ground motion using the stochastic method, Pure Appl. Geophys. 160, 635–676.

Boore, D. M. (2009). Comparing stochastic point-source and finite-source ground-motion simulations: SMSIM and EXSIM, Bull. Seismol. Soc. Am. 99, 3202–3216.

Boore, D. M., and Joyner, W. B. (1997). Site amplifications for generic rock sites. Bulletin of the seismological society of America, 87(2), 327-341.

Boore, D. M., and Thompson, E. M. (2014). Path durations for use in the stochastic [U+2010] method simulation of ground motions. Bulletin of the Seismological Society of America, 104(5), 2541-2552.

Böse, M. (2006). Earthquake early warning for Istanbul using artificial neural networks. Doctoral Dissertation, University of Karlsruhe, Germany.

Çalık, S., (2003). 1894 Yılında İstanbul'da Meydana Gelen Büyük Depreme Ait Anonim Bir Günlük, Üsküdar Belediyesi Yayınları, İstanbul.

Cangül, C. (2011). Istanbul City Notes. https://www.istanbulium.net/ (Last Accessed July 2020).

Çelik, Z. (1993). The remaking of Istanbul: Portrait of an Ottoman city in the nineteenth century (No. 2). Univ. of California Press.

Çelik, Z., 1998. 19. Yüzyılda Değişen Osmanlı Başkenti-Değişen Istanbul. Istanbul: Tarih Vakfı Yurt Yayınları, in Turkish.

Cervati, R. C., (1894). Annuaire Oriental du Commerce, de l'Industrie, de l'Administration et de la Magistrature. Constantinople 1311: The Annuaire Oriental and Printing Co.

Çesmi-zade, M. R. (1766).” ”Cesmizade Tarihi” Ed. BS Kutukoglu, İstanbul Fetih Cemiyeti Yayinlari (1993).

Cezar, M. (1963). Osmanli Devrinde Istanbul'da Tahribat Yapan yanginlar ve Tabii Afetler. Guzel Sanatlar Akademisi Turk Sanati Tarihi Enstitüsü Yayilari, 1, Istanbul.

Chernov, Y. K., and Sokolov, V. Y. (1999). Correlation of seismic intensity with Fourier acceleration spectra. Physics and Chemistry of the Earth, Part A: Solid Earth and Geodesy, 24(6), 523-528.

Chiou, B. S. J., and Youngs, R. R. (2014). Update of the Chiou and Youngs NGA model for the average horizontal component of peak ground motion and response spectra. Earthquake Spectra, 30(3), 1117-1153.

Cplakidas, (2011). Map of Byzantine Constantinople. World History Encyclopedia.

DASK, 2019a. Natural Disaster Insurance Institution Annual Activity Report 2019.

DASK, 2019b. Natural Disaster Insurance Institution, 10/09/2019 Press Release.

Davison, C., (1894). On the Velocity of the Constantinople Earthquake-Pulsations of July 10, 1894. Nature, 50(1297), 450-451.

Davison, C., (1896). The Constantinople earthquake of July 10. 1894. Rait, Henderson and Co., printers.

De Carbognano, Cosimo Comidas, and Erendiz Özbayoğlu. 18. yüzyılın sonunda İstanbul. Eren, 1993.

Durukal, E., (2002). Critical evaluation of strong motion in Kocaeli and Düzce (Turkey) earthquakes. Soil Dynamics and Earthquake Engineering, 22(7), 589-609.

Durukal, E., and Catalyurekli, Y. (2004). Spectral analysis of source parameters of the 1999 Kocaeli and Düzce earthquake aftershock sequences. In 13th World Conference on Earthquake Engineering, Vancouver BC, Canada, Paper(Vol. 421).

Dybowski, X., (1889). Tremblement de Terre de Turquie Observé a Adabazar. La Nature, 22. Année, N.1114, 6 Octobre 1894, 42. Volume, Paris, pp. 289-291.

Eginitis, D., (1984). Le Tremblement de Terre de Constantinople L'Astronomie 13, 427-429.

Eginitis, D., (1895). Le Tremblement De Terre De Constantinople: Du 10 Juillet 1894. In Annales De Géographie (Vol. 4, No. 15, Pp. 151-165). Armand Colin.

Ekin, Ü., (2005). "Bizans ve Osmanlı Dönemi'nde Sakarya Bölgesi'ni Etkileyen Depremler", Sakarya İli Tarihi, C. 1, Sakarya Üniversitesi Yayınları.

ELER v3.1 (2010) Earthquake loss estimation routine. In: Technical manual and users guide. Bogazici University, Department of Earthquake Engineering.

Emre, Ö., Duman, T.Y., Özalp, S., Elmacı, H., Olgun, Ş. ve Şaroğlu, F., 2013, Açıklamalı Türkiye Diri Fay Haritası. Ölçek 1:1.250.000, Maden Tetkik ve Arama Genel Müdürlüğü, Özel Yayın Serisi-30, Ankara-Türkiye. ISBN: 978-605-5310-56-1.

Erdik M., Durukal E. (2002). Simulation Modelling of Strong Ground Motion, in Earthquake Engineering Handbook, W-F. Chen and C. Scawthorn, editors, CRC Press, 2002.

Ergin, K., Güçlü, U., and Uz, Z. (1967). Türkiye ve civarının deprem kataloğu. İTÜ.

Ergin, O. N. (1995). Mecelle-i Umûr-ı Belediyye, Vol:2. İstanbul Büyükşehir Belediyesi Kültür İşleri Daire Başkanlığı, Istanbul.

Eyice, S. (2016), Tarih Boyunca İstanbul. Etkileşim Yayınları.

Finkel, C. F., and Ambraseys, N. N. (1997). The Marmara Sea Earthquake of 10 July 1894 and Its Effects On Historic Buildings. Anatolia Moderna. Yeni Anadolu, 7(1), 49-58.

Genç, M., and Mazak, M., (2001). İstanbul depremleri: fotoğraf ve belgelerde 1894 depremi. İGDAŞ Genel Müdürlüğü, Istanbul.

Goad, Charles Edward. (1904) "Plan d'assurance de Constantinople. Vol. Istamboul. No: 18".

Grünthal, G., and Wahlström, R. (2012). The European-Mediterranean Earthquake Catalogue (EMEC) for the last millennium. Journal of Seismology, 16(3), 535–570.

Hâkim, S., M., (1166-1172). "Vekayi'name-i Hâkim", Bağdat Köşkü 233, Topkapı Sarayı Müzesi Kitaplığı, pages 226,227.

Hammer, J. D. (1835). Histoire de l'empire ottoman. Bellizard, Barthes, Dufour et Lowell, Paris.

Herrmann, R. B. (1985). An extension of random vibration theory estimates of strong ground motion to large distances. Bulletin of the Seismological Society of America, 75(5), 1447-1453.

Horasan, G., Kaşlılar, Ö. A., Boztepe, G. A., Türkelli N. (1998). S wave attenuation in the Marmara region, northwestern Turkey, Geophys. Res. Lett., 25, 2733–2736.

IBB-OYO-KOERI, (2009). İstanbul'un Olası Deprem Kayıpları Tahminlerinin Güncellenmesi İşi, Proje Çalışma Raporu, Boğaziçi Üniversitesi, Deprem Mühendisliği Bölümü, Istanbul.

Irmak, T. S., Yavuz, E., Livaoğlu, H., Şentürk, E., and Sahin, E. Y. (2020). Source parameters for small-moderate earthquakes in Marmara Region (Turkey). Geosciences Journal, 24(5), 541-555.

Istanbul Court Records, İstanbul Mahkemesi 25 Numaralı Sicil (H. 1179-1180 / M. 1765-1767), Cilt: 76.

Istanbul Culture and Tourism Directorate (2010). Istanbul Cultural Heritage and Economy Inventory Project.

Karabulut, H., Güvercin, S. E., Eskiköy, F., Konca, A. Ö., and Ergintav, S., (2020). The moderate size 2019 September M w 5.8 Silivri earthquake unveils the complexity of the Main Marmara Fault shear zone. Geophysical Journal International, 224(1), 377-388.

King, GCP, Hubert-Ferrari, A, Nalbant, SS, Meyer, B, Armijo, R and Bowman, D (2001) Coulomb interactions and the 17 August 1999 Izmit, Turkey Earthquake.

KOERI (2003). Earthquake risk assessment for Istanbul Metropolitan Area, Bogazici University, Kandilli Observatory and Earthquake Research Institute, Istanbul.

KOERI, 2019. “26 Sept. 2019 (13:59) Istanbul-Off Silivri Earthquake, September 26, 2019” Report on Istanbul Earthquake Rapid Response System’s preliminary estimations.

Köseoğlu, A., Özel, N.M., Barış, S¸., Üçer, S.B., and Ottemöller, L., 2014, Specral determination of source parameters in the Marmara Region. Journal of Seismology, 18, 651–669.

Kuban, D., (1998). ”Kent ve Mimarlık Üzerine İstanbul Yazıları, Istanbul.”

Kuban, D., (2010). ”İstanbul Bir Kent Tarihi: Bizantion, Konstantinopolis, İstanbul, çev.” Zeynep Rona, Türkiye İş Bankası Kültür Yayınları, İstanbul.

Le Pichon, X., Chamot Rooke, N., Rangin, C., and Sengör, A. M. C., (2003). The North Anatolian fault in the Sea of Marmara. Journal of Geophysical Research: Solid Earth, 108(B4).

Leonard, M., (2010). Earthquake fault scaling: Self-consistent relating of rupture length, width, average displacement, and moment release. Bulletin of the Seismological Society of America, 100(5A), 1971-1988.

Mantran, R., (1990). 17. Yüzyılın İkinci Yarısında İstanbul Cilt I. Çev. Mehmet Ali Kılıçbay, Enver Özcan), TTK Ankara, 45-46.

Margaris, B. N., and Boore, D. M., (1998). Determination of and 0 from response spectra of large earthquakes in Greece. Bulletin of the Seismological Society of America, 88(1), 170-182.

Mazlum, D., 2011. 1766 İstanbul Depremi Belgeler Işığında Yapı Onarımları (İstanbul: İstanbul Araştırmaları Enstitüsü, 2011), in Turkish.

Meade, B. J., B. H. Hager, S. C. McClusky, R. E. Reilinger, S. Ergintav, O. Lenk, A. Barka, and H. Ozener (2002), Estimates of seismic potential in the Marmara Sea region from block models of secular deformation constrained by Global Positioning System measurements, Bull. Seismol. Soc. Am., 92(1), 208–215.

Ménage, V.L. (1976) "Edirneli Rûhî'ye Atfedilen Osmanlı Tarihi'nden İki Parça", Ord. Prof. İsmail Hakkı Uzunçarşılı 'ya Armağan, Ankara, s. 322–327.

Mendes-Victor, L., Oliveira, C. S., Azevedo, J., and Ribeiro, A. (Eds.). (2008). The 1755 Lisbon Earthquake: Revisited (Vol. 7). Springer Science and Business Media.

Motazedian D, Atkinson G. Stochastic finite-fault modeling based on a dynamic corner frequency. Bull Seismol Soc Am. 2005; 95(3): 995-1010

MTA, (2004). 1/500,000 scale geological maps of Turkey.

Müller-Wiener, Wolfgang., (2001). "İstanbul'un Tarihsel Topografyası." Yapı Kredi Yayınları 1419: 534.

Nakamura, Y., (1989). A method for dynamic characteristics estimation of subsurface using microtremor on the ground surface. Railway Technical Research Institute, Quarterly Reports, 30(1).

Orgun, Z., (1941). 1509 (Hicrî 915) senesinde Istanbul'u baştan başa harab eden zelzelede şehri tamir için alınan tedbirler. Cumhuriyet matbaasi.

Özkılıc, Kucukalioglu , S., (2015). 1894 Depremi Ve İstanbul, Türkiye İş Bankası Kültür Yayınları. (In Turkish).

Öztin, F., (1994). 10 Temmuz 1894 İstanbul Depremi Raporu. TC Bayındırlık Ve İskan Bakanlığı Afet İşleri Genel Müdürlüğü Deprem Araştırma Dairesi.

Öztüre, A., (1981). Nicomedia Yöresindeki Yeni Bulgularla İzmit Tarihi, İstanbul, p. 98-99.

Pamukciyan, K., (1987). "Sarkis Sarraf Hovannesyan'a Göre Istanbul'un 1766 Büyük Depremi".Tarih ve Toplum Dergisi, 8(47), 268-272.

Pamukciyan, K., (2002). "İstanbul Yazıları", Aras Yayıncılık, pages 65-81.

Papazachos B.C., and Papazachou C., (2003). The earthquakes of Greece. Ziti publications, Thessaloniki, Greece, 286 pp. (in Greek).

Parolai, S., Bindi, D., Durukal, E., Grosser, H., and Milkereit, C., (2007), Source parameters and seismic moment-magnitude scaling for Northwestern Turkey. Bulletin of the Seismological Society of America, 97, 655–660.

Parsons, T., (2004). Recalculated probability of M$\geq$ 7 earthquakes beneath the Sea of Marmara, Turkey. Journal of Geophysical Research: Solid Earth, 109(B5).

Pervititch, J., (2000). "Istanbul in the insurance maps of Jacques Pervititch." The History Foundation of Turkey, Istanbul.

Pischiutta, M., Akinci, A., Tinti, E., and Herrero, A., (2021). Broad-band ground-motion simulation of 2016 Amatrice earthquake, Central Italy. Geophysical Journal International, 224(3), 1753-1779.

Pulido, N., Ojeda, A., Atakan, K., and Kubo, T., (2004). Strong ground motion estimation in the Sea of Marmara region (Turkey) based on a scenario earthquake. Tectonophysics, 391(1-4), 357-374.

QGIS Development Team (2018). QGIS Geographic Information System. Open Source Geospatial Foundation Project.

Sağlam, N., (2014). "Ahmed Vâsıf Efendi ve Mehâsinü'l-Âsâr ve Hakaiku'l-Ahbârı 1166-1188/1752-1774 (İnceleme ve Metin)."

Sakin, O., 2002. Tarihsel Kaynaklarıyla İstanbul Depremleri, Kitabevi Yay., İstanbul.

Sanuto, M., (1879-1903). I diarii di Marino Sanuto. (Vol. 9, pp. 261, 563, 564; Vol. 10, pp. 208, 262; Vol. 12, p. 273). Forni.

Schneider, Alfons Maria. (1952). "Onbeşinci Yüzyılda İstanbul'un Nüfusu", Belleten, XVI/62.

Şemdanizade, Fındıklılı Süleyman Efendi. "Müri üt-tevarih, vol. 2.A" Edited by M. Münir Aktepe. Istanbul: İstanbul Üniversitesi Edebiyat Fakültesi (1976).

Şenel, A., N., (2010). "A Reading of the Late 19th Century Istanbul Public Life and Space Through the Tanzimat Novels". Master Thesis in Architecture, Izmir Institute of Tech.

Shaw, Standford J. (1979). "The population of Istanbul in the nineteenth century." International Journal of Middle East Studies 10.2: 265-277.

Shebalin N.V., Karnik V., Hadzievski D. (eds), (1974). Catalogue of earthquakes of the Balkan region. I, UNDP-UNESCO Survey of the seismicity of the Balkan region. Skopje, 600 pp.

Sokolov, V. Y., (2002). Seismic intensity and Fourier acceleration spectra: revised relationship. Earthquake Spectra, 18(1), 161-187.

Sokolov, V. Y., and Chernov, Y. K., (1998). On the correlation of seismic intensity with Fourier amplitude spectra. Earthquake spectra, 14(4), 679-694.

Solakzâde, M.H., (2016). Solakzâde Tarihi, (haz). Vahid Çabuk, Kültür Bakanlığı Yayınları, Ankara.

Sørensen, M. B., Pulido, N., and Atakan, K. (2007). Sensitivity of ground-motion simulations to earthquake source parameters: a case study for Istanbul, Turkey. Bulletin of the Seismological Society of America, 97(3), 881-900.

Soysal H., Sipahioglu S., Kolcak D., Altinok Y., 1981. Turkye ve Cevresinin Tarihsel deprem Katalogu. TUBITAK, Proje no. TBAG 341, Istanbul, 86 pp.

Stucchi M., Rovida A., Gomez Capera A.A., Alexandre P., Camelbeeck T., Demircioglu M.B., Gasperini P., Kouskouna V., Musson R.M.W., Radulian M., Sesetyan K., Vilanova S., Baumont D., Bungum H., Fäh D., Lenhardt W., Makropoulos K., Martinez Solares J.M., Scotti O., Živcic M., Albini P., Batllo J., Papaioannou C., Tatevossian R., Locati M., Meletti C., Viganò D., Giardini D., 2013. The SHARE European Earthquake Catalogue (SHEEC) 1000-1899. Journal of Seismology, 17, 2, 523-544.

Süleyman, H., (2018). Estimation of the High-Frequency Decay Parameter () and Anelastic Attenuation Factor (Q) for Istanbul. M.Sc. Thesis. Boğaziçi University, Dept. of Earthquake Engineering, Istanbul, Turkey. Oct 2018.

Tezcan, S., Acar, Y., and Çivi, A. (1991). İstanbul İçin Deprem Riski Analizi. TMMOB İnşaat Mühendisleri Odası İstanbul ve Deprem Sempozyumu, İT Ü, İstanbul.

Tuzcu, N., (2017). Istanbul Urban Database. `http://istanbulurbandatabase.com/` (Last Accessed July 2020).

Uğur, A., (1985). The Reign of Sultan Selîm I in the Light of the Selîm-nâme Literature.

Uğurhan, B., and Askan, A., (2010). Stochastic strong ground motion simulation of the 12 November 1999 Düzce (Turkey) earthquake using a dynamic corner frequency approach. Bulletin of the Seismological Society of America, 100(4), 1498-1512.

Ürekli, F., (1999). İstanbul'da 1894 Depremi, İletişim Yayınları, İstanbul.

Ürekli, F., Gündoğdu, R., Ünal, E., F., (2018). Osmanlı Arşiv Belgelerinde Istanbul'da Afetler. AFAD, Afet ve Acil Durum Yönetimi Başkanlığı, Istanbul.

Wells, D. L, and K. J. Coppersmith (1994). Empirical relations among magnitude, rupture length, rupture area, and surface displacement, Bull. Seism. Soc. Am. 84, 974–1002.

Yalçınkaya, E., Pinar, A., Uskuloglu, O., Tekebas, S., and Firat, B., (2012). Selecting the most suitable rupture model for the stochastic simulation of the 1999 Izmit earthquake and prediction of peak ground motions. Soil Dynamics and Earthquake Engineering, 42, 1-16.

Yazan, Ü. M. (1988). "Bir Asır Boyunca (1840-1940) İstanbul Şehrinin Nüfusunda Meydana Gelen Değişmelerin Tahlili", Tarih Boyunca İstanbul Semineri (29 Mayıs-1 Haziran 1988) -Bildiriler, İstanbul: İstanbul Üniversitesi Basımevi, 1989, pages 59-74.

Zengin E., and Cakti E. (2012). Scenario Based Ground Motion Simulations for Istanbul, Turkey, 15th World Conference on Earthquake Engineering, Lisbon, Portugal, 24–18 September.

Newspapers and Other Internet Sources

1. CNN Türk, (2019, September 26). "Son dakika... İstanbul Silivri'de deprem: Cami minaresi çöktü, yan yatan bina boşaltıldı". (Retrieved December 8, 2020, from https://www.cnnturk.com/video/turkiye/son-dakika-istanbul-silivride-deprem-avcilarda-hasara-neden-oldu-cami-minaresi-coktu).

2. CNN Türk, (2019-2, September 26). "Son dakika: İstanbul'da büyük deprem!". (Retrieved December 8, 2020, from https://www.cnnturk.com/video/turkiye/son-dakika-istanbulda-buyuk-deprem).

3. Evrensel, (2019, September 28). "İstanbul'da 5.8 büyüklüğünde deprem: Toplam 77 binada ağır hasar tespit edildi". (Retrieved December 8, 2020, from https://www.evrensel.net/haber/387647/istanbulda-5-8-buyuklugunde-deprem-toplam-77-binada-agir-hasar-tespit-edildi).

4. Evrensel, (2019-2, September 27). "Silivri'de hasar gören okul mühürlendi; Avcılar'da 258 bina incelenecek". (Retrieved December 8, 2020, from https://www.evrensel.net/haber/387722/silivride-hasar-goren-okul-muhurlendi-avcilarda-258-bina-incelenecek).

5. Governorship of Istanbul, (2019). "Republic of Turkey Governorship of Istanbul, 29/09/2019 Press Release". (Retrieved December 8, 2020, from http://istanbul.gov.tr/deprem-ile-ilgili-on-hasar-calismalarinda-son-durum).

6. IBB, (2019). "İBB Baskani Ekrem İmamoglu'nun Deprem Seferberlik Sunum Dosyasi". (Retrieved December 8, 2020, from https://depremzemin.ibb.istanbul/deprem-seferberlik-plani/)

7. Haberler, (2020, September 3). “Silivri Depreminde Hasar Gören Cami Yıktırıldı”. (Retrieved December 8, 2020, from https://www.haberler.com/silivri-depremi-nde-hasar-goren-cami-yiktirildi-13566814-haberi/).

8. Silivri Municipality, (2020). 09/03/2020 Press Release. (Retrieved December 8, 2020, from https://www.silivri.bel.tr/haber/news_1583753743_png/4697).

9. Büyükçekmece Municipality, (2020). 17/11/2020 Press Release. (Retrieved December 8, 2020, from https://www.bcekmece.bel.tr/haberdetay?id=186).

10. Beyaz Gazete, (2020, January 29). “Depremde Ağır Hasar Gördü, Mührü Kırıp Oturmaya Devam Ettiler”. (Retrieved December 8, 2020, from https://beyazgazete.com/haber/2020/1/29/depremde-agir-hasar-gordu-muhru-kirip-oturmaya-devam-ettiler-5421580.html).

APPENDIX A: ILLUSTRATING CLASSIFICATION OF DAMAGE FOR THE 10 JULY 1894 ISTANBUL EARTHQUAKE

Figure A.1. Eminönü, Unkapanı Mosque Damage Definition: Spire of the minaret collapsed. Damage Level: D1

Figure A.2. Fatih, Kariye Mosque Damage Definition: The minaret demolished from the balcony level (half part). The madrasa was partially ruined. Damage Level: D2, D4

Figure A.3. Kınalıada, Panagia Greek Church Damage Definition: The walls were largely cracked. Damage Level: D3

Figure A.4. Fatih, Topkapı City Walls Damage Definition: Demolition of the bastions and city walls in Topkapı. Damage Level: D4

Figure A.5. Heybeliada, Ecole de Theologie Damage Definition: Its several buildings have been dislocated and became inhabitable. Damage Level: D4

Figure A.6. Damage Level of Edirnekapı, with different views from inside and outside of the city walls. Damage Definition: The Edirnekapi Gate collapsed and five shops located under the gates were destroyed. Damage Level: D5

Figure A.7. Murat Paşa Mosque Damage Definition: Damaged. Damage Level: D3

Figure A.8. Grand Bazaar Yağlıkçılar Street Damage Definition: Completely collapsed. Damage Level: D4/D5

Figure A.9. A kebap house and three other shops next to the Nuruosmaniye Gate. Damage Definition: Completely collapsed. Damage Level: D5

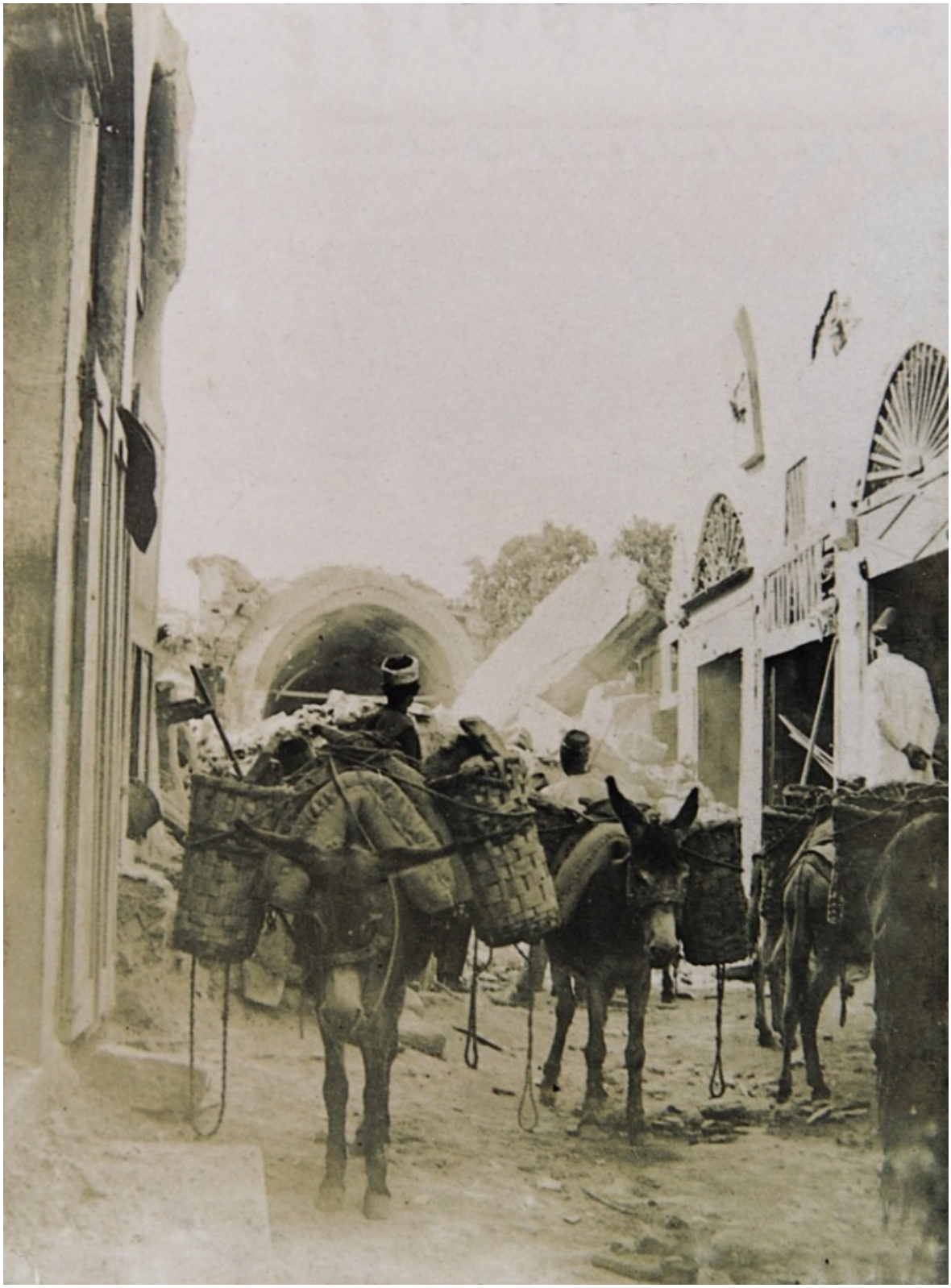

Figure A.10. Grand Bazaar Çadırcılar Street. Damage Definition: Çadırcılar Gate collapsed and one shop has been rebuilted. Damage Level: D5

Figure A.11. Fatih Mosque Damage Definition: One of the minaret in the direction of the Black Sea fell and the top of the other minaret was curved. Some of the courtyard wall collapsed. Damage Level: D1, D4

Figure A.12. Amcazade Hüseyin Paşa Madrasah Damage Definition: Its several domes were destroyed and some parts of the madrasa were damaged. Damage Level: D4

Figure A.13. Süleyman Paşa Inn Damage Definition: Collapsed. Some parts were completely destroyed. Some part and the soda factory located in the middle of the inn were demolished. Damage Level: D4

Figure A.14. Kantarcılar / Sarı Demir /Sarı Timur Mosque Damage Definition: The wall was destroyed. Half of its minaret was destroyed. Damage Level: D4, D4

Figure A.15. Kaptan İbrahim Paşa Mosque, School and Lodge Damage Definition: The front of the school and its roof were damaged. Damage Level: According to picture, damage level is D4, but the definition expresses a slight damage, D2.)

Figure A.16. Vezir Inn. Damage Definition: Mostly demolished/ Partly collapsed /Ruined. Damage Level: D4

Figure A.17. Matbaa-i Osmaniye. Damage Definition: Its benches were disturbed. Damage Level: The picture shows D3, but the definition expresses more slight damage, D1.

Figure A.18. Atik Ali Paşa Madrasah. Damage Definition: Damaged, completely collapsed. Damage Level: The picture shows D4 while the definition describes D5

Figure A.19. Sofcular Inn Damage Definition: Its walls were damaged and became dilapidated, several rooms collapsed. Damage Level: D4

Figure A.20. Maliye Nezareti Damage Definition: Damaged, its eaves fell and the walls partly collapsed. Damage Level: D4

Figure A.21. Coppersmiths close to the tramway in Beyazıt. Damage Definition: Completely collapsed. Damage Level: D5

Figure A.22. Kemankeş Kara Mustafa Paşa Madrasah. Damage Definition: Partly ruined. Damage Level: D4

APPENDIX B: COMPARISON OF OBSERVED AND SIMULATED GROUND MOTIONS IN TIME AND FREQUENCY DOMAIN

B.1. 26 September 2019 Silivri Earthquake (59 Stations)

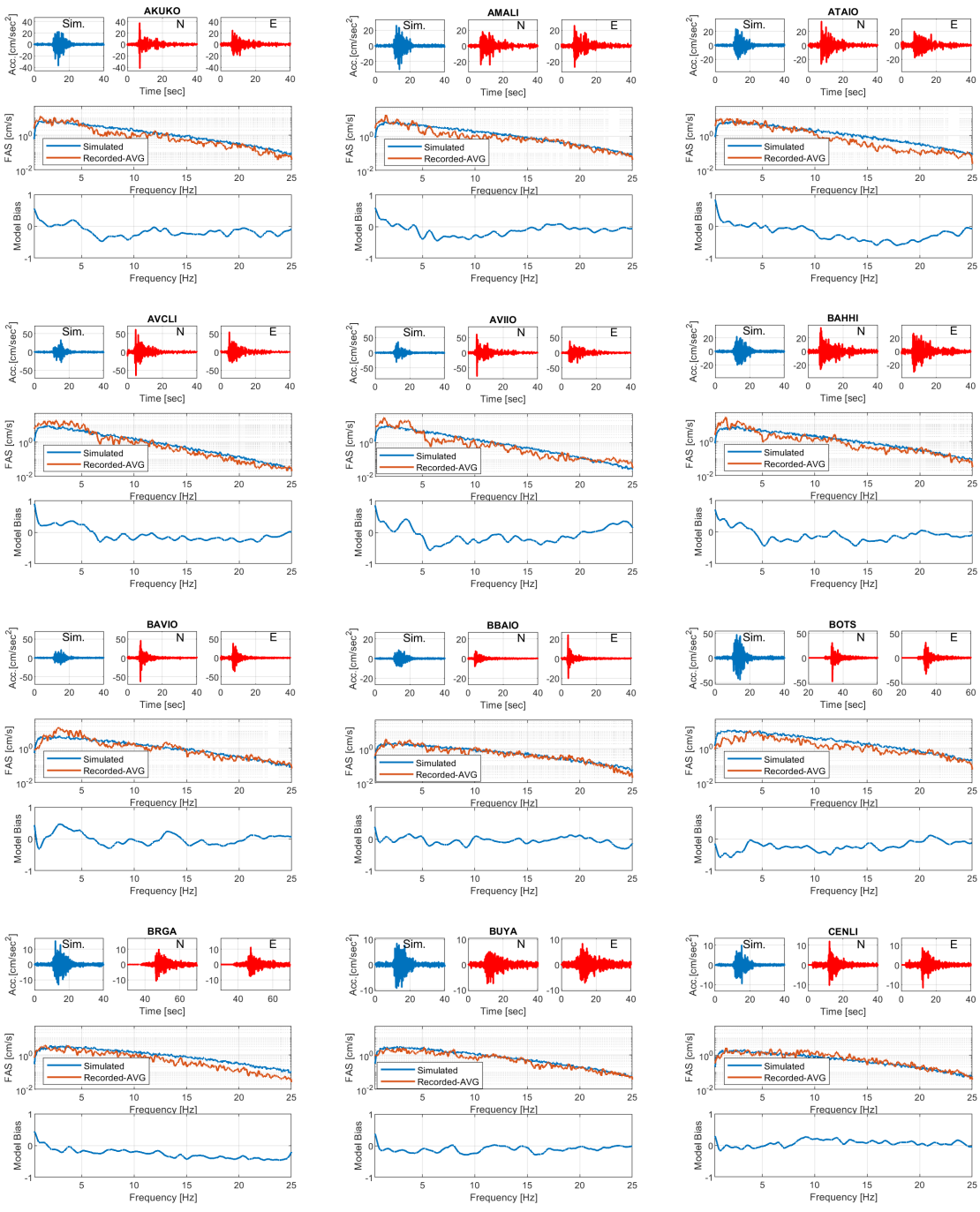

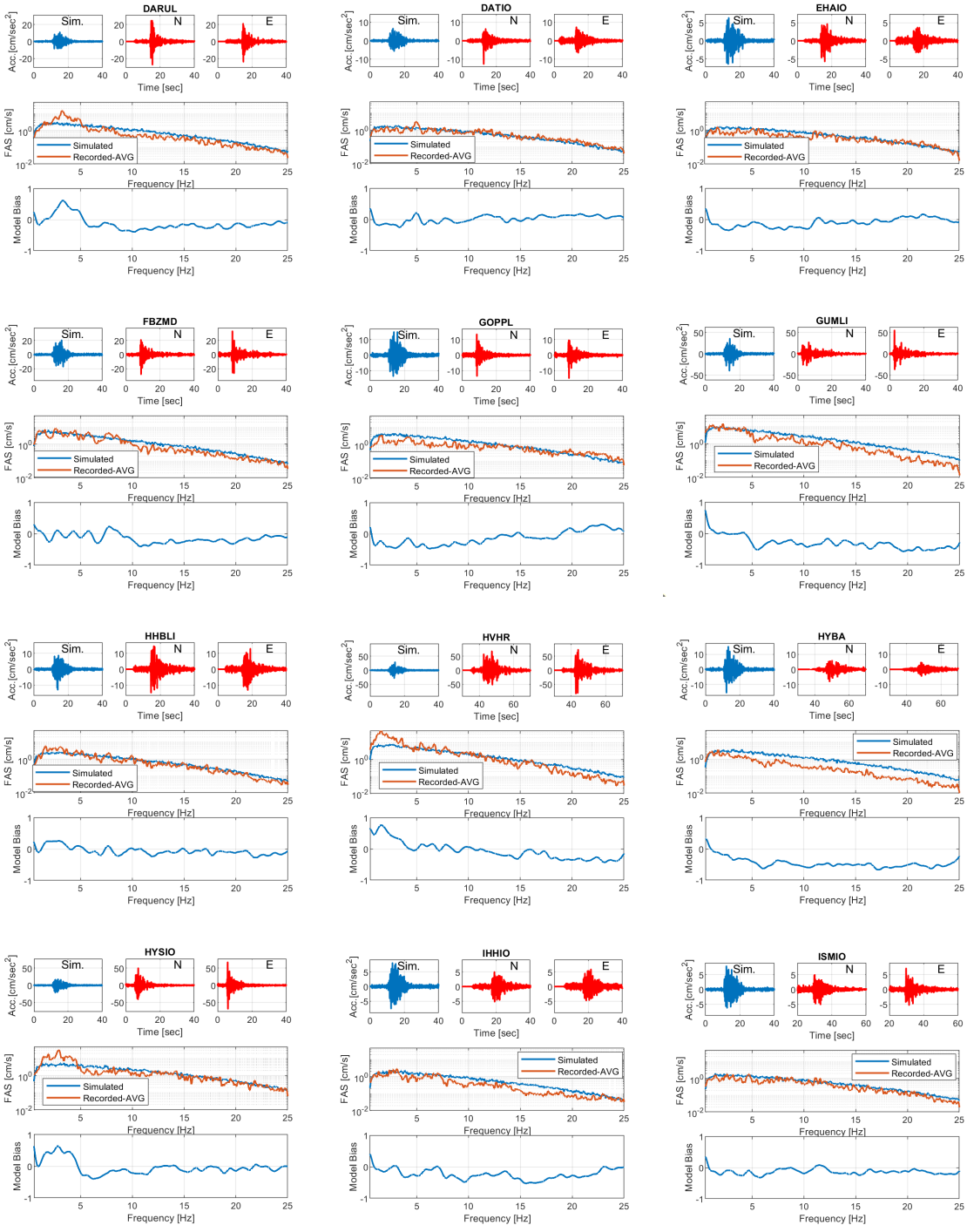
DARUL
DATIO
EHAIO
FBZMD
GOPPL
GUMLI
HHBLI
HVHR
HYBA
HYSIO
IHHIO
ISMIO
Sim.
N
E
Acc.[cm/sec^2]
Time [sec]
FAS [cm/s]
Simulated
Recorded-AVG
Frequency [Hz]
Model Bias

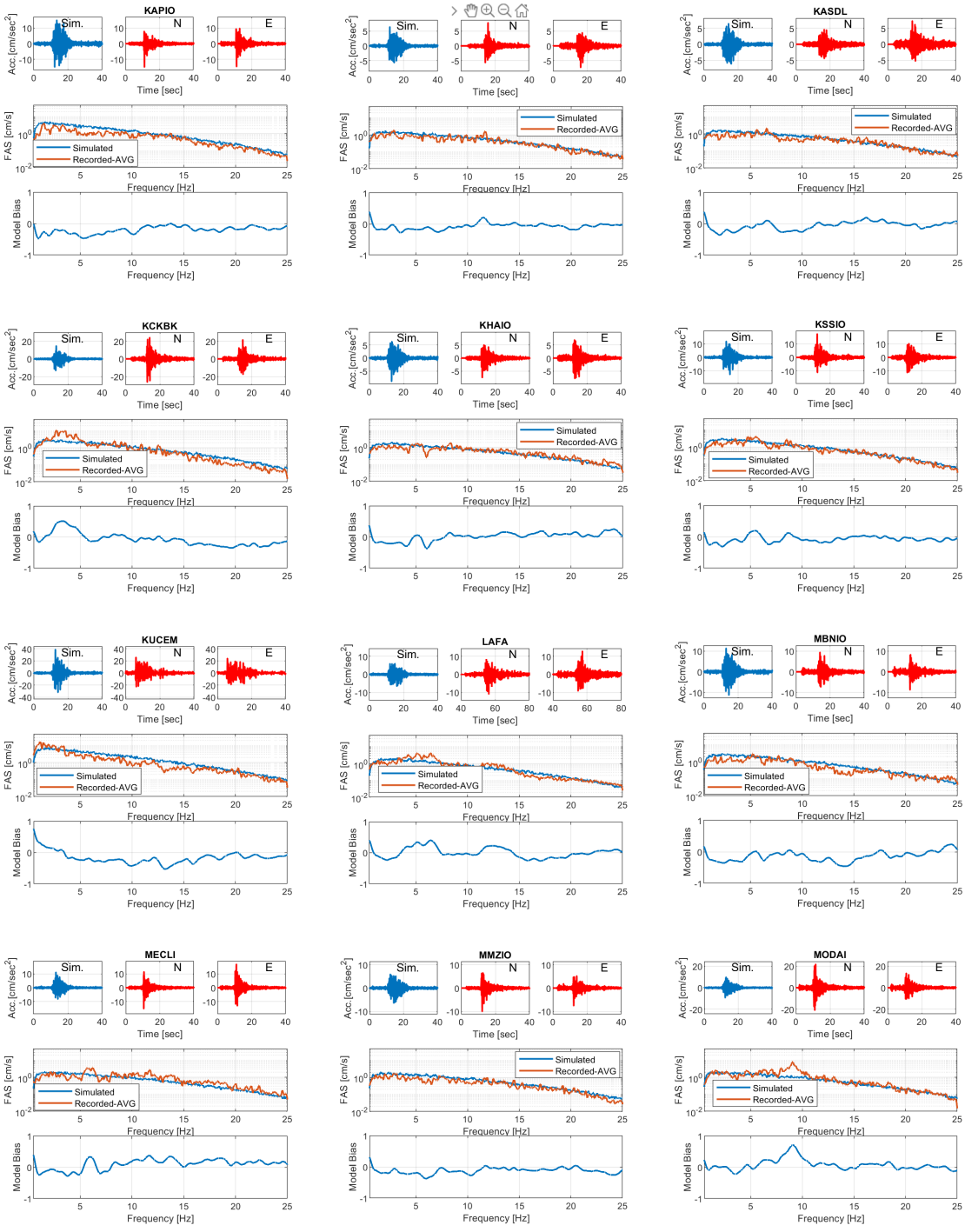
KAPIO
KASDL
KCKBK
KHAIO
KSSIO
KUCEM
LAFA
MBNIO
MECLI
MMZIO
MODAI
Sim.
N
E
Acc. [cm/sec^2]
Time [sec]
FAS [cm/s]
Simulated
Recorded-AVG
Frequency [Hz]
Model Bias

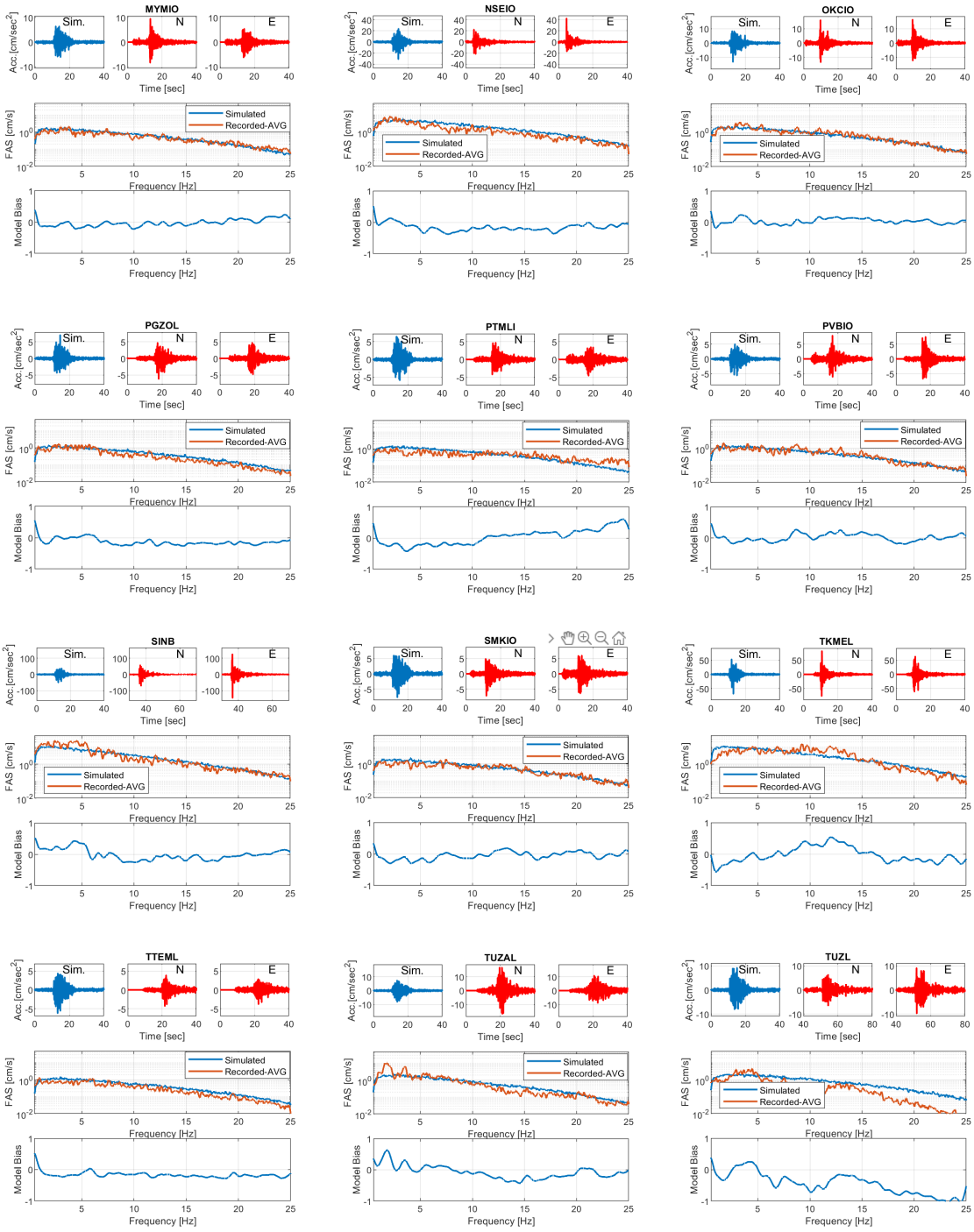
MYMIO
NSEIO
OKCIO
PGZOL
PTMLI
PVBIO
SINB
SMKIO
TKMEL
TTEML
TUZAL
TUZL
Sim.
N
E
Acc. [cm/sec^2]
Time [sec]
FAS [cm/s]
Simulated
Recorded-AVG
Frequency [Hz]
Model Bias

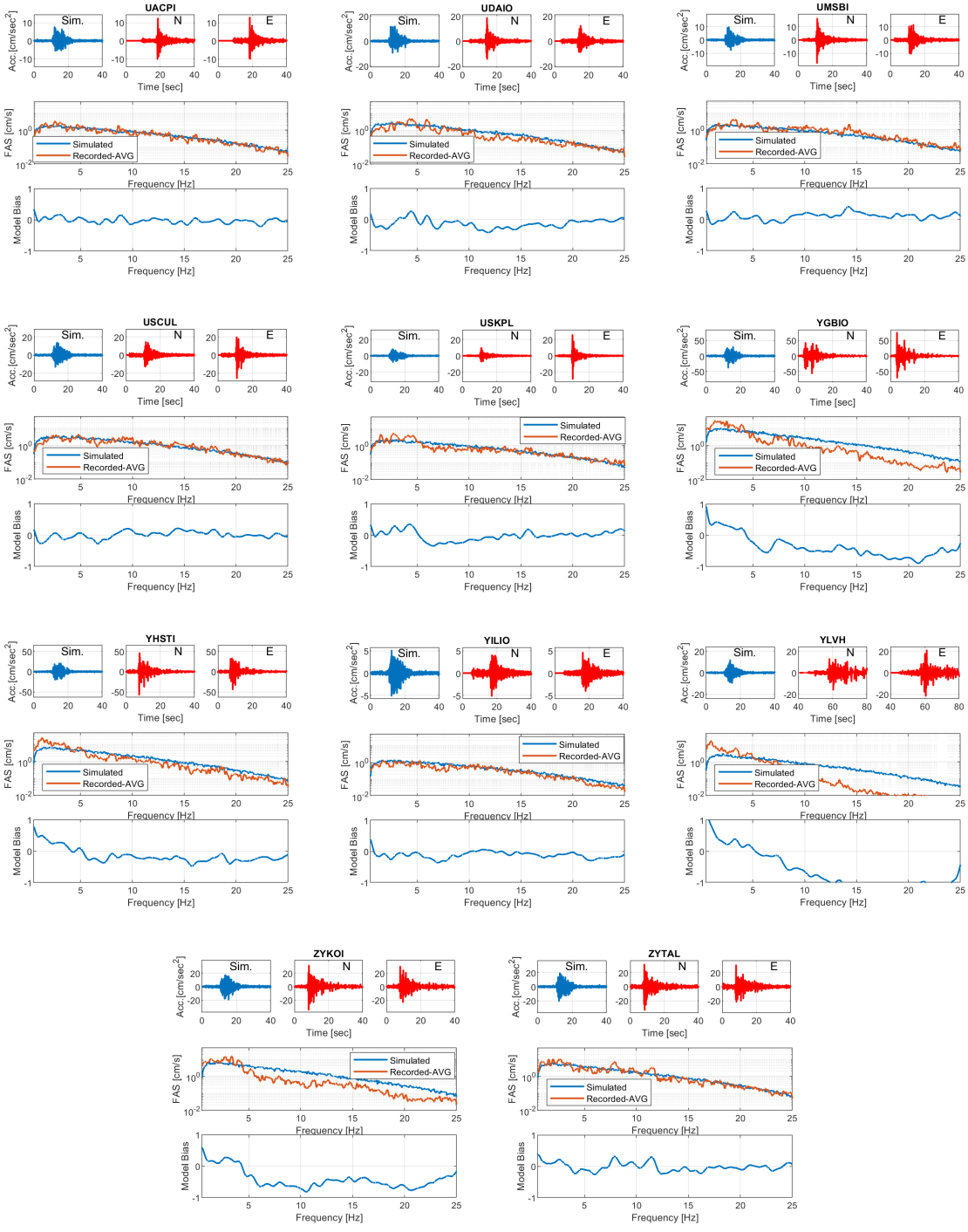
UACPI
UDAIO
UMSBI
USCUL
USKPL
YGBIO
YHSTI
YILIO
YLVH
ZYKOI
ZYTAL
Sim.
N
E
Acc. [cm/sec^2]
Time [sec]
FAS [cm/s]
Simulated
Recorded-AVG
Frequency [Hz]
Model Bias

B.2. 17 August 1999 Kocaeli Earthquake (19 Stations)

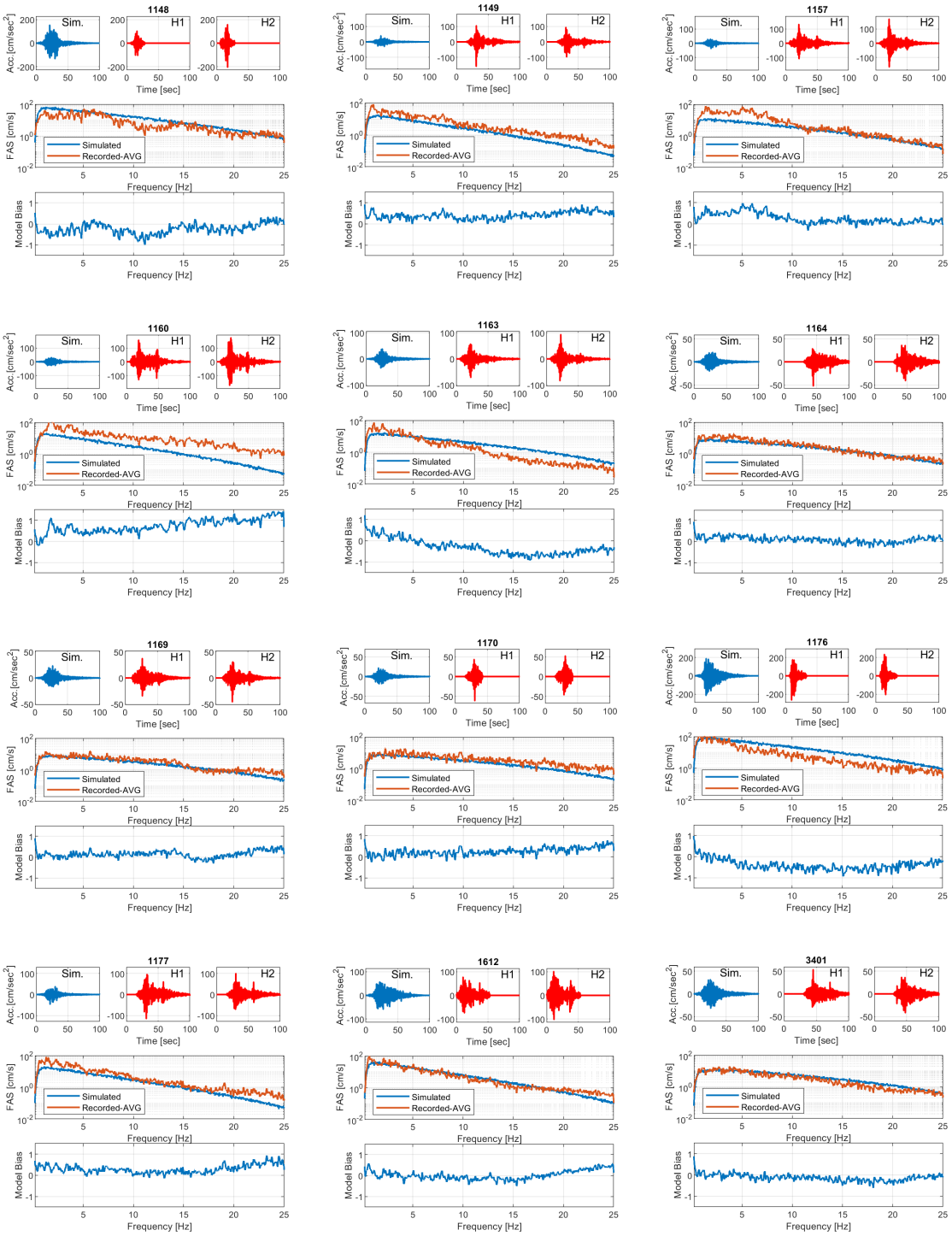

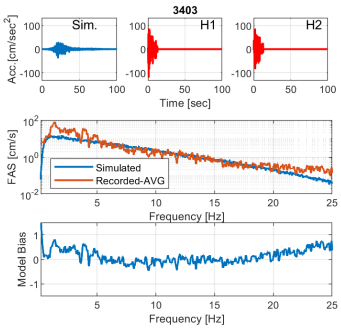
3403
Sim.
H1
H2
Acc.[cm/sec^2]
Time [sec]
FAS [cm/s]
Simulated
Recorded-AVG
Frequency [Hz]
Model Bias
Frequency [Hz]

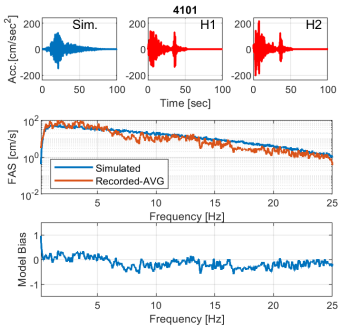
4101
Sim.
H1
H2
Acc.[cm/sec^2]
Time [sec]
FAS [cm/s]
Simulated
Recorded-AVG
Frequency [Hz]
Model Bias
Frequency [Hz]

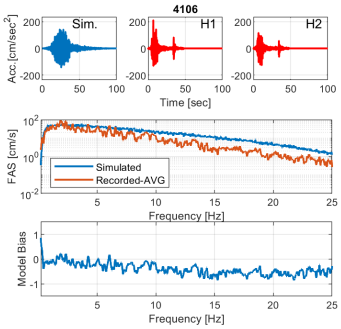
4106
Sim.
H1
H2
Acc.[cm/sec^2]
Time [sec]
FAS [cm/s]
Simulated
Recorded-AVG
Frequency [Hz]
Model Bias
Frequency [Hz]

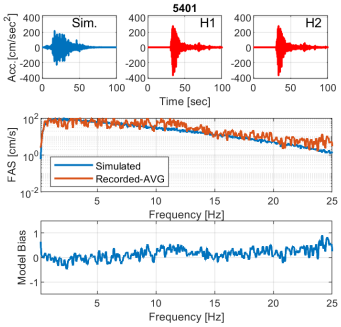
5401
Sim.
H1
H2
Acc.[cm/sec^2]
Time [sec]
FAS [cm/s]
Simulated
Recorded-AVG
Frequency [Hz]
Model Bias
Frequency [Hz]

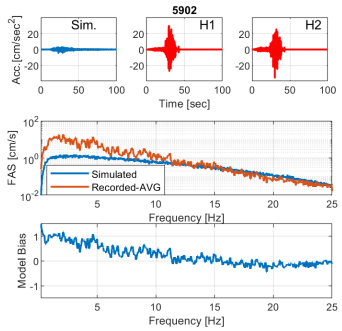
5902
Sim.
H1
H2
Acc.[cm/sec^2]
Time [sec]
FAS [cm/s]
Simulated
Recorded-AVG
Frequency [Hz]
Model Bias
Frequency [Hz]

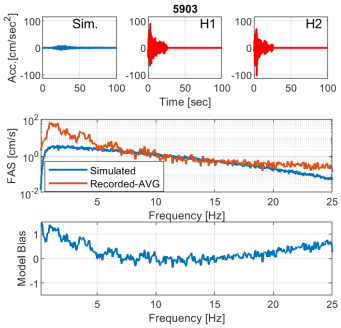
5903
Sim.
H1
H2
Acc.[cm/sec^2]
Time [sec]
FAS [cm/s]
Simulated
Recorded-AVG
Frequency [Hz]
Model Bias
Frequency [Hz]

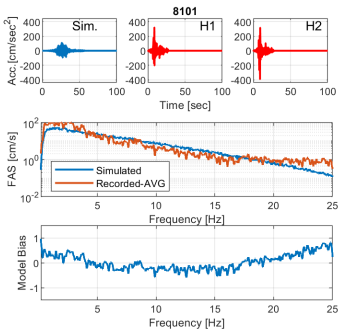
8101
Sim.
H1
H2
Acc.[cm/sec^2]
Time [sec]
FAS [cm/s]
Simulated
Recorded-AVG
Frequency [Hz]
Model Bias
Frequency [Hz]